Mimicking Ribonucleotide Reductases: Biomimetic Manganese Complexes and their Reaction with Superoxide

A thesis presented to the University of Dublin for the degree of Doctor of Philosophy by

Adriana Maria Magherusan

Under the supervision of Dr A. R. McDonald

School of Chemistry
Trinity College Dublin
September 2018

Author's Declaration

I declare that this thesis has not been submitted as an exercise for a degree at this or any other university and is my own work. Parts of the work described here are the result of collaboration and are acknowledged at the beginning of each chapter. I agree to deposit this thesis in the University's open access institutional repository or allow the library to do on my behalf, subject to Irish Copyright legislation and Trinity College Library conditions of use and acknowledgements.

……

Adriana Maria Magherusan

27/09/2018

Summary

An important discovery in class Ib ribonucleotide reductase's chemistry has been the identification of a Mn^{II}_2 active site, that required a superoxide anion ($O_2^{\bullet-}$), rather than dioxygen (O_2), to access a high-valent Mn^{II}_2 oxidant. Many synthetic mononuclear Mn model complexes have been prepared to mimic the structures and reactivity of Mn-metalloenzymes. However, the reactivity of a Mn^{II}_2 model complex with $O_2^{\bullet-}$ has never been investigated and this was the main objective of this thesis. The main topics of the work described in this thesis are the study of $O_2^{\bullet-}$ reactivity of Mn^{II}_2 complexes, preparation and characterisation of intermediates, to mimic the active postulated intermediates observed in class Ib Mn_2 RNRs. In chapter 2, we describe our initial discovery that complex $[Mn^{II}_2(O_2CCH_3)(N\text{-Et-HPTB})](ClO_4)_2$ (**1**) could be reacted with $O_2^{\bullet-}$ at low temperature (≤-40 °C), to form the metastable $[Mn^{II}Mn^{III}(O_2)(O_2CCH_3)(N\text{-Et-HPTB})]^+$ (**2**). This species was characterised by electronic absorption spectroscopy, showing features at λ_{max} = 460, 610 nm, typical of a Mn-peroxide species. EPR spectroscopy of **2** exhibited a 29-line signal characteristic of a $Mn^{II}Mn^{III}$ entity. Furthermore, XANES suggested a formal oxidation state change of Mn^{II}_2 in **1** to $Mn^{II}Mn^{III}$ for **2**. Moreover ESI-MS suggested a $Mn^{II}Mn^{III}$-peroxide complex. Upon activation with proton donors, the $Mn^{II}Mn^{III}$-peroxide (**2**) was capable of oxidising ferrocene and weak O-H bonds. These findings provided support for the postulated mechanism of $O_2^{\bullet-}$ activation at class Ib Mn_2 RNRs.

In successive work, we were interested in mimicking the other Mn-intermediates observed in the catalytic cycle of class Ib RNRs. This involved the preparation of another $Mn^{II}Mn^{III}$-peroxide complex, investigation and characterisation of the species formed upon activation of the peroxide complex with proton donors. Therefore the reactivity of complex $[Mn^{II}_2(O_2CCH_3)_2(BPMP)](ClO_4)$ (**4**) with $O_2^{\bullet-}$ at low temperature (≤-80 °C) was explored, resulting in formation of a metastable species (**5**). Adduct **5** was characterised by electronic absorption and EPR spectroscopies, ESI-MS, displaying features of a $Mn^{II}Mn^{III}$-peroxide complex (**5**). Unlike adduct **2**, whose $Mn^{II}Mn^{III}$-core proved to be unreactive at -40 °C, species **5** proved to be a nucleophilic oxidant in aldehyde deformylation. The preparation of a nucleophilic peroxo-$Mn^{II}Mn^{III}$ oxidant (**5**) was reported in chapter 3. Next, the reactivity of the $Mn^{II}Mn^{III}$-peroxide (**5**) towards acids was investigated. This involved the screening of different reaction conditions as well as different sources of proton donors. Adduct **5** was susceptible to acids at low temperatures (≤-80 °C). The addition of strong acids ($HClO_4$, HBF_4) to **5** resulted in the formation of a metastable adduct (**7**). Adduct **7** exhibited electronic absorption features

typical of a mixed valent $Mn^{II}Mn^{III}$ complex. Unfortunately, the EPR spectrum of **7** was saturated by a signal typical of a Mn^{II} species. Upon addition of strong acids to **5** the formation of a $Mn^{II}Mn^{III}$ species (**7**) was postulated. The reactivity of **5** was also investigated towards weaker acids. Interestingly, the addition of *p*TsOH (1 or 2 equivalents) to **5** exhibited electronic absorption features and an EPR signal typical of a $Mn^{III}Mn^{IV}$ species. Thus, by probing the reaction of peroxo adduct **5** with acids of different strength, distinct adducts formed. Upon addition of a strong acid to **5**, a $Mn^{II}Mn^{III}$ species was postulated while for reaction of **5** with low equivalents of a weak acid the formation of a mixed valent $Mn^{III}Mn^{IV}$ species was proposed. The evidence obtained for formation of mixed valent $Mn^{II}Mn^{III}$ and $Mn^{III}Mn^{IV}$ species was important, as such species have been postulated as intermediates in the catalytic cycle of class Ib Mn_2 RNRs.

The preparation of peroxo-$Mn^{II}Mn^{III}$ species upon reaction of Mn^{II}_2 complexes with $O_2^{\bullet-}$ was achieved in chapters 2 and 3. Besides, proof for formation of mixed valent $Mn^{II}Mn^{III}$ and high valent $Mn^{III}Mn^{IV}$ species was observed in chapter 4. Such adducts were postulated as intermediates in class Ib Mn_2 RNRs. We tried to synthesise another Mn^{II}_2 complex supported by the HPTP ligand. Firstly, when the reaction for the synthesis of the Mn_2 complex supported by the HPTP ligand was performed in air, a mixed valent Mn_6 complex was obtained. Nevertheless, the synthesis of a Mn^{II}_2 complex bridged by HPTP, two perchlorate anions and two acetonitrile solvent molecules was achieved ($[Mn_2(ClO_4^-)_2(CH_3CN)_2(HPTP)](ClO_4^-)$, **11**) under anaerobic conditions. Further studies on the reactivity of this complex with $O_2^{\bullet-}$ will provide further insight into the catalytic cycle of class Ib Mn_2 RNRs.

Besides the RNRs, we maintain a keen interest in the analogous catechol oxidase enzymes. These enzymes catalyse the oxidation of *o*-diphenols (catechols) to the corresponding quinones and contain a Cu_2 core. In the last chapter (chapter 6) of this thesis, we explored synthetic Cu^{II}_2 and Mn^{II}_2 complexes as model systems for catechol enzymes. While Cu^{II}_2 complexes have been widely investigated as catechol oxidase mimics, the catechol oxidase reactivity of Mn^{II}_2 complexes has been less explored. A series of Mn^{II}_2 and Cu^{II}_2 complexes supported by the same poly-benzimidazole ligand framework were synthesised. The catecholase activity of these complexes in acetonitrile medium using 3,5-di-*tert*-butylcatechol (3,5-DTBC) as a substrate was investigated. The Cu^{II}_2 complexes proved to be better catechol oxidase mimics (k_{cat} values ~45 h^{-1}) when compared to Mn^{II}_2 complexes (k_{cat} values ~8-40 h^{-1}).

Acknowledgements

This research project would not have been possible without the help and support of many people. First and foremost, I wish to express my gratitude to the supervisor of this project, Professor Aidan McDonald, for his invaluable support, assistance and guidance. I also thank him for his patience, advice and motivation throughout this project. I'm very grateful for all the opportunities he has offered me throughout my PhD and for always pushing me achieve what I wanted.

I would like to thank all the collaborators that have contributed to this project: Dr Ang Zhou, Subhasree Kal (great friend, you helped me have a great experience in Minnesota) and Prof Lawrence Que Jr (University of Minnesota) for access and training to the Bruker EPP 300 EPR spectrometer as well as the resonance Raman instrument; Dr Eric R. Farquhar (Brookhaven National Laboratory) and Daniel Nelis (Trinity College Dublin) for X-Ray absorption spectroscopy measurements and Max García-Melchor for DFT calculations; Prof. Wesley Browne (University of Groningen) for resonance Raman measurements. I'm also grateful to Prof Lawrence Que Jr for allowing me to work in his research lab in Minnesota for a month performing EPR and resonance Raman studies.

The technical staff in the School of Chemistry have been very supportive. Firstly, I'd like to thank Dr Brendan Twamley for the X-ray data collection and refinement for all the crystal structures reported in this thesis, for his enthusiasm and patience over the last 4 years! I also thank Dr Martin Feeney and Dr Gary Hessman for their help and patience when I had to perform the same mass spectrometry experiment more than 20 times. Dr John O'Brien and Dr Manuel Ruether have been very helpful with the NMR spectroscopic measurements. I am also grateful to Patsy Greene for all his support and advice.

I sincerely thank all of the members of the McDonald group, past and present: Andy, Xin, Paolo, Marta, Ciara, Duenpen, Peppe, Daniel, Philipp, Prasenjit, Bertrand and Ankita. I really enjoyed working with all of you! You've all put up with me over the last four years and I made memories and real friends that I will never forget. Andy was the first person I met in the lab, even though we had our disagreements (small ones!), I learnt a lot from him and we are still friends; he also read over part of this thesis and I want to thank him for that. I've known Ciara for 8 years and I must thank her for her support and for always making me laugh; Marta for her continues encouragement, help with chemistry and life in general, loads of advices, a true friend over the last 2 years! (Our lunches helped a lot with thesis writing😊). Paolo always had an answer for

every question I'd ask him and Peppe always helped with either research or computer advice. Daniel performed the XAS measurements and analysis and I'd like to thank him for that and for reading most of this thesis. I am grateful for everyone's help.

I'd also like to thank the very good friends I have made within the department. Thorri's group, in particular Amy, Sandra, Hannah and Isabel have always been there when things did not go great. Our trips (Madrid, Cork), cocktails, festivals, concerts and nights out make great memories that I'll never forget, and I am thankful for that. Amy (a faithful friend) deserves some special thanks for her constant encouragement and support, and a constant enthusiasm. All our chats, concerts (Little Hours and The Coronas) and donut breaks will be greatly missed! You made the PhD experience very enjoyable!

I would also like to thank my non-chemistry friends. Rachel, Aisling and Aoife, our coffee and dinners helped with the research, especially when I had a bad day in the lab. Cathal, you have been a source of encouragement, a constant support and thanks for always cheering me up.

Finally, I'd like to say a special thank you to my family. My sister (Cristina) and my mum (Viorica) have always been there for me during the good as well as the difficult moments. They have offered me invaluable support and always believed in me! I couldn't have done this without you. My sister (my best friend) has provided me with constant encouragement and I'm grateful for that. I'd also like to thank my grandparents, auntie and my uncle for their encouragement, without understanding what I am actually doing.

Abbreviations

(H_2)pda	picolyldiglycylamine
(sal)pn	1,3-bis(salicylideneamino)-2-propanol)
12-TMC	1,4,7,10-tetramethyl-1,4,7,10-tetraazacyclododecane
13-TMC	1,4,7,10-tetramethyl-1,4,7,10-tetraazacyclotridecane
14-TMC	1,4,8,11-tetramethyl-1,4,8,11-tetraazacyclotetradecane
3,5-DTBC	3,5-di-*tert*-butylcatechol
$6Me_2$-BPP	N,N-bis(6-methyl-2pyridylmethyl)-3-aminopropionate
6-Me-DPEN	N,N-bis(6-methyl-2-pyridilmethyl)ethane-1,2-diamine
$Ar^{tol}CO_2^-$	2,6-di(p-tolyl)benzoate
ATR-FTIR	attenuated total reflectance - Fourier transform infrared
B. anthracis	*Bacillus anthracis*
B. subtilis	*Bacillus subtilis*
Bcmp	2,6-bis(1,4,7-triazacyclonon-1-ylmethyl)-4-methylphenol
BDE	bond dissociation energy
bispicMe_2en	N,N'-bis(2-pyridylmethyl)-N,N'-dimethyl-1,2-ethanediamine
BPCPMP	2,6-bis({(carboxymethyl([(1-pyridyl)methylamino}methyl)-4-methylphenolato
Bpg	bis-picolylglycylamine
Bpmp	2,6-bis[bis(2-pyridylmethyl)aminomethyl]-4-methylphenol
Bpy	2,2'-bipyridine
C. trachomatis	*Chlamydia trachomatis*
CCA	cyclohexanecarboxaldehyde
Cyclen	1,4,7,10-tetraazacycledodecane-diaminopropane
DCM	dichloromethane
DFT	density functional theory
Dien	diethylenetriamine
DMF	N,N-dimethylformamide
DPH	diphenylhydrazine

E. coli	*Escherichia coli*
EDTA	ethylenediaminetetraacetate
EPR	electron paramagnetic resonance
ESI-MS	electrospray ionisation mass spectrometry
Et_2O	diethyl ether
Et_3N	triethylamine
EXAFS	extended X-ray absorption fine structure
FT-IR	fourier transform infrared
H_2TPP	5,10,15,20-tetraphenylporphyrin
H_3bpaa	N-[bis(6-pivalamido-2-pyridylmethyl)](N'-fluorophenylcarbamoylmethyl)amine
H_3bupa	bis[(N'-tert-butylurealy)-N-ethyl]-(6-pivalamido-2-pyridylmethyl)amine
HAA	hydrogen atom abstraction
HAT	hydrogen atom transfer
HBPMP	2,6-bis[(bis(2-pyridylmethyl)amino)methyl]-4-methylphenol
HPTB	N,N,N',N'-tetrakis(2- (benzimidazolyl))-2-hydroxy-1,3-diaminopropane
HPTP	N,N,N'N'-tetrakis(2-pyridylmethyl)1,3-diamino-2-hydroxypropane
Htppdo	N,N,N',N'-tetrakis(6-pivalamido-2-pyridylmethyl)-1,3-diaminopropan-2-ol
imL_5^2	N-methyl-N,N',N'-tris((1-methyl-4-imidazolyl)methyl)ethane-1,2-diamine
$L^7iso\text{-}q_2$	1,4-bis[(2-isoquinolinyl)methyl]-1,4-diazepane
$L^7py_2^H$	1,4-bis(2-pyridylmethyl)-1,4-diazepane
L^7q_2	1,4-bis[(2-quinolinyl)methyl]-1,4-diazepane
LMCT	ligand to metal charge transfer
L^{Ph4}	N,N,N',N'-tetrakis[(1-methyl-2-phenyl-4-imidazolyl)methyl]-1,3-diamino-2-propanolate.
M. tuberculosis	*Mycobacterium tuberculosis*
MCD	magnetic circular dichroism
Me_4alkox	1,3-bis(4,7-dimethyl-1,4,7-trizacyclononyl)-2-propanol
Me_2-EBC	4,11-dimethyl-1,4,8,11-tetraazabicyclo[6.6.2]hexadecane
Me_4-tpdp	N,N,N',N'-tetrakis{2-(6-methylpyridyl)methyl}-1,3-diaminopropan-2-

	olate
mL_5^2	N-methyl-N,N',N''-tris(2-pyridylmethyl)ethane-1,2-diamine
MnCat	manganese-catalase
Mn-HPCD	manganese homoprotocatechuate 2,3-dioxygenase
Mn-SOD	manganese-superoxide dismutase
$[MST]^{3-}$	N,N,N''-[2,2',2''-nitrilotris(ethane-2,1-dyil)]tris(2,4,6-) trimethylbenzenesulfonamido
N,N-bispicen	N,N-bis(2-pyridylmehyl)-1,2-diaminoethane
N4py	N,N'-bis(2-pyridylmethyl)-N-bis(2-pyridyl)methylamine
N-Et-HPTB	N,N,N',N'-tetrakis(2-(1-ethylbenzimidazolyl))-2-hydroxy-1,3-diaminopropane.
NrdI	flavodoxin
$NrdI_{hq}$	flavodoxin hydroquinone
$NrdI_{sq}$	flavodoxin semiquinone
OAT	oxygen atom transfer
OEC	oxygen evolving complex
OTf	trifluoromethanesulfonate
PCET	proton-coupled electron transfer
Ph-BIMP	2,6-bis[bis{2-(1-methyl-4,5-diphenylimidazolyl)methyl}aminomethyl]-4-methylphenolate
Phen	1,10-phenanthroline
Pmap	bis[2-(2-pyridyl)ethyl]-2-pyridylmethylamine
*p*MMO	particulate methane monooxygenase
PPA	2-phenylpropionaldehyde
PPh_3	triphenylphosphine
*p*TsOH	*para*-toluene sulfonic acid
PyOTf	pyridinium trifluoromethanesulfonate
Py-terpy	4'-(4-pyridyl)-2,2':6',2''-terpyridine
RFQ	rapid freeze quench
RNR	ribonucleotide reductase

RNRdb	ribonucleotide reductase database
ROS	reactive oxygen species
S. aureus	*Staphylococcus aureus*
S. typhimurium	*Salmonella typhimurium*
*s*MMO	soluble methane monooxygenase
TAML	tetraamido macrocyclic ligand
TBACl	tetrabutylammonium chloride
TBAOH	tetrabutylammonium hydroxide
TEMPO	(2,2,6,6-tetramethyl-piperidin-1-yl)oxyl
TEMPOH	2,2,6,6tetramethyl-piperidin-1-ol
Terpy	2,2':6',2''-terpyridine
TFA	trifluoroacetic acid
THF	tetrahydrofuran
TMC	tetramethylcyclam
TMP	tetramesitylporphyrin
Tmpa	tris(2-pyridylmethyl)amine
TMTACN	Me_3tacn; 1,4,7-trimethyl-1,4,7-triazacyclononane
ToF	time of flight
Tpa	tris-picolylamine
Tp^{iPr}(L)	hydrotis(3,5-diisopropyl-1-pyrazolyl)borate; L = pz^{iPr}H (3,5-diisopropylpyrazole) or 2-MeIm (2-methylimidazole)
Tp^{iPr2}	tris(3,5-diisopropyl-1-pyrazolyl)borate.
UV-Vis	ultraviolet - visible
XANES	X-ray absorption near-edge spectroscopy
XAS	X-ray absorption spectroscopy
XRD	X-ray diffraction

Contents

Chapter 1

Introduction

1.1 Metals in biology

Metalloproteins containing different metal centres such as iron, copper and manganese perform a variety of functions in biological systems. Nature developed iron metalloprotein systems that use dioxygen.[1] For example, hemerythrin, a carboxylate-bridged diiron (Fe_2) protein found in marine invertebrates, is a dioxygen carrier protein.[2] Methane monooxygenase is a widely investigated Fe_2 metalloenzyme that uses dioxygen to catalyse the oxidation of methane to methanol.[3] Copper proteins that activate dioxygen also perform a variety of biological functions. These include dioxygen transport (hemocyanin), aromatic ring oxidations (tyrosinase, cathechol oxidase) and methane oxidation (particulate methane monooxygenase).[4] Manganese is another transition metal used in nature to promote a variety of oxidative transformations. Manganese containing non-heme metalloenzymes that react with oxygen and its reduced derivatives ($O_2^{\bullet-}$, H_2O_2, H_2O) play important roles in biological systems. For example, manganese-superoxide dismutase (Mn-SOD) and manganese-catalases (MnCat) act as defence systems against reactive oxygen species (ROS) by their reaction with superoxide and hydrogen peroxide, respectively.[5, 6] Manganese dioxygenases[7, 8] and oxalate oxidases[9] perform substrate oxidations by reacting with molecular oxygen. Finally, ribonucleotide reductases (RNRs) are essential enzymes, which convert ribonucleotides into their corresponding deoxyribonucleotides, providing the precursors required for DNA synthesis and repair in all organisms.[10-12]

1.1.1 O_2-activating Fe_2 metalloenzymes

Dinuclear iron (Fe_2) metalloenzymes have been extensively studied by the scientific community.[13] The reactions performed by these enzymes make them an important field of research in both biochemistry and chemistry. For example, the role of RNR enzymes in DNA biosynthesis made them important targets for pharmaceutical applications such as antiviral and anticancer agents. Moreover, in chemistry, the development of environmentally friendly oxidation catalysts is essential.[13] The most studied of these enzymes is methane monooxygenase.[14-17] This enzyme can convert methane into methanol and exits in two forms: a particulate form (*p*MMO), which contains a Cu_2 site, and a soluble form (*s*MMO) that contains Fe_2 atoms in its active site. Other Fe_2 enzymes whose mechanisms have been widely investigated are toluene monooxygenase,[18] stearoyl-ACP Δ^9- desaturase,[19-21] and RNR.[22] In the mechanisms of all these enzymes, dioxygen is the active oxidant and a peroxo-Fe^{III}_2 adduct has been proposed to be a key intermediate (Scheme 1.1). Furthermore, depending on the

enzyme, the peroxo-Fe^{III}_2 intermediate was found to either react with a substrate or progress toward the formation of a high-valent Fe-oxo species.[1] The reactivity of O_2 activating Fe_2 enzymes depended on the stability and geometry of the peroxo intermediates. However, whereas peroxo-Fe^{III}_2 and high valent iron oxo species have been extensively studied, less attention has been paid to Mn enzymes.

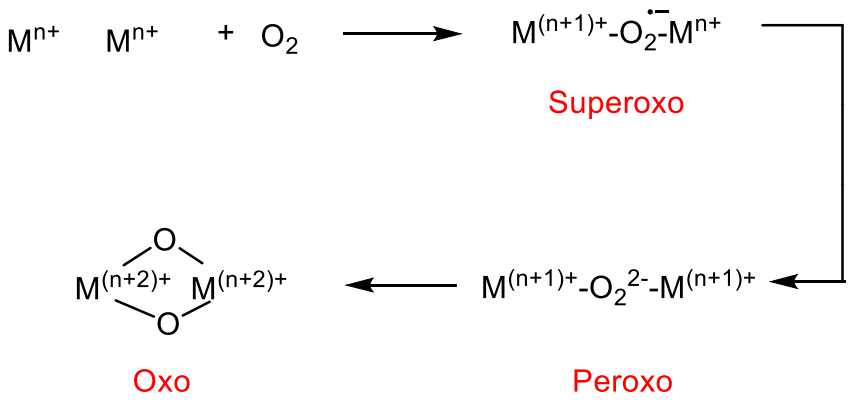

Scheme 1.1. Dioxygen activation by dinuclear complexes (M = metal).

1.1.2 Manganese metalloenzymes

In contrast to Fe dioxygen chemistry, Mn oxygen chemistry has only started to be explored in the last few decades.[23] Nature utilises Mn ions to perform a range of biological functions such as defence against ROS, biosynthesis of DNA and organic hydroperoxides and water splitting.[24, 25] These enzymes include Mn-SOD,[26, 27] MnCat,[6] RNRs,[28] and the oxygen evolving complex (OEC) of photosystem II.[29, 30] A characteristic of this broad class of metalloenzymes is that upon the reaction with dioxygen and its reduced species ($O_2^{\bullet-}$, H_2O_2, H_2O), reactive Mn-oxygen species such as Mn-superoxo, -peroxo and -oxo intermediates are proposed to form (Scheme 1.1). There are, however, very few well-characterised biological and synthetic models of Mn-enzymes when compared to the Fe enzymes. By exploring the model Mn enzymes, we should be able to improve our understanding on Mn intermediates and the mechanisms by which they are formed.

1.2 Ribonucleotide reductases (RNRs)

Life in all organisms is maintained by a pool of DNA building blocks for processes such as cell division and DNA damage repair.[31] This pool is maintained by the enzymatic machine ribonucleotide reductase. RNRs are essential enzymes, that convert ribonucleotides to their corresponding deoxyribonucleotides, providing the precursors required for DNA synthesis and repair in all organisms.[10, 32] The production of a balanced supply of deoxyribonucleotides is required for cellular DNA synthesis and growth, as this process is allosterically regulated, especially in higher organisms. The initial and rate limiting step in DNA synthesis is represented by the RNR system.[33]

RNRs play a pivotal role in the regulation of DNA synthesis. The discovery of the first RNR protein was carried out in the 1960s by Reichard and co-workers in *Escherichia coli* (*E. coli*).[34, 35] They observed a reaction involving ribonucleotides, where a carbon bound OH-group could be exchanged by a hydrogen atom (Scheme 1.2). Since then, many new crystal structures have been obtained of the protein subunits of RNRs, that are collected in a database, the ribonucleotide reductase database (RNRdb).[36] The main role of this archive is to supply a resource for RNR diversity and distribution in nature. The key role of RNR enzymes in DNA synthesis and repair is a very important target for anticancer, antibacterial or antiviral agents. In recent years novel and crucial developments have occurred in the RNR field, such as several RNR inhibitors have entered clinical trials, new 3D structures of di-Mn/Fe RNRs have been reported, and structural developments of human and yeast RNR advanced.[28, 37-39]

RNRs are structurally complex molecular machines that require a protein radical for activity. They use a free radical mechanism to convert a C-OH bond at the 2'-position of the ribose moiety to a C-H bond (Scheme 1.2). All RNRs share a common catalytic mechanism involving the activation of the ribonucleotide by abstraction of the 3'-hydrogen atom of the ribose by a transient thiyl radical of the enzyme.[22, 40] RNRs have been divided into three classes (I, II and III) based on differences in their metal cofactors, their interaction with oxygen and the way in which they generate their thiyl radical.[22, 41, 42] Class I RNRs use iron and oxygen for their tyrosyl radical generation, class II require a radical of the cobalamin cofactor (vitamin B12) while anaerobic class III forms a stable glycyl radical by means of an iron-sulfur cluster.[22, 41, 42] The radicals are important in the reaction mechanism as they are involved in the conversion of ribonucleotides to deoxyribonucleotides.

Scheme 1.2. Reduction of ribonucleotides to their corresponding deoxyribonucleotides.[40]

In summary, major advances in recent years concern the structure and regulation of RNRs. These have led to a better understanding of the structural basis of these enzymes. However, until now, few synthetic model complexes that mimic the active sites of the enzymes have been reported. Thus, we are interested in gaining a better understanding of RNRs by using biomimetic complexes. Firstly, a detailed description of the core dimensions, structures and active sites of RNRs will be given below.

1.2.1 Class I RNRs

Class I RNRs are strictly aerobic enzymes. They are the best-known and most-studied of the RNRs. Class I RNRs are found in a wide range of organisms: eukaryotes, prokaryotes, viruses and bacteriophages.[31] Class I has been further divided into three subclasses Ia, Ib and Ic, based on the type of metal centre required for the protein radical (Table 1.1). Class Ia uses a Fe_2 metallocofactor *in vivo*, class Ib a Mn_2 or a Fe_2 cofactor and class Ic uses a Mn-Fe cofactor.[41] Class Ia exists in eukaryotes, prokaryotes, viruses and bacteriophages, while classes Ib and Ic have only been found in prokaryotes. All three class I subclasses contain two homodimeric subunits α (R1) and β (R2). The catalytic subunit is the α-subunit, which harbours the active site for nucleotide reduction and two allosteric sites, for substrate specificity and general enzyme activity. The β subunit contains the cofactor essential for the initiation of nucleotide reduction.[41]

Table 1.1. Overview of the three classes of RNR.[41]

	Class Ia	Class Ib	Class Ic	Class II	Class III
Subunit structure	$\alpha_2\beta_2$	$\alpha_2\beta_2$	$\alpha_2\beta_2$	α or α_2	$\alpha_2\beta_2$
Metal site	Fe_2	Mn_2 or Fe_2	MnFe	Deoxyadenosyl-Cobalamin	4Fe-4S, S-adenosylmethionine
Radicals involved in turnover	Tyrosyl, Cysteinyl	Tyrosyl, Cysteinyl	Mn-Fe, $Fe^{IV}Fe^{III}$, Cysteinyl	Cysteinyl	Glycyl, Cysteinyl
Oxygen dependence	Aerobic	Aerobic	Aerobic	No dependency	Anaerobic
Occurrence	Eukaryotes, Prokaryotes, Bacteriophages, Viruses	Eubacteria	Eubacteria	Archaebacteria, Eubacteria	Archaebacteria, Eubacteria, Bacteriophages

1.2.2 Class II RNRs

Class II RNRs are found in bacteria and archaea. This class is oxygen independent and these enzymes can function under both aerobic and anaerobic conditions. Class II RNRs contain a single subunit and have been isolated either as monomers or dimers. A characteristic feature of class II RNRs is the requirement for adenosylcobalamin, a vitamin B_{12} derivative, as a cofactor (Table 1.1).[22] This cofactor interacts directly with an active site cysteine to form the cysteine radical, used for ribonucleotide reduction.[22]

1.2.3 Class III RNRs

Class III RNRs are found in anaerobic bacteria and some bacteriophages. Unlike class I and class II RNRs, these enzymes are anaerobic, and they are inhibited by oxygen (Table 1.1). They consist of two subunits; two dimeric proteins are required for activity. This class contains a redox-active [4Fe-4S] centre, which together with S-adenosylmethionine and reduced flavodoxin generates a stable oxygen-sensitive glycyl radical.[41] This radical helps in generating a cysteine radical, which it is required for conversion of ribonucleotides to deoxyribonucleotides.

1.3 Catalytic cycle class I RNRs

1.3.1 Catalytic cycle class Ia RNRs

As discussed above, RNRs catalyse the rate-limiting step in DNA biosynthesis in all organisms (reduction of ribonucleotides to their corresponding deoxyribonucleotides). RNRs use a free radical mechanism for initiation of ribonucleotide reduction. In class I RNRs the radical needed for the reduction of ribonucleotides is stored on the protein subunit R2, separate from the active subunit R1. This radical is deeply buried inside the R2 subunit protected from the solvent and it is generated on a tyrosine residue close to a Fe_2 centre.[41] Class Ia RNRs are found in all eukaryotes and some prokaryotes, such as *E. coli*. The first crystal structure of a class Ia RNR was the *E. coli* R2 published by Nordlund *et. al* in 1990[43] with some refinements in 1993.[44] The crystal structure obtained from *E. coli* confirmed that two Fe atoms were found in the R2 binding site with a potential tyrosyl radical (Y_{122}) site close by (Figure 1.1).

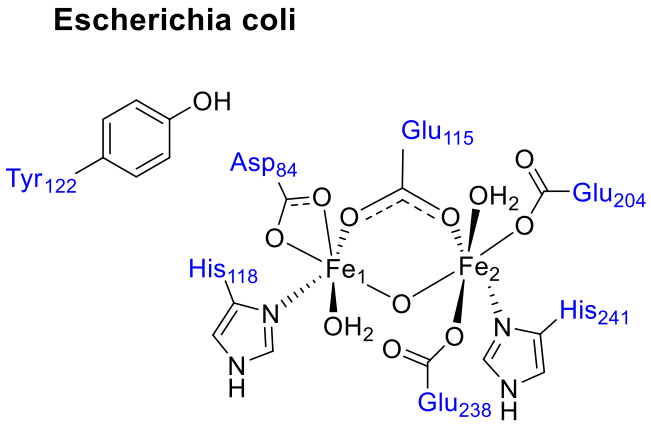

Figure 1.1. Metallocofactor structure found in class Ia RNR in *E. coli*.[44]

The protein has a α-helical structure and each of the Fe_2 centres is coordinated by one aspartate (Asp_{84}), two histidines (His_{118} and His_{241}) and three glutamate residues (Glu_{115}, Glu_{204} and Glu_{238}), that are brought together on the inside of a four α-felix bundle. The oxygen activation of the Fe_2 centre *in vivo* is poorly understood and little data is available. However, in the purified *E. coli* samples, *in vitro* O_2 incorporation has been studied in detail in a process called the reconstitution reaction.[45-49] The Fe_2 centre and the tyrosyl radical were formed when molecular oxygen reacted with the Fe_2R_2 subunit (Scheme 1.3).[33]

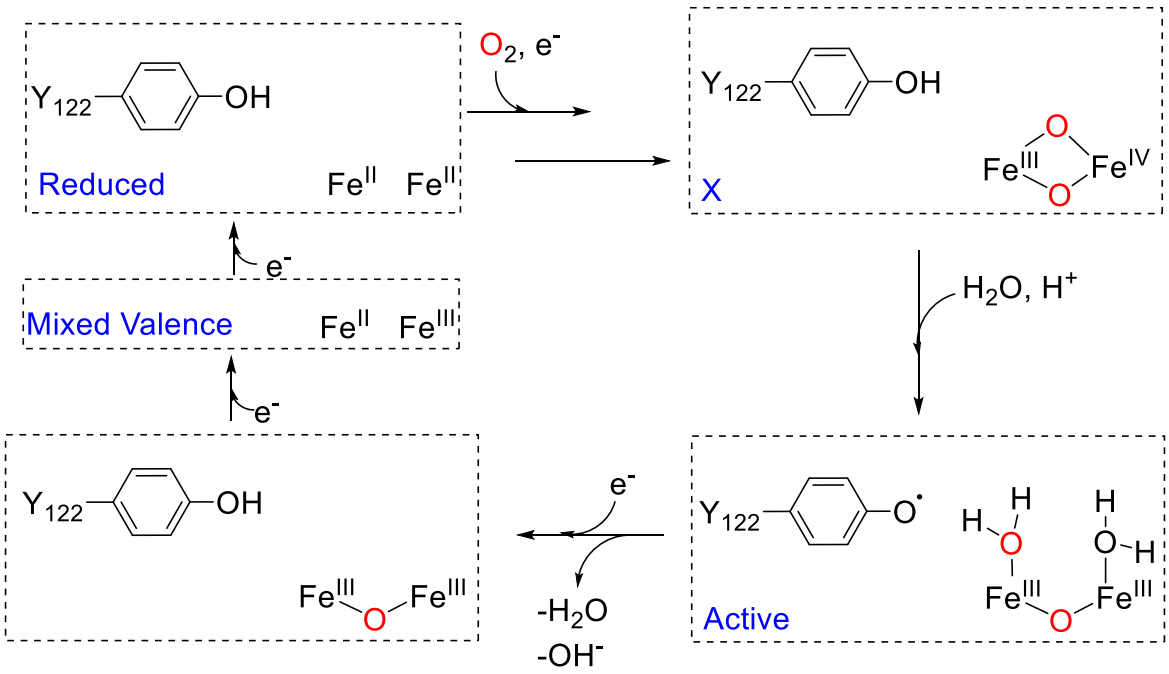

Scheme 1.3. Proposed O_2-activation pathway in Fe^{III}_2-$Y^{\bullet}$ cofactor of class Ia RNR in *E. coli* (Y = tyrosine, X = intermediate).[33]

Four electrons are required for the reduction of dioxygen into water. A postulated reaction pathway for the generation of tyrosyl radical in class Ia *E. coli* R2 has been proposed (Scheme 1.3). The Fe_2 cofactor reacted with O_2 to form intermediate X. Intermediate X has been characterised by a series of spectroscopic techniques: electronic absorption spectroscopy, Mössbauer, electron paramagnetic resonance (EPR), extended X-ray absorption fine structure spectroscopy (EXAFS) and magnetic circular dichroism (MCD).[50-58] Based on these structural studies, adduct X was shown to have a $Fe^{III}Fe^{IV}$ centre with at least one oxo-bridge. In the $Fe^{III}Fe^{IV}$ core, the Fe^{IV} centre was at the distal position to the tyrosine residue, which was oxidised by X to generate the tyrosine radical. The high-valent intermediate X then abstracted a hydrogen atom from a nearby tyrosine. The newly formed tyrosyl radical then transferred the resulting electron hole over ~35 Å by a series of hole-hopping and/or proton-coupled electron transfer (PCET) steps, ultimately leading to the initiation of substrate reduction by abstraction of the 3'-H. In summary, the oxidation of Fe^{II}_2 to Fe^{III}_2 generated two electrons, while the oxidation of a tyrosine residue (Y_{122}) to the tyrosyl radical ($Y_{122}^{\bullet}$) active metal site provided the third electron. The last electron could come from an external reductant, but the exact source is still uncertain.

These investigations provided fundamental insight into the O_2-activation mechanism of the Fe^{II}_2 site and how the tyrosine radical is generated. Nonetheless, there are still concerns whether the

oxo bridge is protonated.[56, 57, 59] Therefore efforts are still ongoing to trap and characterise the intermediates formed in class Ia *E. coli* RNR subunit.

1.3.2 Catalytic cycle of class Ic RNRs

Class Ic RNR from *Chlamydia trachomatis* (*C. trachomatis*) uses a Mn/Fe heterobinuclear cofactor, rather than a Fe/Fe cofactor found in the R2 subunit of class Ia RNR enzymes, to react with O_2.[60] Also, the position occupied by the tyrosine residue (Y_{122}) in class Ia is instead occupied by a phenylalanine (Phe_{127}, Figure 1.2), which does not produce a radical.

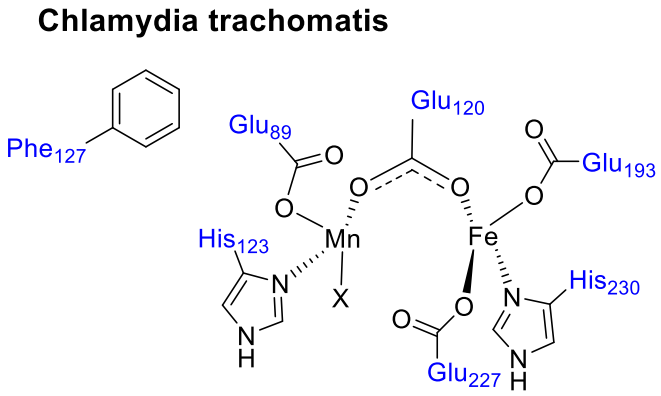

Figure 1.2. Metallocofactor structure in class Ic RNR (X = solvent).[60]

Based on many studies of class Ic RNRs, a metal centre with the $Mn^{IV}Fe^{III}$ redox state was found responsible for the radical initiation. The reaction of the $Mn^{II}Fe^{II}$ site with O_2 generated the oxidised cofactor. The reaction proceeded through a $Mn^{IV}Fe^{IV}$ intermediate, that underwent one electron reduction[61] to form the catalytically active $Mn^{IV}Fe^{III}$ site (Scheme 1.4).[62] The structure of this cofactor has not yet been crystallographically established, but a series of spectroscopic techniques such as Mössbauer, EXAFS and X-ray diffraction crystallography have been used to study the cofactor site.[63-66] Based on the atomic distances a structure with oxo, hydroxo bridges was favoured and the Mn was observed in the metal site 1, close to Phe_{127}.[65-67] The four oxidising equivalents required to form the $Mn^{IV}Fe^{IV}$ intermediate from $Mn^{II}Fe^{II}$ could also be provided by two equivalents of H_2O_2 and a stepwise mechanism. The first equivalent oxidised the $Mn^{II}Fe^{II}$ cluster to the $Mn^{III}Fe^{III}$ state. The $Mn^{IV}Fe^{IV}$ state formed upon reaction of the $Mn^{III}Fe^{III}$ state with a second equivalent of H_2O_2. As with O_2-activation, the $Mn^{IV}Fe^{IV}$ state was reduced to the active $Mn^{IV}Fe^{III}$ cofactor.[31] However, the geometric and electronic structure of the $Mn^{IV}Fe^{III}$ adduct and how the transport mechanism relates to the analogues processes in the tyrosine-radical dependent class Ia still remains unclear.

The protein *C. trachomatis* generated a radical equivalent $Mn^{IV}Fe^{III}$ oxidation state of the metal site,[63, 65] as opposed to the thiyl radical generated by the other subclasses. X-ray crystallography was used to show that the Mn ion was at metal position 1 in this cofactor.[65] This is the position proximal to the thiyl radical site in the other proteins.[33] Thus, it had been postulated that the high valent Mn^{IV} species acts as a direct substitute for the tyrosyl radical.

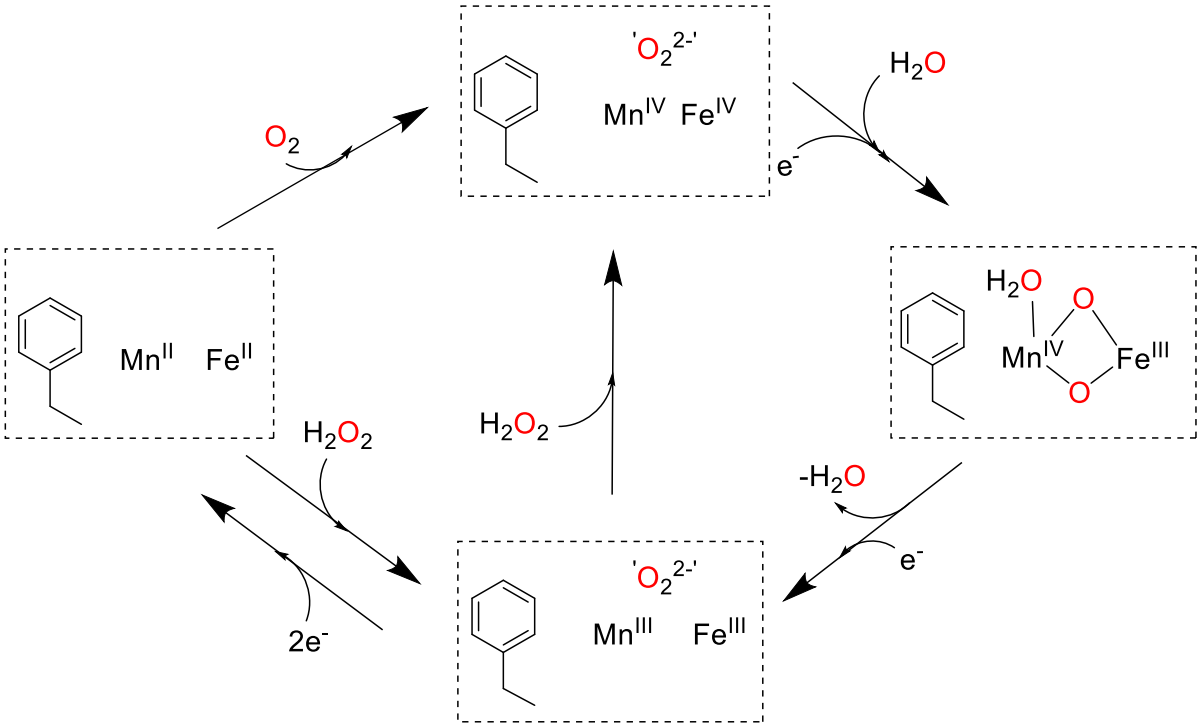

Scheme 1.4. Proposed catalytic cycle for class Ic MnFe RNRs in *C. trachomatis*.[63-67]

1.4 Structural description of class Ib Mn_2 RNRs

Class Ia RNR uses a Fe_2 cofactor for catalytic activity, class Ic uses a MnFe cofactor and class Ib RNRs can use either a Mn_2 or a Fe_2 centre for formation of the protein radical. Class Ib RNRs have identical metal-binding residues to class Ia RNR and class Ib RNR, which have been long assumed to contain only Fe^{III}_2-Y• cofactors. It was not until 2010, when the Stubbe group provided evidence that class Ib RNR can also have a Mn^{III}_2-Y• cofactor, as well as a Fe^{III}_2-Y• cofactor.[68]

Class Ib RNRs are one of the most studied enzymes. Class Ib RNRs are found in prokaryotes and numerous pathogens such as *Staphylococcus aureus (S. aureus), Mycobacterium tuberculosis (M. tuberculosis), Bacillus anthracis (B. anthracis), E. coli, C. ammoniagenes* and *Bacillus subtilis (B. subtilis)*. Class Ib RNR comprises of two subunits α2 (NrdE) and β2 (NrdF), that are structurally homologous to class Ia subunits having almost identical metal-binding residues, with subtle differences in the second coordination sphere. The catalytic subunit is the

α-subunit, which harbours the active site for nucleotide reduction and two allosteric sites, for substrate specificity and general enzyme activity. The β subunit contains the cofactor essential for initiation of nucleotide reduction.[69] Class Ib RNRs have structural similarities to class Ia RNRs. We will mainly focus on description of *E. coli*, *C. ammoniagenes* and *B. subtilis*, as the structure of the active sites of these metalloenzymes was of interest to us.

The crystal structure reported of *E. coli* Mn_2^{II}-NrdF revealed the presence of two fully occupied Mn_2 sites.[28] The Mn···Mn distance was 3.7 Å and the two Mn centres were bridged by three glutamate residues: Glu_{98}, Glu_{158} and Glu_{192} (Figure 1.3). While one of the Mn centres was also coordinated by His_{101}, Asp_{67} and a H_2O molecule, the second Mn atom was coordinated by His_{145} and a terminal H_2O molecule. Each Mn^{II} was six-coordinate and it has been proposed that ligand reorganisation or dissociation of H_2O molecules was necessary for reaction of the oxidant with the cluster.

The crystal structure of *B. subtilis* Mn_2^{II}-NrdF has also been reported, being different from that of *E. coli* Mn_2^{II}-NrdF with a fully ordered and occupied Mn_2 site.[70] The results obtained prove that diverse coordination geometries can serve as a starting point for the Mn_2^{III}-$Y^{\bullet}$ cofactor assembly in class Ib RNRs. The distance between the two metal sites in *B. subtilis* Mn_2^{II} was 3.9 Å, the two Mn centres being further apart than the ones in *E. coli* Mn_2^{II}-NrdI. While both Mn ions were bridged by residues Glu_{97} and Glu_{198}, one of the Mn centres was also coordinated by His_{201}, Glu_{164} (as a bidentate ligand) and a weakly bound H_2O molecule (Figure 1.3). Thus, one of the Mn centres was coordinatively saturated, as the one in *E. coli*. However, the second Mn was five-coordinate, bridged by His_{101} and Asp_{66} in a bidentate mode.

A crystal structure for the Mn dimer of the R_2F subunit of the ribonucleotide reductases of *C. ammoniagenes* has also been reported.[71] X-ray crystallography showed that the active site of *C. ammoniagenes* contains an oxo/hydroxo-bridged Mn dimer, near a tyrosine residue (Y_{115}, Figure 1.3). While one of the Mn centres was proximal to the tyrosine residue, the second Mn centre was distal. The distance between the Mn centres was 3.3 Å. A glutamic acid as well as a histidine residue coordinated the two Mn centres in *C. ammoniagenes*. An aspartate residue coordinated one of the Mn centres, while the second Mn centre was bridged by two glutamic acids.[71] A Mn-$O_{oxo/hydroxo}$-Mn angle of ~120 ° was observed in this enzyme. In addition to the oxo/hydroxo oxygen, an asymmetric oxygen has also been observed in *C. ammoniagenes*. One of the Mn centres was also bridged by an oxygen atom from a terminal water molecule, which was not coordinated to the second metal centre.

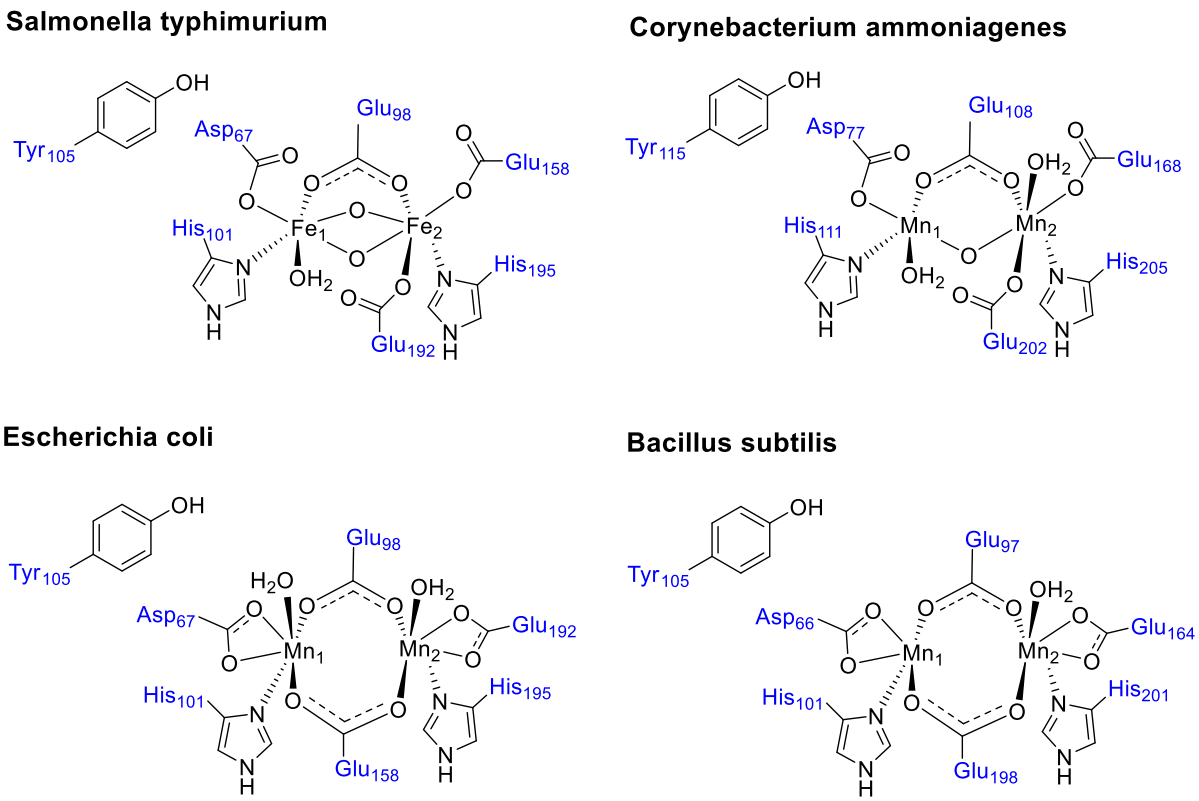

Figure 1.3. Metallocofactors structures found in class Ib RNRs.[28, 70-72]

All three class Ib Mn_2-RNRs (*E. coli*, *B. subtilis* and *C. ammoniagenes*) described above were structurally similar. The two metal centres of all three bacteria were either five or six-coordinate (Table 1.2), and it has been proposed that dissociation of the water molecule was required for reaction of the cluster with the oxidant. Furthermore, the separation between the two metal centres of *C. ammoniagenes* was shorter than the one found in *E. coli* Mn_2^{II}-NrdF subunit, 3.7 Å and *B. subtilis* Mn^{II}_2, 3.9 Å. Whereas both Mn centres in *C. ammoniagenes* were in an oxidation state of +3, a longer Mn···Mn separation would be expected in the reduced Mn^{II}_2 form of the enzyme, as observed in Mn catalases, *T. thermophilius* and *L. plantarum*. Another difference consisted in the number and bridging modes of carboxylate groups that coordinate to the metal centres of these bacteria.

Table 1.2. Comparison of structural properties of *E. coli*, *B. subtilis*, *C. ammoniagenes* and *S. typhimurium* of class Ib RNR (M = metal).

	Class Ib RNRs							
	***E. coli* (Mn^{II}_2)**		***B. subtilis* (Mn^{II}_2)**		***C. ammoniagenes* (Mn^{III}_2)**		***S. typhimurium* (Fe^{III}_2)**	
	Mn1	Mn2	Mn1	Mn2	Mn1	Mn2	Fe1	Fe2
Coordination Number	6	6	6	5	6	5	6	6
M···M (Å)	3.7		3.9		3.3		3.3	

All the above class Ib RNRs used a Mn_2 metallocofactor for catalytic activity. However, class Ib could also use a Fe_2 centre and one example was *Salmonella typhimurium* (*S. typhimurium*). The two Fe atoms of *S. typhimurium* were ligated by two histidines, three glutamates and one aspartate (Figure 1.3).[72] The two ferric ions were bridged by one of the glutamate residues and an O^{2-} ion. The Fe···Fe bond distance between the two ions was 3.3 Å (Table 1.2). Also, the distances between the O^{2-} ion and the Fe centres were 1.8 Å. The coordination environment of both Fe ions was octahedral, as indicated in Figure 1.3. The metal-metal bond distance in *S. typhimurium* was the same as the one observed in *C. ammoniagenes*. Even though they had a different metal in the active site (Mn for *C. ammoniagenes* and Fe for *S. typhimurium*), they had the same oxidation state so similarly bond lengths would be expected. Also, the coordination of Fe_2 in *S. typhimurium* was identical to that in class Ia *E. coli* R2 structure (Figure 1.1 from class Ia).

Therefore, class Ib RNRs had either a Mn^{II}_2 or a Fe^{II}_2 metallocofactor, and they were structurally similar (Table 1.2), the metal centres were either 5- or 6-coordinate. The metal-metal bond distance was longer in *E. coli* and *B. subtilis*, as they had a Mn^{II}_2 core and as expected a shorter metal-metal distance was observed in *C. ammoniagenes* and *S. typhimurium*, where the metal centres are in a +3-oxidation state. Additionally, the catalytic cycle of *E. coli*, *C. ammoniagens* and *B. subtilis* will be described below.

1.4.1 Class Ia and Ib RNRs

As seen above (section 1.3), in class Ia RNRs, O_2 was the active oxidant. The metallocofactor responsible for the conversion of tyrosine to tyrosyl radical was a high valent Fe_2 species. The high valent $Fe^{III}Fe^{IV}$ intermediate abstracted a hydrogen atom from the tyrosine residue forming the tyrosyl radical.[33] This radical was responsible for conversion of ribonucleotides to deoxyribonucleotides. In contrast, in class Ib RNRs, the proposed oxidant was either $O_2^{\bullet-}$ or H_2O_2 (see below).

1.4.2 *E. coli* catalytic cycle

Class Ib *E. coli* RNR was expressed under Fe-limited and oxidatively stressed conditions. In the first step of the catalytic cycle $NrdI_{hq}$ was proposed to reduce O_2 to H_2O_2 (Scheme 1.5). The oxidant travelled to the metal site and it was proposed to bind terminally to one of the Mn centres.[46][73] A second equivalent of H_2O_2 was needed to generate the $Y^{\bullet}$ (second step, catalytic cycle in Scheme 1.5). A mixed valent $Mn^{III}Mn^{IV}$ intermediate formed, that abstracted a hydrogen atom from the tyrosine residue forming the tyrosyl radical.[74-78] This was also observed in the mechanistic pathway of class Ia RNRs Fe^{III}_2-$Y^{\bullet}$ cofactor assembly.[51, 79, 80]

1.4.3 *C. ammoniagenes* catalytic cycle

The structure of *C. ammoniagenes* R2F, together with EPR data helped provide further insight into the mechanism of oxygen activation at class Ib RNRs. Mechanistic pathways have been proposed by the research laboratories of Stubbe and Lubitz/Auling by which the Mn^{II}_2 cluster was oxidised to the Mn^{III}_2-$Y^{\bullet}$ species (Scheme 1.5).[31, 68, 71, 81] These were based on structural data, model systems and the mechanism of MnCat.[74, 82]

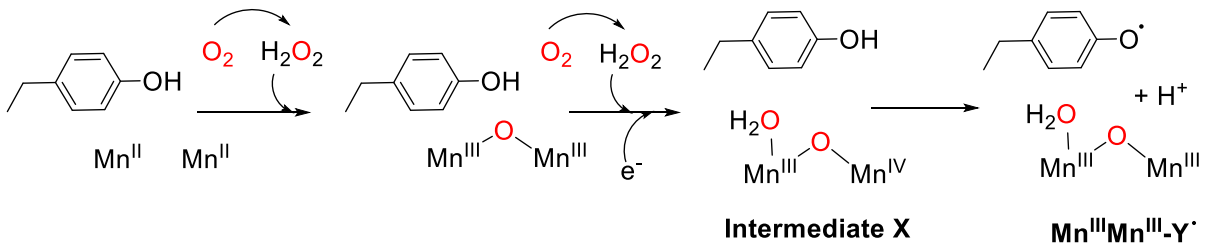

Scheme 1.5. Proposed catalytic cycle for class Ib Mn_2 RNRs in *E. coli* and *C. ammoniagenes*.[31, 68, 71, 81]

In the first step, the $Mn^{II}Mn^{II}$ cluster was oxidised through a two-electron oxidation to $Mn^{III}Mn^{III}$. The second step involved a μ-oxo bridged $Mn^{III}Mn^{III}$ species that generated "intermediate X" (Scheme 1.5). This intermediate had sufficient oxidising power to extract both one electron and a proton (i.e. a hydrogen atom) from the tyrosine.[23, 31, 68, 71, 73, 81] Therefore, "intermediate X" extracted a hydrogen atom from the tyrosine Y_{115}, resulting in the formation of the $Mn^{III}Mn^{III}$-$Y^{\bullet}$ cofactor. In summary the same catalytic cycle was proposed for class Ib *E. coli* and *C. ammoniagenes* RNRs, where H_2O_2 was the active oxidant.

1.4.4 *B. subtilis* catalytic cycle

B. subtilis is another class Ib RNR, that contains a Mn^{II}_2 metallocofactor. As in the case of *E. coli* and *C. ammoniagenes*, it was difficult to determine whether the active oxidant was $O_2^{\bullet-}$ or H_2O_2. The previous results of Stubbe and co-workers showed that the Mn^{III}_2-$Y^{\bullet}$ cofactor assembly reconstitution required the presence of Mn^{II}_2, O_2 and $NrdI_{hq}$. In comparison to *B. subtilis*, studies of Mn^{III}_2-$Y^{\bullet}$ assembly in *E. coli* suggested that NrdI (flavodoxin) reacted with O_2 to generate an oxidant capable to oxidise the Mn^{II}_2 cluster.[68] NrdI can generate either H_2O_2 or $O_2^{\bullet-}$ as oxidant. Until 2013, the proposed biosynthetic pathway for the metallocofactor of class Ib RNRs is shown below (Figure 1.6). The mechanism A (Scheme 1.6) was originally proposed in which NrdI acts as a source of HO_2^-. The mechanism B (Scheme 1.6) is an alternative route in which NrdI acts as a source of $O_2^{\bullet-}$. Both pathways resulted in generation of a mixed valent $Mn^{III}Mn^{IV}$ intermediate, that can abstract a hydrogen atom from tyrosine, resulting in the formation of a tyrosyl radical. Up until 2013 experiments were unable to distinguish whether the oxidant in *B. subtilis* class Ib Mn_2-RNRs was H_2O_2 or $O_2^{\bullet-}$.[31, 68] Recently, Stubbe and colleagues demonstrated that the Mn^{II}_2 cofactor showed no reaction with O_2, the active oxidant was $O_2^{\bullet-}$. A detailed description of the catalytic cycle of class Ib *B. subtilis* will be given below.

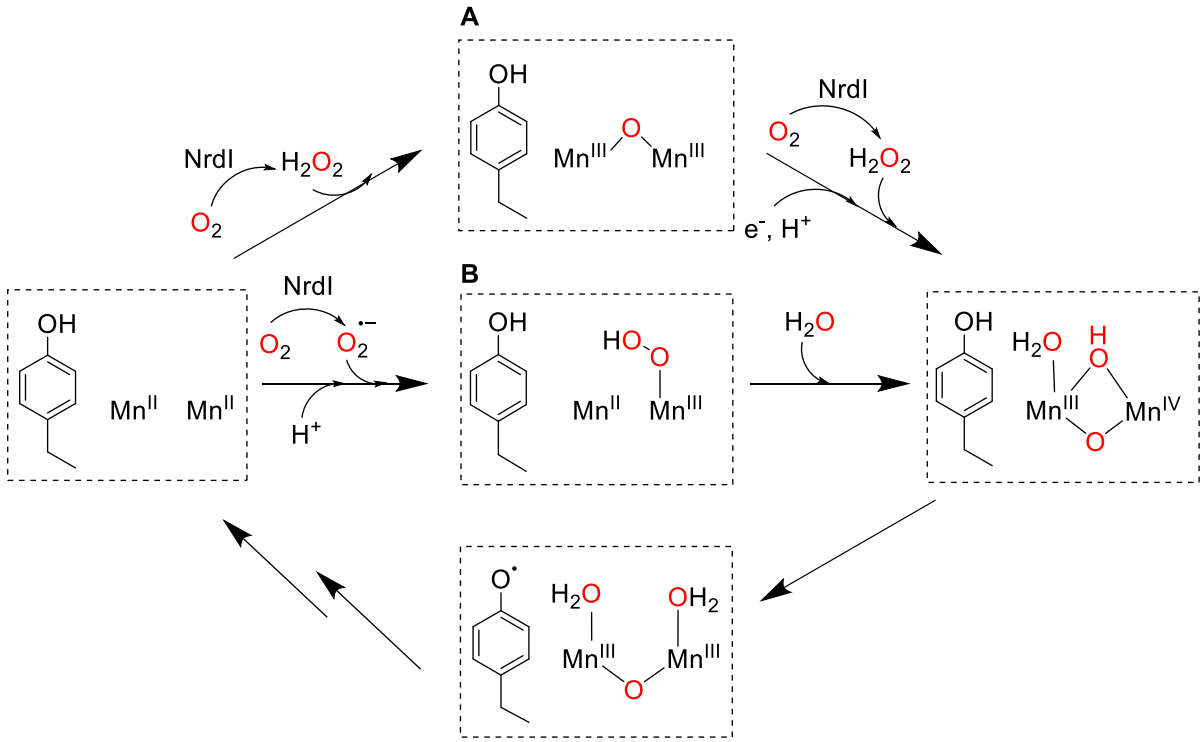

Scheme 1.6. Two proposed mechanisms for Mn^{III}_2-Y• cofactor assembly in class Ib Mn_2 RNRs (NrdI = flavodoxin protein).[31, 68]

1.4.5 Superoxide in *B. subtilis* class Ib Mn_2-RNRs

Many studies on class Ib Mn^{II}_2 RNRs have been carried out.[68, 71, 81, 83] In 2013, Stubbe and co-workers made a very important discovery, demonstrating the active oxidant in *B. subtilis* class Ib Mn_2-RNRs was $O_2^{\bullet-}$ (Scheme 1.7). We became interested in the role of the superoxide anion. Stubbe and colleagues demonstrated that the Mn_2 cofactor showed no reaction with O_2.[83] However, in the presence of a flavodoxin protein ($NrdI_{hq}$, flavodoxin hydroquinone) O_2 was reduced to $O_2^{\bullet-}$. The $O_2^{\bullet-}$ was proposed to react with the Mn^{II}_2 core, by inner or outer-sphere electron transfer, possibly coupled with proton transfer. The $O_2^{\bullet-}$ was suggested to bind the Mn^{II} metal site farthest away from the tyrosine residue in the protonated form ($HO_2^{\bullet}$). Thus, the initial formation of a $Mn^{II}Mn^{III}$-peroxide or a $Mn^{II}Mn^{III}$-hydroperoxide was proposed.[81] Rapid freeze quench (RFQ) EPR studies revealed no evidence of a $Mn^{II}Mn^{III}$ intermediate. The oxidation of the site 2 Mn^{II} to generate a $Mn^{II}Mn^{III}$ intermediate was expected to be very fast, similar to the analogous reaction in SOD (reaction rate constant = 10^9 $M^{-1}s^{-1}$ for Mn^{II}-SOD[84]). The inability to detect this intermediate was attributed to the fact that all steps between $O_2^{\bullet-}$ production and formation of $Mn^{III}Mn^{IV}$ species (see below) were rate-limited by a

conformational change correlated with $O_2^{\bullet-}$ reaching the metal site.[81] Subsequent cleavage of the O–O bond to generate a Mn^{III}(μ-OH)(μ-O)Mn^{IV} species, that oxidises tyrosine was also proposed.[83] RFQ-EPR measurements of the mixed valent $Mn^{III}Mn^{IV}$ species exhibited a 16-line signal at 10 K. These features were very similar to those of mixed valent $Mn^{III}Mn^{IV}$ dimers. The $Mn^{III}Mn^{IV}$ species was the first example of a $Mn^{III}Mn^{IV}$ dimer in biology and the analogue to Intermediate X in Fe^{III}_2-Y$^{\bullet}$ cofactor assembly.

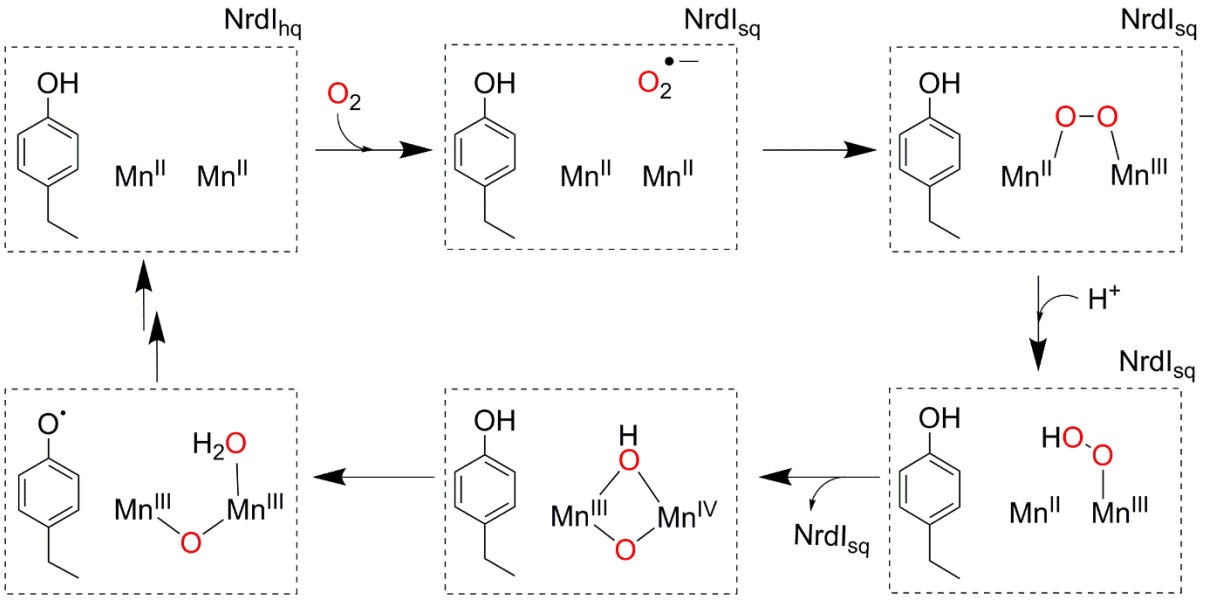

Scheme 1.7. Proposed catalytic cycle for class Ib Mn_2 RNRs in *B. subtilis* (NrdI$_{hq}$ = Flavodoxin hydroquinone, NrdI$_{sq}$ = Flavodoxin semiquinone).[31, 69, 83]

Based on the above catalytic cycles of class I RNRs the active oxidant was either O_2 (class Ia and Ic) or $O_2^{\bullet-}$/H_2O_2 (class Ib). The process catalyzed by bimetallic active sites in class Ib Mn^{II}_2 RNRs in *B. subtilis* could be divided into two steps: binding of the oxidant to the metal atoms, followed by cleavage of the O-O bond. In *B. subtilis*, a $Mn^{II}Mn^{III}$-peroxide species was postulated to form after binding of superoxide, that converted to a Mn^{III}(μ-OH)(μ-O)Mn^{IV} species after cleavage of the O-O bond. The high valent species oxidised tyrosine to tyrosyl radical, that was involved in ribonucleotide reduction. In class I RNR, various metallic-oxygen intermediates have been identified or proposed during the catalytic cycle. The presence of these intermediates in the catalytic cycle of RNRs has triggered the study of related model complexes. More importantly, mimicking of class Ib Mn_2 RNRs, where the postulated oxidant was $O_2^{\bullet-}$ by using synthetic Mn^{II}_2 model complexes and $O_2^{\bullet-}$ is essential. The reactivity of biomimetic Mn^{II}_2 complexes and $O_2^{\bullet-}$ has not been investigated before. Moreover, this would help provide further support for the postulated mechanism of $O_2^{\bullet-}$ activation at class Ib Mn_2 RNRs.

1.5 Model complexes

In biological systems, there are examples of Mn containing non-heme metalloenzymes that react with molecular oxygen or one of its reduced derivatives (i.e., superoxide, hydrogen peroxide and water).[6, 85] These enzymes catalyse processes crucial to health and the environment. For example, Mn-SOD[26, 86] and MnCat[6] are involved in detoxification of ROS (superoxide and hydrogen peroxide respectively). Substrate oxidations are performed by Mn-dependent dioxygenases[7, 87] and oxalate oxidase[9] in their reaction with molecular oxygen. The oxidation of water to dioxygen is carried out by the tetramanganese cofactor in the OEC of photosystem II.[30, 88] Finally, as described above (section 1.1), Mn_2 RNRs convert ribonucleotides to their corresponding deoxyribonucleotides, that are involved in DNA synthesis.[68, 81, 89]

Regardless of the diversity in structures and active-site function, some of the proposed mechanisms of the redox-active Mn enzymes involved peroxo-intermediates. Spectroscopic evidence for Mn-SOD[90, 91] and Mn homoprotocatechuate 2,3-dioxygenase (Mn-HPCD)[7] for a peroxo-intermediate was obtained. The majority of peroxo-Mn^{III} intermediates were postulated based on reaction chemistry and were supported by computational studies.[92-94] Moreover as seen in section 1.4.5, in the catalytic cycle of class Ib Mn_2 RNRs, a (hydro)peroxo-$Mn^{II}Mn^{III}$ intermediate was proposed prior to the formation of a bis(μ-hydroxo)$Mn^{III}Mn^{IV}$ intermediate.[83] Additionally, peroxo-Mn^{III} adducts were proposed as key intermediates in water oxidation by the OEC.[30, 95, 96] Therefore, Mn-enzymes reacted via peroxo/hydroxo/bis(μ-oxo) Mn-intermediates. Preparation of model complexes of these metalloenzymes helps us gain a better understanding of their active sites and behaviour in formation of Mn-intermediates.

In the last four decades, investigations of metalloenzymes have long benefited from complementary studies of synthetic models that mimic structural, spectroscopic and reactivity studies. Examination of the spectroscopic properties and reactivity of Fe-, Cu- and Mn-containing model complexes have played a prominent role in advancing our understanding of these metalloenzymes. Many synthetic model complexes have been prepared that model the active site and reactivity of these enzymes. For a complete understanding of Mn-enzymes, an examination of structures, spectroscopic properties and reactivity of Mn-containing model complexes is critical. The next section describes progress towards understanding the structure and reactivity of peroxo-Mn^{III}, mixed valent $Mn^{II}Mn^{III}$ and bis(μ-oxo)$Mn^{III}Mn^{IV}$ adducts using synthetic model systems. Attention is focussed on peroxo-Mn^{III} and bis(μ-

oxo/hydroxo)$Mn^{III}Mn^{IV}$ adducts as these have been postulated as intermediates in class Ib Mn_2 RNRs.

1.5.1 Peroxo-Mn^{III} complexes

The first crystallographically characterised peroxo-Mn^{III} complex $[Mn^{III}(O_2)(TPP)]^-$ (TPP = 5,10,15,20-tetraphenylporphyrin) was reported in 1987 by VanAtta *et al*.[97] In the 31 years since that report, only seven peroxo-Mn^{III} complexes have been structurally characterised.[98-104] The lack of these structures could be attributed to the low stability of peroxo-Mn^{III} species. However, there are many other peroxo-Mn^{III} compounds, whose structures were supported by many techniques such as mass-spectrometry or other spectroscopic techniques and computational studies.[100, 101, 103, 105-110] Firstly, the methods by which the peroxo-Mn^{III} complexes were prepared will be described, followed by their structural and vibrational properties. Finally, the chemical reactivity of the complexes will be discussed.

The first structurally characterised peroxo-Mn^{III} complex, $[Mn^{III}(O_2)(TPP)]^-$ was formed using potassium superoxide (Figure 1.4).[97] The synthesis of this complex was carried out as described below. The $[Mn^{III}(TPP)Cl]$ complex was reduced with zinc amalgam in toluene. This metathesis reaction helped remove the chloride ion from solution. The zinc amalgam was removed by filtration, while toluene was removed by vacuum distillation. Next, the $Mn^{II}TPP$ complex was dissolved in THF with an excess cryptand (K222) and small pieces of KO_2. The reaction was left stirring for a few days. Green crystals of $[Mn^{III}(O_2)(TPP)][K(K222)]$ were obtained.[97] Additionally, the large size of K222 made it a good counterion for crystallisation of the porphyrin anion ($[Mn^{III}(O_2)(TPP)]^-$). The $O_2^{\bullet-}$ oxidant has also been used to generate a number of peroxo-Mn^{III} adducts, from Mn^{II} precursors supported by pentadentate N_5 (N,N'-bis(2-pyridylmethyl)-N-bis(2-pyridyl)methylamine (= N4py) and N-methyl-N,N',N'-tris(2-pyridylmethyl)ethane-1,2-diamine (= mL_5^2)),[106, 111] tetradentate N_4 (1,4-bis(2-pyridylmethyl)-1,4-diazepane (= $L_7py_2^R$) and related)[105, 107, 108] and macrocylic ligands (4,11-dimethyl-1,4,8,11-tetraazabicyclo[6.6.2]hexadecane (= Me_2EBC)) (Figure 1.4).[112] Superoxide presumably acts as a one-electron oxidant of the Mn^{II} centre.

On the other hand, peroxo-Mn^{III} complexes supported by hydrotis-(3,5-diisopropyl-1-pyrazolyl)borate (= Tp^{iPr})[98, 99] and 1,4,8,11-tetramethyl-1,4,8,11-tetraazacyclotetradecane (=TMC-ligands)[100, 101] have been generated using aqueous H_2O_2 (Figure 1.4). The mechanism for formation of peroxo-Mn^{III} complexes using H_2O_2 has not been established. In some cases, a large excess of H_2O_2 was needed.[98, 99, 113, 114] Also, the addition of a base such as triethylamine

(Et_3N) was required for generation of the peroxo-Mn^{III} complexes[100, 101, 103, 105-109] or anhydrous H_2O_2-urea was needed.[103, 106, 113]

Peroxo-Mn^{III} adducts are most commonly trapped at low temperatures (≤ 0 °C)[105-108, 111, 113] but there are a few examples at higher temperatures (> 0 °C).[98-101] The yields of the peroxo-Mn^{III} complexes are usually low to moderate and this has prevented their characterisation by Mn K-edge X-ray absorption spectroscopy. Higher yields of peroxo-Mn^{III} adducts have been obtained from Mn^{II} precursors supported by N_5 (pentadentate amino pyridine and imidazole) ligands using electrochemically generated $O_2^{\bullet-}$.[115] The three complexes used for this study were $[Mn^{II}(imL_5^2)(ClO_4)](ClO_4)$ (where imL_5^2 = N-methyl-N,N',N'-tris((1-methyl-4-imidazolyl)methyl)ethane-1,2-diamine), $[Mn^{II}(mL_5^2)(OH_2)](BPh_4)_2.2H_2O$ (where mL_5^2 = N-methyl-N,N',N'-tris(2-pyridylmethyl)ethane-1,2-diamine) and $[Mn^{II}(N4py)(OTf)](OTf)$ (where OTf = trifluoromethanesulfonate).[115] Bulk electrolysis (-1.2 V vs SCE) of air saturated DMF solutions containing 1 mM of the Mn^{II} complexes supported by imL_5^2, mL_5^2 and N4py resulted in reduction of dissolved O_2 to $O_2^{\bullet-}$. Air saturated DMF solutions were prepared by bubbling with dried air for 10 minutes before electrolysis. *In situ*, the $O_2^{\bullet-}$ was proposed to react with the solvated Mn^{III} complexes to generate the corresponding peroxo-Mn^{III} complexes. At 233 K, UV-Vis spectroelectrochemical experiments using a Pt grid working electrode in a thin layer spectroelectrochemical cell confirmed the formation of peroxo-Mn^{III} complexes. Intense bands developed in the UV-Vis absorption spectra upon application of the reductive potential.[115] Absorption bands at λ_{max} = 542, 585 and 617 nm corresponded to the formation of $[Mn^{III}(O_2)(imL_5^2)]^+$, $[Mn^{III}(O_2)(mL_5^2)]^+$ and $[Mn^{III}(O_2)(N4py)]^+$.[106, 111, 113]

Importantly, higher extinction coefficients were obtained for the peroxo-Mn^{III} complexes using electrochemically generated $O_2^{\bullet-}$, from those obtained for the same peroxo-species prepared chemically by H_2O_2 or KO_2.[106, 111, 113] The $O_2^{\bullet-}$ anion formed at the electrode *in situ* was proposed to react instantly with the excess of Mn^{II} complexes. Additionally, as the product diffused away from the electrode, side reactions were unfavorable. Therefore, higher yields of peroxo-Mn^{III} complexes were obtained. Hopefully this will help improve X-ray absorption spectroscopy studies.

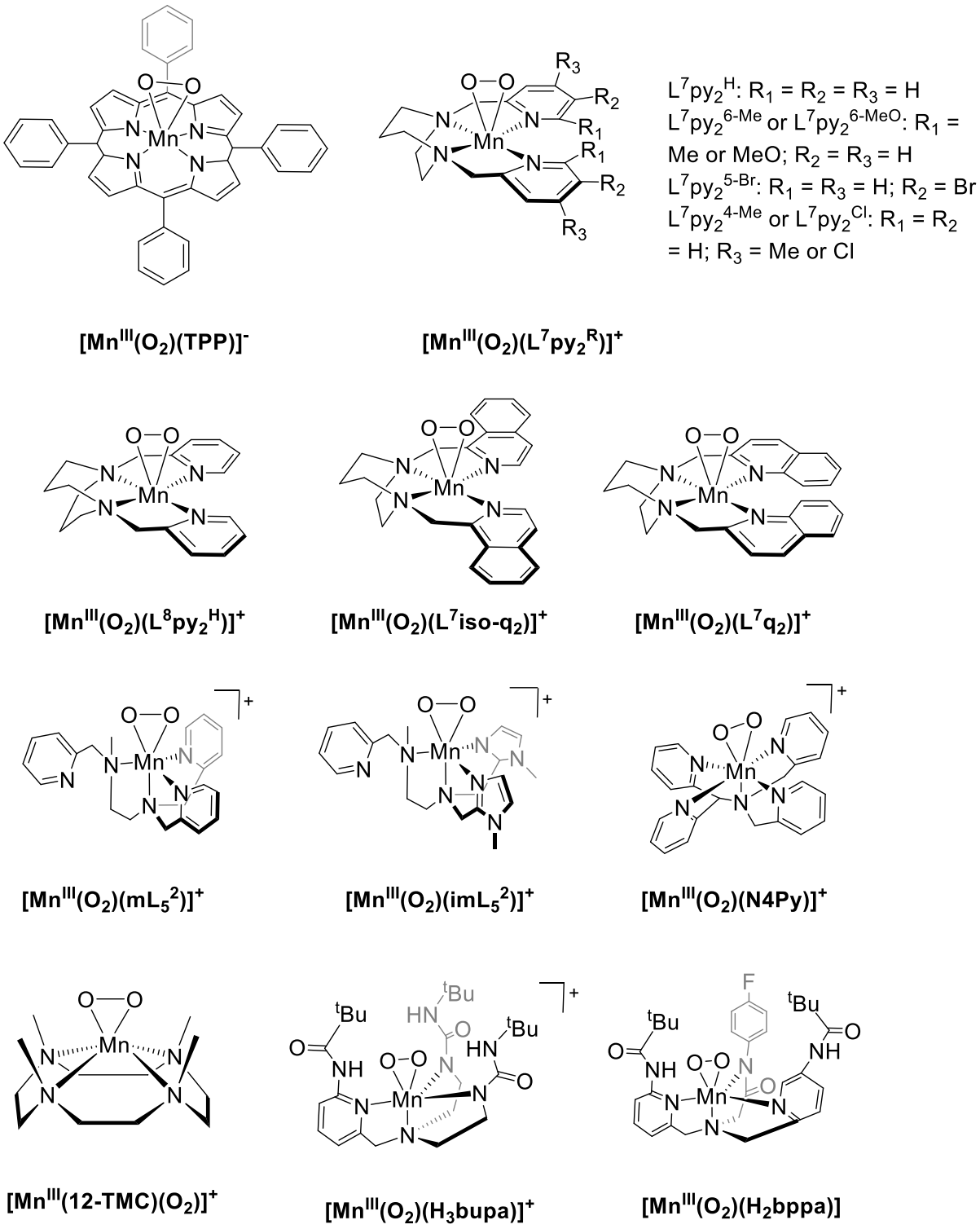

Figure 1.4. Structures of peroxo-Mn^{III} compounds.[110]

Two peroxo-Mn^{III} complexes[114, 116] and one binuclear Mn-peroxo complex[117] have been prepared using dioxygen. Treatment of the precursor $[Mn^{II}(H_2bupa)]^-$ complex with O_2 at room temperature resulted in formation of $[Mn^{III}(O_2)(H_3bupa)]^+$ (where H_3bupa = bis[(N'-tert-butylurealy)-N-ethyl]-(6-pivalamido-2-pyridylmethyl)amine, Figure 1.4) in 50% yield.[116] H_2bupa is a trianionic tripodal ligand that contains a hydrogen-bonding cavity around the

dioxygen-binding site. When the oxygenation reaction was performed in the presence of 0.5 equivalents of diphenylhydrazine (DPH), the reaction increased from 30 mins to 10 mins and the yield of $[Mn^{III}(O_2)(H_3bupa)]^-$ increased to 80%.[116] A mechanism was proposed involving the formation of a superoxo-Mn^{III} intermediate, that reacted with solvent or DPH (generating azobenzene), *via* a H-atom abstraction process to initially produce a hydroperoxo-Mn^{III} complex. Additionally it was proposed that DPH stabilised the intermediate formed, increasing the rate and yield of the product formed.[116] Likewise the $[Mn^{II}(H_2bpaa)]$ (where H_3bpaa = N-[bis(6-pivalamido-2-pyridylmethyl)](N'-fluorophenylcarbamoylmethyl)amine) complex reacted with O_2 in the presence of hydrogen-atom donors (DPH, indene and fluorene) to form $[Mn^{III}(O_2)(H_2bpaa)]$.[114] It was suggested that the Mn^{II} precursors reacted with dioxygen to form superoxo-Mn^{III} species, that abstracted a hydrogen atom to give hydroperoxo-Mn^{III} adducts. Subsequent deprotonation or intramolecular proton transfer was suggested to account for the formation of the observed η^2- peroxo-Mn^{III} complexes. The first example of a binuclear Mn-peroxo derived from O_2 was reported by Kovacs and co-workers.[117] Treatment of the $[Mn^{II}(S^{Me2}N_4(6\text{-Me-DPEN}))](BF_4)$ (where 6-Me-DPEN = N,N-bis(6-methyl-2-pyridilmethyl)ethane-1,2-diamine) with dioxygen at low temperature resulted in the formation of $\{[Mn^{III}(S^{Me2}N_4(6\text{-Me-DPEN}))]_2(\text{trans-}\mu\text{-}1,2\text{-}O_2)\}^{2+}$ (Figure 1.5), which was characterised crystallographically. The peroxo-adduct converted to a binuclear mono-oxo-bridged $\{[Mn^{III}(S^{Me2}N_4(6\text{-Me-DPEN}))]_2(\mu\text{-}O)\}^{2+}$ within minutes at -40 °C. Thus, this represented the first characterised example of a binuclear Mn^{III}-peroxo which subsequently, converted to a binuclear μ-oxo bridged product derived from O_2.

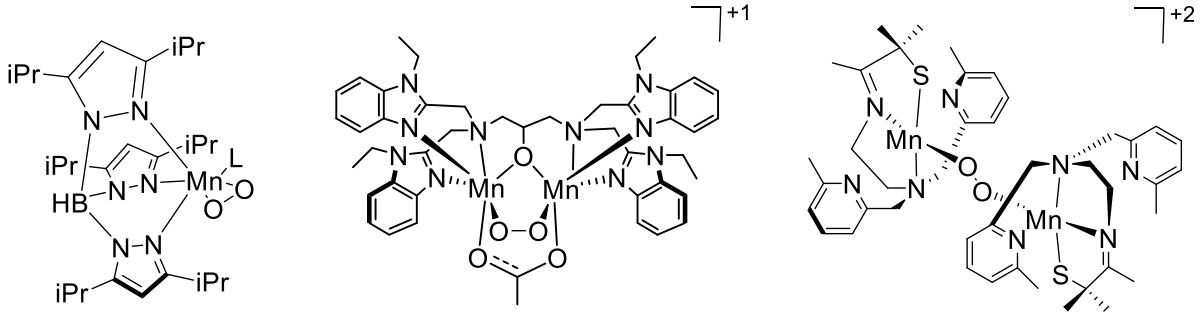

$[Mn^{III}(O_2)(Tp^{iPr})(L)]$ L = $pz^{iPr}H$, 2-MeIm

$[Mn^{II}Mn^{III}(O_2)(O_2CCH_3)((N\text{-Et-HPTB})]^{1+}$

$\{[Mn^{III}(S^{Me2}N_4(6\text{-Me-DPEN})]_2(\text{trans-}\mu\text{-}1,2\text{-}O)_2\}^{2+}$

Figure 1.5. Structures of a peroxo-Mn^{III} complex, a peroxo-$Mn^{II}Mn^{III}$ complex and a binuclear peroxo-Mn^{III}_2 complex (from left to right).[98, 99, 116, 124]

1.5.1.1 Structural properties of peroxo-Mn^{III} complexes

Chemdraw representations of X-ray crystal structures of peroxo-Mn^{III} complexes supported by TPP,[97] Tp^{iPr}[98, 99] and N_4 macrocyclic (TMC, 1,4,7,10-tetramethyl-1,4,7,10-tetraazacyclotridecane (= 13-TMC) and 1,4,7,10-tetramethyl-1,4,7,10-tetraazacyclododecane (= 12-TMC))[100, 101, 103] ligands are shown above (Figure 1.4). All complexes displayed six-coordinate Mn^{III} centres with η^2-peroxo ligands. The Mn-O bond lengths of these complexes ranged from 1.838 to 1.901 Å, while the O-O bond lengths ranged from 1.402 to 1.43 Å. Almost all these η^2-peroxo-Mn^{III} complexes had symmetric Mn-O bonds, with the bond distances differing by less than 0.015 Å. The peroxo-Mn^{III} complex $[Mn^{III}(O_2)(Tp^{iPr})(MeIm)]$ (where MeIm = methylimidazole) displayed a more asymmetric Mn-O bond due to intermolecular hydrogen bonds between MeIm and peroxo ligands of adjacent molecules.[99] An additional peroxo-Mn^{III} complex ($[Mn^{III}(O_2)(Tp^{iPr2})(pz^{iPr2})]$, where pz^{iPr2} = 3,5-diisopropylpyrazole) was first prepared at -20 °C using H_2O_2 as oxidant. Interestingly, it was observed that the UV-Vis spectrum of a toluene solution of the peroxo-Mn complex at -78 °C, exhibited a λ_{max} = 583 nm, which upon warming at -20 °C revealed a shoulder at λ_{max} ~ 560 nm.[98] The thermochroism of the peroxo-Mn^{III} complex $[Mn(O_2)(Tp^{iPr})(pz^{iPr2})]$ was reflected in its isomers where upon cooling from -20 to -78 °C, a brown to blue conversion was observed (Figure 1.6). X-ray crystal structures were obtained for both isomers. Similarly to the $[Mn^{III}(O_2)(Tp^{iPr})(MeIm)]$ complex (see above), the $[Mn^{III}(O_2)(Tp^{iPr2})(pz^{iPr2})]$ (where pz^{iPr2} = 3,5-diisopropylpyrazole) complex also had asymmetric Mn-O bonds in its blue form that distinguish it from the brown isomer.[98] The N(pz^{iPr2}) to O(peroxo) bond lengths in the blue isomer were 2.82(2) and 2.99(2) Å while in the brown isomer were 3.298(8) and 3.083(3) Å (Figure 1.6, Table 1.3). Thus, shorter N(pz^{iPr2}) to O(peroxo) distances suggested that the slight asymmetry in the Mn^{III}-O_2 unit it was due to intramolecular hydrogen bonds.

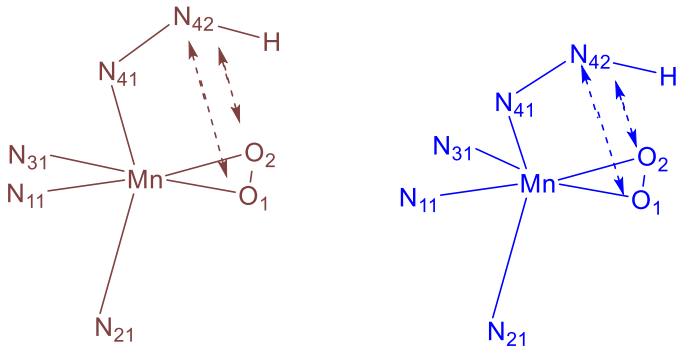

Figure 1.6. Structure of the core of the brown (left) and blue isomers (right) of the $[Mn(O_2)(Tp^{iPr})(pz^{iPr2})]$ complex.[98]

The coordination geometry of the Mn^{II} centre can be calculated using the τ_5 parameter as square pyramidal ($\tau_5 = 0$) to trigonal bipyramidal ($\tau_5 = 1$). The η^2-peroxo-Mn^{III} complexes supported by the Tp^{iPr2} ligand were very close to a trigonal bipyramidal geometry ($\tau_5 = 1$) with large axial bond elongations. For the TMC-derived complexes, as the ring sizes decreased, the geometries become closer to square pyramidal. The first crystal structure of a peroxo-bridged Mn^{III} complex was that of $[Mn^{III}_3(cis\text{-}\mu\text{-}1,2\text{-}O_2)(\mu_3\text{-}O)(\mu\text{-}OAc)_2(dien)_3]^{3+}$ (where dien = diethylenetriamine). The complex was formed by refluxing $Mn^{III}(OAc)_3$ and dien in methanol, after which the mixture was cooled under air.[118] Large uncertainties in the metric parameters were observed due to the inability to define the structure because of its high symmetry. The only high-resolution structure of a bridged Mn^{III}_2 species was obtained from the $\{[Mn^{III}(S^{Me2}N_4(6\text{-Me-DPEN}))]_2(trans\text{-}\mu\text{-}1,2\text{-}O_2)\}^{2+}$ complex.[117] This complex had a peroxo ligand with a trans-μ-1,2-geometry and a long O-O bond distance of 1.452(5) Å and short Mn-O bond distances of 1.832(3) Å.[117] Comparable O-O (1.46(3) Å) and Mn-O (1.83(2) Å) bond lengths have been observed in a Mn^{IV}_2 complex supported by a cis-μ-1,2-peroxo bridge and two oxo bridges.[119] Similar O-O bond lengths of ~1.41 Å were observed in peroxo-bridges Fe^{III}_2 species when compared to $\{[Mn^{III}(S^{Me2}N_4(6\text{-Me-DPEN}))]_2(trans\text{-}\mu\text{-}1,2\text{-}O_2)\}^{2+}$.[120] However, peroxo-bridged Cu^{II}_2 species exhibited O-O bond distances ranging from 1.368(9) to 1.540(5) Å.[121, 122]

Table 1.3. Selected bond lengths for peroxo-Mn^{III} complexes from X-ray crystallography.

Complexes	Selected Bond lengths (Å)		
	Mn-O	**O-O**	**Ref**
$[Mn(O_2)(TPP)]^-$	1.888, 1.901	1.421	[97]
$[Mn^{III}(O_2)(Tp^{iPr2})(pz^{iPr2})]$-brown	1.850,1.851	1.428	[98]
$[Mn^{III}(O_2)(Tp^{iPr2})(pz^{iPr2})]$-blue	1.841, 1.878	1.420	[98]
$[Mn^{III}(O_2)(Tp^{iPr2})(Me\text{-}Im)]$	1.838, 1.872	1.420	[99]
$[Mn(O_2)(TMC)]^+$	1.884, 1.884	1.402	[100]
$[Mn(O_2)(13\text{-}TMC)]^+$	1.855, 1.863	1.410	[101]
$[Mn(O_2)(12\text{-}TMC)]^+$	1.853	1.408	[103]

1.5.1.2 Vibrational properties

Up to now resonance Raman experiments on most mononuclear η^2-peroxo-Mn^{III} adducts failed because of laser irradiation causing sample degradation.[100, 111] Thus, little vibrational data is available and $\nu_{O\text{-}O}$ have only been observed for six complexes using IR measurements.[97-99, 114, 116, 123] One example includes an Mn^{IV}-peroxide complex supported by a tetraamido macrocyclic ligand (TAML) recently reported by Nam and co-workers.[123] The $\nu_{O\text{-}O}$ stretching

vibration of the Mn^{IV}-peroxide complex was found in the IR spectrum at 905 cm^{-1}, that shifted to 860 cm^{-1} on substitution of $^{16}O_2$ with $^{18}O_2$.[123] Mn-O stretching vibrations (ν_{Mn-O}) have not been identified. Thus, there is a lack of vibrational data (ν_{O-O} and ν_{Mn-O}) for mononuclear peroxo-Mn^{III} complexes. The few previously reported ν_{O-O} values are within the narrow range of 875-896 cm^{-1} (Table 1.4). In contrast, the binuclear peroxo-Mn complex $\{[Mn^{III}(S^{Me2}N_4(6\text{-Me-DPEN}))]_2(\text{trans-}\mu\text{-}1,2\text{-}O_2)\}^{2+}$ exhibited a lower-energy ν_{O-O} band at 819 cm^{-1} on the resonance Raman spectrum. Thus, further studies must be done into the vibrational spectroscopy of Mn-dioxygen adducts.

1.5.1.3 Electronic absorption spectroscopy

η^2-peroxo-Mn^{III} complexes exhibit weak absorption bands in the visible region (λ_{max} = 415-670 nm; ε = 60-490 $M^{-1}cm^{-1}$) that arise from a combination of peroxide-to-metal charge transfer and *d-d* transitions.[103, 107, 109] The well-characterised peroxo-Mn^{III} complexes $[Mn^{III}(O_2)(12\text{-TMC})]^+$,[103] $[Mn^{III}(O_2)(13\text{-TMC})]^+$[124] and $[Mn^{III}(O_2)(14\text{-TMC})]^+$[124] displayed an intense absorption at less than 460 nm and a broader band in the 560-590 nm range. These spectral features were also resembled by peroxo-Mn^{III} complexes supported by polydentate amine ligands ($[Mn^{III}(O_2)(L1)]^+$ (where L1 = N,N'-bis-(2-pyrid-2-ylmethyl)-1,4-diazepane) and $[Mn^{III}(O_2)(L2)]^+$ (where L2 = N-(6-methylpyrid-2-ylmethyl)-N'-(pyrid-2-ylmethyl)-1,4-diazepane),[109] Table 1.4), exhibiting a prominent band at λ_{max} = 430-450 nm and a weaker band at λ_{max} = 550-600 nm. Additionally, the electronic absorption spectrum of a peroxo-Mn^{III} complex supported by another polypyridine amine ligand (N4py), prepared upon addition of $O_2^{\bullet-}$, displayed weak absorbance features at λ_{max} = 438 and 617 nm.[125] Moreover, the first example of a mixed valent $Mn^{II}Mn^{III}$-peroxide ($[Mn^{II}Mn^{III}(O_2)(\text{N-Et-HPTB})]^{2+}$, where N-Et-HPTB = N,N,N',N'-tetrakis(2-(1-ethylbenzimidazolyl))-2-hydroxy-1,3-diaminopropane) species displayed low intensity absorbance bands at λ_{max} = 460 and 610 nm.[126] Likewise, reaction of the $([Mn_2(O_2CCH_3)_2(BPMP)](ClO_4)$ (HBPMP = 2,6-bis[bis(2-pyridylmethyl)aminomethyl]-4-methylphenol; complex **4**, chapter 3) with $O_2^{\bullet-}$ formed a second peroxo-$Mn^{II}Mn^{III}$ complex (**5**). The electronic absorption spectrum of **5** displayed two low intensity features at λ_{max} = 440 and 590 nm (chapter 3). These features were characteristic of Mn^{III}-peroxide complexes. In summary, all the previously reported peroxo-Mn^{III} complexes exhibited comparable electronic absorption features.

Table 1.4. Experimental $\nu_{O\text{-}O}$ frequencies (cm^{-1}), electronic absorption maxima (λ_{max}) and extinction coefficients (ε) for peroxo-Mn^{III} complexes.

Complex	$\nu_{O\text{-}O}$ ($\Delta^{18}O$)	λ_{max} in nm (ε in $M^{-1}cm^{-1}$)	Ref
$[Mn^{III}(O_2)(N4py)]^+$	-	438 (22800), 617 (16200)	[125]
$[Mn^{III}(O_2)(12\text{-}TMC)]^+$	-	280 (2600), 455 (250), 620 (200)	[103]
$[Mn^{III}(O_2)(13\text{-}TMC)]^+$	-	288 (2400), 452 (390), 615 (190)	[124]
$[Mn^{III}(O_2)(14\text{-}TMC)]^+$	-	453 (490), 630 (120)	[124]
$[Mn^{III}(O_2)(L1)]^+$	-	448 (197), 556 (42)	[109]
$[Mn^{III}(O_2)(L2)]^+$	-	440 (175), 597 (41)	[109]
$[Mn^{III}(O_2)(Tp^{iPr2})(pz^{iPr2})]$-brown	892 (51)	561 (50)	[98]
$[Mn^{III}(O_2)(Tp^{iPr2})(pz^{iPr2})]$-blue	892 (51)	583 (60)	[98]
$[Mn^{III}(O_2)(Tp^{iPr2})(Me\text{-}Im)]$	896 (-)	381 (314), 478 (173)	[99]
$[Mn^{III}(O_2)(H_3bupa)]^-$	885 (48)	660 (300), 490 (NA)	[116]
$[Mn^{III}(O_2)(H_2bppa)]$	891 (52)	590 (58)	[114]
$[Mn^{III}(O_2)(TPP)]^-$	983 (50)	NA	[97]
$[Mn^{II}Mn^{III}(O_2)(N\text{-}Et\text{-}HPTB)]^{2+}$	-	460 (-), 610 (-)	[126]
$\{[Mn^{III}(S^{Me2}N_4(6\text{-}Me\text{-}DPEN))]_2(trans\text{-}\mu\text{-}1,2\text{-}O_2)\}^{2+}$	819 (47)	640 (830)	[117]
$[Mn^{IV}(O_2)(TAML)]^{2-}$	905 (45)	600 (720)	[123]

1.5.1.4 Chemical reactivity of η^2-peroxo-Mn^{III} adducts

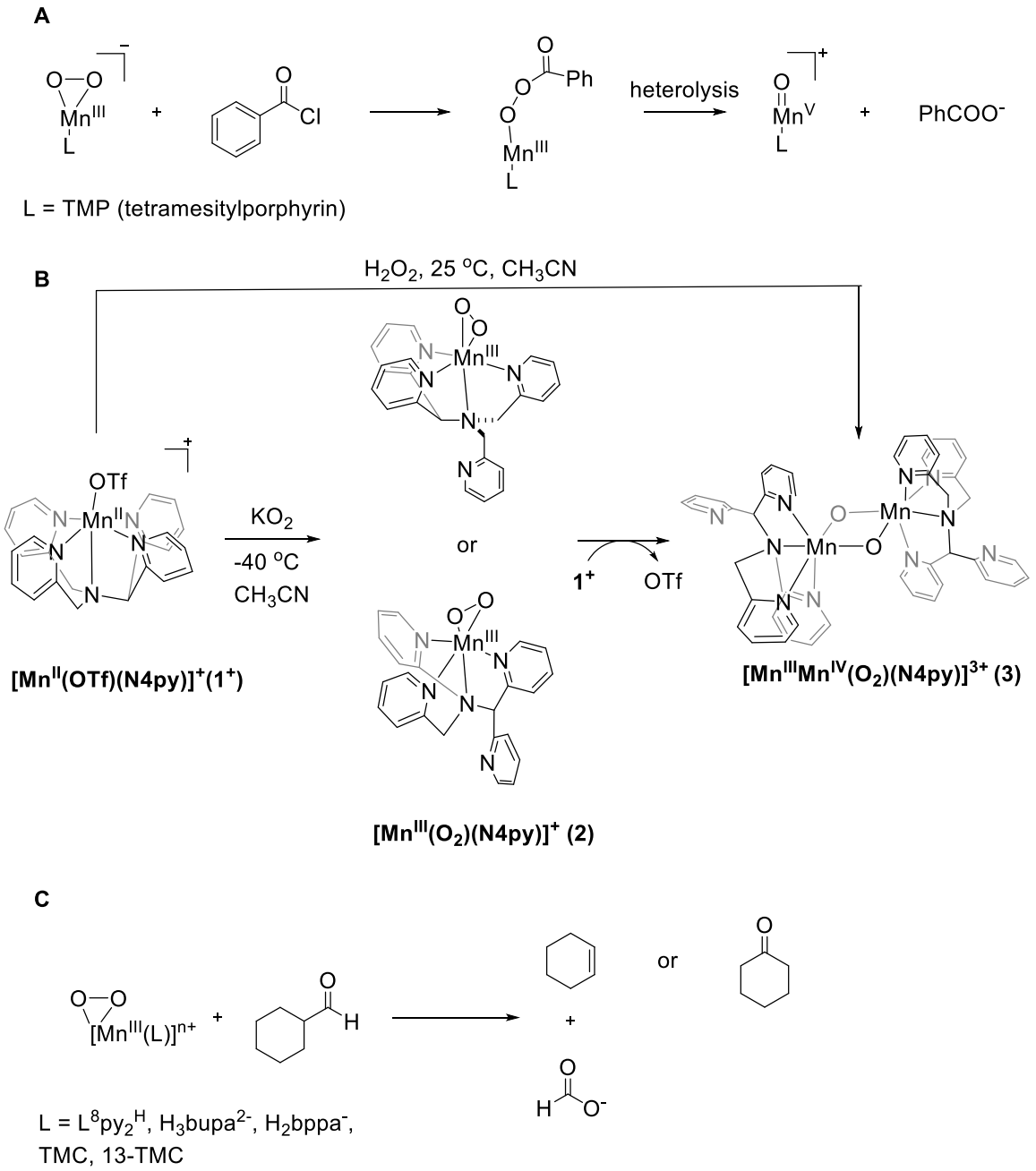

Scheme 1.8. Structural representations of chemical reactivity of peroxo-Mn^{III} complexes ($L^8py_2^H$ = 1,4-bis(2-pyridylmethyl)-1,4-diazepane; H_3bupa = bis[(N'-tert-butylurealy)-N-ethyl]-(6-pivalamido-2-pyridylmethyl)amine; H_3bpaa = N-[bis(6-pivalamido-2-pyridylmethyl)](N'-fluorophenylcarbamoylmethyl)amine; TMC = tetramethylcyclam; 13-TMC = 1,4,7,10-tetramethyl-1,4,7,10-tetraazacyclotridecane).[100, 101, 103, 108, 113, 115, 123, 125, 126]

η^2-Peroxo-Mn^{III} complexes were found to react with aldehydes, protons, acid chlorides and anhydrides and thus they are nucleophilic. For example, η^2-peroxo-Mn^{III}-porphyrin complexes reacted with benzoyl chloride or benzoyl anhydride to give acylperoxo-Mn^{III} species. These

undergo O-O heterolysis to produce the corresponding oxo-Mn^{V} complexes (Scheme 1.8 A).[127-129]

Treatment of the $[Mn^{III}(O_2)(mL_5^2)]^+$ complex with acids generated 2-pyridinecarboxylate by oxidative degradation of the ligand (mL_5^2). Jackson and co-workers recently reported the formation of a bis(μ-oxo)$Mn^{III}Mn^{IV}$ species using $O_2^{\bullet-}$ as oxidant from mononuclear Mn^{II} precursors (Scheme 1.8 B).[125] Initially a mononuclear peroxo-Mn^{III} adduct formed, which subsequently reacted with the mononuclear Mn^{II} precursor forming the bis(μ-oxo)$Mn^{III}Mn^{IV}$ species (Scheme 1.8 B). This conversion mimics the currently proposed mechanism for assembly of the $Mn^{III}Mn^{IV}$ cofactor in Mn ribonucleotide reductase.[83] The bis(μ-oxo)$Mn^{III}Mn^{IV}$ species could also be formed directly by reaction of the Mn^{II} precursor complex with H_2O_2. The reaction mechanism of this step is still not fully understood. Upon reaction of $[Mn^{II}(N4py)(OTf)]^+$ with H_2O_2, a Mn^{III}-O_2 adduct was postulated as one of the intermediates on the way to formation of the bis(μ-oxo)$Mn^{III}Mn^{IV}$ complex. While there are many reports on the formation of oxo-bridged Mn_2 compounds by reaction of a Mn^{II} species with H_2O_2,[6, 85, 88, 124] the exact mechanism by which the dimeric species are obtained is not well established. For example, a peroxo-bridged Mn^{III}_2 intermediate ($[Mn^{III}_2(\mu\text{-}O_2)(mL_5^2)]^{4+}$) was postulated to form upon reaction of $[Mn^{III}(O_2)(mL_5^2)]^+$ with $[Mn^{III}(OH_2)(mL_5^2)]^{3+}$ in a basic aqueous medium.[113] The formation of the dinuclear peroxo-bridged adduct was proposed by Groni *et al*. as an intermediate towards formation of the bis(μ-oxo)$Mn^{III}Mn^{IV}$ product ($[Mn^{III}Mn^{IV}(\mu\text{-}O_2)(mL_5^2)]^{3+}$.[113] In the literature, there are few examples of peroxo-bridged Mn_2 complexes. To the best of our knowledge, the only well-characterised example of such a complex was reported by Coggins *et al*. The $\{[Mn^{III}(S^{Me2}N_4(6\text{-Me-DPEN}))]_2(\text{trans-}\mu\text{-}1,2\text{-}O_2)\}^{2+}$ complex revealed two Mn^{III} ions bridged by a peroxo ligand.[117] A peroxo-Mn^{III}_2 $[Mn_3(dien)_2(OAc)_2(\mu\text{-}O_2)Cl](ClO_4)_2$[118] (dien = diethylenetriamine) and a bis(μ-oxo)$Mn^{III}Mn^{IV}$ with a cis-μ-1,2-peroxo bridge $[L_2Mn_2(\mu\text{-}O)_2(\mu\text{-}O_2)](ClO_4)_2$ (L = 1,4,7-trimethyl-1,4,7-triazacyclononane)[119] have also been reported. Furthermore, mononuclear Cu^{II}-O_2 and Ni^{III}-O_2 complexes also performed this type of reactivity, by reacting with a second metal complex to form heterodinuclear and homodinuclear complexes with bis(μ-oxo) or μ-peroxo cores.[130-132]

η^2-peroxo-Mn^{III} complexes also displayed a nucleophilic character and were shown to be capable of aldehyde deformylation. This type of reactivity has been reported for η^2-peroxo-Mn^{III} complexes supported by H_3bupa^{2-},[116] H_2bpaa^-,[114] TMC-derived[100, 101, 103] and $L^7py_2{}^R$[108] ligands (Figure 1.8 C). A series of $[Mn^{III}(O_2)(13\text{-TMC})(X)]$ (where X = CN^-, NCS^-, $CF_3CO_2^-$, N_3^-) complexes were investigated in cyclohexanecarboxaldehyde (CCA) deformylation activity. The product obtained from this oxidation reaction was cyclohexanone

(Scheme 1.8, C). It was reported that the rate for this aldehyde deformylation increased with the electron-donating ability of the axial ligand trans to the peroxo.[101] Notably, it was found that complex $[Mn^{III}(O_2)(13\text{-}TMC)(N_3)]$ was involved in CCA deformylation with a rate of 10^4 times larger than that of $[Mn^{III}(O_2)(13\text{-}TMC)]^+$. Thus, the nucleophilicity of the Mn^{III}-O_2 unit was enhanced by the strongly electron donating ligand, possibly a more end-on structure was favoured. The deformylation activity of peroxo-metal complexes ($[M^{III}(O_2)(TMC)]^+$, M = Fe, Mn and Co) supported by the TMC ligand was also reported.[133] The Mn and Cu complexes supported by the TMC ligand exhibited similar reaction rates and they were an order of magnitude faster than the Fe complex ($[Fe^{III}(O_2)(TMC)]^+$).[133]

The reactivity of non-porphyrin η^2-peroxo-Mn^{III} complexes towards electrophilic substrates is scarce. However the O-O bond in $[Mn^{III}(O_2)(H_3bupa)]^-$ was activated by treatment with a hydrogen-atom donor. $[Mn^{II}(H_2bupa)]^-$ was used in the catalytic reduction of O_2 to H_2O with either DPH or hydrazine as the reductant.[134] The η^2-peroxo-Mn^{III} $[Mn^{III}(O_2)(H_3bupa)]^-$ was formed from the precursor $[Mn^{II}(H_2bupa)]^-$, O_2 and 0.5 equivalents of DPH. Then an additional equivalent of DPH gave the Mn^{III}-peroxo unit with two hydrogen atoms. The resulting species underwent O-O cleavage forming a Mn^{III} adduct (Mn^{III}-O and Mn^{III}-OH hybrid) and H_2O. Strong hydrogen bonding was observed for this species with the supporting ligand. Furthermore, this intermediate reacted with another 0.5 equivalents of DPH to generate $[Mn^{III}(H_2bupa)]^-$ and a second H_2O molecule.[134] This type of reactivity of the $[Mn^{III}(O_2)(H_3bupa)]^-$ complex was interesting as the peroxo-Fe^{III} complex ($[Fe^{III}(O_2)(EDTA)]^{3-}$ (where EDTA = ethylenediaminetetraacetate) was unreactive towards one-electron and two-electron reductants such as $Na_2S_2O_4$ and $NaBH_4$.[135]

In summary, many peroxo-Mn^{III} complexes have been prepared using either O_2, $O_2^{\bullet-}$ or H_2O_2 as oxidant. Most of the peroxo-Mn^{III} complexes were relatively unstable at room temperature and were thus prepared at low temperatures (< 0 °C). While few of the peroxo-Mn^{III} complexes were crystallographically characterized, only one crystal structure of a binuclear Mn-peroxide was previously reported. Furthermore, little vibrational data for mononuclear Mn-peroxide complexes is available because of laser irradiation producing sample degradation. Nevertheless, previously reported peroxo-Mn^{III} complexes displayed characteristic absorbance bands at λ_{max} = 410-460 nm (assigned to peroxo-to-Mn^{III} charge transfer transition) and at λ_{max} = 550-670 nm (assigned to *d-d* transitions). Additionally, many of the peroxo-Mn^{III} species proved to be good nucleophilic oxidants in their reaction with aldehydes. Therefore, the most widely used spectroscopic techniques for characterization of previously reported peroxo-Mn^{III} complexes were electronic absorption spectroscopy, IR and X-ray crystallography.

In the past 11 years many reports on peroxo-Mn^{III} complexes have been published. Crystal structures of several peroxo-Mn^{III} adducts have been reported[98-104] and even some of the more unstable complexes can now be generated in higher yields, allowing their structure and reactivity studies.[115] Even though advances have been made, trapping of Mn intermediates involved in the catalytic cycles remains a challenge. For example, the activation of O_2 by Mn_2 centres[116] has been achieved with trapping of key intermediates[117] but few studies in this area have been done. Nevertheless, the studies done in the field of peroxo-Mn model complexes are coupled with the advances in understanding the mechanisms of Mn-dependent enzymes. Thus, studies of enzymes and model complexes are very important for an understanding of Mn in biology.

Aside from synthesis of peroxo-Mn^{III} synthetic model complexes for Mn enzymes, mixed valent $Mn^{III}Mn^{IV}$ and $Mn^{II}Mn^{III}$ complexes have also been prepared to mimic some of the intermediates observed in the catalytic cycles of Mn enzymes. A description of the characteristic features of these mixed valent complexes is given below.

1.5.2 Bis(μ-oxo)$Mn^{III}Mn^{IV}$ complexes

A series of bis(μ-oxo)$Mn^{III}Mn^{IV}$ complexes have been synthesised and characterised either as mimics of the catalytic cycle of class Ib RNRs described above,[125] as mimics of the OEC of photosystem II,[136] for water oxidation catalysis[137-140] or as model complexes of MnCat.[124, 141] While the X-ray crystal structures of many bis(μ-oxo)$Mn^{III}Mn^{IV}$ complexes have been reported (Figure 1.7, Table 1.5),[125, 137, 139, 140, 142-151] they have also been characterised by electronic absorption, EPR and IR spectroscopies (Table 1.5), and mass spectrometry.

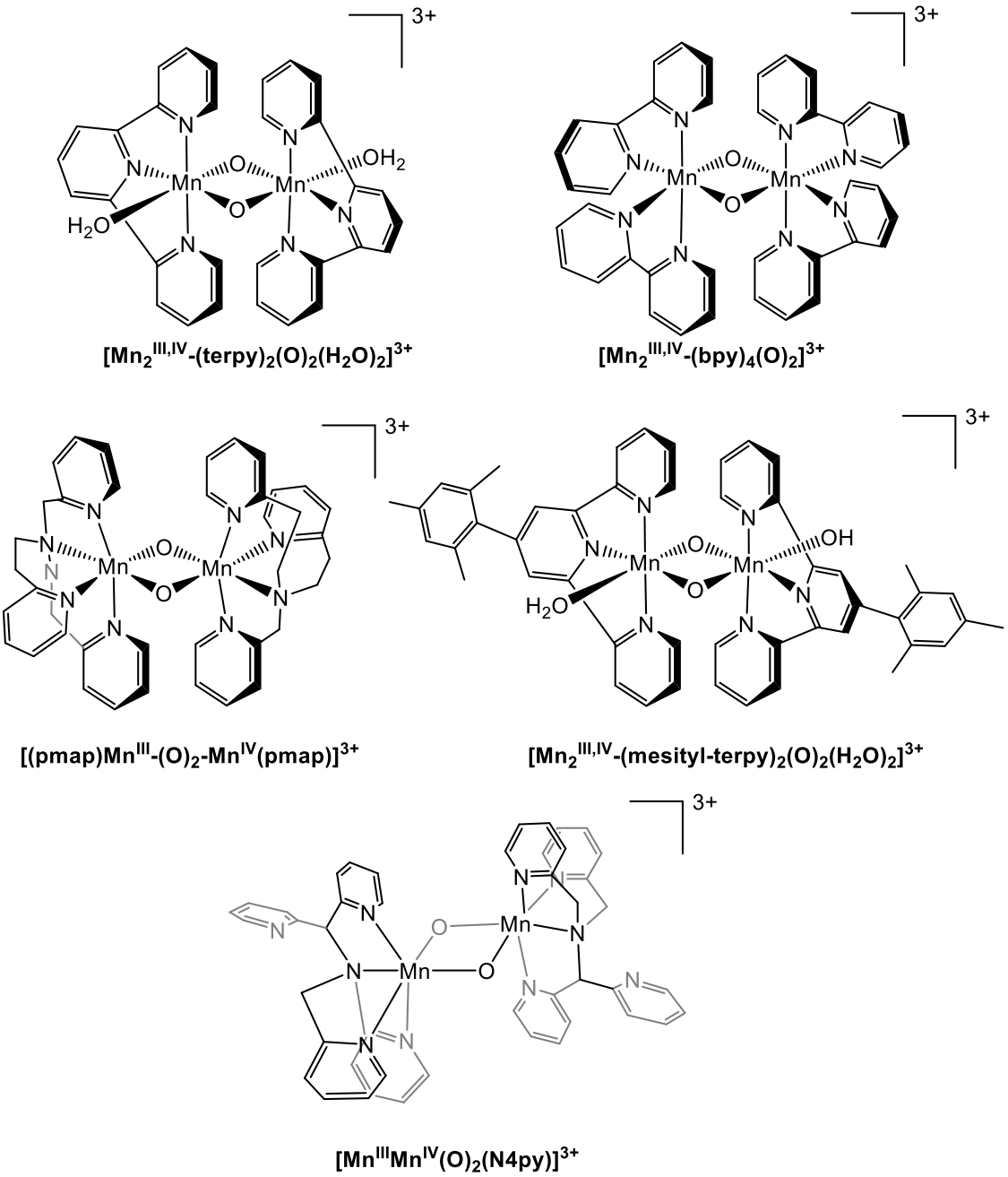

Figure 1.7. Selected structures of synthesised bis(μ-oxo)$Mn^{III}Mn^{IV}$ complexes.[123, 135, 151, 154, 155]

The majority of mixed valent bis(μ-oxo)$Mn^{III}Mn^{IV}$ complexes have been prepared by reaction of the precursor Mn^{II} complex either with $KMnO_4$,[137] oxone,[139] H_2O_2 as an oxidant[141, 146, 150, 152] or by electrochemical oxidation.[147]

All mixed valent bis(μ-oxo)$Mn^{III}Mn^{IV}$ complexes exhibited slight differences in the electronic absorption spectra in the visible region, giving a characteristic absorption band between 520-570 nm assigned to a *d-d* transition band while bands between 590-700 nm could be attributed to a O to Mn charge transfer band (Table 1.5).[140, 142, 153, 154] An exception was the $[Mn_2(\mu\text{-}O)_2(bpy)_2(Ar^{tol}CO_2)_2](ClO_4)$ complex (where bpy = 2,2'-bypiridine and $Ar^{tol}CO_2^-$ = 2,6-di(p-

tolyl)benzoate).[151] This was the first example of a synthetic dinuclear complex, where the metal centres were bridged simultaneously by a pair of oxo groups and a pair of carboxylate groups. Furthermore, this complex had the shortest Mn-Mn distance (2.505(1) Å) and the smallest Mn-O-Mn angles (average 88.3 °) reported for any $[Mn_2(\mu\text{-}O)_2]$ species.[151] The shortening of the Mn-Mn bond length and the diminishment of the Mn-O-Mn angles could be due to the presence of the fourth bridging carboxylate group between the Mn centres.[151] Moreover, the electronic absorption spectrum of this complex was remarkably different from that of any other $[Mn^{III,IV}\text{-}(\mu\text{-}O)_2]^{3+}$ complexes, emphasizing its unusual electronic properties. EPR displayed a 16-line signal centred at g ~ 2 analogous to that observed for all other $[Mn^{III,IV}{}_2(\mu\text{-}O)_2]$ species discussed below. In addition, in IR spectra of bis(μ-oxo)$Mn^{III}Mn^{IV}$ complexes, the peak around 700 cm^{-1} was assigned to the asymmetric stretch (ν_{as}) of the Mn-O-Mn bond according to the literature (Table 1.5). The Mn-O-Mn symmetric stretch has only been found in few bis(μ-oxo)$Mn^{III}Mn^{IV}$ complexes around 600 cm^{-1}.[143, 155] Besides electronic absorption and IR spectroscopies, bis(μ-oxo)$Mn^{III}Mn^{IV}$ complexes have also been characterised by X-ray crystallography and EPR spectroscopy.

Table 1.5. Electronic absorption and IR data for bis(μ-oxo)$Mn^{III}Mn^{IV}$ complexes.

Complex	UV-Vis Data λ in nm (ε in $M^{-1}cm^{-1}$)	IR Data (Mn-O-Mn Stretch) ν_{as} (cm^{-1}) ν_{s} (cm^{-1})	Ref
$[MnO_2(bpy)]_2(ClO_4)_3$	525 (530), 555 (455), 684 (561)	ND	[153]
$[MnO_2(phen)]_2(ClO_4)_3$	525 (509), 555 (427), 684 (553)	ND	[153]
$[MnO_2(tmpa)]_2(ClO_4)_3$	443 (1490), 561 (760), 658 (620)	ND	[154]
$[Mn_2O_2(N,N\text{-}bispicen)_2](ClO_4)_3$	433 (1080), 555 (511), 645 (450)	ND	[142]
$[Mn_2(\mu\text{-}O)_2(py\text{-}terpy)(OH_2)][NO_3)_3.8H_2O$	552 (612), 655 (608)	700	[140]
$[Mn_2O_2(terpy)_2(OH_2)_2](NO_3)_3.6H_2O$	553 (678), 654 (585)	706	[156]
$[(pmap)Mn_2(\mu\text{-}O)_2(pmap)](ClO_4)_3$	556 (ND), 662 (ND)	ND	[157]
$[Mn_2(O_2)(tpa)_2](ClO_4)_3$	660 (500), 559 (621), 505 (650), 439 (1250), 382 (1400)	703 611	[143]
$[Mn_2(O_2)(bpg)_2](ClO_4)_3$	640 (420), 545 (550), 434 (1250), 380 (1480)	697 605	[143]
$\{[Mn_2(O_2)(pda)_2]Na(H_2O)_6\}_n$	590 (450), 537 (600), 413 (1550), 375 (ND)	694 610	[143]
$[Mn_2(cyclen)_2(\mu\text{-}O)_2](ClO_4)_3.4H_2O$	553 (ND), 644 (ND)	690 570	[155]
$[Mn(O)(bispicMe_2en)]_2(ClO_4)_3.H_2O$	659 (458), 552 (480), 430 (1155), 380 (1472)	ND	[145]
$[Mn_2(\mu\text{-}O)_2(terpy)_2(CF_3CO_2)_2](CF_3CO_2).2H_2O$	278 (31000), 324 (25000), 550 (725), 620 (650)	ND	[148]
$[(phen)_2Mn(\mu\text{-}O)_2Mn(phen)_2](PF_6)_3.CH_3CN$	523 (580), 550 (460), 680 (550), 800 (ND)	686	[158]
$[Mn_2(\mu\text{-}O)_2(bpy)_2(Ar^{tol}CO_2)_2](ClO_4)$	Shoulder at ~760 nm	ND	[151]
$[(OH_2)(R\text{-}terpy)Mn(\mu\text{-}O)_2Mn(R\text{-}terpy)(OH_2)][NO_3)_3$			
• **R = Cl**	552 (610), 658 (603)	712	[137]
• **R = H**	551 (605), 655 (600)	698	
• **R = MeS**	552 (616), 655 (604)	700	
• **R = Me**	551 (619), 655 (608)	702	
• **R = EtO**	552 (620), 655 (598)	705	
• **R = PrO**	552 (610), 655 (603)	703	
• **R = MeO**	552 (619), 655 (603)	703	
• **R = BuO**	551 (623), 650 (610)	704	

(phen = 1,10-phenanthroline; tmpa = tris(2-pyridylmethyl)amine; N,N-bispicen = N,N-bis(2-pyridylmehyl)-1,2-diaminoethane; py-terpy = 4'-(4-pyridyl)-2,2':6',2''-terpyridine; terpy = 2,2':6',2''-terpyridine; pmap = bis[2-(2-pyridyl)ethyl]-2-pyridylmethylamine; tpa = tris-picolylamine; bpg = bis-picolylglycylamine; (H_2)pda = picolyldiglycylamine; cyclen = 1,4,7,10-tetraazacycledodecane; bispicMe_2en = N,N'-bis(2-pyridylmethyl)-N,N'-dimethyl-1,2-ethanediamine).

Many bis(μ-oxo)$Mn^{III}Mn^{IV}$ complexes have been crystallographically characterised. All bis(μ-oxo)$Mn^{III}Mn^{IV}$ complexes had a similar Mn-Mn bond length of ~2.7 Å (Table 1.6). The Mn-O bond lengths in these complexes were between 1.7 and 2 Å, with the two Mn metal centres being relatively symmetric. The reported crystal structures of bis(μ-oxo)$Mn^{III}Mn^{IV}$ complexes

showed that both Mn centres were in an octahedral coordination environment, in comparison to the peroxo-Mn^{III} complexes described above, where the metal centre was either square pyramidal or trigonal bipyramidal. While the peroxo-Mn^{III} complexes proved to be good deformylating agents, the bis(μ-oxo)$Mn^{III}Mn^{IV}$ complexes proved to be unreactive towards substrates. This could be due to poor accessibility of the substrate to the active metal core.

Table 1.6. Selected bond lengths from X-ray crystallography for bis(μ-oxo)$Mn^{III}Mn^{IV}$ complexes.

Complex	Bond Lengths (Å)					
	Mn1-Mn2	Mn1-O1	Mn1-O2	Mn2-O1	Mn2-O2(H_2O)	Ref
$[Mn_2O_2(N,N\text{-bispicen})_2](ClO_4)_3$	2.646(2)	1.783(4)	1.788(4)	1.836(4)	1.838(4)	[142]
$[Mn_2(\mu\text{-}O)_2(py\text{-}terpy)(OH_2)](NO_3)_3.8H_2O$	2.729(1)	1.821(2)	-	1.811(3)	2.009(3)	[140]
$[Mn_2O_2(terpy)_2(OH_2)_2](NO_3)_3.6H_2O$	2.7315(12)	1.813(3)	-	1.812(3)	2.069(3)	[156]
$[(OH_2)(MeS\text{-}terpy)Mn(\mu\text{-}O)_2Mn(MeS\text{-}terpy)(OH_2)](NO_3)_3$	2.7183(8)	1.822(2)	-	1.803(2)	2.043(2)	[137]
$[(OH_2)(Me\text{-}terpy)Mn(\mu\text{-}O)_2Mn(Me\text{-}terpy)(OH_2)](NO_3)_3$	2.753(1)	1.820(2)	-	1.817(2)	2.004(2)	[137]
$[Mn_2(\mu\text{-}O)_2(terpy)_2(CF_3CO_2)_2](CF_3CO_2).CH_3CN$	2.7265(5)	1.8517(16)	1.8508(17)	1.7786(17)	1.7786(17)	[148]

Another spectroscopic technique used in the literature for the characterisation of bis(μ-oxo)$Mn^{III}Mn^{IV}$ complexes is EPR. The EPR spectra of these complexes showed a characteristic 16 line signal centred around g ~ 2.[136, 138, 141, 151, 157, 159] The 16-line EPR signal corresponded to a fingerprint of a mixed valent $Mn^{III}Mn^{IV}$ dimeric complex in which the Mn^{III} and the Mn^{IV} ions were anti-ferromagnetically coupled with each other. The 16-line EPR spectral pattern arise from the electron-nuclear hyperfine interaction of the ^{55}Mn nuclei (nuclear spin, I = 5/2) in the paramagnetic $Mn^{III}Mn^{IV}$ dimeric core (electron spin, S = ½). Sometimes the $Mn^{III}Mn^{IV}$ complexes were supported by N-containing ligands. The interactions of the paramagnetic $Mn^{III}Mn^{IV}$ dimeric core with the ^{14}N atoms (nuclear spin, I = 1) of the respective ligands coordinated to the Mn ions could have also contributed to the 16-line signal, resulting in magnetic splitting. However, the line splitting that resulted from the ^{14}N hyperfine interactions were usually weak. For example, the EPR spectrum of [(pmap)Mn^{III}-(μ-$O)_2$-Mn^{IV}(pmap)]$(ClO_4)_3$ (Figure 1.7) measured at 100 K in N-methylformamide exhibited the characteristic 16-line signal centred around g ~ 2.003.[157] Similarly a frozen dichloromethane solution of $[Mn_2(\mu\text{-}O)_2(bpy)_2(Ar^{tol}CO_2)_2](ClO_4)$ at 4 K, also displayed a 16 line signal centred at g ~ 2.[151] This type of spectrum has been assigned to the S = ½ ground state of the complex indicating antiferromagnetic coupling between two high spin Mn^{III} and Mn^{IV} ions.[151, 157]

Furthermore, the EPR spectrum of $[Mn_2^{III,IV}(tpdm)_2(\mu\text{-}O)_2(\mu\text{-}OAc)](ClO_4)_2$ (where tpdm = tris(2-pyridyl)methane) complex, that was oxidised electrochemically, also exhibited a 16 line signal at g ~ 2 at 5 K.[138] Thus, until now bis(μ-oxo)$Mn^{III}Mn^{IV}$ complexes are known to give rise to similar EPR spectra. Moreover, the postulated bis(μ-O)(OH)$Mn^{III}Mn^{IV}$ adduct obtained in class Ib *B. subtilis* Mn^{II}_2 RNRs, was also characterised by EPR exhibiting a 16-line EPR signal at 10 K.[83] Thus, EPR is a very useful spectroscopic technique not only for characterisation of model complexes but also for Mn enzymes.

Therefore synthetic bis(μ-oxo)$Mn^{III}Mn^{IV}$ complexes as models of RNRs, MnCat and the OEC of photosystem II have been prepared and characterised by electronic absorption and IR spectroscopies, mass spectrometry and EPR. The crystal structures of many of these bis(μ-oxo)$Mn^{III}Mn^{IV}$ complexes have also been reported. We are mainly interested in mimicking the catalytic cycle of class Ib RNRs and thus in trapping a bis(μ-oxo)$Mn^{III}Mn^{IV}$ species as a model complex for the catalytic cycle of class Ib RNRs. Another intermediate involved in the catalytic cycle of class Ib RNRs was a mixed valent $Mn^{II}Mn^{III}$ species. A description, preparation and characterisation of synthetic mixed valent $Mn^{II}Mn^{III}$ complexes is given below.

1.5.3 Mixed valent $Mn^{II}Mn^{III}$ complexes

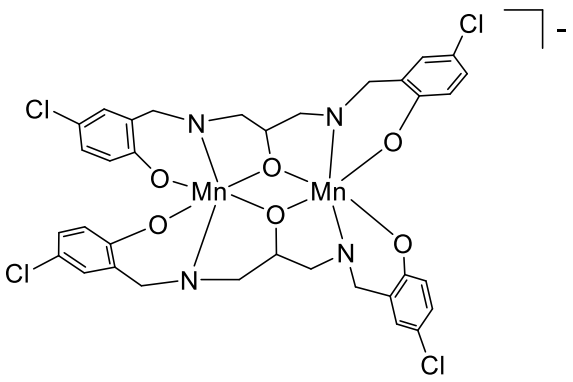

$[Mn^{II,III}_2(2\text{-}OH(5\text{-}ClSal)pn)_2]^-$

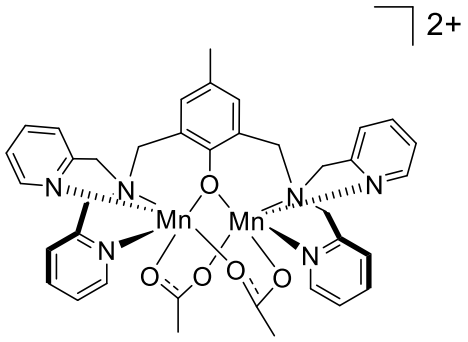

$[Mn^{II,III}_2(O_2CCH_3)_2(BPMP)]^{2+}$

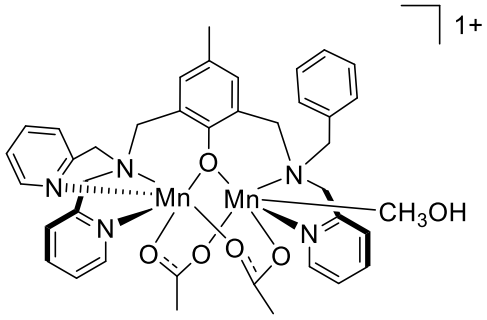

$[Mn^{II,III}_2(O_2CCH_3)_2(CH_3OH)(L)]^+$

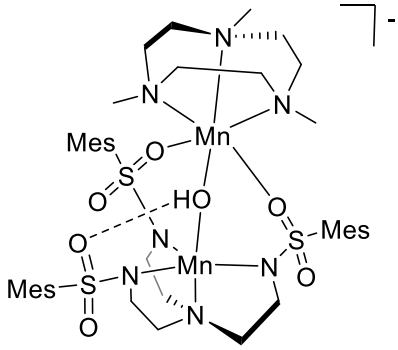

$[(TMTACN)Mn^{II}\text{-}(OH)\text{-}Mn^{III}(MST)]^-$

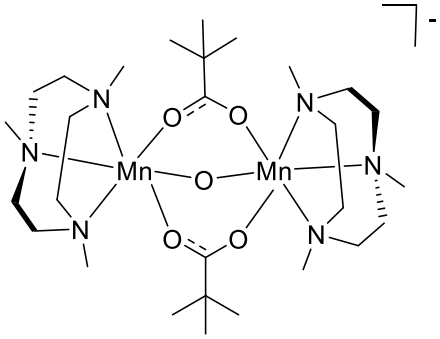

$[Mn^{II}Mn^{III}(O)(piv)_2(Me_3tacn)_2]^-$

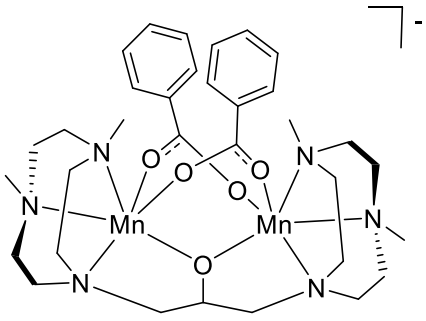

$[Mn^{II}Mn^{III}(PhCO_2)_2(Me_4alkox)]^-$

Figure 1.8. Structures of selected mixed valent $Mn^{II}Mn^{III}$ complexes.[78, 159-163]

Binuclear mixed valent $Mn^{II}Mn^{III}$ species play an important role in biology as they have been postulated as intermediates in the catalytic cycle of metalloenzymes, catalase, liver arginase[164] and RNRs.[83] Few synthetic mixed valent $Mn^{II}Mn^{III}$ complexes have been prepared to mimic the active sites of these metalloenzymes (Figure 1.8).[78, 159-161] The main spectroscopic techniques used for the characterisation of these complexes are X-ray crystallography, electronic absorption spectroscopy and EPR. Most of these mixed valent complexes have been

prepared either starting from a Mn^{III} salt,[159, 160, 165] or by electrochemical oxidation of Mn^{II} precursors.[166] Some of these binuclear mixed valent $Mn^{II}Mn^{III}$ complexes have been characterised crystallographically, having similar Mn···Mn bond lengths (Table 1.7). The mixed valent $Mn^{II}Mn^{III}$ complex (TEA)[Mn_2(2-OH(5-Cl-sal)pn)$_2$].C_6H_6.CH_3OH (where (sal)pn = 1,3-bis(salicylideneamino)-2-propanol) (Table 1.7) exhibited a shorter Mn···Mn bond distance when compared to the other crystallographically characterised $Mn^{II}Mn^{III}$ complexes, which could be due to the ligand.[78] Furthermore the Mn···Mn bond lengths in the Mn^{II}_2, Mn^{III}_2 and $Mn^{III,IV}_2$ complexes supported by the (sal)pn ligand were 3.3, 3.36 and 3.25 Å, differing by only 0.11 Å, showing that the basic core structure was highly invariant.[78] Thus small differences were observed in the Mn···Mn distance across mixed valent $Mn^{II}Mn^{III}$ complexes.

Table 1.7. Electronic absorption and X-ray crystallography data for selected mixed valent $Mn^{II}Mn^{III}$ complexes.

Complex	UV-Vis Data	Bond Length	Ref
	λ_{max} in nm (ε in $M^{-1}cm^{-1}$)	Mn-Mn (Å)	
[Mn_2(bpmp)(μ-OAc)$_2$](ClO_4)$_2$.2H_2O	430 (ND), 480 (ND), 620 (ND)	3.447(1)	[160]
[Mn_2(bcmp)(μ-OAc)$_2$](ClO_4)$_2$.CH_2Cl_2	450 (ND), 590 (ND)	3.422(3)	[160]
[Mn_2(L)(OAc)$_2$(H_2O)](ClO_4)2.H_2O	380 (1270), 485 (960), 627 (680).	3.497	[159]
(TEA)[Mn_2(2-OH(5-Cl-sal)pn)$_2$].C_6H_6.CH_3OH	380 (1600)	3.360(7)	[78]
[(TMTACN)Mn-(μ-OH)-Mn(MST)](OTf)	275 (11500), 420 (683), 481 (490), 643 (616)	3.472(2)	[163]
[Mn_2(μ-O)(μ-piv)$_2$(Me_3tacn)$_2$](ClO_4)	486 (ND), 521 (ND)	3.084(3)	[76, 162]
[Mn_2(BCPMP)(OAc)$_2$]	270 (ND), 315 (ND), 450 (ND)	3.473	[167]

(bpmp = 2,6-bis[bis(2-pyridylmethyl)aminomethyl]-4-methylphenol; bcmp = 2,6-bis(1,4,7-triazacyclonon-1-ylmethyl)-4-methylphenol; L = 2-(bis(2-pyridylmethyl)aminomethyl)-6-((2-pyridylmethyl)(benzyl)-aminomethyl)-4-methylphenol; TMTACN = Me_3tacn = 1,4,7-trimethyl-1,4,7-triazacyclononane; $[MST]^{3-}$ = N,N,N''-[2,2',2''-nitrilotris(ethane-2,1-dyil)]tris(2,4,6-trimethylbenzenesulfonamido); Piv = $(CH_3)_3CCO_2$; Ph = phenyl; Me_4alkox = 1,3-bis(4,7-dimethyl-1,4,7-trizacyclononyl)-2-propanol; $(BPCPMP)^{3-}$ = 2,6-bis({(carboxymethyl([(1-pyridyl)methylamino}methyl)-4-methylphenolato).

Previously reported $Mn^{II}Mn^{III}$ complexes have also been characterised by electronic absorption spectroscopy (Table 1.7). These complexes exhibited electronic absorption bands between 360-400 nm, that have been assigned to phenoxo-Mn^{III} ligand to metal charge transfer (LMCT) band while electronic absorption bands between 450-480 nm and 580-630 nm have been assigned to *d-d* transitions of the Mn^{III} ions (Table 1.7).[159, 160] Another very useful spectroscopic technique for characterisation of mixed valent $Mn^{II,III}_2$ complexes is EPR. X-band EPR spectra of frozen solutions of $Mn^{II}Mn^{III}$ complexes have previously been reported. The frozen glass spectra of

these complexes exhibited 29-line Mn hyperfine features that associate with the g ~ 2 signal.[160, 161, 163, 168, 169] The 29-line Mn hyperfine pattern resulted from molecules in the S = ½ ground state. For example, for a binuclear complex with two equivalent ^{55}Mn nuclei and an isotropic g tensor for the S = ½ ground state, 11 Mn hyperfine lines were expected in the EPR spectrum. If the S_T = ½ ground state of a mixed valent trapped $Mn^{II}Mn^{III}$ complex had an isotropic g tensor then 36 ($(2I_1+1)(2I_2+1) = 6*6 = 36$) manganese hyperfine lines were expected.[160, 168] If the g tensor for the S = ½ ground state was axial, then 72 Mn hyperfine lines were expected in the EPR spectrum. Furthermore, a rhombic g tensor should form 108 hyperfine lines.[160] Previous reports of EPR spectra of frozen solutions of mixed valent $Mn^{II}Mn^{III}$ complexes exhibited 29 line Mn hyperfine and showed a dramatic temperature dependence. Below 15 K, a g ~ 2 multiline Mn signal was observed that arises from the S = ½ ground state of the complex, consistent with weak antiferromagnetic coupling between the Mn ions. Above 15 K, a broad g ~ 4 signal was observed in the mixed valent $Mn^{II}Mn^{III}$ complexes that was attributed to complexes in the S = 3/2 state.[159, 160, 165] Simulation of these EPR spectra using different computer programs have been very difficult. Only few simulations of EPR spectra of mixed valent $Mn^{II}Mn^{III}$ complexes have been reported in the literature.[160, 169] All of the EPR measurements performed on binuclear Mn_2 complexes had to be carried out at very low temperatures (<15 K) in order to obtain well-resolved Mn hyperfine features.[159-161, 168, 170] Thus, while synthetic mixed valent $Mn^{II,III}{}_2$ complexes have been characterised using EPR, the mixed valent $Mn^{II}Mn^{III}$-OOH intermediate postulated in the catalytic cycle of class Ib *B. subtilis* RNR has not been able to be trapped and characterised by EPR.[83] However EPR of the mixed valent bis(μ-O)(OH)$Mn^{III}Mn^{IV}$ adduct from class Ib *B. subtilis* RNR has been obtained, exhibiting a 16-line EPR signal described above. In summary, the synthesis and characterisation of synthetic mixed valent $Mn^{II}Mn^{III}$ complexes it is very important, as these complexes proved to be intermediates in the catalytic cycle of metalloenzymes.

Over the last two decades, many synthetic Mn complexes such as peroxo-Mn^{III}, bis(μ-oxo)$Mn^{III}Mn^{IV}$ and $Mn^{II}Mn^{III}$ complexes have been prepared, to model the active site and mechanisms of Mn_2 enzymes. Moreover, as mentioned above the chemistry of synthetic peroxo-$Fe^{III}{}_2$ complexes capable of mimicking the active site of Fe_2 enzymes has been extensively studied over the last 40 years. A description of the characteristic features of peroxo-$Fe^{III}{}_2$ complexes is given below.

1.5.4 Fe^{III}_2-peroxide model complexes

The most studied Fe_2 oxygenases and whose mechanisms have been widely investigated are the methane monooxygenase,[14-17] toluene monooxygenase,[18] stearoyl- acyl carrier protein Δ^9-desaturase,[19-21] RNR[22] and cyanobacterial aldehyde deformylase oxygenase.[171] As outlined above, class Ib incorporate a Mn^{II}_2 cofactor while class Ia RNRs contain a Fe^{II}_2 cofactor. As described above (section 1.3), in the catalytic cycle of class Ia RNRs, upon activation of the Fe^{II}_2 core with dioxygen, few Fe_2-enzymatic intermediates have been postulated. Interestingly, while Mn-model complexes of class Ib RNRs have been prepared over the last two decades, the generation of synthetic model complexes of Fe_2 enzymes has been studied over the last four decades. More importantly, dioxygen adducts of Fe_2 complexes supported by benzimidazole ligands (N-Et-HPTB) have proved to be good biomimetic models of class Ia RNRs and methane monooxygenase. The same benzimidazole ligands (HPTB, N-Et-HPTB) were used for preparation of Mn_2 complexes as model systems for class Ib RNRs (see chapters 2 and 6). Therefore, a description of how synthetic models of Fe_2 metalloenzymes are prepared, together with their characterisation (electronic absorption, IR and X-ray crystallography) is fundamental (Table 1.8).

Table 1.8. Electronic absorption, resonance Raman parameters and selected bond lengths from X-ray crystallography for a number of peroxo-Fe^{III}_2 complexes.

Complex	UV-Vis	rRaman	Bond Lengths (Å)		
	λ_{max} in nm (ε in $M^{-1}cm^{-1}$)	ν_{O-O} ($\Delta^{18}O_2$)	Fe-Fe	O-O	Ref
$[Fe_2(O_2)(Me_4\text{-tpdp})(O_2CPh)(H_2O)](BF_4)_2$	616 (2000)	918 (-47)	-	-	[172]
$[Fe_2(Ph\text{-}BIMP)(O_2)(O_2CPh)]^{2+}$	500-700 (~ 1700)	-	3.328	1.426(6)	[173]
$[Fe_2(N\text{-}Et\text{-}HPTB)(O_2)(O_2CPh)]^{2+}$	500 (~ 1500)	900 (-50)	-	-	[174-176]
$[Fe_2(N\text{-}Et\text{-}HPTB)(O_2)(OPPh_3)_2]^{3+}$	-	-	3.462(3)	1.416(7)	[174]
$[Fe_2(Tp^{iPr2})(O_2)(O_2CCH_2Ph)]$	694 (2650)	888 (-46)	4.004	1.406(8)	[177]
$[Fe_2(Tp^{iPr2})(O_2)(O_2CPh)]$	682 (3450)	876 (-48)	-	-	[178, 179]
$[Fe_2(O_2)(Htppdo)(O_2CPh)](ClO_4)_3$	610 (1700)	887 (-48)	-	-	[180]
$[Fe_2(6Me_2\text{-}BPP)(O_2)(O)](OTf)_2$	644 (3000)	896 (-47)	-	-	[181]
$[Fe_2(6Me_2\text{-}BPP)(O_2)(O)](3\text{-}ClPh)_2$	577 (1500)	-	3.396(1)	1.396(5)	[181]
$[Fe_2(O_2)(L^{Ph4})(Ph_3CCO_2)]^{2+}$	665 (~2300)	873 (-50)	3.31	1.40	[182]

(Me_4-tpdp = N,N,N',N'-tetrakis{2-(6-methylpyridyl)methyl}-1,3-diaminopropan-2-olate; Ph-BIMP = 2,6-bis[bis{2-(1-methyl-4,5-diphenylimidazolyl)methyl}aminomethyl]-4-methylphenolate; N-Et-HPTB = N,N,N',N'-tetrakis(2-(1-ethylbenzimidazolyl))-2-hydroxy-1,3-diaminopropane; Tp^{iPr2} = tris(3,5-diisopropyl-1-pyrazolyl)borate; Htppdo = N,N,N',N'-tetrakis(6-pivalamido-2-pyridylmethyl)-1,3-diaminopropan-2-ol; $6Me_2$-BPP = N,N-bis(6-methyl-2pyridylmethyl)-3-aminopropionate;

L^{Ph4} = N,N,N',N'-tetrakis[(1-methyl-2-phenyl-4-imidazolyl)methyl]-1,3-diamino-2-propanolate).

The interaction of Fe_2 enzymes with dioxygen results in the formation of key intermediates such as peroxo-Fe^{III} intermediates. However, there is a lack of crystal structures for these enzymatic intermediates resulting in a difficult understanding of their catalytic mechanism. Thus, numerous synthetic models of Fe_2 intermediates have been developed over the last 30 years. In 1983, the first Fe_2 model complexes as structural models of Fe_2 enzymes were prepared.[183] However, only in 1996 the first crystal structure of a μ-peroxo-Fe^{III}_2 complex was reported by Suzuki *et al*.[173] The $[Fe^{II}_2(Ph\text{-}BIMP)(O_2CPh)](BF_4)_2$ complex, when exposed to dioxygen was found to form a μ-peroxo-Fe^{III}_2 complex ($[Fe^{II}_2(\mu\text{-}1,2\text{-}O_2)(Ph\text{-}BIMP)(O_2CPh)](BF_4)_2$, Figure 1.9). This μ-peroxo-Fe^{III}_2 complex was described as relatively stable at room temperature and could bind O_2 reversibly at room temperature. Shortly after, Que *et al*. published the crystal structure of another μ-peroxo-Fe^{III}_2 species.[174] Triphenylphosphine oxide was used for the crystallisation of the $[(N\text{-}Et\text{-}HPTB)Fe^{III}_2(\mu\text{-}1,2\text{-}O_2)(OPPh_3)_2](BF_4)_3$ complex (Figure 1.9), increasing the lifetime of the μ-peroxo-Fe^{III}_2 adduct formed upon treatment of the Fe^{II}_2 complex ($[(N\text{-}Et\text{-}HPTB)Fe^{II}_2(OPPh_3)_2](BF_4)_2$ with dioxygen. It was postulated that in the absence of triphenylphosphine, the peroxo-Fe^{III}_2 adduct was not stable and it decomposed by homolytic O-O bond cleavage, resulting in the formation of a Fe^{IV}_2 species.[174] In the same year, the third crystal structure of a μ-peroxo-Fe^{III}_2 complex ($[Fe_2(Tp^{iPr2})(\mu\text{-}1,2\text{-}O_2)(O_2CCH_2Ph)]$) was reported by Lippard and co-workers[177] prepared in a similar way as the above described μ-peroxo-Fe^{III}_2 adducts. The bulky Tp^{iPr2} ligand stabilised this intermediate. Since then, the next crystal structure of a μ-peroxo-Fe^{III}_2 species was published by Suzuki *et al*. in 2005.[181] This adduct was formed differently to the ones above, H_2O_2 was added as an oxidant to a Fe^{III}_2 complex, $[Fe_2(6Me_2\text{-}BPP)_2(O)(OH)](OTf)$ at -80 °C in methanol forming $[Fe_2(6Me_2\text{-}BPP)_2(\mu\text{-}1,2\text{-}O_2)(O)]B(3\text{-}ClPh)_4$ complex (Figure 1.9). From the crystallographic data, the O-O bond length of the peroxo ligand of this complex was 1.396(5) Å, which it was slightly shortened relative to the other three peroxo-Fe_2 adducts described above (1.406(8) to 1.426(6) Å).[184] More recently, in 2017 the X-ray crystal structure of a peroxo-Fe^{III}_2 ($[Fe^{III}_2(O_2)(L^{Ph4})(Ph_3CCO_2)]^{2+}$) complex was published by Suzuki and co-workers.[182] This complex was prepared by the reaction of the precursor Fe^{II}_2 complex ($[Fe_2(L^{Ph4})(Ph_3CCO_2)]^{2+}$) with dioxygen, as a functional model for toluene monooxygenase.[182] Therefore, to date there are only five crystal structures of synthetic μ-peroxo-Fe^{III}_2 complexes (Figure 1.9).[173, 174, 177, 181, 182] One common feature of all these complexes is that they are highly symmetrical (except the crystal structure of the Fe_2 complex supported by the $6Me_2$-BPP ligand described above) that could be a key characteristic of their high stability.

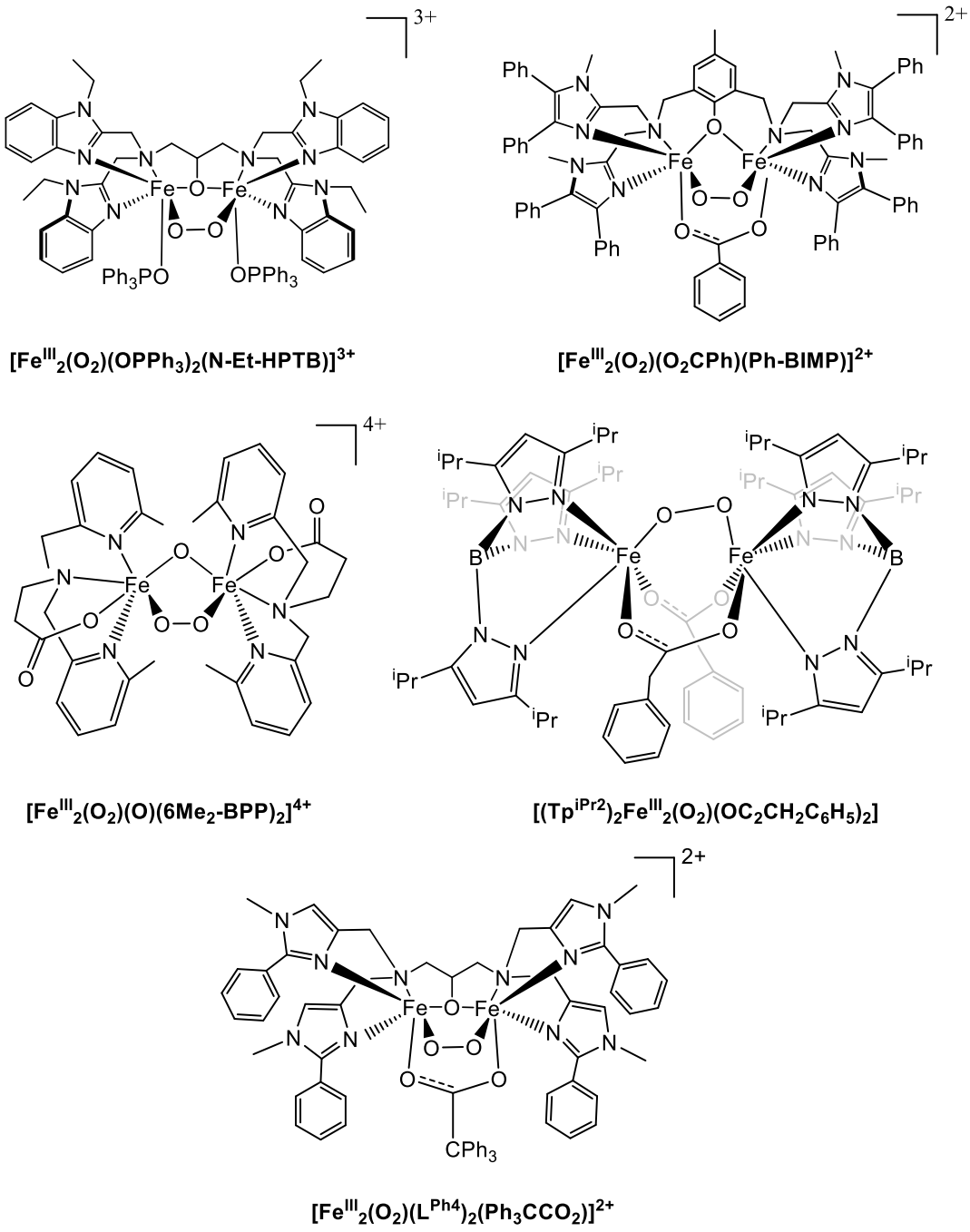

Figure 1.9. Chemdraw representations of the five crystal structures of peroxo-Fe^{III}_2 complexes previously published.[173, 174, 177, 181, 182]

Besides these five crystallised peroxo-Fe^{III}_2 species, other Fe_2 complexes have been prepared, which have been characterised by a variety of spectroscopic techniques such as electronic absorption, resonance Raman and Mössbauer spectroscopy (Table 1.8).[13, 185] A spectroscopic technique that has been widely used for characterisation of synthetic peroxodifferic complexes is electronic absorption spectroscopy (Table 1.8). These complexes exhibited a peroxo-to-Fe^{III} LMCT transition in the visible region, that corresponded to a visible absorption maximum ranging from 450 to 730 nm. Most of the synthetic complexes characterised so far adopted a μ-

1,2-peroxo binding mode and some of these complexes had an additional μ-oxo bridge. These two bridging units had characteristic absorption bands at ~ 500 and ~ 650 nm, that have been assigned to oxo-to-Fe^{III} and peroxo-to-Fe^{III} LMCT transitions based on the excitation of their resonance Raman bands.[13] In the resonance Raman spectrum excitation into the lower energy LMCT band enhanced vibrations from the peroxo bridge, which were found at ~ 850 cm^{-1} for the ν_{O-O}, at 460 cm^{-1} for the ν_{sym}(Fe-O_2-Fe) and at 520 cm^{-1} for the ν_{asym}(Fe-O_2-Fe) mode. Furthermore, excitation into the higher energy LMCT band gave rise to the oxo bridge with the ν_{sym}(Fe-O-Fe) and ν_{asym}(Fe-O-Fe) modes usually observed at 520 and 700 cm^{-1}.[186, 187] Only two of the five crystallised peroxo-Fe^{III}_2 complexes have been characterised by resonance Raman vibration spectroscopy.[177, 182] The ν_{Fe-O} vibrations of these complexes have been assigned at 415 and 465 cm^{-1} while the ν_{O-O} vibrations were found at 888 and 847 cm^{-1}. Thus, resonance Raman spectroscopy is a very useful technique for the characterisation of Fe^{III}_2-peroxide intermediates.

Finally, Mössbauer spectroscopy is another technique used for the characterisation of Fe_2 complexes. It provides information about the spin state of the Fe ions and the geometry of the coordination sphere. The isomer shifts, and the quadrupole splitting can be compared to those of the enzyme intermediates. The Fe^{III} ions in the Fe^{III}_2-peroxide complexes were typically high spin (S = 5/2) centres and they had isomer shifts that fall within the range of 0.47-0.66 mm/s.[13, 185]

The above described Fe^{III}_2-peroxide complexes have been capable of forming Fe^{IV}_2-oxo intermediates that are responsible for oxygen atom transfer. However, none of these intermediates can perform catalytic reactions for mimicking the O_2 activating enzymes such as cyanobacterial aldehyde deformylase oxygenase or the arylamine oxygenases. Thus, new functional models are highly needed to understand the mechanisms of O_2 activating Fe_2 enzymes.

1.6 Conclusions

In the last decades, considerable efforts were invested in the search and study of Mn enzymes. The catalytic cycles of many Mn enzymes such as Mn containing-superoxide dismutase, extradiol catechol dioxygenases, MnCat and RNRs have been investigated. For some of these Mn enzymes it has been proposed to feature peroxo-Mn intermediates in their catalytic cycles. Recent efforts have been involved in mimicking these intermediates using synthetic model complexes, providing insight into mechanistic studies of the enzymes. RNRs are a class of

enzymes involved in DNA synthesis and repair. Class Ia RNRs contain a Fe_2 cofactor and it had been shown that the active oxidant in this catalytic cycle was dioxygen. However, it was only in 2013 when it has been postulated that the active oxidant in class Ib RNRs, that contain a Mn_2 cofactor was superoxide ($O_2^{\bullet-}$). Stubbe and co-workers have shown that Mn^{II}_2 cofactor of class Ib RNRs reacted with $O_2^{\bullet-}$ in the presence of a proton source to form a hydroperoxo-$Mn^{II}Mn^{III}$ and subsequently, a high valent $Mn^{III}Mn^{IV}$ intermediate (Scheme 1.9). While these mechanistic postulates are valid, little experimental support for them exists. We were particularly interested in the role $O_2^{\bullet-}$ plays. In order to attempt to verify the above mechanistic postulates, using synthetic Mn^{II}_2 complexes we explored the interaction between Mn^{II}_2 complexes and $O_2^{\bullet-}$.

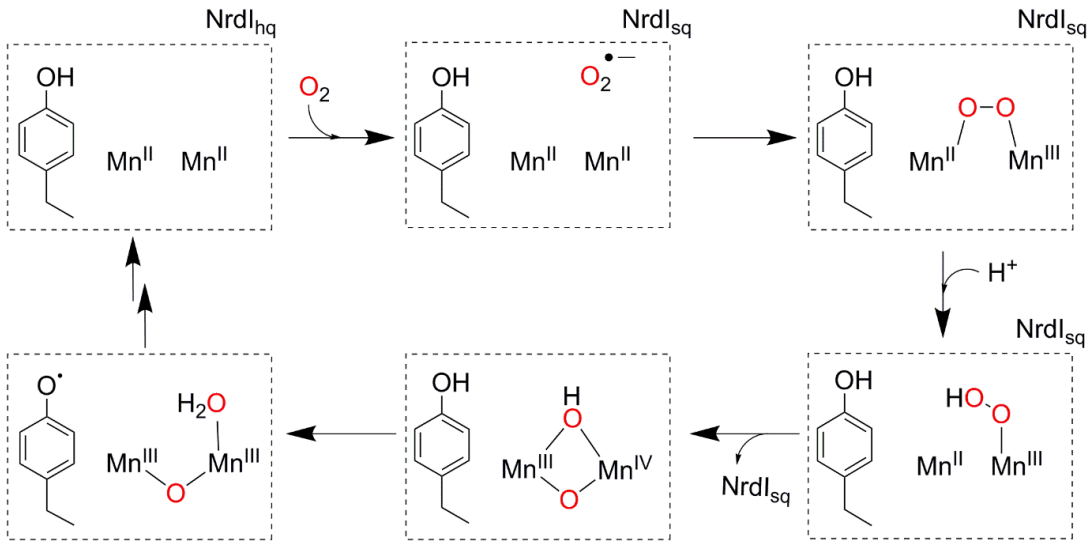

Scheme 1.9. Proposed catalytic cycle for class Ib Mn_2 RNRs in *B. subtilis* ($NrdI_{hq}$ = Flavodoxin hydroquinone, $NrdI_{sq}$ = Flavodoxin semiquinone).[31, 69, 83]

As seen above (Scheme 1.9), two of the postulated active intermediates in this catalytic cycle were a $Mn^{II}Mn^{III}$-OOH and a high valent $Mn^{III}Mn^{IV}$ species. Moreover, a series of synthetic model complexes such as peroxo-Mn^{III}, bis(μ-oxo)$Mn^{III}Mn^{IV}$, and mixed valent $Mn^{II}Mn^{III}$ complexes have been reported. However, to the best of our knowledge, before this project nobody has isolated a $Mn^{II}Mn^{III}$-peroxide complex, and this was the main aim.

1.7 Aims

The aim of this project was to mimic the catalytic cycle of class Ib Mn^{II}_2 RNRs by using synthetic Mn_2 model complexes. It has recently been shown by Stubbe and co-workers that superoxide ($O_2^{\bullet-}$), rather than dioxygen (O_2), was the active oxidant in class Ib Mn^{II}_2 RNRs. The $O_2^{\bullet-}$ anion was proposed to react with the Mn^{II}_2 core of class Ib RNRs in the presence of a proton source yielding a $Mn^{II}Mn^{III}$-hydroperoxide intermediate. A $Mn^{III}(\mu\text{-OH})(\mu\text{-O})Mn^{IV}$ species was postulated to form after cleavage of the O-O bond.[83] The high valent species was postulated to oxidise tyrosine. While the $Mn^{III}Mn^{IV}$ intermediate was characterised by EPR spectroscopy, no insight into the $Mn^{II}Mn^{III}$-hydroperoxide was obtained.[83] Thus, the central focus is mimicking this reaction by probing the reactivity of biomimetic Mn_2 complexes towards $O_2^{\bullet-}$. We are also interested in the protonation reaction to obtain a $Mn^{II}Mn^{III}$-hydroperoxide adduct and subsequently a mixed valent $Mn^{III}Mn^{IV}$ species. This will allow us to better understand the active site of Mn^{II}_2 RNRs. While the reactivity of mononuclear Mn complexes with $O_2^{\bullet-}$ has already been reported as described above, no studies on dinuclear Mn complexes and $O_2^{\bullet-}$ have previously been conducted.

The first step in the investigation is the synthesis and characterisation of ligands. We chose to employ bulky, polydentate ligands (N,N,N',N'-tetrakis(2-(1-ethylbenzimidazolyl))-2-hydroxy-1,3-diaminopropane (= N-Et-HPTB), 2,6-bis[(bis(2-pyridylmethyl)amino)methyl]-4-methylphenol (= HBPMP) and N,N,N'N'-tetrakis(2-pyridylmethyl)1,3-diamino-2-hydroxypropane (= HPTP)) as shown below (Figure 1.10), as an ideal framework for the preparation of Mn_2 complexes. Once the ligands are prepared, the synthesis of dinuclear complexes supported by these ligands will be carried out. Following that, the reaction of the Mn_2 complexes with $O_2^{\bullet-}$ will be investigated. Metastable adducts can be prepared using low temperature techniques and characterised by many spectroscopic techniques such as electronic absorption, resonance Raman, mass spectrometry, EXAFS, XANES and EPR spectroscopies.

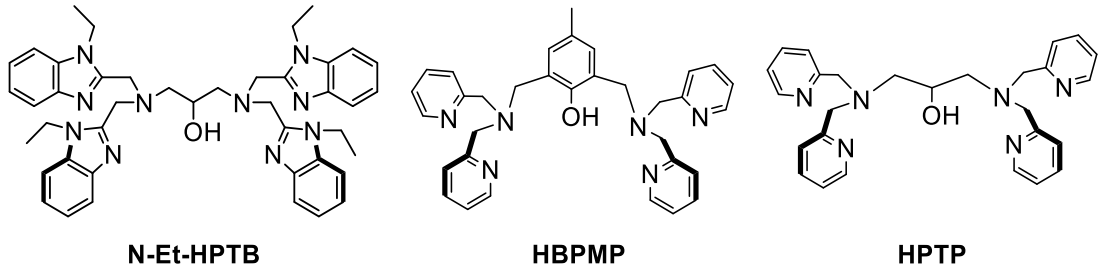

Figure 1.10. Ligands used in this project for synthesis of Mn^{II}_2 complexes.

Aside from their spectroscopic characterisation, we are also interested in the reactivity of these adducts in oxidation reactions. Thus, by investigating the reactivity of the adducts formed in the reaction of Mn_2 complexes with $O_2^{\bullet-}$, we will be able to determine whether they have a nucleophilic or electrophilic character. Previously reported Mn-peroxide complexes showed to have a nucleophilic character in aldehyde deformylation reactions. It would be interesting to compare the reactivities of mononuclear peroxo-Mn and peroxo-Mn_2 complexes.

References

[1] E. Y. Tshuva, S. J. Lippard, *Chem. Rev.* **2004**, *104*, 987-1012.
[2] Y. Okamoto, A. Onoda, H. Sugimoto, Y. Takano, S. Hirota, D. M. Kurtz, Jr., Y. Shiro, T. Hayashi, *Inorg. Chem.* **2013**, *52*, 13014-13020.
[3] L. Westerheide, *Curr. Opin. Chem. Biol.* **2000**, *4*, 235-241.
[4] E. A. Lewis, W. B. Tolman, *Chem. Rev.* **2004**, *104*, 1047-1076.
[5] S. Signorella, C. Hureau, *Coord. Chem. Rev.* **2012**, *256*, 1229-1245.
[6] A. J. Wu, J. E. Penner-Hahn, V. L. Pecoraro, *Chem. Rev.* **2004**, *104*, 903-938.
[7] W. A. Gunderson, A. I. Zatsman, J. P. Emerson, E. R. Farquhar, L. Que, Jr., J. D. Lipscomb, M. P. Hendrich, *J. Am. Chem. Soc.* **2008**, *130*, 14465-14467.
[8] M. R. Kumar, A. Zapata, A. J. Ramirez, S. K. Bowen, W. A. Francisco, P. J. Farmer, *Proc. Natl. Acad. Sci. USA* **2011**, *108*, 18926-18931.
[9] O. Opaleye, R. S. Rose, M. M. Whittaker, E. J. Woo, J. W. Whittaker, R. W. Pickersgill, *J. Biol. Chem.* **2006**, *281*, 6428-6433.
[10] M. Bennati, F. Lendzian, M. Schmittel, H. Zipse, *Biol. Chem.* **2005**, *386*, 1007-1022.
[11] Y. Aye, M. Li, M. J. Long, R. S. Weiss, *Oncogene* **2015**, *34*, 2011-2021.
[12] E. Torrents, *Front. Cell. Infect. Microbiol.* **2014**, *4*, 52.
[13] A. Trehoux, J.-P. Mahy, F. Avenier, *Coord. Chem. Rev.* **2016**, *322*, 142-158.
[14] M. Merkx, D. A. Kopp, M. H. Sazinsky, J. L. Blazyk, J. Müller, S. J. Lippard, *Angew. Chem. Int. Ed.* **2001**, *40*, 2782-2807.
[15] M. H. Baik, M. Newcomb, R. A. Friesner, S. J. Lippard, *Chem. Rev.* **2003**, *103*, 2385-2419.
[16] C. E. Tinberg, S. J. Lippard, *Acc. Chem. Res.* **2011**, *44*, 280-288.
[17] S. J. Lee, *J. Microbiol.* **2016**, *54*, 277-282.
[18] A. D. Bochevarov, J. Li, W. J. Song, R. A. Friesner, S. J. Lippard, *J. Am. Chem. Soc.* **2011**, *133*, 7384-7397.
[19] J. Shanklin, J. E. Guy, G. Mishra, Y. Lindqvist, *J. Biol. Chem.* **2009**, *284*, 18559-18563.
[20] J. A. Broadwater, C. Achim, E. Münck, B. G. Fox, *Biochemistry* **1999**, *38*, 12197-12204.
[21] K. S. Lyle, P. Möenne-Loccoz, J. Ai, J. Sanders-Loehr, T. M. Loehr, B. G. Fox, *Biochemistry* **2000**, *39*, 10507-10513.
[22] P. Nordlund, P. Reichard, *Annu. Rev. Biochem.* **2006**, *75*, 681-706.
[23] G. C. Dismukes, *Chem. Rev.* **1996**, *96*, 2909-2926.
[24] Y. Sheng, I. A. Abreu, D. E. Cabelli, M. J. Maroney, A. F. Miller, M. Teixeira, J. S. Valentine, *Chem. Rev.* **2014**, *114*, 3854-3918.
[25] J. Yano, V. Yachandra, *Chem. Rev.* **2014**, *114*, 4175-4205.
[26] A. F. Miller, *Curr. Opin. Chem. Biol.* **2004**, *8*, 162-168.
[27] C. Bull, E. C. Niederhoffer, T. Yoshida, J. A. Fee, *J. Am. Chem. Soc.* **1991**, *113*, 4069.
[28] J. A. C. A. K. Boal, J. Stubbe, A. C. Rosenzweig, *Science* **2010**, *329*, 1526-1530.
[29] Y. Umena, K. Kawakami, J. R. Shen, N. Kamiya, *Nature* **2011**, *473*, 55-60.
[30] J. P. McEvoy, G. W. Brudvig, *Chem. Rev.* **2006**, *106*, 4455-4483.
[31] J. A. Cotruvo, J. Stubbe, *Annu. Rev. Biochem.* **2011**, *80*, 733-767.
[32] A. Willing, H. Follmann, G. Auling, *Eur. J. Biochem.* **1988**, *175*, 167-173.
[33] A. B. Tomter, G. Zoppellaro, N. H. Andersen, H.-P. Hersleth, M. Hammerstad, Å. K. Røhr, G. K. Sandvik, K. R. Strand, G. E. Nilsson, C. B. Bell, A.-L. Barra, E. Blasco, L. Le Pape, E. I. Solomon, K. K. Andersson, *Coord. Chem. Rev.* **2013**, *257*, 3-26.
[34] A. Holmgren, R. Sengupta, *Free Radic. Biol. Med.* **2010**, *49*, 1617-1628.
[35] P. Reichard, *Biochem Biophys. Res. Commun.* **2010**, *396*, 19-23.
[36] D. Lundin, E. Torrents, A. M. Poole, B. M. Sjoberg, *BMC Genomics* **2009**, *10*, 589.
[37] B. M. Sjoberg, *Science* **2010**, *329*, 1475-1476.
[38] A. K. Rohr, H. P. Hersleth, K. K. Andersson, *Angew. Chem. Int. Ed. Engl.* **2010**, *49*, 2324-2327.

[39] J. W. Fairman, S. R. Wijerathna, M. F. Ahmad, H. Xu, R. Nakano, S. Jha, J. Prendergast, R. M. Welin, S. Flodin, A. Roos, P. Nordlund, Z. Li, T. Walz, C. G. Dealwis, *Nat. Struct. Mol. Biol.* **2011**, *18*, 316-322.
[40] M. Fontecave, *Cell. Mol. Life. Sci.* **1998**, *54*, 684-695.
[41] M. Kolberg, K. R. Strand, P. Graff, K. K. Andersson, *Biochim. Biophys. Acta* **2004**, *1699*, 1-34.
[42] A. Jordan, P. Reichard, *Annu. Rev. Biochem.* **1998**, *67*, 71-98.
[43] P. Nordlund, B. M. Sjoberg, H. Eklund, *Nature* **1990**, *345*, 593-598.
[44] P. Nordlund, H. Eklund, *J. Mol. Biol.* **1993**, *232*, 123-164.
[45] P. E. M. Siegbahn, *J. Am. Chem. Soc.* **1998**, *120*, 8417-8429.
[46] M. E. Andersson, M. Högbom, A. Rinaldo-Matthis, K. K. Andersson, B.-M. Sjöberg, P. Nordlund, *J. Am. Chem. Soc.* **1999**, *121*, 2346-2352.
[47] T. C. B. E. I. Solomon, M. I. Davis, J. N. Kemsley, S. Lee, N. Lehnert, F. Neese, A. J. Skulan, Y. Yang, J. Zhou, *Chem. Rev.* **2000**, *100*, 235-349.
[48] T. Lovell, J. Li, L. Noodleman, *J. Biol. Inorg. Chem.* **2002**, *7*, 799-809.
[49] P. E. M. S. F. Himo, *Chem. Rev.* **2003**, *103*, 2421-2456.
[50] J. Bollinger, D. Edmondson, B. Huynh, J. Filley, Norton, J. Stubbe, *Science* **1991**, *253*, 292-298.
[51] J. M. Bollinger, W. H. Tong, N. Ravi, B. H. Huynh, D. E. Edmonson, J. Stubbe, *J. Am. Chem. Soc.* **1994**, *116*, 8015-8023.
[52] N. Ravi, J. M. Bollinger, B. H. Huynh, J. Stubbe, D. E. Edmondson, *J. Am. Chem. Soc.* **1994**, *116*, 8007-8014.
[53] B. E. Sturgeon, D. Burdi, S. Chen, B.-H. Huynh, D. E. Edmondson, J. Stubbe, B. M. Hoffman, *J. Am. Chem. Soc.* **1996**, *118*, 7551-7557.
[54] D. Burdi, B. E. Sturgeon, W. H. Tong, J. Stubbe, B. M. Hoffman, *J. Am. Chem. Soc.* **1996**, *118*, 281-282.
[55] N. Mitic, L. Saleh, G. Schenk, J. M. Bollinger, Jr., E. I. Solomon, *J. Am. Chem. Soc.* **2003**, *125*, 11200-11201.
[56] M. D. C. N. Mitic, L. Saleh, J. M. Bollinger, Jr., E. I. Solomon, *J. Am. Chem. Soc.* **2007**, *129*, 9049-9065.
[57] M. Shanmugam, P. E. Doan, N. S. Lees, J. Stubbe, B. M. Hoffman, *J. Am. Chem. Soc.* **2009**, *131*, 3370-3376.
[58] J. M. Bollinger, S. Chen, S. E. Parkin, L. M. Mangravite, B. A. Ley, D. E. Edmondson, B. H. Huynh, *J. Am. Chem. Soc.* **1997**, *119*, 5976-5977.
[59] W. G. Han, T. Liu, T. Lovell, L. Noodleman, *J. Inorg. Biochem.* **2006**, *100*, 771-779.
[60] Y. Kwak, W. Jiang, L. M. Dassama, K. Park, C. B. Bell, 3rd, L. V. Liu, S. D. Wong, M. Saito, Y. Kobayashi, S. Kitao, M. Seto, Y. Yoda, E. E. Alp, J. Zhao, J. M. Bollinger, Jr., C. Krebs, E. I. Solomon, *J .Am. Chem. Soc.* **2013**, *135*, 17573-17584.
[61] W. Jiang, L. Saleh, E. W. Barr, J. Xie, M. M. Gardner, C. Krebs, J. M. Bollinger, Jr., *Biochemistry* **2008**, *47*, 8477-8484.
[62] W. Jiang, L. M. Hoffart, C. Krebs, J. M. Bollinger, Jr., *Biochemistry* **2007**, *46*, 8709-8716.
[63] W. Jiang, J. M. Bollinger, Jr., C. Krebs, *J. Am. Chem. Soc.* **2007**, *129*, 7504-7505.
[64] J. M. Younker, C. M. Krest, W. Jiang, C. Krebs, J. M. Bollinger, Jr., M. T. Green, *J. Am. Chem. Soc.* **2008**, *130*, 15022-15027.
[65] C. S. Andersson, M. Ohrstrom, A. Popovic-Bijelic, A. Graslund, P. Stenmark, M. Hogbom, *J. Am. Chem. Soc.* **2012**, *134*, 123-125.
[66] L. M. Dassama, A. K. Boal, C. Krebs, A. C. Rosenzweig, J. M. Bollinger, Jr., *J. Am. Chem. Soc.* **2012**, *134*, 2520-2523.
[67] L. M. Dassama, C. Krebs, J. M. Bollinger, Jr., A. C. Rosenzweig, A. K. Boal, *Biochemistry* **2013**, *52*, 6424-6436.
[68] J. A. Cotruvo, Jr., J. Stubbe, *Biochemistry* **2010**, *49*, 1297-1309.
[69] J. A. Cotruvo, Jr., J. Stubbe, *Metallomics* **2012**, *4*, 1020-1036.
[70] A. K. Boal, J. A. Cotruvo, Jr., J. Stubbe, A. C. Rosenzweig, *Biochemistry* **2012**, *51*, 3861-3871.
[71] N. Cox, H. Ogata, P. Stolle, E. Reijerse, G. Auling, W. Lubitz, *J. Am. Chem. Soc.* **2010**, *132*, 11197-11213.

[72] M. Eriksson, A. Jordan, H. Eklund, *Biochemistry* **1998**, *37*, 13359-13369.
[73] V. V. Barynin, M. M. Whittaker, S. V. Antonyuk, V. S. Lamzin, P. M. Harrison, P. J. Artymiuk, J. W. Whittaker, *Structure* **2001**, *9*, 725-738.
[74] M. M. Whittaker, V. V. Barynin, T. Igarashi, J. W. Whittaker, *Eur. J. Biochem.* **2003**, *270*, 1102-1116.
[75] G. C. D. A. E. M. Boelrijk, *Inorg. Chem.* **2000**, *39*, 3020-3028.
[76] K. Wieghardt, U. Bossek, D. Ventur, J. Weiss, *J. Chem. Soc., Chem. Commun.* **1985**, 347-349.
[77] J. E. Sheats, R. S. Czernuszewicz, G. C. Dismukes, A. L. Rheingold, V. Petrouleas, J. Stubbe, W. H. Armstrong, R. H. Beer, S. J. Lippard, *J. Am. Chem. Soc.* **1987**, *109*, 1435-1444.
[78] M. L. K. A. Gelasco, J. W. Kampf, V. L. Pecoraro, *Inorg. Chem.* **1997**, *36*, 1829-1837.
[79] J. M. Bollinger, W. H. Tong, N. Ravi, B. H. Huynh, D. E. Edmondson, J. Stubbe, *J. Am. Chem. Soc.* **1994**, *116*, 8024-8032.
[80] J. Baldwin, C. Krebs, B. A. Ley, D. E. Edmondson, B. H. Huynh, J. M. Bollinger, *J. Am. Chem. Soc.* **2000**, *122*, 12195-12206.
[81] A. K. Boal, J. A. Cotruvo, Jr., J. Stubbe, A. C. Rosenzweig, *Science* **2010**, *329*, 1526-1530.
[82] S. Mukhopadhyay, S. K. Mandal, S. Bhaduri, W. H. Armstrong, *Chem. Rev.* **2004**, *104*, 3981-4026.
[83] J. A. Cotruvo, Jr., T. A. Stich, R. D. Britt, J. Stubbe, *J. Am. Chem. Soc.* **2013**, *135*, 4027-4039.
[84] M. Pick, J. Rabani, F. Yost, I. Fridovich, *J. Am. Chem. Soc.* **1974**, *96*, 7329-7333.
[85] V. L. Pecoraro, M. J. Baldwin, A. Gelasco, *Chem. Rev.* **1994**, *94*, 807-826.
[86] T. A. Jackson, T. C. Brunold, *Acc. Chem. Res.* **2004**, *37*, 461-470.
[87] J. P. Emerson, E. G. Kovaleva, E. R. Farquhar, J. D. Lipscomb, L. Que, Jr., *Proc. Natl. Acad. Sci. U.S.A.* **2008**, *105*, 7347.
[88] C. S. Mullins, V. L. Pecoraro, *Coord. Chem. Rev.* **2008**, *252*, 416-443.
[89] J. A. Cotruvo, Jr., J. Stubbe, *Proc. Natl. Acad. Sci. U S A* **2008**, *105*, 14383-14388.
[90] C. Bull, E. C. Niederhoffer, T. Yoshida, J. A. Fee, *J. Am. Chem. Soc.* **1991**, *113*, 4069-4076.
[91] A. S. Hearn, C. Tu, H. S. Nick, D. N. Silverman, *J. Biol. Chem.* **1999**, *274*, 24457-24460.
[92] M. Srnec, F. Aquilante, U. Ryde, L. Rulisek, *J. Phys. Chem. B* **2009**, *113*, 6074-6086.
[93] M. Lundberg, P. E. Siegbahn, *J .Phys. Chem. B* **2005**, *109*, 10513-10520.
[94] P. E. M. Siegbahn, *Curr. Opin. Chem. Biol.* **2002**, *6*, 227-235.
[95] J. Messinger, M. Badger, T. Wydrzynski, *Proc. Natl. Acad. Sci. U S A* **1995**, *92*, 3209-3213.
[96] V. L. Pecoraro, M. J. Baldwin, M. T. Caudle, W. Y. Hsieh, N. A. Law, *Pure Appl. Chem.* **1998**, *70*, 925-929.
[97] R. B. VanAtta, C. E. Strouse, L. K. Hanson, J. S. Valentine, *J. Am. Chem. Soc.* **1987**, *109*, 1425-1434.
[98] N. Kitajima, H. Komatsuzaki, S. Hikichi, M. Osawa, Y. Moro-oka, *J. Am. Chem. Soc.* **1994**, *116*, 11596.
[99] U. P. Singh, A. K. Sharma, S. Hikichi, H. Komatsuzaki, Y. Moro-oka, M. Akita, *Inorg. Chim. Acta* **2006**, *359*, 4407-4411.
[100] M. S. Seo, J. Y. Kim, J. Annaraj, Y. Kim, Y. M. Lee, S. J. Kim, J. Kim, W. Nam, *Angew. Chem. Int. Ed.* **2007**, *46*, 377-380.
[101] J. Annaraj, J. Cho, Y. M. Lee, S. Y. Kim, R. Latifi, S. P. de Visser, W. Nam, *Angew. Chem. Int. Ed.* **2009**, *48*, 4150-4153.
[102] J. Cho, R. Sarangi, W. Nam, *Acc. Chem. Res.* **2012**, *45*, 1321-1330.
[103] H. Kang, J. Cho, K. B. Cho, T. Nomura, T. Ogura, W. Nam, *Chem. Eur. J.* **2013**, *19*, 14119-14125.
[104] H. E. Colmer, R. A. Geiger, D. F. Leto, G. B. Wijeratne, V. W. Day, T. A. Jackson, *Dalton Trans.* **2014**, *43*, 17949-17963.
[105] R. A. Geiger, G. B. Wijeratne, V. W. Day, T. A. Jackson, *Eur. J. Inorg. Chem.* **2012**, *2012*, 1598-1608.
[106] R. A. Geiger, D. F. Leto, S. Chattopadhyay, P. Dorlet, E. Anxolabehere-Mallart, T. A. Jackson, *Inorg. Chem.* **2011**, *50*, 10190-10203.
[107] R. A. Geiger, S. Chattopadhyay, V. W. Day, T. A. Jackson, *J. Am. Chem. Soc.* **2010**, *132*, 2821-2831.

[108] R. A. Geiger, S. Chattopadhyay, V. W. Day, T. A. Jackson, *Dalton Trans.* **2011**, *40*, 1707-1715.
[109] N. Saravanan, M. Sankaralingam, M. Palaniandavar, *RSC Advances* **2014**, *4*, 12000.
[110] D. F. Leto, T. A. Jackson, *J. Biol. Inorg. Chem.* **2014**, *19*, 1-15.
[111] S. Groni, G. Blain, R. Guillot, C. Policar, E. Anxolabehere-Mallart, *Inorg. Chem.* **2007**, *46*, 1951-1953.
[112] H. E. Colmer, A. W. Howcroft, T. A. Jackson, *Inorg. Chem.* **2016**, *55*, 2055-2069.
[113] S. Groni, P. Dorlet, G. Blain, S. Bourcier, R. Guillot, E. Anxolabehere-Mallart, *Inorg. Chem.* **2008**, *47*, 3166-3172.
[114] R. L. Shook, A. S. Borovik, *Inorg. Chem.* **2010**, *49*, 3646-3660.
[115] S. El Ghachtouli, H. Y. Ching, B. Lassalle-Kaiser, R. Guillot, D. F. Leto, S. Chattopadhyay, T. A. Jackson, P. Dorlet, E. Anxolabehere-Mallart, *Chem. Commun.* **2013**, *49*, 5696-5698.
[116] R. L. Shook, W. A. Gunderson, J. Greaves, J. W. Ziller, M. P. Hendrich, A. S. Borovik, *J. Am. Chem. Soc.* **2008**, *130*, 8888-8889.
[117] M. K. Coggins, X. Sun, Y. Kwak, E. I. Solomon, E. Rybak-Akimova, J. A. Kovacs, *J. Am. Chem. Soc.* **2013**, *135*, 5631-5640.
[118] R. Bhula, G. J. Gainsford, D. C. Weatherburn, *J. Am. Chem. Soc.* **1988**, *110*, 7550-7552.
[119] T. W. U. Bossek, K. Wieghardt, B. Nuber, J. Weiss, *J. Am. Chem. Soc.* **1990**, *112*, 6387-6388.
[120] M. Costas, M. P. Mehn, M. P. Jensen, L. Que, Jr., *Chem. Rev.* **2004**, *104*, 939-986.
[121] L. M. Mirica, X. Ottenwaelder, T. D. Stack, *Chem. Rev.* **2004**, *104*, 1013-1045.
[122] G. Y. Park, M. F. Qayyum, J. Woertink, K. O. Hodgson, B. Hedman, A. A. Narducci Sarjeant, E. I. Solomon, K. D. Karlin, *J. Am. Chem. Soc.* **2012**, *134*, 8513-8524.
[123] S. Hong, K. D. Sutherlin, J. Park, E. Kwon, M. A. Siegler, E. I. Solomon, W. Nam, *Nat. Commun.* **2014**, *5*, 5440.
[124] D. R. Gamelin, M. L. Kirk, T. L. Stemmler, S. Pal, W. H. Armstrong, J. E. Penner-Hahn, E. I. Solomon, *J. Am. Chem. Soc.* **1994**, *116*, 2392-2399.
[125] D. F. Leto, S. Chattopadhyay, V. W. Day, T. A. Jackson, *Dalton Trans.* **2013**, *42*, 13014-13025.
[126] A. M. Magherusan, A. Zhou, E. R. Farquhar, M. Garcia-Melchor, B. Twamley, L. Que, Jr., A. R. McDonald, *Angew. Chem. Int. Ed. Engl.* **2018**, *57*, 918-922.
[127] J. T. Groves, Y. Watanabe, T. J. McMurry, *J. Am. Chem. Soc.* **1983**, *105*, 4489-4490.
[128] S. E. Creager, S. A. Raybuck, R. W. Murray, *J. Am. Chem. Soc.* **1986**, *108*, 4225-4227.
[129] S. E. Creager, R. W. Murray, *Inorg. Chem.* **1987**, *26*, 2612-2618.
[130] N. W. Aboelella, J. T. York, A. M. Reynolds, K. Fujita, C. R. Kinsinger, C. J. Cramer, C. G. Riordan, W. B. Tolman, *Chem. Commun.* **2004**, 1716-1717.
[131] M. T. Kieber-Emmons, C. G. Riordan, *Acc. Chem. Res.* **2007**, *40*, 618-625.
[132] C. J. Cramer, W. B. Tolman, *Acc. Chem. Res.* **2007**, *40*, 601-608.
[133] Y. Jo, J. Annaraj, M. S. Seo, Y. M. Lee, S. Y. Kim, J. Cho, W. Nam, *J. Inorg. Biochem.* **2008**, *102*, 2155-2159.
[134] R. L. Shook, S. M. Peterson, J. Greaves, C. Moore, A. L. Rheingold, A. S. Borovik, *J. Am. Chem. Soc.* **2011**, *133*, 5810-5817.
[135] F. Neese, E. I. Solomon, *J. Am. Chem. Soc.* **1998**, *120*, 12829-12848.
[136] R. Chatterjee, S. Milikisiyants, K. V. Lakshmi, *Phys. Chem. Chem. Phys.* **2012**, *14*, 7090-7097.
[137] H. Yamazaki, S. Igarashi, T. Nagata, M. Yagi, *Inorg. Chem.* **2012**, *51*, 1530-1539.
[138] H. M. Berends, A. M. Manke, C. Nather, F. Tuczek, P. Kurz, *Dalton. Trans.* **2012**, *41*, 6215-6224.
[139] H. Chen, R. Tagore, S. Das, C. Incarvito, J. W. Faller, R. H. Crabtree, G. W. Brudvig, *Inorg. Chem.* **2005**, *44*, 7661-7670.
[140] H. Yamazaki, T. Ueno, K. Aiso, M. Hirahara, T. Aoki, T. Nagata, S. Igarashi, M. Yagi, *Polyhedron* **2013**, *52*, 455-460.
[141] J. A. Lessa, A. Horn, Jr., E. S. Bull, M. R. Rocha, M. Benassi, R. R. Catharino, M. N. Eberlin, A. Casellato, C. J. Noble, G. R. Hanson, G. Schenk, G. C. Silva, O. A. Antunes, C. Fernandes, *Inorg. Chem.* **2009**, *48*, 4569-4579.
[142] O. Horner, M.-F. Charlot, A. Boussac, E. Anxolabéhère-Mallart, L. Tchertanov, J. Guilhem, J.-J. Girerd, *Eur. J. Inorg. Chem.* **1998**, *1998*, 721-727.

[143] L. Dubois, J. Pecaut, M. F. Charlot, C. Baffert, M. N. Collomb, A. Deronzier, J. M. Latour, *Chemistry* **2008**, *14*, 3013-3025.
[144] D. Huang, W. Wang, X. Zhang, C. Chen, F. Chen, Q. Liu, D. Liao, L. Li, L. Sun, *Eur. J. Inorg. Chem.* **2004**, *2004*, 1454-1464.
[145] J. Glerup, P. A. Goodson, A. Hazell, R. Hazell, D. J. Hodgson, C. J. McKenzie, K. Michelsen, U. Rychlewska, H. Toftlund, *Inorg. Chem.* **1994**, *33*, 4105-4111.
[146] Y. Gultneh, T. B. Yisgedu, Y. T. Tesema, R. J. Butcher, *Inorg. Chem.* **2003**, *42*, 1857-1867.
[147] C. Hureau, G. Blondin, M. F. Charlot, C. Philouze, M. Nierlich, M. Cesario, E. Anxolabehere-Mallart, *Inorg. Chem.* **2005**, *44*, 3669-3683.
[148] C. Baffert, M.-N. Collomb, A. Deronzier, J. Pécaut, J. Limburg, R. H. Crabtree, G. W. Brudvig, *Inorg. Chem.* **2002**, *41*, 1404-1411.
[149] J. Limburg, J. S. Vrettos, H. Chen, J. C. de Paula, R. H. Crabtree, G. W. Brudvig, *J. Am. Chem. Soc.* **2001**, *123*, 423-430.
[150] C. Hureau, G. Blondin, M. Cesario, S. Un, *J. Am. Chem. Soc.* **2003**, *125*, 11637-11645.
[151] S. Mukhopadhyay, W. H. Armstrong, *J. Am. Chem. Soc.* **2003**, *125*, 13010-13011.
[152] J. Glerup, P. A. Goodson, A. Hazell, R. Hazell, D. J. Hodgson, C. J. McKenzie, K. Michelsen, U. Rychlewska, H. Toftlund, *Inorg. Chem.* **2002**, *33*, 4105.
[153] S. R. Cooper, M. Calvin, *J. Am. Chem. Soc.* **1977**, *99*, 6623-6630.
[154] M. Suzuki, S. Tokura, M. Suhara, A. Uehara, *Chem. Lett.* **1988**, *17*, 477-480.
[155] L. J. R.Y. Wei, Z. F. Xing, Z. J. Hua, G. Hui, *Chin. J. Chem.* **2005**, *23*, 418-420.
[156] M.-N. Collomb, A. Deronzier, A. l. Richardot, J. Pe´caut, *New J. Chem.* **1999**, *23*, 351-354.
[157] S. Schindler, O. Walter, J. Z. Pedersen, H. Toftlund, *Inorg. Chim. Acta* **2000**, *303*, 215-219.
[158] A. L. M. Stebler, H. B. Burgi, *J. Am. Chem. Soc.* **1986**, *25*, 4743-4750.
[159] L. Dubois, D. F. Xiang, X. S. Tan, J. Pecaut, P. Jones, S. Baudron, L. Le Pape, J. M. Latour, C. Baffert, S. Chardon-Noblat, M. N. Collomb, A. Deronzier, *Inorg. Chem.* **2003**, *42*, 750-760.
[160] H. Diril, H. R. Chang, M. J. Nilges, X. Zhang, J. A. Potenza, H. J. Schugar, S. S. Isied, D. N. Hendrickson, *J. Am. Chem. Soc.* **1989**, *111*, 5102-5114.
[161] G. C. Dismukes, J. E. Sheats, J. A. Smegal, *J. Am. Chem. Soc.* **1987**, *109*, 7202-7203.
[162] C. Teutloff, K. O. Schafer, S. Sinnecker, V. Barynin, R. Bittl, K. Wieghardt, F. Lendzian, W. Lubitz, *Magn. Reson. Chem.* **2005**, *43* S51-64.
[163] Y. Sano, A. C. Weitz, J. W. Ziller, M. P. Hendrich, A. S. Borovik, *Inorg. Chem.* **2013**, *52*, 10229-10231.
[164] S. V. Khangulov, P. J. Pessiki, V. V. Barynin, D. E. Ash, G. C. Dismukes, *Biochemistry* **1995**, *34*, 2015-2025.
[165] R. M. Buchanan, K. J. Oberhausen, J. F. Richardson, *Inorg. Chem.* **1988**, *27*, 971-973.
[166] P. J. Pessiki, S. V. Khangulov, D. M. Ho, G. C. Dismukes, *J. Am. Chem. Soc.* **1994**, *116*, 891-897.
[167] R. Singh, M. Haukka, C. J. McKenzie, E. Nordlander, *Eur. J. Inorg. Chem.* **2015**, *2015*, 3485-3492.
[168] H. Diril, H. R. Chang, X. Zhang, S. K. Larsen, J. A. Potenza, C. G. Pierpont, H. J. Schugar, S. S. Isied, D. N. Hendrickson, *J. Am. Chem. Soc.* **1987**, *109*, 6207-6208.
[169] N. Cox, W. Ames, B. Epel, L. V. Kulik, L. Rapatskiy, F. Neese, J. Messinger, K. Wieghardt, W. Lubitz, *Inorg. Chem.* **2011**, *50*, 8238-8251.
[170] A. E. M. Boelrijk, S. V. Khangulov, G. C. Dismukes, *Inorg. Chem.* **2000**, *39*, 3009-3019.
[171] E. N. Marsh, M. W. Waugh, *ACS Catal.* **2013**, *3*, 2515-2521.
[172] Y. Hayashi, T. Kayatani, H. Sugimoto, M. Suzuki, K. Inomata, A. Uehara, Y. Mizutani, T. Kitagawa, Y. Maeda, *J. Am. Chem. Soc.* **1995**, *117*, 11220-11229.
[173] T. Ookubo, H. Sugimoto, T. Nagayama, H. Masuda, T. Sato, K. Tanaka, Y. Maeda, H. Ōkawa, Y. Hayashi, A. Uehara, M. Suzuki, *J. Am. Chem. Soc.* **1996**, *118*, 701-702.
[174] Y. Dong, S. Yan, V. G. Young, L. Que, *Angew. Chem. Int. Ed.* **1996**, *35*, 618-620.
[175] Y. Dong, S. Menage, B. A. Brennan, T. E. Elgren, H. G. Jang, L. L. Pearce, L. Que, *J. Am. Chem. Soc.* **1993**, *115*, 1851-1859.
[176] J. R. Frisch, V. V. Vu, M. Martinho, E. Munck, L. Que, Jr., *Inorg. Chem.* **2009**, *48*, 8325-8336.
[177] K. Kim, S. J. Lippard, *J. Am. Chem. Soc.* **1996**, *118*, 4914-4915.

[178] N. Kitajima, N. Tamura, H. Amagai, H. Fukui, Y. Moro-oka, Y. Mizutani, T. Kitagawa, R. Mathur, K. Heerwegh, *J. Am. Chem. Soc.* **1994**, *116*, 9071-9085.
[179] T. C. Brunold, N. Tamura, N. Kitajima, Y. Moro-oka, E. I. Solomon, *J. Am. Chem. Soc.* **1998**, *120*, 5674-5690.
[180] H. Arii, S. Nagatomo, T. Kitagawa, T. Miwa, K. Jitsukawa, H. Einaga, H. Masuda, *J. Inorg. Biochem.* **2000**, *82*, 153-162.
[181] X. Zhang, H. Furutachi, S. Fujinami, S. Nagatomo, Y. Maeda, Y. Watanabe, T. Kitagawa, M. Suzuki, *J. Am. Chem. Soc.* **2005**, *127*, 826-827.
[182] M. Sekino, H. Furutachi, R. Tojo, A. Hishi, H. Kajikawa, T. Suzuki, K. Suzuki, S. Fujinami, S. Akine, Y. Sakata, T. Ohta, S. Hayami, M. Suzuki, *Chem. Commun.* **2017**, *53*, 8838-8841.
[183] W. H. Armstrong, S. J. Lippard, *J. Am. Chem. Soc.* **1983**, *105*, 4837-4838.
[184] M. Suzuki, H. Furutachi, H. Ōkawa, *Coord. Chem. Rev.* **2000**, *200-202*, 105-129.
[185] A. J. Jasniewski, L. Que, Jr., *Chem. Rev.* **2018**, *118*, 2554-2592.
[186] A. T. Fiedler, X. Shan, M. P. Mehn, J. Kaizer, S. Torelli, J. R. Frisch, M. Kodera, L. Que, Jr., *J. Phys. Chem. A* **2008**, *112*, 13037-13044.
[187] M. A. Cranswick, K. K. Meier, X. Shan, A. Stubna, J. Kaizer, M. P. Mehn, E. Munck, L. Que, Jr., *Inorg. Chem.* **2012**, *51*, 10417-10426.

Chapter 2

Mimicking class Ib Mn_2-ribonucleotide reductase: a Mn^{II}_2 complex and its reaction with superoxide

The work described in this chapter has been previously published in an article in Angewandte Chemie International Edition. The EPR measurements were performed by Dr Ang Zhou under supervision of Prof. Lawrence Que (University of Minnesota, USA); the XAS data collection and analysis were done by Dr Eric R. Farquhar (Brookhaven National Laboratory, USA); the DFT calculations were performed by Prof. Max García-Melchor (Trinity College Dublin); the XRD data collection and structure solutions and refinements were done by Dr Brendan Twamley (Trinity College Dublin).

Reproduced in part with permission from: Magherusan, A. M.; Zhou, A.; Farquhar, E. R.; Garcia-Melchor, M.; Twamley, B.; Que, L., Jr.; McDonald, A. R. *Angew. Chem. Int. Ed.* **2018**, 57, 918-922.

2.1 Introduction

As outlined in sections 1.5.2 and 1.5.3, the spectroscopic features of many peroxo-Mn^{III} and bis(μ-oxo)$Mn^{III}Mn^{IV}$ complexes reported in the literature have been described. All these complexes mimic the active sites of Mn containing enzymes and have been generated by using mainly O_2 or H_2O_2 as oxidant. Many spectroscopic techniques such as X-ray crystallography, electronic absorption spectroscopy, EPR and mass spectrometry have been used for the characterisation of these complexes. At the start of this work, no examples of mixed valent peroxo-$Mn^{II}Mn^{III}$ complexes were known.

Inspired by a recent study on class Ib dimanganese (Mn_2) RNRs,[1-4] we became interested in the role of superoxide anion ($O_2^{\bullet-}$). Stubbe and colleagues demonstrated that the Mn_2 cofactor showed no reaction with O_2.[1] However, in the presence of a flavodoxin protein ($NrdI_{hq}$, flavodoxin hydroquinone) O_2 was reduced to $O_2^{\bullet-}$. The $O_2^{\bullet-}$ was proposed to react with the Mn^{II}_2 core yielding a $Mn^{II}Mn^{III}$-peroxide entity.[4] Subsequent cleavage of the O–O bond to generate a Mn^{III}(μ-OH)(μ-O)Mn^{IV} species that oxidizes tyrosine was also proposed.[1] EPR spectroscopy supported the formation of a $Mn^{III}Mn^{IV}$ intermediate, but no insight into the initial species was obtained.[1]

Synthetic Mn_2 model complexes that mimic some of the intermediates in class Ib Mn RNRs have been prepared.[5, 6] A series of mononuclear Mn^{III}-peroxide and -hydroperoxide species have been reported.[7-17] These species were generated by treating mononuclear Mn^{II} precursors with a variety of oxidants including O_2,[16, 17] $O_2^{\bullet-}$,[10, 13] and H_2O_2.[7-12, 14] To the best of our knowledge, however, a $Mn^{II}Mn^{III}$-peroxide complex has not been previously reported. Furthermore, no investigations into the reaction between Mn^{II}_2 complexes and $O_2^{\bullet-}$ have been reported. In order to probe the above mechanistic postulates, herein we explore the interaction between a synthetic Mn^{II}_2 complex and $O_2^{\bullet-}$.

2.2 Synthesis and characterisation of a biomimetic Mn^{II}_2 complex

$[Mn_2(O_2CCH_3)$(N-Et-HPTB)$](ClO_4)_2$ (**1**, N-Et-HPTB = N,N,N',N'-tetrakis(2-(1-ethylbenzimidazolyl))-2-hydroxy-1,3-diaminopropane[18, 19]) was synthesised using a slight modification of the procedure reported for the preparation of $[Mn_2(O_2CCH_3)$(HPTB)$](ClO_4)_2$ (**3**, HPTB = N,N,N',N'-tetrakis(2-(benzimidazolyl))-2-hydroxy-1,3-diaminopropane).[20] Elemental analysis and matrix assisted laser desorption ionisation time of flight (MALDI-ToF) mass spectrometry confirmed the elemental composition of **1**. The electron paramagnetic

resonance (EPR) spectra of complexes **1** and previously reported **3** showed very similar signals (g = 2.0, Figures A.1-A.2). The obtained EPR signal was assigned to axially distorted Mn^{II} sites, as described by Boelrijk *et al*. for complex **3**.[21]

Crystals of **1** suitable for X-ray diffraction measurements were grown from acetonitrile (CH_3CN) by diethyl ether (Et_2O) vapour diffusion. **1** was found to consist of two five-coordinate Mn^{II} atoms both with a distorted trigonal-bipyramidal geometry (Figure 2.1). The average Mn-N_{amine} and Mn-N_{benz} bond lengths of **1** were shorter than those of **3**,[20] presumably as a result of the higher basicity of the alkylated ligand (N-Et-HPTB) in **1**. **3** displayed a Mn···Mn separation of 3.5 Å versus 3.6 Å for **1**. Interestingly, the $Mn^{2+}\cdots Mn^{2+}$ distance in the X-ray crystal structure reported for class Ib Mn_2 RNRs from *E. coli* was 3.7 Å,[4] from *B. subtilis* 3.9 Å, while from *C. ammoniagenes* a $Mn^{3+}\cdots Mn^{3+}$ separation was 3.3 Å.[3] For all three structures of Mn_2 RNRs, the Mn active sites displayed either at least one vacant site on the metal, or a labile ligand, presumably the location of $O_2^{\bullet-}$ binding. Importantly in **1**, the Mn ions were similarly not coordinatively saturated. The structural data obtained for **1** thus compares favourably with these enzymes suggesting that **1** is a good structural mimic for class Ib Mn_2 RNRs.

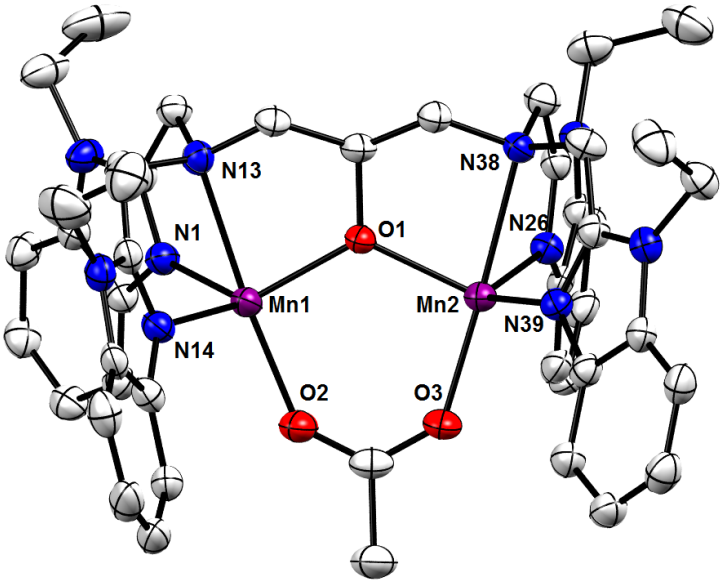

Figure 2.1. ORTEP plot of **1**. Hydrogen atoms and perchlorate anions have been omitted for clarity. Ellipsoids are shown at 50% probability. Selected bond distances (Å): Mn1-Mn2: 3.6; Mn1-O1: 2.05, Mn1-O2: 2.08, Mn1-N13: 2.42, Mn1-N1: 2.12, Mn1-N14: 2.13, Mn2-O1: 2.04, Mn2-O3: 2.07, Mn2-N38: 2.41, Mn2-N26: 2.13, Mn2-N39: 2.13.

2.3 Formation and characterization of a peroxo-$Mn^{II}Mn^{III}$ adduct

To a CH_3CN solution containing complex **1** (1 mM, 2 mL) cooled to -40 °C was added a N,N-dimethylformamide (DMF, 0.3 mL) solution containing 3 equiv. KO_2 (20 mM in DMF solution) and 18-crown-6 (59 mM in DMF solution) (Scheme 2.1). An immediate reaction occurred (complete in 35 s) resulting in the formation of a new species (**2**), as evidenced by electronic absorption spectroscopy (Figure 2.2). The electronic absorption spectrum of **2** displayed low-intensity features at λ_{max} = 460 and 610 nm (Figure 2.2), whereas **1** displayed limited absorptivity above 300 nm. At higher concentrations of **1**, lower yields of **2** were obtained (Figure A.3). This is presumably as a result of intermolecular interactions preventing the formation or accelerating the decay of **2** at higher concentrations of **1**.[22-24]

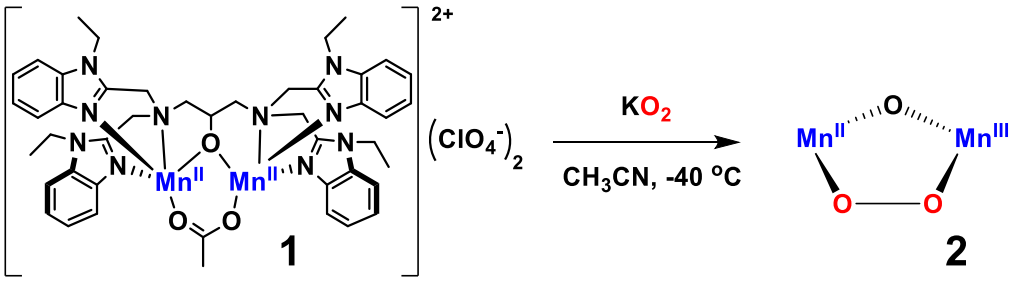

Scheme 2.1. Reaction of **1** with $O_2^{\bullet-}$ forming a $Mn^{II}Mn^{III}$-peroxide complex, **2**.

We noted that the electronic absorption features for **2** were characteristic of Mn^{III}-peroxide complexes.[25-27] Previously reported Mn^{III}-peroxide complexes $[Mn^{III}(O_2)(TMC)]^+$ (TMC = 1,4,8,11-tetramethyl-1,4,8,11-tetraazacyclotetradecane), $[Mn^{III}(O_2)(13\text{-}TMC)]^+$ (13-TMC = 1,4,7,10-tetramethyl-1,4,7,10-tetraazacyclotridecane), and $[Mn^{III}(O_2)(Tp^{iPr})]^+$ (Tp^{iPr} = tris(3,5-diisopropylpyrazolyl)borate), all exhibited an absorption band at around 460 nm attributed to peroxide-to-metal charge transfer[28] and a broader band in the 560-620 nm range, derived from *d-d* transitions.[28] In addition, Mn^{III}-peroxides supported by other polydentate amine ligands exhibited a prominent band at λ_{max} = 430-445 nm and a weaker band at λ_{max} = 590-610 nm.[29] We therefore concluded that **2** contained a Mn-peroxide core.

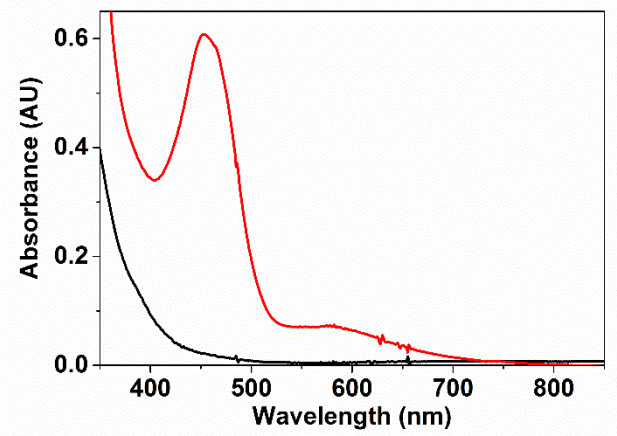

Figure 2.2. Electronic absorption spectra of **1** (black trace, 1 mM) and **2** (red trace, from **1** (1 mM) + KO_2) at -40 °C in CH_3CN (path length = 1 cm).

2.3.1 ESI mass spectrometry

Cold injection electrospray ionisation mass spectrometry (ESI-MS) experiments on a just-thawed CH_3CN solution of **2** revealed ion peaks consistent with **2** being a $Mn^{II}Mn^{III}$-peroxide complex. A mass peak (*m/z* = 431.54) consistent with the formulation of the di-cation $[Mn_2(O_2)(N\text{-Et-HPTB})]^{2+}$ (Figure 2.3, left) was obtained. When **2** was prepared with $K^{18}O_2$, cold injection ESI-MS of the ^{18}O-labelled **2** resulted in a mass peak at *m/z* = 433.48, a mass that can be ascribed to the di-cation $[Mn_2(^{18}O_2)(N\text{-Et-HPTB})]^{2+}$ (Figure 2.3, right). These results led us to define **2** as a $Mn^{II}Mn^{III}$-peroxide complex derived from $O_2^{\bullet-}$.

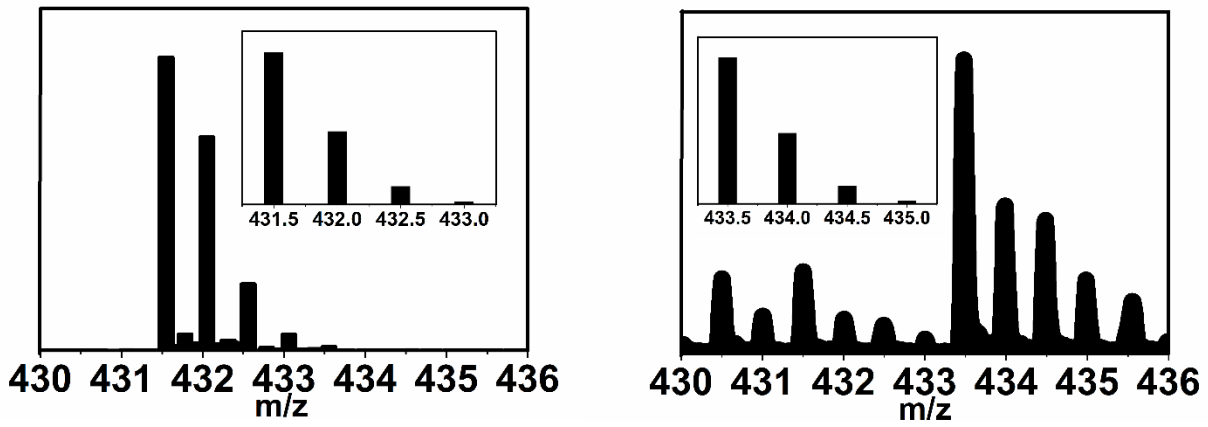

Figure 2.3. ESI-MS spectra of **2** prepared using KO_2 (left) and $K^{18}O_2$ (right). Insets: simulated mass spectra.

Raman and infra-red spectroscopy studies on **2** were attempted but failed to provide any insight. In contrast, Kovacs and co-workers were successful in observing the $\nu_{o\text{-}o}$ and the $\nu_{Mn\text{-}O}$ of a thiolato-Mn^{III}_2-peroxide complex by resonance Raman spectroscopy,[17] while Nam and

Solomon reported the $\nu_{o\text{-}o}$ of a Mn^{IV}-peroxide complex.[30] These are the only two examples of a vibrational analysis of Mn-dioxygen species.[7, 8, 11]

2.3.2 EPR spectroscopy

2 displayed a 29-line EPR signal at 2 K (Figure 2.4), resembling those observed for several $Mn^{II}Mn^{III}$ complexes.[31-34] This group includes a recent example reported by Borovik and co-workers to have a Mn^{II}-(μ-OH)-Mn^{III} core.[35] The signal is typical of a $Mn^{II}Mn^{III}$ species with an effective S = ½ ground state (g ~ 1.96).[34] The observation of multiple lines derives from hyperfine interactions with the two non-equivalent Mn ions. The yield of **2**, as determined by EPR integration, was ~80% (see appendix, Figure A.4). The broad signal at ~1000 G has been seen in previously reported $Mn^{II}Mn^{III}$ complexes and was assigned by those groups to an S = 3/2 spin state.[31, 33, 36] The similarities in EPR data between the previously reported $Mn^{II}Mn^{III}$ complexes and that obtained for **2** lead us to assign **2** as a $Mn^{II}Mn^{III}$ complex.

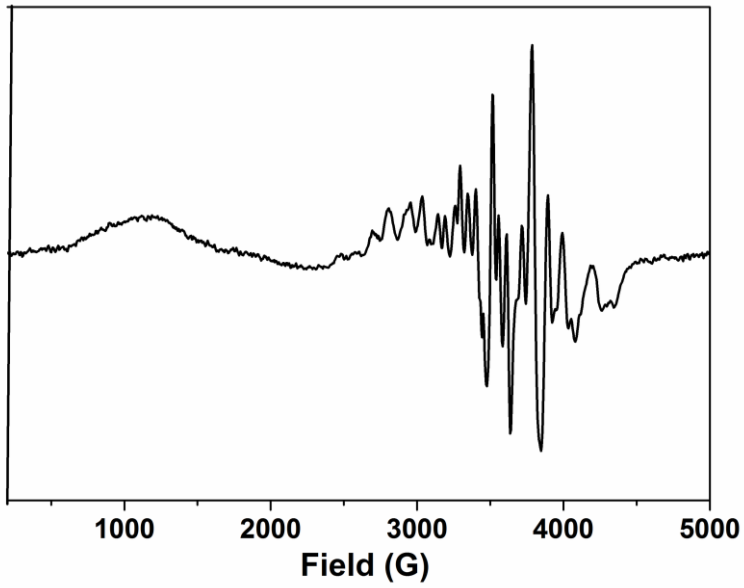

Figure 2.4. Perpendicular mode EPR spectrum of **2** at 2 K (obtained from the reaction of 1 mM **1** and KO_2 in CH_3CN) (9.64 GHz, 0.2 mW microwave power, 1 mM of **1**).

2.3.3 X-ray absorption near-edge spectroscopy (XANES)

In order to further understand the Mn oxidation states in **2** we performed Mn K-edge X-ray absorption near-edge spectroscopy (XANES) on frozen solutions of **1** and **2**. The first inflection of the rising edge was found to be 6547.7 eV for **1** (Figure 2.5), consistent with assignment to the Mn^{II} state. **2** exhibited an increase in edge energy of ~1 eV, to 6548.7 eV, relative to **1**. Notably, the 1s-to-3d pre-edge transition was found at identical energy (6540.4 eV) for both complexes. Previous reports suggest that each integer change in Mn oxidation state was

accompanied by a 2-4 eV blue-shift in Mn K-edge energy, while the pre-edge energies were largely invariant for the Mn^{II} and Mn^{III} states.[37-39] Our observation of a 1-eV blue-shift in edge energy and unchanged pre-edge energy is consistent with a half-integer change in average Mn valence, and assignment of **2** as a $Mn^{II}Mn^{III}$ complex. Extended X-ray absorption fine structure (EXAFS) measurements were not performed because we were unable to obtain **2** in sufficiently high concentration (optimal yield obtained at 1 mM of **1**) to allow accurate EXAFS analyses.

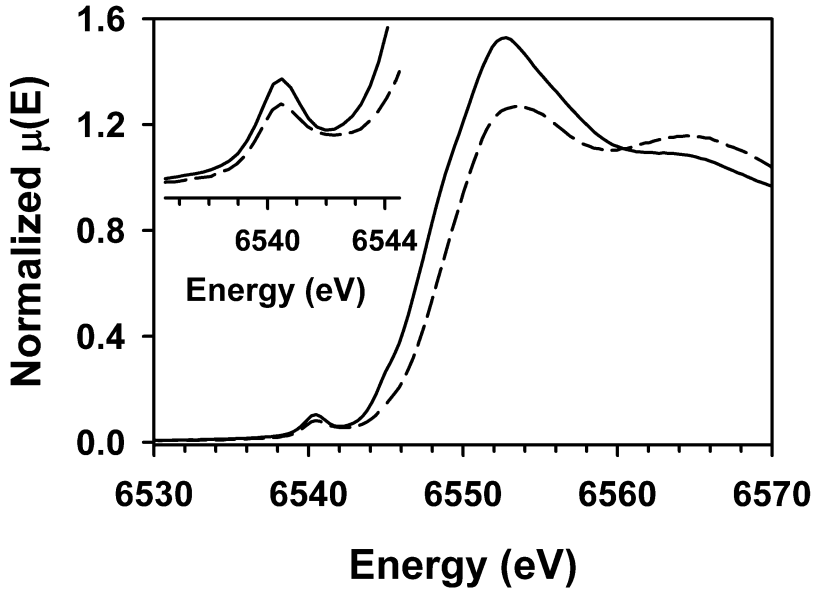

Figure 2.5. Normalized XANES spectra of **1** (—) and **2** (---). The inset shows an expansion of the pre-edge region.

2.4 Reactivity studies of 2

2 decayed very slowly at low temperatures (-40 °C, $t_{1/2}$ ~ 4 hours) but it decayed within 4 minutes upon warming to room temperature. At -40 °C the electronic absorption spectrum of **2** was unaffected by the addition of triphenylphosphine (PPh_3), cyclohexene, or substrates containing weak C–H bonds (all added in 60-fold excess, including TEMPO-H (2,2,6,6-tetramethyl-piperidine-1-ol, C–H bond dissociation energy (BDE) = 70.6 kcal/mol),[40] 1-methyl-1,4-cyclohexadiene ($BDE_{C–H}$ = 77 kcal/mol),[41] and dihydroanthracene ($BDE_{C–H}$ = 78 kcal/mol)[42]). The lack of any reaction with this group of substrates demonstrated that **2** was not a capable electrophilic oxidant. Furthermore, **2** was unreactive towards aldehydes, indicating it was also a poor nucleophilic oxidant.[7, 28, 29, 43] **2** did not react with ferrocene. We thus concluded that the $Mn^{II}Mn^{III}$-peroxide unit in **2** was unreactive at -40 °C.

2 reacted readily with proton donors (*para*-toluenesulfonic acid (*p*TsOH), HBF_4) resulting in the immediate disappearance/bleaching of the electronic absorption features associated with **2**

(Figure A.5). The addition of HBF_4 to **2** in the presence of ferrocene likewise caused the immediate decay of the features associated with **2**, *alongside* the appearance of electronic absorption features attributed to the ferrocenium cation (Figure 2.6). The yield of ferrocenium formed was calculated to be ~ 20% with respect to the concentration of **1** in the initial reaction mixture through electronic absorption spectroscopy. Ferrocene was not oxidised under the same reaction conditions in the absence of **1** or **2**, demonstrating that H^+-donor mediated activation of **2** yielded a capable Mn oxidant. Furthermore, ferrocene did not react with KO_2 or H_2O_2 under the same conditions. Similarly, when **2** was reacted with HBF_4 in the presence of TEMPO-H we identified TEMPO radical as a product of the reaction using EPR spectroscopy (Figures 2.6, A.5, A.6). Although TEMPO-H did not react with KO_2, it did react with H_2O_2 under the same reaction conditions, suggesting that the oxidation of TEMPO-H could be caused by either a Mn_2 oxidant or released H_2O_2. We also observed the formation of free Mn^{II} ions, as evidenced by a 6-line EPR signal, which can be ascribed to de-complexation, although the mechanism for this event is not as yet clear.

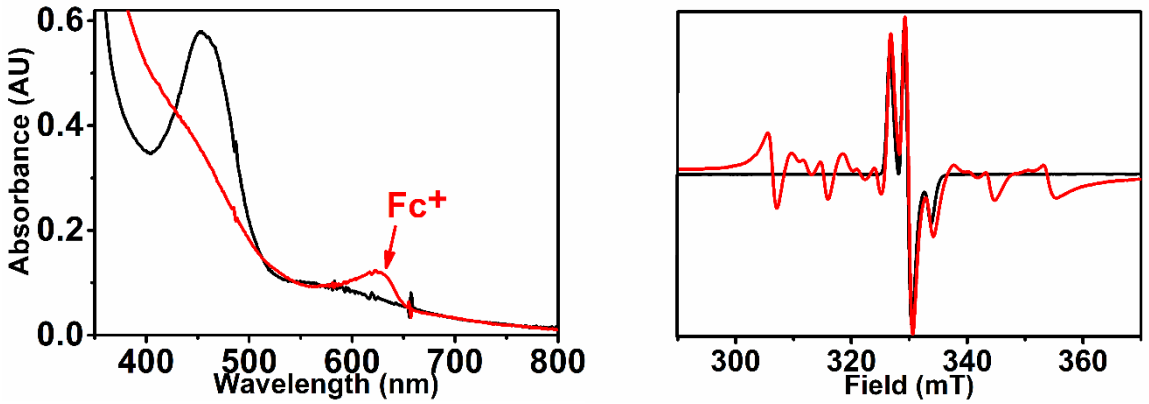

Figure 2.6. Electronic absorption spectra (left) showing formation of ferrocenium (Fc^+, λ_{max} = 620 nm, red trace) from the reaction of **2** (black trace) with H^+ in the presence of ferrocene; normalised EPR spectrum (right) exhibiting the reference TEMPO radical (black trace) and TEMPO radical formation (red trace) from the reaction of **2** with H^+ in the presence of TEMPO–H.

We surmise that the H^+-donor activated the $Mn^{II}Mn^{III}$-peroxide core of **2**, yielding an oxidant that was capable of electron transfer (ferrocene) and hydrogen atom transfer (TEMPO-H). This mimics the postulated role of proton donors in class Ib Mn_2 RNRs, where protonation of the metal-bound peroxide is postulated to precede formation of the tyrosine-oxidising high-valent Mn_2 oxidant.[1]

2.5 Conclusions

We have provided experimental insight into Stubbe's proposed mechanism of $O_2^{\bullet-}$ activation at Mn_2 RNRs. The Mn_2 complex **1** reacted with $O_2^{\bullet-}$, yielding a $Mn^{II}Mn^{III}$-peroxide complex (**2**). **2** was further shown to be activated by proton donors, yielding an unidentified species capable of electron transfer and oxidative activation of O–H bonds, presumably through hydrogen atom transfer. This provides experimental insight into the postulated biochemistry of Mn_2 RNRs, where both a proton and $O_2^{\bullet-}$ are postulated to be required to access a high-valent oxidant via a $Mn^{II}Mn^{III}$-peroxide intermediate. This constituted the first synthetic example of a mixed valent $Mn^{II}Mn^{III}$-peroxide complex. Work continues in our labs to probe this mechanism further and trap the putative high-valent oxidant.

2.6 Experimental section

Materials

All reactions with air sensitive materials were conducted in a glove box under an N_2 atmosphere or under an inert atmosphere using standard Schlenk techniques. All reagents and solvents were purchased from commercial sources. Anhydrous N,N-dimethylformamide (DMF) was purchased and used without further purification. Anhydrous tetrahydrofuran, acetonitrile (MeCN), and diethyl ether (Et_2O) were dispensed through an Innovative Technology PureSolvEN solvent purification system and deoxygenated by purging with Ar. N,N,N',N'-tetrakis(2-benzimidazolylmethyl)-2-hydroxo-1,3-diaminopropane (HPTB) and N,N,N',N'-tetrakis(2-(1-ethylbenzimidazolyl))-2-hydroxy-1,3-diaminopropane (N-Et-HPTB) were synthesized as previously described.[19] **3** was synthesized as previously reported.[20] TEMPO-H (2,2,6,6-tetramethyl-piperidine-1-ol) was synthesized according to a published procedure.[44] $K^{18}O_2$ was prepared using a reported procedure.[45]

Caution: KO_2 and perchlorate salts of metal complexes are potentially explosive and must be handled with care and in small quantities. No problems were encountered during the synthesis of the below dimanganese complexes on the scales reported.

Physical Methods

^{1}H NMR analysis was performed on a Bruker Avance III 400 MHz instrument. Electrospray ionisation (ESI) mass spectra were obtained using a micromass time of flight spectrometer (TOF), interfaced to a Waters 2690 HPLC, or by direct injection in the mass spectrometry instrument. Matrix assisted laser desorption ionisation (MALDI) mass spectra were acquired using a Maldi Q-ToF Premier MS System. Attenuated total reflectance Fourier transform infra-red spectra (ATR-FTIR) were recorded using a Perkin-Elmer Spectrum 100 Fourier Transform infrared spectrometer. CHN elemental content analyses were performed on an Exeter Analytical CE 440 elemental analyzer fitted with a Varian 55B SpectraAA atomic absorption spectrometer by University College Dublin elemental analysis lab. Electronic absorption spectra were recorded in quartz cuvettes on a Hewlett Packard (Agilent) 8453 diode array spectrophotometer (190-1100 nm range) coupled to a liquid nitrogen cooled cryostat from Unisoku Scientific Instruments (Osaka, Japan). X-ray crystallography was performed on a Bruker APEX Kappa Duo system at 100 K using an Oxford Cobra cryosystem. EPR (Electron Paramagnetic Resonance) spectra were measured on a Bruker EMX spectrometer equipped with an Oxford Instruments CE 5396, ESR9 continuous flow cryostat and an Oxford Instruments CE 5396 Precision temperature controller for the 77 K measurements. At 2 K the

measurements were conducted on a Bruker EPP 300 spectrometer equipped with an Oxford ESR 910 liquid helium cryostat and an Oxford temperature controller. The quantification of the 2 K signals was relative to a $Cu(NO_3)_2$ spin standard in methanol.

Mn K-edge X-Ray absorption spectroscopy data was collected at the Stanford Synchrotron Radiation Lightsource (SSRL, Menlo Park, CA) on beamline 9-3. SSRL operated at 3.0 GeV and 500 mA in top-off mode. At beamline 9-3, the optical configuration consisted of a Rh-coated collimating mirror set to a 10 keV cutoff to suppress higher harmonics, a liquid nitrogen cooled Si(220) double crystal monochromator for energy selection, and a Rh-coated toroidal focusing mirror. XAS data was obtained in fluorescence using a 100 pixel monolithic solid state germanium detector (Canberra). Chromium oxide filters of 3 and 6 absorption lengths were used in combination with a set of Soller slits to maintain detector linearity (ICRs / element <50 kHz). Energy calibration was provided by a Mn metal foil reference, with the first inflection of the reference spectrum set to 6539.0 eV. Samples were maintained at 10 K using an Oxford liquid helium cryostat. Data was monitored for evidence of photoreduction during collection, and new spots on the sample window exposed as appropriate. XAS data was inspected, averaged, calibrated, and normalized using Athena.

Synthesis

Synthesis of $[Mn_2(O_2CCH_3)(N\text{-}Et\text{-}HPTB)](ClO_4)_2$ (1)

The complex was synthesized using a similar procedure as reported for the synthesis of complex $[Mn_2(O_2CCH_3)(HPTB)](ClO_4)_2$ (**3**).[20, 46] N-Et-HPTB (0.5 g, 0.69 mmol), acetic acid (0.07 g, 1.11 mmol), and NaOAc (0.18 g, 2.21 mmol) were combined in a premixed 3:1 ethanol-water solution (140 mL). After stirring for 15 min, $Mn^{II}(OAc)_2.4H_2O$ (0.27 g, 1.11 mmol) dissolved in ethanol (20 mL) was added. The mixture was allowed to stir for 30 min, after which time $NaClO_4$ (1.08 g, 8.86 mmol) was added dissolved in an 1:1 ethanol/water solution (10 mL). The reaction mixture was allowed to stir for 2 h and then the volume was reduced under vacuum. It was then allowed to sit at 0 °C for 2 h. A crystalline pink precipitate formed and was collected by filtration (0.6 g, 87%). The product was recrystallized from CH_3CN/Et_2O to yield crystals suitable for X-ray diffraction measurements.

Anal. Calcd (found) for $C_{45}H_{52}Cl_2Mn_2N_{10}O_{11}.H_2O$: C, 48.79 (48.94); H, 4.91 (4.66); N, 12.64 (12.49). ν_{max} (ATR-FTIR)/cm^{-1}: μ_2-carboxylate 1560 (asymmetric) and 1438 (symmetric). Maldi-Tof MS (*m/z*): Found 989.2470 ($[M - ClO_4^-]^+$ expected = 989.2475 ($C_{45}H_{52}ClMn_2N_{10}O_7^+$)).

General procedure for the reaction of 1 with KO_2

Either a CH_3CN or 3:1 THF/DMF solution (1 mM) of complex **1** was prepared. In a quartz cuvette 2 mL of a 1 mM solution of complex **1** was cooled to -40 °C. KO_2 (20 mM) and 18-crown-6 (59 mM) were dissolved in DMF. 300 μL of this solution was added to the solution containing the dimanganese complex. The reaction progress was monitored using electronic absorption spectroscopy.

EPR and XAS sample preparation

Samples for EPR analysis were prepared by transferring ~1 mL of the desired solution from the quartz cuvette at -40 °C, via a pre-cooled pipette into a pre-cooled EPR tube and immediately freezing it in liquid nitrogen. All EPR spectra were recorded at either 77 K (9.21 GHz, 2 mW microwave power and a 0.5 mT field modulation amplitude) or 2 K (9.64 GHz, 0.2 mW microwave power and a 1 mT field modulation amplitude). Samples for X-ray absorption spectroscopy (XAS) analysis were prepared by tranferring solutions of **1** (1 mM, acetonitrile) and **2** (acetonitrile) into XAS smaple cups pre-cooled in a liquid nitrogen bath and immediately freezing them.

Reactivity studies

A solution of **2** in acetonitrile at -40 °C was prepared using the above procedure. Substrates were added as concentrated acetonitrile solutions to solutions of **2** at -40 °C. The reactions were monitored using electronic absorption spectroscopy. For the protonation studies, concentrated acetonitrile solutions of HBF_4 (40 mM, 75 μl, 1.5 equivalents) and *para*-toluenesulfonic acid (40 mM, 150 μl, 3 equivalents) were added to **2** in acetonitrile at -40 °C. The substrates used in the proton-mediated reactivity studies were ferrocene (40 mM, 50 μl, 1 equivalent) and TEMPO-H (40 mM, 75 μl, 1.5 equivalents). The acid used in the substrate reactivity studies was HBF_4 (1.5 equivalents for the TEMPO-H reaction and 5 equivalents in the ferrocene reaction).

The lifetime of **2** in CH_3CN at 25 °C was measured by monitoring the decay of the absorbance features at λ_{max} = 460, 610 nm versus time, by warming up the cuvette containing **2** from -40 °C to 25 °C.

X-ray Diffraction Methods and Structure Refinements

A specimen of $C_{45}H_{52}Cl_2Mn_2N_{10}O_{11}$, approximate dimensions 0.030 mm x 0.070 mm x 0.100 mm, was used for the X-ray crystallographic analysis using a MiTeGen micromount. Bruker APEX software was used to collect, correct for Lorentz and polarization effects, and reduce the data.[47] The structure was solved using the XT[48] structure solution program with Intrinsic Phasing and refined with the XL[49] refinement package with Least Squares minimisation using the space group $P2_1/n$, with Z = 4 for the formula unit, $C_{45}H_{52}Cl_2Mn_2N_{10}O_{11}$. The main bimetallic cluster is disordered in two conformations (79:21%). One perchlorate anion was disordered around an O11-Cl2 bond resulting in 4 alternate orientations of the three remaining Cl-O bonds with refined occupancies of ca. 24: 32: 29: 16%. Restraints (SAME, SADI) and constraints (EADP) were used for refinement convergence.

Table S1. Crystal data and structure refinement for $[Mn_2(O_2CCH_3)(N\text{-}Et\text{-}HPTB)](ClO_4)_2$ (**1**)

Empirical formula	$C_{45}H_{52}Cl_2Mn_2N_{10}O_{11}$	
Formula weight	1089.74	
Temperature	100(2) K	
Wavelength	1.54178 Å	
Crystal system	Monoclinic	
Space group	$P2_1/n$	
Unit cell dimensions	a = 13.8839(5) Å	α = 90°.
	b = 22.3768(8) Å	β = 93.6868(19)°.
	c = 15.6449(6) Å	γ = 90°.
Volume	4850.5(3) $Å^3$	
Z	4	
Density (calculated)	1.492 Mg/m^3	
Absorption coefficient	5.841 mm^{-1}	
F(000)	2256	
Crystal size	0.100 x 0.070 x 0.030 mm^3	
Theta range for data collection	3.452 to 66.740°.	
Index ranges	$-16\leq h\leq 16$, $-26\leq k\leq 26$, $-18\leq l\leq 18$	
Reflections collected	62124	
Independent reflections	8566 [R(int) = 0.0543]	
Completeness to theta = 66.741°	99.6 %	
Absorption correction	Semi-empirical from equivalents	
Max. and min. transmission	0.7528 and 0.5962	
Refinement method	Full-matrix least-squares on F^2	
Data / restraints / parameters	8566 / 112 / 778	
Goodness-of-fit on F^2	1.022	
Final R indices [$I>2\sigma(I)$]	R1 = 0.0487, wR2 = 0.1236	
R indices (all data)	R1 = 0.0598, wR2 = 0.1288	
Largest diff. peak and hole	0.777 and -0.678 $e.Å^{-3}$	

References

[1] J. A. Cotruvo, Jr., T. A. Stich, R. D. Britt, J. Stubbe, *J. Am. Chem. Soc.* **2013**, *135*, 4027-4039.

[2] J. A. Cotruvo, Jr., J. Stubbe, *Biochemistry* **2010**, *49*, 1297-1309.

[3] N. Cox, H. Ogata, P. Stolle, E. Reijerse, G. Auling, W. Lubitz, *J. Am. Chem. Soc.* **2010**, *132*, 11197-11213.

[4] A. K. Boal, J. A. Cotruvo, Jr., J. Stubbe, A. C. Rosenzweig, *Science* **2010**, *329*, 1526-1530.

[5] A. J. Wu, J. E. Penner-Hahn, V. L. Pecoraro, *Chem. Rev.* **2004**, *104*, 903-938.

[6] S. Mukhopadhyay, S. K. Mandal, S. Bhaduri, W. H. Armstrong, *Chem. Rev.* **2004**, *104*, 3981-4026.

[7] R. A. Geiger, S. Chattopadhyay, V. W. Day, T. A. Jackson, *Dalton Trans.* **2011**, *40*, 1707-1715.

[8] J. Annaraj, J. Cho, Y. M. Lee, S. Y. Kim, R. Latifi, S. P. de Visser, W. Nam, *Angew. Chem. Int. Ed.* **2009**, *48*, 4150-4153.

[9] K. Fujisawa, M. Tanaka, Y. Moro-oka, N. Kitajima, *J. Am. Chem. Soc.* **1994**, *116*, 12079-12080.

[10] R. A. Geiger, S. Chattopadhyay, V. W. Day, T. A. Jackson, *J. Am. Chem. Soc.* **2010**, *132*, 2821-2831.

[11] M. S. Seo, J. Y. Kim, J. Annaraj, Y. Kim, Y. M. Lee, S. J. Kim, J. Kim, W. Nam, *Angew. Chem. Int. Ed.* **2007**, *46*, 377-380.

[12] U. P. Singh, A. K. Sharma, S. Hikichi, H. Komatsuzaki, Y. Moro-oka, M. Akita, *Inorg. Chim. Acta* **2006**, *359*, 4407-4411.

[13] S. Groni, G. Blain, R. Guillot, C. Policar, E. Anxolabehere-Mallart, *Inorg. Chem.* **2007**, *46*, 1951-1953.

[14] S. Groni, P. Dorlet, G. Blain, S. Bourcier, R. Guillot, E. Anxolabehere-Mallart, *Inorg. Chem.* **2008**, *47*, 3166-3172.

[15] R. B. VanAtta, C. E. Strouse, L. K. Hanson, J. S. Valentine, *J. Am. Chem. Soc.* **1987**, *109*, 1425-1434.

[16] R. L. Shook, W. A. Gunderson, J. Greaves, J. W. Ziller, M. P. Hendrich, A. S. Borovik, *J. Am. Chem. Soc.* **2008**, *130*, 8888-8889.

[17] M. K. Coggins, X. Sun, Y. Kwak, E. I. Solomon, E. Rybak-Akimova, J. A. Kovacs, *J. Am. Chem. Soc.* **2013**, *135*, 5631-5640.

[18] L. Westerheide, F. K. Müller, R. Than, B. Krebs, J. Dietrich, S. Schindler, *Inorg. Chem.* **2001**, *40*, 1951-1961.

[19] V. McKee, M. Zvagulis, J. V. Dagdigian, M. G. Patch, C. A. Reed, *J. Am. Chem. Soc.* **1984**, *106*, 4765-4772.

[20] P. J. Pessiki, S. V. Khangulov, D. M. Ho, G. C. Dismukes, *J. Am. Chem. Soc.* **1994**, *116*, 891-897.

[21] A. E. M. Boelrijk, S. V. Khangulov, G. C. Dismukes, *Inorg. Chem.* **2000**, *39*, 3009-3019.

[22] *It is common that such Mn_2 clusters form larger tetranuclear clusters,[12] and we postulate that at higher concentrations of **1** such larger clusters form and prevent a reaction with KO_2 to form **2**.*

[23] M. K. Chan, W. H. Armstrong, *J. Am. Chem. Soc.* **1989**, *111*, 9121-9122.

[24] F. B. Larsen, A. Boisen, K. J. Berry, B. Moubaraki, K. S. Murray, V. McKee, R. C. Scarrow, C. J. McKenzie, *Eur. J. Inorg. Chem.* **2006**, *19*, 3841-3852.

[25] D. F. Leto, S. Chattopadhyay, V. W. Day, T. A. Jackson, *Dalton Trans.* **2013**, *42*, 13014-13025.

[26] J. Cho, R. Sarangi, W. Nam, *Acc. Chem. Res.* **2012**, *45*, 1321-1330.

[27] D. R. Gamelin, M. L. Kirk, T. L. Stemmler, S. Pal, W. H. Armstrong, J. E. Penner-Hahn, E. I. Solomon, *J. Am. Chem. Soc.* **1994**, *116*, 2392-2399.

[28] H. Kang, J. Cho, K. B. Cho, T. Nomura, T. Ogura, W. Nam, *Chem. Eur. J.* **2013**, *19*, 14119-14125.

[29] N. Saravanan, M. Sankaralingam, M. Palaniandavar, *RSC Advances* **2014**, *4*, 12000.

[30] S. Hong, K. D. Sutherlin, J. Park, E. Kwon, M. A. Siegler, E. I. Solomon, W. Nam, *Nat. Commun.* **2014**, *5*, 5440.

[31] R. M. Buchanan, K. J. Oberhausen, J. F. Richardson, *Inorg. Chem.* **1988**, *27*, 971-973.

[32] H. Diril, H. R. Chang, X. Zhang, S. K. Larsen, J. A. Potenza, C. G. Pierpont, H. J. Schugar, S. S. Isied, D. N. Hendrickson, *J. Am. Chem. Soc.* **1987**, *109*, 6207-6208.
[33] H. Diril, H. R. Chang, M. J. Nilges, X. Zhang, J. A. Potenza, H. J. Schugar, S. S. Isied, D. N. Hendrickson, *J. Am. Chem. Soc.* **1989**, *111*, 5102-5114.
[34] N. Cox, W. Ames, B. Epel, L. V. Kulik, L. Rapatskiy, F. Neese, J. Messinger, K. Wieghardt, W. Lubitz, *Inorg. Chem.* **2011**, *50*, 8238-8251.
[35] Y. Sano, A. C. Weitz, J. W. Ziller, M. P. Hendrich, A. S. Borovik, *Inorg. Chem.* **2013**, *52*, 10229-10231.
[36] L. Dubois, D. F. Xiang, X. S. Tan, J. Pecaut, P. Jones, S. Baudron, L. Le Pape, J. M. Latour, C. Baffert, S. Chardon-Noblat, M. N. Collomb, A. Deronzier, *Inorg. Chem.* **2003**, *42*, 750-760.
[37] R. E. Schreiber, H. Cohen, G. Leitus, S. G. Wolf, A. Zhou, L. Que, Jr., R. Neumann, *J. Am. Chem. Soc.* **2015**, *137*, 8738-8748.
[38] T. C. Weng, W. Y. Hsieh, E. S. Uffelman, S. W. Gordon-Wylie, T. J. Collins, V. L. Pecoraro, J. E. Penner-Hahn, *J. Am. Chem. Soc.* **2004**, *126*, 8070-8071.
[39] F. Farges, *Phys. Rev. B* **2005**, *71*.
[40] J. J. Warren, T. A. Tronic, J. M. Mayer, *Chem. Rev.* **2010**, *110*, 6961-7001.
[41] T. Matsumoto, K. Ohkubo, K. Honda, A. Yazawa, H. Furutachi, S. Fujinami, S. Fukuzumi, M. Suzuki, *J. Am. Chem. Soc.* **2009**, *131*, 9258-9267.
[42] C. Arunkumar, Y. M. Lee, J. Y. Lee, S. Fukuzumi, W. Nam, *Chem. Eur. J.* **2009**, *15*, 11482-11489.
[43] P. Pirovano, A. M. Magherusan, C. McGlynn, A. Ure, A. Lynes, A. R. McDonald, *Angew. Chem. Int. Ed.* **2014**, *53*, 5946-5950.
[44] K. S. Chan, X. Z. Li, W. I. Dzik, B. de Bruin, *J. Am. Chem. Soc.* **2008**, *130*, 2051-2061.
[45] P. J. Donoghue, A. K. Gupta, D. W. Boyce, C. J. Cramer, W. B. Tolman, *J. Am. Chem. Soc.* **2010**, *132*, 15869-15871.
[46] P. J. Pessiki, G. C. Dismukes, *J. Am. Chem. Soc.* **1994**, *116*, 898-903.
[47] Bruker, *APEX2 Ver. 2014.11-0, Bruker AXS Inc., Madison, WI, USA.*, 1-142.
[48] G. M. Sheldrick, *Acta Crystallogr. C Struct. Chem.* **2015**, *71*, 3-8.
[49] G. M. Sheldrick, *Acta Crystallogr. A* **2008**, *64*, 112-122.

Chapter 3

A $Mn^{II}Mn^{III}$-peroxide complex that reacts as a nucleophilic oxidant

The 2 K EPR measurements were performed by Ms. Subhasree Kal (University of Minnesota, Minneapolis). The XAS data collection and analysis were done by Daniel Nelis (Trinity College Dublin) and Dr Eric R. Farquhar (Brookhaven National Laboratory, USA).

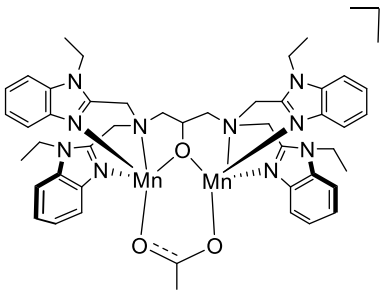

$[Mn^{II}Mn^{II}(O_2CCH_3)((N\text{-}Et\text{-}HPTB)]^{2+}$

1

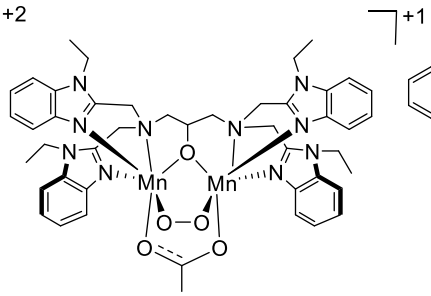

$[Mn^{II}Mn^{III}(O_2)(O_2CCH_3)((N\text{-}Et\text{-}HPTB)]^{1+}$

2

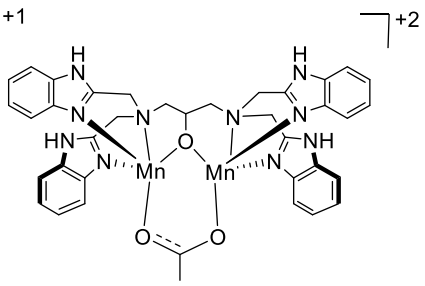

$[Mn^{II}Mn^{II}(O_2CCH_3)((HPTB)]^{2+}$

3

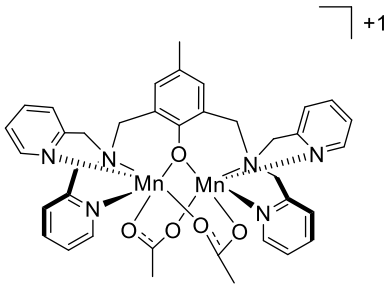

$[Mn^{II}Mn^{II}(O_2CCH_3)_2(BPMP)]^{1+}$

4

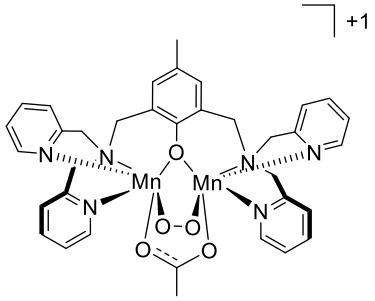

$[Mn^{II}Mn^{III}(O_2)(O_2CCH_3)(BPMP)]^{1+}$

5

3.1 Introduction

The first example of a synthetic $Mn^{II}Mn^{III}$-peroxide adduct, that mimics one of the intermediates in class Ib Mn_2 RNRs was recently reported by our group (adduct **2**, chapter 2).[1] The mixed valent species was prepared upon reaction of a Mn^{II}_2 complex (($[Mn_2(O_2CCH_3)$(N-Et-HPTB)]$(ClO_4)_2$, where N-Et-HPTB = N,N,N',N'-tetrakis(2-(1-ethylbenzimidazolyl))-2-hydroxy-1,3-diaminopropane)) with $O_2^{\bullet-}$ at low temperature. Electronic absorption spectroscopy, electron paramagnetic resonance (EPR), X-ray absorption near edge spectroscopy (XANES) and electrospray ionisation mass spectrometry (ESI-MS) supported the formation of the $Mn^{II}Mn^{III}$-peroxide complex.[1] The $Mn^{II}Mn^{III}$-peroxide (**2**) adduct proved to be a poor electrophilic and nucleophilic oxidant at -40 °C. Nevertheless, **2** was capable of oxidising ferrocene and weak O-H bonds (2,2,6,6-tetramethyl-piperidine-1-ol (= TEMPO-H)) upon activation with proton donors.[1] Since the previously reported synthetic $Mn^{II}Mn^{III}$-peroxide complex proved to be a poor electrophilic and nucleophilic oxidant, we were interested in preparing a more powerful $Mn^{II}Mn^{III}$-peroxide oxidant. Previously reported mononuclear Mn^{III}-peroxide complexes displayed a nucleophilic character by being involved in aldehyde deformylation.[2-7] However, to the best of our knowledge the nucleophilic reactivity of a synthetic $Mn^{II}Mn^{III}$-peroxide complex has not been explored before. Herein, we describe our efforts towards further mimicking class Ib Mn_2 RNRs by probing the nucleophilic reactivity of a $Mn^{II}Mn^{III}$-peroxide model complex.

In this chapter we describe the preparation of a $Mn^{II}Mn^{III}$-peroxide species (**5**), by investigating the reactivity of a Mn^{II} precursor complex ($[Mn_2(O_2CCH_3)_2$(BPMP)](ClO_4) (**4**) where HBPMP = 2,6-bis[(bis(2-pyridylmethyl)amino)methyl]-4-methylphenol))) supported by a polypyridine ligand (HBPMP) towards $O_2^{\bullet-}$. The nucleophilic reactivity of the adduct formed ($Mn^{II}Mn^{III}$-peroxide, **5**) was investigated in aldehyde deformylation.

3.2 Characterization of a peroxo-$Mn^{II}Mn^{III}$ adduct (5)

3.2.1 UV-Vis absorption spectroscopy

$[Mn_2(O_2CCH_3)_2(BPMP)](ClO_4)$ (**4**, where HBPMP = 2,6-bis[(bis(2-pyridylmethyl)amino)methyl]-4-methylphenol)) was synthesised as previously described.[8, 9] To a 1:9 CH_3CN/tetrahydrofuran (THF) solution of **4** (1.5 mM, 2 mL) cooled to -90 °C, was added an *N*,*N*-dimethylformamide (DMF, 0.25 mL) solution containing KO_2 (1.25 equivalents, 15 mM) and 18-crown-6 ether (40 mM). An immediate reaction occurred (complete within 30 seconds), as evidenced by changes in the electronic absorption spectrum (Figure 3.1), resulting in the formation of a new species (**5**, purple trace, Figure 3.1). Lower yields were observed (less intense absorption features) with higher equivalencies of KO_2 and at higher concentrations of **4**. The latter was also observed in the case of the $Mn^{II}Mn^{III}$-peroxide complex $[Mn_2(O_2)(N\text{-Et-HPTB})]^{2+}$.[1]

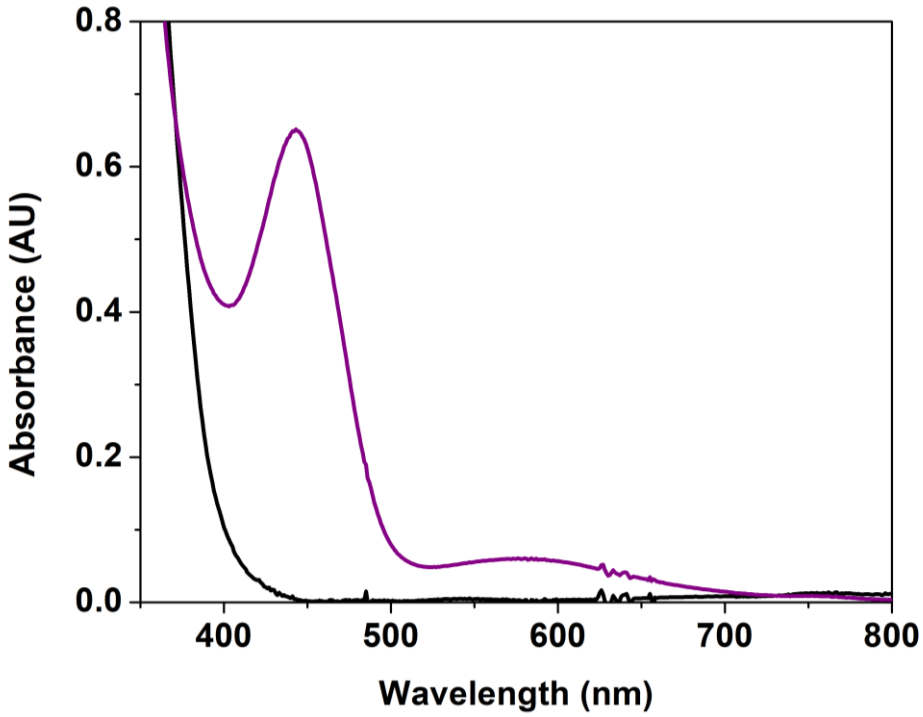

Figure 3.1. Electronic absorption spectra of **4** (black trace, 1.5 mM) and **5** (purple trace, from **4** (1.5 mM) + 1.25 equivalents KO_2) at -90 °C in 1:9 CH_3CN/THF (path length = 1 cm).

The electronic absorption spectrum of **4** displayed very weak absorbance bands above 300 nm (*d-d* transitions), whereas **5** displayed two low intensity features at λ_{max} = 440 and 590 nm (Figure 3.1). The electronic absorption features of **5** were remarkably similar to those of a $Mn^{II}Mn^{III}$-peroxide complex, supported by the N-Et-HPTB

(N,N,N',N'-tetrakis(2-(1-ethylbenzimidazolyl))-2-hydroxy-1,3-diaminopropane) ligand, that we recently reported (λ_{max} = 460, 610 nm, Figure A.7, red trace).[1] Furthermore, previously reported Mn^{III}-peroxide complexes $[Mn^{III}(O_2)(TMC)]^+$ (TMC = 1,4,8,11-tetramethyl-1,4,8,11-tetraazacyclotetradecane), $[Mn^{III}(O_2)(13\text{-}TMC)]^+$ (13-TMC = 1,4,7,10-tetramethyl-1,4,7,10-tetraazacyclotridecane), and $[Mn^{III}(O_2)(Tp^{iPr})]^+$ (Tp^{iPr} = tris(3,5-diisopropylpyrazolyl)borate), all exhibited an absorption band at around 460 nm attributed to peroxide-to-metal charge transfer[6] and a broader band in the 560-620 nm range, derived from *d-d* transitions.[6] Moreover, $[Mn^{III}(O_2)(H_3bupa)]^-$ (H_3bupa = bis[(N'-tert-butylurealy)-N-ethyl]-(6-pivalamido-2-pyridylmethyl)amine) also exhibited electronic absorption features at λ_{max} = 490 and 660 nm.[2] Additionally, Mn^{III}-peroxides supported by other polydentate amine ligands displayed a prominent band at λ_{max} = 430-445 nm and a weaker band at λ_{max} = 590-610 nm.[10] This led us to conclude that species **5** was the second example of a $Mn^{II}Mn^{III}$-peroxide complex.

3.2.2 ESI mass spectrometry of 5

Cold injection electrospray ionisation mass spectrometry (ESI-MS) on a just-thawed solution of **5** revealed an ion peak consistent with **5** being a $Mn^{II}Mn^{III}$-peroxide complex. A mass peak (*m/z* = 770.2933) consistent with the formulation of the mono-cation $\{[Mn_2(O_2)(BPMP)](ClO_4)\}^+$ (Figure 3.2) was observed. In this cation both acetate ligands from the precursor complex **4** were absent. This mirrors our observations made with the $Mn^{II}Mn^{III}$-peroxide complex supported by N-Et-HPTB (adduct **2**, chapter 2), where the starting material contained an acetate ligand, but by ESI-MS we identified the $[Mn_2(O_2)(N\text{-}Et\text{-}HPTB)]^{2+}$ dication for the $Mn^{II}Mn^{III}$-peroxide complex.[1]

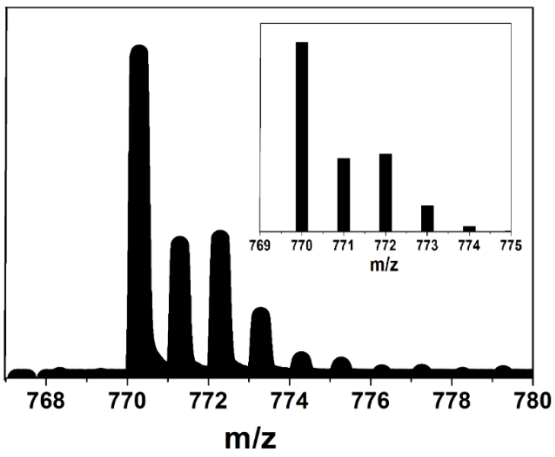

Figure 3.2. ESI-MS spectrum of **5** (m/z = 770 associated with the $\{[Mn_2(O_2)(BPMP)](ClO_4)\}^+$ ion). Inset shows the simulated mass spectrum.

3.2.3 EPR spectroscopy of 5

At 2 K, complex **5** displayed a 22-line electron paramagnetic resonance (EPR) signal at g ~ 1.96 (Figure 3.3). The signal displayed a wide spectral width and was only observed below 10 K. Such signals have previously been observed in $Mn^{II}Mn^{III}$ complexes, where 24-29 line signals have been ascribed to the $Mn^{II}Mn^{III}$ oxidation states.[11-15] Furthermore, the wide spectral width and temperature dependence are indicative of a low coupling constant, and therefore have been ascribed to $Mn^{II}Mn^{III}$ complexes.[14] The EPR spectrum obtained for **5** also looked remarkably similar to that obtained for the analogous $Mn^{II}Mn^{III}$-peroxide complex supported by the N-Et-HPTB ligand, which displayed a 29-line EPR signal at 2 K with wide spectral width and only well-resolved below 10 K (Figure A.8).[1]

The mixed valent form of complex **4** ($[Mn^{II}Mn^{III}(O_2CCH_3)_2(BPMP)](ClO_4)_2$) reported by Hendrickson and co-workers displayed a g ~ 2 signal with 29 Mn hyperfine lines at 7.5 K.[12] **5** exhibited a 24-line EPR signal at 2 K. We thus concluded that complex **5** represents a unique $Mn^{II}Mn^{III}$ complex support by the BPMP ligand, that differs markedly from the previously reported mixed-valent complex $[Mn^{II}Mn^{III}(O_2CCH_3)_2(BPMP)](ClO_4)_2$. The yield of **5** was determined by EPR integration to be ~50% (Figure A.9, see appendix for details).

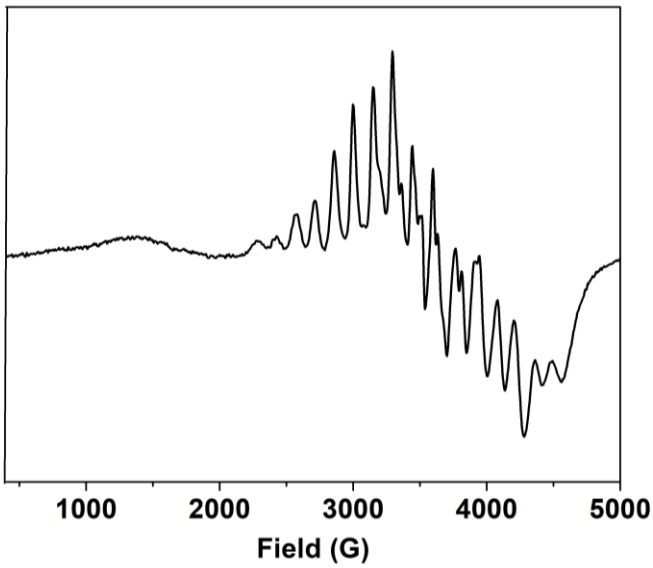

Figure 3.3. Perpendicular mode EPR spectrum of **5** at 2 K (obtained from the reaction of 1.5 mM **4** and KO_2 in 1:9 CH_3CN/THF) (9.64 GHz, 0.2 mW microwave power, 1.5 mM of **4**).

Moreover, besides the difference in the number of EPR signals observed for complexes **5** and mixed valent form of **4**, they also differ in their electronic absorption spectra. While the electronic absorption spectrum of **5** exhibited two weak absorbance bands at λ_{max} = 440 and

590 nm, the mixed valent form of complex **4** displayed three weak absorbance bands at λ_{max} = 427, 478 and 620 nm.[8, 12] This supports our postulate that complex **5** and the mixed valent form of complex **4** are two different species, the former containing a peroxide ligand.

3.2.4 X-ray absorption near-edge spectroscopy (XANES)

To gain a better insight into the oxidation state of **5**, Mn K-edge X-ray absorption near edge spectroscopy (XANES) was carried out on frozen samples of **4** and **5**. The first inflection point of the rising edge can be used to define changes in the oxidation state of a metal centre in XANES.[16] The edge energy of **4** was found to be 6548.4 eV, while that of **5** was 6548.9 eV, an increase of 0.5 eV (Figure 3.4). For Mn K-edge XAS, a shift of 2-4 eV is expected for every integer change in formal oxidation state.[16-18] Therefore, for a mixed valent Mn_2 species, a shift of 1 eV would be expected upon oxidation of a $Mn^{II}Mn^{II}$ (**4**) to a $Mn^{II}Mn^{III}$ (**5**). The yield of **5** was only ~50%, according to EPR analysis. Therefore, the shift of 0.5 eV is consistent with the formation of 50% of a $Mn^{II}Mn^{III}$ species. For the previously reported complex N-Et-HPTB-supported $Mn^{II}Mn^{III}$-peroxide, we observed an ~1 eV shift upon conversion of the Mn^{II}_2 starting material to the $Mn^{II}Mn^{III}$-peroxide species (obtained in 80% yield).[1]

Notably, the pre-edge energy, 6540.3 eV, was not found to differ between **4** and **5**, and there was a significant increase in the pre-edge area (Figure 3.4), which is characteristic of a decrease in the metal site symmetry.[19] These observations are consistent with our previously characterised $Mn^{II}Mn^{III}$-peroxide complex.[1] The shift of the edge energy by 0.5 eV as well as the apparent decreased site symmetry as characterised by the increase of the pre-edge area support our assignment of **5** as a $Mn^{II}Mn^{III}$ species. Extended X-ray absorption fine structure (EXAFS) analysis on **5** was not carried due to the low yield (~ 50%).

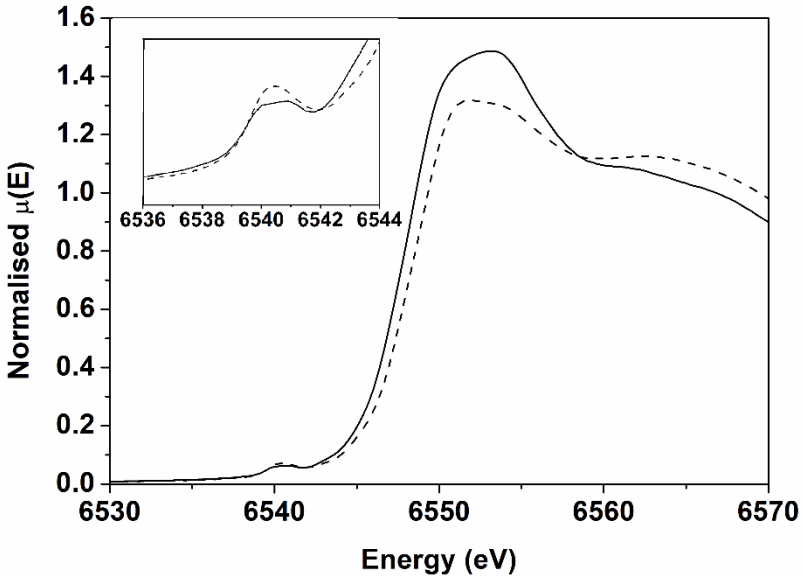

Figure 3.4. Normalised XANES spectra of **4** (solid) and **5** (dashed). The inset shows an expansion of the pre-edge region.

3.3 Reactivity studies of 5

At -90 °C, **5** displayed a $t_{1/2}$ ~ 2 hours, but decayed fully within 3 minutes upon warming to room temperature. The electronic absorption spectrum of **5** at -90 °C, remained unchanged upon the addition of triphenylphosphine (PPh_3), cyclohexene, or substrates containing weak X–H bonds (all added in 100-fold excess, including 1-methyl-1,4-cyclohexadiene (bond dissociation energy ($BDE_{C–H}$) = 77 kcal/mol),[20] dihydroanthracene ($BDE_{C–H}$ = 78 kcal/mol),[21] and 2,4-di-*tert*-butylphenol ($BDE_{O–H}$ = 82 kcal/mol)).[22, 23] Hence, **5** was determined to be a very poor electrophilic oxidant as it showed no reaction with this group of substrates. This observation was consistent with our observations for the (N-Et-HPTB)-$Mn^{II}Mn^{III}$ -peroxide complex,[1] which was also unreactive towards such substrates.

Fascinatingly, however, **5** reacted readily with a series of aldehyde substrates including 2-phenylpropionaldehyde (PPA), cyclohexanecarboxaldehyde (CCA), and *para*-substituted benzaldehydes (*p*-R-$C_6H_4C(H)O$). **5** reacted with PPA (Figures A.10-A.12) to yield acetophenone as evidenced by gas chromatography mass spectrometry (GC-MS, Figure A.14). By plotting the change in the absorbance intensity of the λ_{max} = 440 nm feature of **5** against time and fitting the resulting curve (Figure A.10), a first order rate constant (k_{obs}) for the reaction with PPA was determined. A second order rate constant (k_2) was calculated by plotting k_{obs}

values for a series of substrate concentrations (Figure A.12). The k_2 value determined for the reaction between **5** and PPA was 6.38 $\times 10^{-4}$ $M^{-1}s^{-1}$ (determined at relatively low [PPA]). When relatively high concentrations of PPA were added to **5**, the k_{obs} values increased unexpectedly (Figure A.13). We postulate that at higher [PPA], the increase in the rate of the reaction could be due residual 2-phenylpropionic acid present in PPA. This behaviour was not observed for any of the other aldehyde substrates investigated, and we therefore did not include the unexpectedly high k_2 data points in our calculations.

Adduct **5** also reacted with CCA at -90 °C in 1:9 CH_3CN/THF (Figures A.15-A.17). GC-MS analysis of the reaction mixture showed the formation of cyclohexanone (Figure A.18). The k_2 value obtained for the reaction between **5** and CCA was 0.012 $M^{-1}s^{-1}$. However, **5** did react with benzaldehyde (k_2 = 6.7 $\times$ 10^{-3} $M^{-1}s^{-1}$, Figures A.19-A.21). The product of this reaction was benzoic acid (Figure A.22). In the reaction of **5** with electron poor *para*-substituted benzaldehydes, the k_2 value determined for *p*-Cl-PhC(O)H was 0.01 $M^{-1}s^{-1}$ (Figures A.23-A.25), for *p*-CF_3-C_6H_4C(H)O was 0.015 $M^{-1}s^{-1}$ (Figures A.26-S28), for *p*-CN-PhC(O)H was 0.017 $M^{-1}s^{-1}$ (Figures A.29-A.31) while for *p*-NO_2-PhC(O)H a k_2 value of 0.021 $M^{-1}s^{-1}$ was obtained (Figures A.32-A.34). Product analysis of the post reaction mixtures showed the formation of *para*-substituted benzoates (Figure A.35). No reaction was observed when **2** was reacted with ~3000 equivalents of *p*-OCH_3-C_6H_4C(H)O or *p*-CH_3-C_6H_4C(H)O at -90 °C, in 1:9 CH_3CN/THF. Thus, **5** showed no reaction towards electron rich *para*-substituted benzaldehydes but reacted with electron poor *para*-substituted benzaldehydes. A Hammett plot of the log($^Rk_2/^Hk_2$) versus the *para*-substituent (σ_p) was linear and resulted in a positive ρ value of 0.64, as shown in Figure 3.5. Previous reports showed that the nucleophilic character of the $\{M^{III}O_2\}$ unit (M = Mn, Ni, Co) can be confirmed by using *para*-substituted benzaldehydes (*p*-R-PhC(O)H, R = H, OMe, Me, Cl, NO_2). For these metal-peroxides a Hammett plot of log($^Rk_2/^Hk_2$) versus σ_p was linear with a positive ρ value.[5, 24-26] Thus, the results obtained indicated that the rate determining step in the reaction of **2** and *p*-R-C_6H_4C(H)O was nucleophilic attack of the peroxide ligand on the electrophilic carbonyl group of the aldehyde.

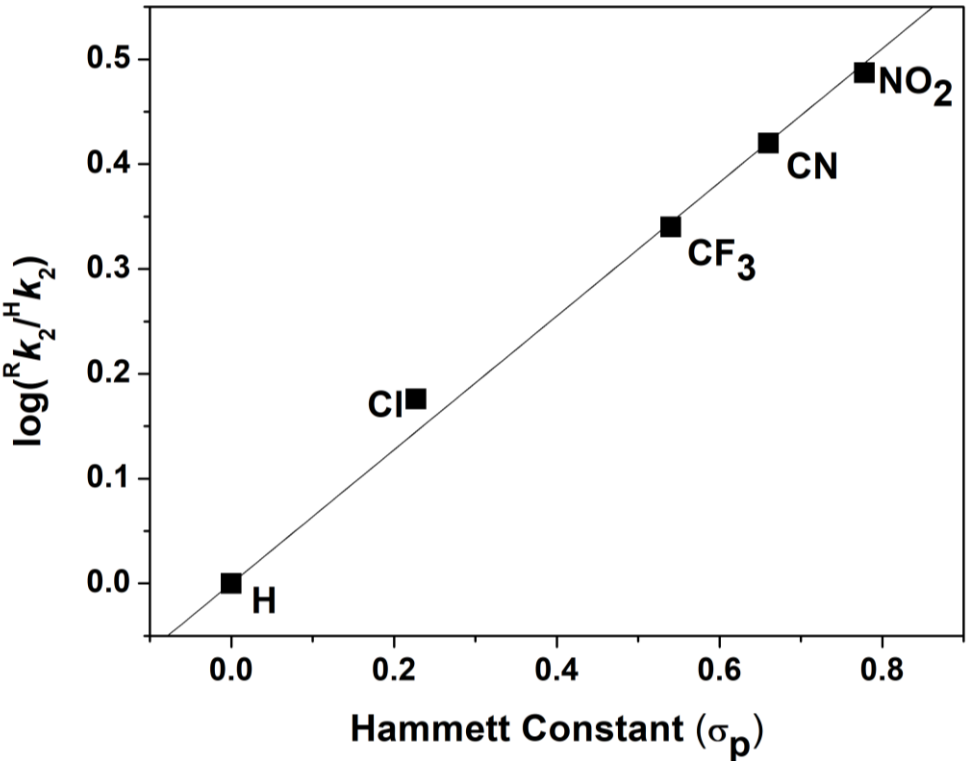

Figure 3.5. Hammett plot for the reaction between **5** and *p*-R-PhC(O)H (R = H, Cl, CF_3, CN, NO_2).

Previously reported peroxo-Mn^{III} complexes proved to be good deformylating agents. Notably, peroxo-Mn^{III} complexes supported by H_3bupa^{2-} (bis[(N'-tert-butylurealy)-N-ethyl]-(6-pivalamido-2-pyridylmethyl)amine),[2] H_2bpaa^- (N-[bis(6-pivalamido-2-pyridylmethyl)](N'-fluorophenylcarbamoylmethyl)amine),[3] TMC-derived (tetramethylcyclam)[4-6] and tetradentate N_4[7] ligands proved to be nucleophilic oxidants in their reaction with aldehydes such as PPA and CCA (Table 3.1). For PPA, at -90 °C, **5** displayed a relatively low k_2 compared to k_2 values determined for peroxo-Mn^{III} complexes supported by TMC ligands. It is important, however, to consider the different temperatures these measurements were performed at, -90 °C for **5**, and 20 °C for $[Mn^{III}(O_2)(12\text{-TMC})]^+$, $[Mn^{III}(O_2)(13\text{-TMC})]^+$, and $[Mn^{III}(O_2)(14\text{-TMC})]^+$. In contrast, **5** oxidised CCA at -90 °C, at rates comparable to those determined for $[Mn^{III}(O_2)(13\text{-TMC})]^+$ and $[Mn^{III}(O_2)(14\text{-TMC})]^+$ at significantly higher temperatures (10 °C, Table 3.1). Overall, **5** proved to be an effective deformylating reagent considering the low temperature the PPA/CCA reactivity was performed under.[4-6]

Table 3.1. Rate constants for PPA and CCA deformylation by peroxo-Mn^{III} complexes.

	PPA		CCA	
Complex	**k_2 [$M^{-1}s^{-1}$] (T [°C])**	**Ref**	**k_2 [$M^{-1}s^{-1}$] (T [°C])**	**Ref**
5	6.38×10^{-4} (-90)	This work	0.012 (-90)	This work
$[Mn^{III}(O_2)(12\text{-TMC})]^+$	4.4×10^{-2} (20)	[6]	$3.2(2) \times 10^{-1}$ (0)	[4]
$[Mn^{III}(O_2)(13\text{-TMC})]^+$	2.9×10^{-2} (20)	[6]	$2.0(2) \times 10^{-2}$ (10)	[5]
$[Mn^{III}(O_2)(14\text{-TMC})]^+$	4.3×10^{-2} (20)	[6]	4.0×10^{-2} (10)	[5]
$[Mn^{III}(O_2)(L^7py_2^{6\text{-Me}})]^+$			0.32 (-40)	[7]
$[Mn^{III}(O_2)(L^7py_2^{4\text{-Me}})]^+$			0.40 (-40)	[7]
$[Mn^{III}(O_2)(L^8py_2^{H})]^+$			0.19 (-40)	[7]

(TMC = tetramethylcyclam; 12-TMC = 1,4,7,10-tetramethyl-1,4,7,10-tetraazacyclododecane; 13-TMC = 1,4,7,10-tetramethyl-1,4,7,10-tetraazacyclotridecane; 14-TMC = 1,4,8,11-tetramethyl-1,4,8,11-tetraazacyclotetradecane; $L^7py_2^{6\text{-Me}}$ = 1,4-bis(6-methyl-2-pyridylmethyl)-1,4-diazepane; $L^7py_2^{4\text{-Me}}$ = 1,4-bis(4-methyl-2-pyridylmethyl)-1,4-diazepane; $L^8py_2^{H}$ = 1,5-bis(2-pyridylmethyl)-1,5-diazacyclooctane).

Therefore, it was determined that the rate-limiting step in this oxidation was nucleophilic attack of the peroxide core on the aldehyde substrate, using kinetic analysis. Our studies provided insight into the mechanism of O_2-activation in class Ib Mn_2 RNRs, and the highly reactive intermediates in their catalytic cycle.

3.4 Conclusions

We were interested in further understanding the chemistry of class Ib Mn_2 RNRs and the role $O_2^{\bullet-}$ plays in generating a high valent Mn_2 oxidant. We probed the reactivity of a synthetic Mn^{II}_2 complex (**4**) towards $O_2^{\bullet-}$ at -90 °C. This resulted in the formation of a new metastable species (**5**) that we postulate was a $Mn^{II}Mn^{III}$-peroxide complex. The metastable adduct displayed features typical of $Mn^{II}Mn^{III}$-peroxide complexes by electronic absorption spectroscopy, mass spectrometry, EPR and XANES. Furthermore, **5** was found to be an efficient nucleophilic deformylating reagent, exhibiting comparable reaction rates to previously reported mononuclear Mn-peroxide complexes. To the best of our knowledge this is the first example of a synthetic $Mn^{II}Mn^{III}$-peroxide entity displaying nucleophilic reactivity. We have thus demonstrated that a synthetic Mn^{II}_2 complex can be activated by $O_2^{\bullet-}$ to yield a $Mn^{II}Mn^{III}$-peroxide entity, that proved to be a nucleophilic oxidant. Thus, we prepared a second synthetic model for class Ib Mn_2 RNRs. Next chapter focusses on the reactivity of **5** with acids to investigate whether **5** can be activated by proton donors, further mimicking class Ib Mn_2 RNRs.

3.5 Experimental section

Materials

All reactions with air sensitive materials were conducted in a glove box under an N_2 atmosphere or under an inert atmosphere using standard Schlenk techniques. All reagents and solvents were purchased from commercial sources. Anhydrous N,N-dimethylformamide (DMF) was purchased and used without further purification. Anhydrous tetrahydrofuran, acetonitrile (CH_3CN), and diethyl ether (Et_2O) were dispensed through an Innovative Technology PureSolvEN solvent purification system and deoxygenated by purging with Ar.

N,N-bis(2-picolyl)amine and 2,6-bis(chloromethyl)-4-methylphenol were synthesised as previously described.[27, 28] The ligand HBPMP (2,6-bis[(bis(2-pyridylmethyl)amino)methyl]-4-methylphenol) was synthesised as previously reported.[29] Synthesis of complex **4** ($[Mn_2(O_2CCH_3)_2(BPMP)](ClO_4)$) was carried out as previously reported.[8] The product was recrystallised from CH_3CN/Et_2O to give crystals suitable for X-ray diffraction. A unit cell check confirmed the crystal structure already published. TEMPO-H (2,2,6,6-tetramethyl-piperidine-1-ol) was synthesized according to a published procedure.[30] $K^{18}O_2$ was prepared using a reported procedure.[31]

Caution: KO_2 and perchlorate salts of metal complexes are potentially explosive and must be handled with care and in small quantities. No problems were encountered during the synthesis of the above dimanganese complex.

Physical Methods

^1H NMR analysis was performed on a Bruker Avance III 400 MHz instrument. Electrospray ionisation (ESI) mass spectra were obtained using a micromass time of flight spectrometer (TOF), interfaced to a Waters 2690 HPLC, or by direct injection in the mass spectrometry instrument. Matrix assisted laser desorption ionisation (MALDI) mass spectra were acquired using a Maldi Q-TOF Premier MS System. Attenuated total reflectance Fourier transform infra-red spectra (ATR-FTIR) were recorded using a Perkin-Elmer Spectrum 100 Fourier Transform infrared spectrometer. Electronic absorption spectra were recorded in quartz cuvettes on a Hewlett Packard (Agilent) 8453 diode array spectrophotometer (190-1100 nm range) coupled to a liquid nitrogen cooled cryostat from Unisoku Scientific Instruments (Osaka, Japan). X-ray crystallography was performed on a Bruker APEX Kappa Duo system at 100 K using an Oxford Cobra cryosystem. EPR (Electron Paramagnetic Resonance) spectra were measured on a Bruker EMX spectrometer equipped with an Oxford Instruments CE 5396, ESR9 continuous

flow cryostat and an Oxford Instruments CE 5396 Precision temperature controller for the 77 K measurements. At 2 K the measurements were conducted on a Bruker EPP 300 spectrometer equipped with an Oxford ESR 910 liquid helium cryostat and an Oxford temperature controller. The quantification of the 2 K signals was relative to a $Cu(NO_3)_2$ spin standard in methanol.

XAS methods: The Mn-K-edge X-ray absorption data were collected on beam line 7-3 at SSRL (*Stanford Synchrotron Radiation Lightsource*, SLAC National Accelerator Lab, Menlo Park, CA, USA). Data were collected with the storage ring operating at ca. 3 GeV and 500 mA, using a LN_2 cooled Si (220), $\phi = 90^{\circ}$ double-crystal monochromator, calibrated by using the first inflection point of a Mn foil (6539 eV). The monochromator was detuned by ~50% for higher harmonic rejection. The fluorescence detector used was a Canberra 30-element Ge solid state detector, cooled with LN_2. All the measurements were performed at ambient pressure at ~17 K, gained by an Oxford Helium cryostat, cooled by closed-cycle He gas loop. The parameters used for the scans were the following: 10 eV steps/1 second integration time in the pre-edge region, 0.3 eV steps /2 second integration time in the edge, and 0.05 k steps in the EXAFS, with integration time increasing in a k^2-weighted fashion from 2 to 4 seconds over the energy range (k_{max} = 12.1k). The total detector counts were in the range between 3 k – 7 k, within the linear range of the detector electronics. Each sample was monitored for photoreduction. The high valent samples were found to be photoreduced by the X-rays and so only one scan was obtained per spot used on the high valent species. The samples were analysed as frozen samples using Delrin ® Mossbauer/XAS cups with sample windows of 4 mm x 10 mm. The high-valent samples were prepared as 1:9 acetonitrile/tetrahydrofuran solutions, while the low-valent samples were prepared as Nujol™ dispersions.

Elaboration of the XAS data, including averaging, background removal and normalization, was performed using Athena.[32] Edge energies were obtained by taking the first derivative of the rising edge. EXAFS analysis was carried out using Artemis,[32] which incorporates the IFEFFIT fitting engine and FEFF6 for *ab initio* EXAFS phase and amplitude parameters. Crystal structures were used for FEFF6 input to identify significant paths.

General procedure for the reaction of 4 with KO_2

A 1:9 CH_3CN/THF solution (1.5 mM) of complex **4** was prepared. In a quartz cuvette 2 mL of a 1.5 mM solution of complex **4** was cooled to -90 °C. KO_2 (15 mM) and 18-crown-6 (40 mM) were dissolved in DMF. 250 μL of this solution was added to the solution containing the Mn_2 complex (**4**). The reaction progress was monitored using electronic absorption spectroscopy.

EPR and XAS sample preparation

Samples for EPR analysis were prepared by transferring ~1 mL of the desired solution from the quartz cuvette at -90 °C, via a pre-cooled pipette into a pre-cooled EPR tube and immediately freezing it in liquid nitrogen. The EPR spectra were recorded at 2 K (9.64 GHz, 0.2 mW microwave power and a 1 mT field modulation amplitude). Samples for X-ray absorption spectroscopy (XAS) analysis were prepared by transferring solutions of **4** (1.5 mM, 1:9 acetonitrile/tetrahydrofuran) and **5** (acetonitrile/tetrahydrofuran) into XAS sample cups pre-cooled in a liquid nitrogen bath and immediately freezing them.

Reactivity studies

A solution of **5** in 1:9 acetonitrile/tetrahydrofuran at -90 °C was prepared using the above procedure. Substrates were added as concentrated acetonitrile/tetrahydrofuran solutions to solutions of **5** at -90 °C. The reactions were monitored using electronic absorption spectroscopy. To a solution of **5** (1.5 mM, 1:9 acetonitrile/ tetrahydrofuran) at -90 °C was added the appropriate substrate. For the aldehyde deformylation studies, the substrate was added as a 4 M concentrated acetonitrile/tetrahydrofuran solution of CCA (cyclohexanecarboxaldehyde), PPA (2-phenylpropionaldehyde) and *para*-substituted benzaldehydes. Reactions were monitored using UV-Vis spectroscopy. Each experiment was repeated 3 times, and the average k_{obs} was used for the determination of k_2. Post-reaction product analyses were performed by GC-MS analyses, allowing for identification of products.

The lifetime of **5** in 1:9 acetonitrile/tetrahydrofuran at -90 °C was measured by monitoring the decay of the absorbance features at λ_{max} = 440, 590 nm versus time, and it was calculated to be ~ 2 h.

References

[1] A. M. Magherusan, A. Zhou, E. R. Farquhar, M. Garcia-Melchor, B. Twamley, L. Que, Jr., A. R. McDonald, *Angew. Chem. Int. Ed. Engl.* **2018**, *57*, 918-922.

[2] R. L. Shook, W. A. Gunderson, J. Greaves, J. W. Ziller, M. P. Hendrich, A. S. Borovik, *J. Am. Chem. Soc.* **2008**, *130*, 8888-8889.

[3] R. L. Shook, A. S. Borovik, *Inorg. Chem.* **2010**, *49*, 3646-3660.

[4] M. S. Seo, J. Y. Kim, J. Annaraj, Y. Kim, Y. M. Lee, S. J. Kim, J. Kim, W. Nam, *Angew. Chem. Int. Ed.* **2007**, *46*, 377-380.

[5] J. Annaraj, J. Cho, Y. M. Lee, S. Y. Kim, R. Latifi, S. P. de Visser, W. Nam, *Angew. Chem. Int. Ed.* **2009**, *48*, 4150-4153.

[6] H. Kang, J. Cho, K. B. Cho, T. Nomura, T. Ogura, W. Nam, *Chem. Eur. J.* **2013**, *19*, 14119-14125.

[7] R. A. Geiger, S. Chattopadhyay, V. W. Day, T. A. Jackson, *Dalton Trans.* **2011**, *40*, 1707-1715.

[8] M. Suzuki, M. Mikuriya, S. Murata, A. Uehara, H. Oshio, S. Kida, K. Saito, *Bull. Chem. Soc. Jpn.* **1987**, *60*, 4305-4312.

[9] S. Blanchard, G. Blondin, E. Riviere, M. Nierlich, J. J. Girerd, *Inorg. Chem.* **2003**, *42*, 4568-4578.

[10] N. Saravanan, M. Sankaralingam, M. Palaniandavar, *RSC Advances* **2014**, *4*, 12000.

[11] R. M. Buchanan, K. J. Oberhausen, J. F. Richardson, *Inorg. Chem.* **1988**, *27*, 971-973.

[12] H. Diril, H. R. Chang, X. Zhang, S. K. Larsen, J. A. Potenza, C. G. Pierpont, H. J. Schugar, S. S. Isied, D. N. Hendrickson, *J. Am. Chem. Soc.* **1987**, *109*, 6207-6208.

[13] H. Diril, H. R. Chang, M. J. Nilges, X. Zhang, J. A. Potenza, H. J. Schugar, S. S. Isied, D. N. Hendrickson, *J. Am. Chem. Soc.* **1989**, *111*, 5102-5114.

[14] N. Cox, W. Ames, B. Epel, L. V. Kulik, L. Rapatskiy, F. Neese, J. Messinger, K. Wieghardt, W. Lubitz, *Inorg. Chem.* **2011**, *50*, 8238-8251.

[15] Y. Sano, A. C. Weitz, J. W. Ziller, M. P. Hendrich, A. S. Borovik, *Inorg. Chem.* **2013**, *52*, 10229-10231.

[16] F. Farges, *Phys. Rev. B* **2005**, *71*.

[17] R. E. Schreiber, H. Cohen, G. Leitus, S. G. Wolf, A. Zhou, L. Que, Jr., R. Neumann, *J. Am. Chem. Soc.* **2015**, *137*, 8738-8748.

[18] T. C. Weng, W. Y. Hsieh, E. S. Uffelman, S. W. Gordon-Wylie, T. J. Collins, V. L. Pecoraro, J. E. Penner-Hahn, *J. Am. Chem. Soc.* **2004**, *126*, 8070-8071.

[19] T. L. Stemmler, T. M. Sossong, Jr., J. I. Goldstein, D. E. Ash, T. E. Elgren, D. M. Kurtz, Jr., J. E. Penner-Hahn, *Biochemistry* **1997**, *36*, 9847-9858.

[20] T. Matsumoto, K. Ohkubo, K. Honda, A. Yazawa, H. Furutachi, S. Fujinami, S. Fukuzumi, M. Suzuki, *J. Am. Chem. Soc.* **2009**, *131*, 9258-9267.

[21] C. Arunkumar, Y. M. Lee, J. Y. Lee, S. Fukuzumi, W. Nam, *Chem. Eur. J.* **2009**, *15*, 11482-11489.

[22] J. S. Wright, E. R. Johnson, G. A. DiLabio, *J. Am. Chem. Soc.* **2001**, *123*, 1173-1183.

[23] T. Osako, K. Ohkubo, M. Taki, Y. Tachi, S. Fukuzumi, S. Itoh, *J. Am. Chem. Soc.* **2003**, *125*, 11027-11033.

[24] J. Cho, R. Sarangi, J. Annaraj, S. Y. Kim, M. Kubo, T. Ogura, E. I. Solomon, W. Nam, *Nat. Chem.* **2009**, *1*, 568.

[25] Y. Jo, J. Annaraj, M. S. Seo, Y. M. Lee, S. Y. Kim, J. Cho, W. Nam, *J. Inorg. Biochem.* **2008**, *102*, 2155-2159.

[26] J. Cho, R. Sarangi, H. Y. Kang, J. Y. Lee, M. Kubo, T. Ogura, E. I. Solomon, W. Nam, *J. Am. Chem. Soc.* **2010**, *132*, 16977-16986.

[27] M. A. Raycroft, C. I. Maxwell, R. A. Oldham, A. S. Andrea, A. A. Neverov, R. S. Brown, *Inorg. Chem.* **2012**, *51*, 10325-10333.

[28] A. S. Borovik, V. Papaefthymiou, L. F. Taylor, O. P. Anderson, L. Que, *J. Am. Chem. Soc* **1989**, *111*, 6183-6195.

[29] S. Torelli, C. Belle, I. Gautier-Luneau, J. L. Pierre, E. Saint-Aman, J. M. Latour, L. Le Pape, D. Luneau, *Inorg. Chem.* **2000**, *39*, 3526-3536.

[30] K. S. Chan, X. Z. Li, W. I. Dzik, B. de Bruin, *J. Am. Chem. Soc.* **2008**, *130*, 2051-2061.

[31] P. J. Donoghue, A. K. Gupta, D. W. Boyce, C. J. Cramer, W. B. Tolman, *J. Am. Chem. Soc.* **2010**, *132*, 15869-15871.
[32] B. Ravel, M. Newville, *J. Synchrotron Rad.* **2005**, *12*, 537-541.

Chapter 4

Activation of the $Mn^{II}Mn^{III}$-peroxide core

The 2 K EPR measurements were performed by Ms. Subhasree Kal (University of Minnesota, Minneapolis) and the 77 K EPR measurements were done by Ms. Marta Lovisari (Trinity College Dublin).

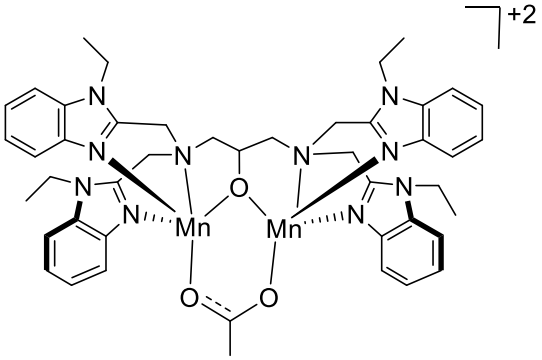

$[Mn^{II}Mn^{II}(O_2CCH_3)((N\text{-}Et\text{-}HPTB)]^{2+}$

1

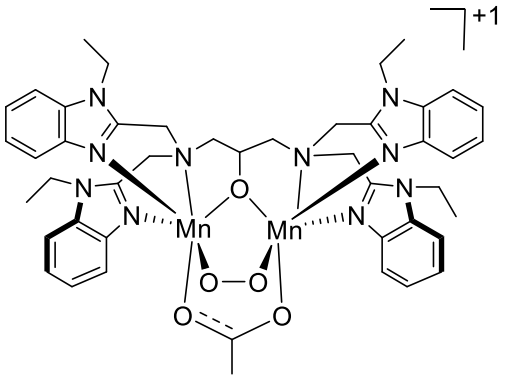

$[Mn^{II}Mn^{III}(O_2)(O_2CCH_3)((N\text{-}Et\text{-}HPTB)]^{1+}$

2

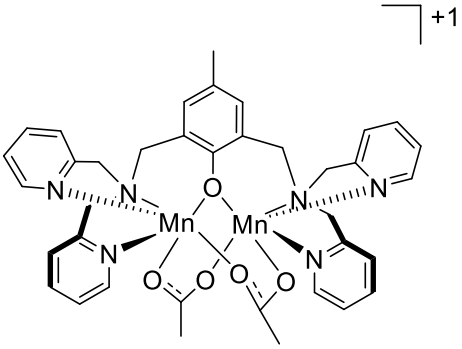

$[Mn^{II}Mn^{II}(O_2CCH_3)_2(BPMP)]^{1+}$

4

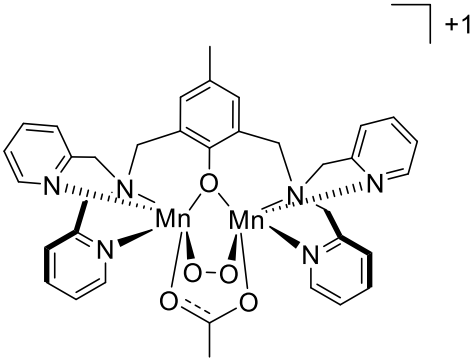

$[Mn^{II}Mn^{III}(O_2)(O_2CCH_3)(BPMP)]^{1+}$

5

4.1 Introduction

The first example of a synthetic $Mn^{II}Mn^{III}$-peroxide complex (**2**) supported by a benzimidazole ligand (N,N,N',N'-tetrakis(2-(1-ethylbenzimidazolyl))-2-hydroxy-1,3-diaminopropane (= N-Et-HPTB)) was reported in chapter 2.[1] However, the $Mn^{II}Mn^{III}$-peroxide unit in **2** was unreactive at -40 °C in CH_3CN, and it was only capable of oxidising ferrocene and weak O-H bonds upon activation with proton donors.[1] This provided experimental support into the postulated biochemistry of class Ib Mn_2 RNRs, where both $O_2^{\bullet-}$ and a proton were required to access a high valent Mn oxidant via a $Mn^{II}Mn^{III}$-hydroperoxide intermediate.[2]

We surmised that changing the ligand system of adduct **2**, could improve the reactivity of the peroxide complex. Furthermore, a second peroxo-$Mn^{II}Mn^{III}$ complex (**5**) was prepared upon reaction of a Mn^{II}_2 complex (**4**) supported by a polypyridine ligand (2,6-bis[(bis(2-pyridylmethyl)amino)methyl]-4-methylphenol (= HBPMP), chapter 3) with $O_2^{\bullet-}$. While the peroxo-$Mn^{II}Mn^{III}$ adduct (**2**) described in chapter 2 was a poor nucleophilic and electrophilic oxidant, the second peroxo-$Mn^{II}Mn^{III}$ complex (**5**) reported in chapter 3 proved to be a good nucleophilic oxidant in aldehyde deformylation. Moreover, **5** represented the first example of a nucleophilic peroxo-$Mn^{II}Mn^{III}$ species.

As described in the introduction, a series of mononuclear peroxo-Mn^{III} have been prepared in the literature.[3-14] These complexes have been shown to react with acids, by protonation, forming hydroperoxo species.[15, 16] For instance, the first example of a hydroperoxo-Mn^{III} complex was reported by Nam and co-workers in 2014,[15] upon treatment of a $[Mn^{III}(O_2)TMC]^+$ (where TMC = 1,4,8,11-tetramethyl-1,4,8,11-tetraazacyclotetradecane) adduct with $HClO_4$ at -40 °C in CH_3CN. Recently, another mononuclear hydroperoxo-Mn^{III} complex was reported upon reaction of a $[Mn^{III}(O_2)(13\text{-TMC})]^+$ (where 13-TMC =1,4,7,10-tetramethyl-1,4,7,10-tetraazacyclotridecane) complex with either $HClO_4$ or trifluoromethanesulfonic acid (= CF_3SO_3H) at -40 °C in CH_3CN.[16] The hydroperoxo-Mn^{III} species was shown to be an electrophilic oxidant in its reaction with *para*-substituted thioanisoles.[16]

We postulated that the mixed valent peroxide adduct **5** could be reactive towards acids. Indeed, the previously reported peroxo-$Mn^{II}Mn^{III}$ complex (**2**)[1] and mononuclear peroxo-Mn^{III} complexes were susceptible to proton donors.[15, 16]

Furthermore, the Mn^{II}_2 core of class Ib Mn_2 RNRs had been shown to react with superoxide in the presence of a proton source to form a postulated hydroperoxo-$Mn^{II}Mn^{III}$ species.[2] Additionally O-O bond cleavage of the mixed valent hydroperoxo-Mn_2 species was proposed

to generate a $Mn^{III}(\mu\text{-}OH)(\mu\text{-}O)Mn^{IV}$ unit.[2] This high valent species was characterised by EPR spectroscopy. Consequently, upon activation of peroxide-Mn systems with a proton source, either hydroperoxo-Mn adducts or high valent $Mn^{III}Mn^{IV}$ species could form. As described above, recently, two hydroperoxo-Mn^{III} species have been characterised.[15, 16] Many synthetic high valent $Mn^{III}Mn^{IV}$ complexes have also been reported,[17-30] by reaction of the precursor Mn^{II} complex with either $KMnO_4$,[26] oxone,[27] H_2O_2 as an oxidant[23, 29, 31, 32] or by electrochemical oxidation.[24] Such complexes have also been postulated as intermediates in the catalytic cycle of class Ib Mn_2 RNRs. Moreover, the acid reactivity of the peroxo-$Mn^{II}Mn^{III}$ (**5**) complex would provide further insight into the catalytic cycle of class Ib Mn_2 RNRs.

Furthermore, gaining an understanding of the decay product of the mixed valent peroxo-Mn_2 complex (**5**) is essential. For example, Anxolabehere-Mallart *et at*. reported a $[(L)Mn^{II}]^{2+}$ (where L = N-methyl-N,N',N'-tris(2-pyridylmethyl)ethane-1,2-diamine) complex to react with H_2O_2 at low temperature, in acetonitrile medium to form a peroxo species ($[Mn^{III}(O_2)(L)]^+$), that was characterised by UV-Vis and EPR spectroscopies and ESI-mass spectrometry.[33] In an aqueous basic medium, the peroxo-Mn^{III} complex decayed to a bis(μ-oxo)$Mn^{III}Mn^{IV}$ species, while in an acidic medium, no oxo bridges were observed, but ligand oxidation was detected by X-ray crystallography.[33] Another example where a peroxo-Mn^{III} complex converted to a bis(μ-oxo)$Mn^{III}Mn^{IV}$ species was reported by Jackson and co-workers.[19] Upon treatment of $[Mn^{II}(N4py)(OTf)](OTf)$ (where N4py = N,N'-bis(2-pyridylmethyl)-N-bis(2-pyridyl)methylamine and OTf = trifluoromethanesulfonate) with $O_2^{\bullet-}$ at -40 °C in acetonitrile medium, the formation of a $[Mn^{III}(O_2)(N4py)]^+$ was observed.[19] The peroxo-Mn^{III} species was only stable at low temperature. The product obtained upon thermal decay of the $[Mn^{III}(O_2)(N4py)]^+$ species was found to be a bis(μ-oxo)$Mn^{III}Mn^{IV}$ complex.[19] The high valent species was characterised by electronic absorption and EPR spectroscopies and X-ray crystallography. Therefore, high valent $Mn^{III}Mn^{IV}$ adducts were found to be the thermal decay products of peroxo-Mn^{III} species.[19, 33]

In this chapter, the thermal decay of the peroxo-$Mn^{II}Mn^{III}$ adduct (**5**) is investigated. Moreover, the reactivity of adduct **5** towards a series of acids ($HClO_4$, HBF_4, HCl and *para*-toluene sulfonic acid (*p*TsOH)) is also described. We present investigations into the thermal decay of **5**, the addition of different equivalents of acid to **5** and monitor the reactions by UV-Vis and EPR spectroscopies.

4.2 Thermal decay of 5

At -90 °C, **5** decayed slowly ($t_{1/2}$ ~ 2 hours, chapter 3), while at room temperature it decayed within 3 minutes. The peroxide species **5** was thermally unstable above -80 °C, decaying within minutes upon warming. Since we were also interested in the thermal decay product of **5**, the electronic absorption spectrum and the 2 K EPR spectrum of the decay product of **5** were measured. After being left at room temperature for 15 mins, solutions of **5** changed color from yellow to pale brown (forming a new species - **6**). The electronic absorption spectrum of adduct **6** exhibited a broad absorbance band in the visible region (Figure 4.1). The solution of complex **5** was also warmed up in the UV-Vis spectrometer from -90 °C to -50 °C, -20 °C, and 0 °C (Figure A.36) respectively, but no intermediates were observed between the electronic absorption spectrum of **5** (Figure 3.1, chapter 3) and that of **6** (Figure 4.1, left).

Adduct **6** was characterized by EPR spectroscopy. The EPR spectrum of **6** at 2 K exhibited a 16-line signal centered at g ~ 2.02 (Figure 4.1, right), quite different from the one observed for **5** at 2 K (g ~ 1.96, 24-line signal, Figure 3.3, chapter 3). Besides the difference in the number of EPR signals exhibited by complexes **5** and **6**, the spectrum of **6** also displayed a narrower spectral width when compared to **5**. Thus, complex **5** and its thermal decay (adduct **6**) had different EPR features. As discussed in the introduction, the 16-line EPR signal observed for **6** was characteristic of mixed valent $Mn^{III}Mn^{IV}$ complexes previously reported in the literature.[30, 31, 34-37] An example included the mixed valent $Mn^{III}Mn^{IV}$ complex, $[(pmap)Mn^{III}(\mu\text{-}O)_2Mn^{IV}(pmap)](ClO_4)_3$ (where pmap = bis[2-(2-pyridyl)ethyl]-2-pyridylmethylamine) (see introduction, section 1.5.2), whose EPR spectrum measured at 100 K in N-methylformamide exhibited the characteristic 16-line signal centred around g = 2.003.[34] Likewise, a frozen dichloromethane solution of $[Mn_2(\mu\text{-}O)_2(bpy)_2(Ar^{tol}CO_2)_2](ClO_4)$ at 4 K (see introduction, section 1.5.2) also displayed a 16 line signal centred at g ~ 2.[30] Therefore, complex **6** exhibited EPR signals characteristic of mixed valent $Mn^{III}Mn^{IV}$ complexes.

As mentioned above, adduct **6** exhibited a broad absorbance feature in the visible region (Figure 4.1). Importantly, a previously reported $Mn^{III}Mn^{IV}$ complex ($[Mn_2(\mu\text{-}O)_2(bpy)_2(Ar^{tol}CO_2)_2](ClO_4)$ complex where bpy = 2,2'-bypiridine and $Ar^{tol}CO_2^-$ = 2,6-di(p-tolyl)benzoate)[30] displayed an electronic absorption spectrum similar to that observed for **6**, with only a single weak shoulder at ~760 nm.[30] However, the majority of previously reported mixed valent $Mn^{III}Mn^{IV}$ complexes displayed absorption band between 520-570 nm assigned to a *d-d* transition band while bands between 590-700 nm were attributed to a O to Mn charge transfer band (see chapter 1, section 1.5.2).[17, 18, 38, 39] The slightly different electronic features

observed for the ($[Mn_2(\mu\text{-}O)_2(bpy)_2(Ar^{tol}CO_2)_2](ClO_4)$) complex when compared to the other $Mn^{III}Mn^{IV}$ complexes was due to the two metal centres being bridged simultaneously by a pair of oxo groups and a pair of carboxylate groups.[30] Thus, the absorbance features observed for compound **6** were comparable to those previously observed for a mixed valent $Mn^{III}Mn^{IV}$ complex.[30] Additionally, further characterisation of adduct **6** must be done using mass spectrometry. This will provide more insight into the structure of **6**.

Consequently, the results obtained by EPR and electronic absorption spectroscopy for complex **6** provided evidence for its assignment as a mixed valent $Mn^{III}Mn^{III}$ entity. This provided a compelling result, as one of the postulated intermediates in the catalytic cycle of class Ib Mn_2 RNRs was a mixed valent $Mn^{III}Mn^{IV}$ species.[2] Stubbe and co-workers have recently shown that the Mn^{II}_2 core from *B. subtilis* class Ib Mn_2 RNRs reacted with superoxide in the presence of a proton source to form a postulated hydroperoxo-$Mn^{II}Mn^{III}$ intermediate.[2] O-O Bond cleavage in this adduct resulted in the formation of a $Mn^{III}(\mu\text{-}OH)(\mu\text{-}O)Mn^{IV}$, that was proposed to oxidise tyrosine to tyrosyl radical.[2] The tyrosyl radical was then involved in conversion of ribonucleotides to deoxyribonucleotides. Therefore, it would be interesting to investigate whether adduct **6** would be capable to perform any oxidation reactions (hydrogen atom abstraction (= HAA) or oxygen atom transfer (= OAT) reactivity), further mimicking the catalytic cycle of class Ib Mn_2 RNRs.

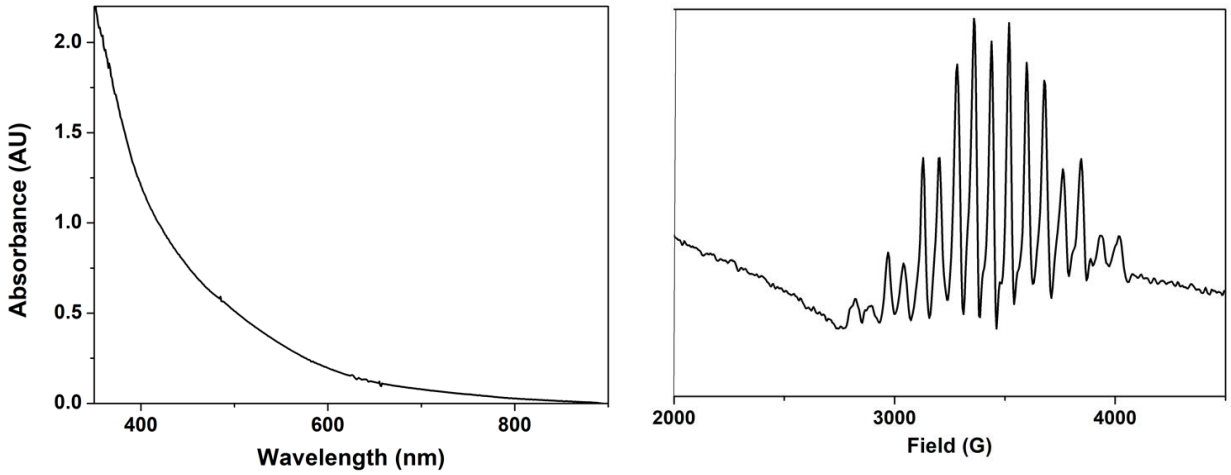

Figure 4.1. Left: Electronic absorption spectrum of **6** (thermal decay of **5**) at -90 °C in 1:9 CH_3CN/THF (path length = 1 cm). Right: Perpendicular mode EPR spectrum of **6** at 2 K (9.64 GHz, 0.2 mW microwave power).

4.3 Reactivity studies of 5 with strong acids

4.3.1 $HClO_4$ and HBF_4 addition to 5

Addition of a strong acid (8 equivalents of perchloric acid ($HClO_4$) or tetrafluoroboric acid (HBF_4)) to a solution of **5** (peroxo-$Mn^{II}Mn^{III}$) in 1:9 CH_3CN/THF, at -90 °C resulted in formation of a new species (**7**). Adduct **7** displayed an electronic absorption spectrum with three electronic absorption features at λ_{max} = 400, 510, 745 nm (Figure 4.2) and a lifetime of ~1 h at -90 °C. Lower equivalents of $HClO_4$ were added to **5** but the highest yield of complex **7** by electronic absorption spectroscopy was obtained with 8 equivalents of $HClO_4$.

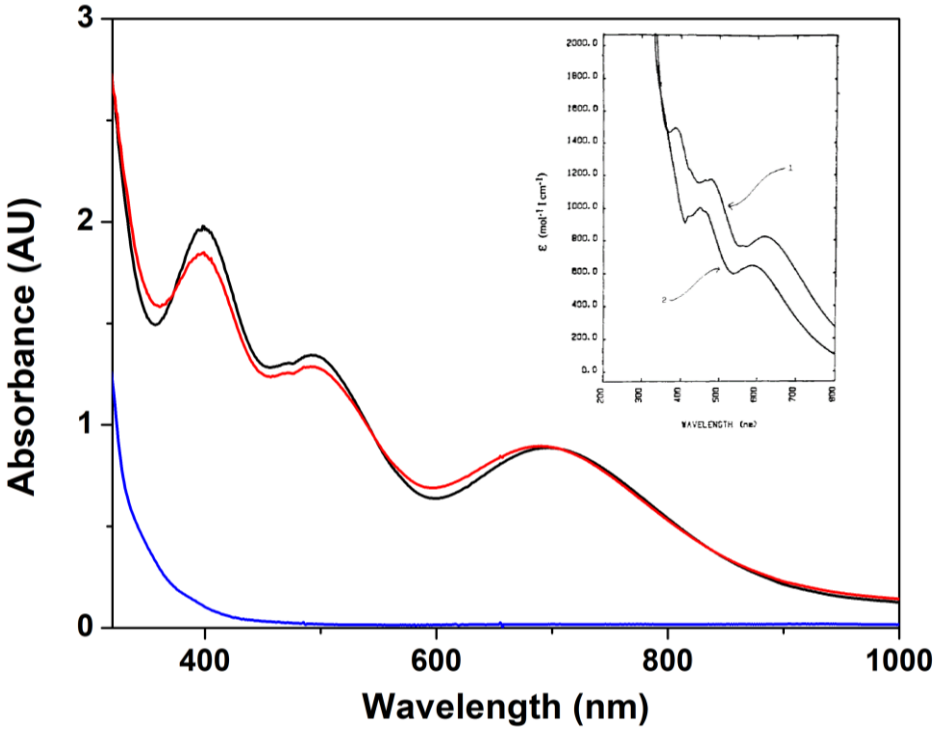

Figure 4.2. Comparison of electronic absorption spectra upon addition of $HClO_4$ (8 equivalents, 0.25 M, black trace) and HBF_4 (8 equivalents, 0.25 M, red trace) to **5** at -90 °C in 1:9 CH_3CN/THF, with that of $Mn(ClO_4)_2.6H_2O$ (1 mM, blue trace) (path length = 1 cm). Inset displays the electronic absorption spectrum of $[Mn^{II}Mn^{III}(O_2CCH_3)_2(BPMP)](ClO_4)_2$ (trace represented by 1 in the spectrum) in CH_3CN previously reported by Hendrickson and co-workers.[40]

The electronic absorbance features observed for **7** were comparable to those observed for mixed valent $Mn^{II}Mn^{III}$ complexes.[37, 40] As described in the introduction (section 1.5.3), previously reported $Mn^{II}Mn^{III}$ complexes supported by phenolate ligands in the literature exhibited slight differences in the electronic absorption spectra, having characteristic absorption bands between 360-400 nm, that have been assigned to phenoxo-Mn^{III} ligand to metal charge transfer (LMCT)

band while electronic absorption bands between 450-480 nm and 580-630 nm have been attributed to *d-d* transitions of the Mn^{III} ions (chapter 1, Table 1.7).[37, 40] More importantly, the mixed valent form of complex **4** ($[Mn^{II}Mn^{III}(O_2CCH_3)_2(BPMP)](ClO_4)_2$) reported by Hendrickson and co-workers displayed electronic absorption bands at λ_{max} = 427, 478 and 620 nm (Figure 4.2, inset).[40] The energies of the absorbance bands displayed by $[Mn^{II}Mn^{III}(O_2CCH_3)_2(BPMP)](ClO_4)_2$ were slightly shifted to those obtained for species **7**, obtained upon treatment of the peroxo-$Mn^{II}Mn^{III}$ adduct (**5**) with strong acids (Figure 4.2). Thus, complex **7** was not the same species as the mixed valent $[Mn^{II}Mn^{III}(O_2CCH_3)_2(BPMP)](ClO_4)_2$ complex. Comparison of the absorbance bands of complex **7** with those of $[Mn^{II}Mn^{III}(O_2CCH_3)_2(BPMP)](ClO_4)_2$, let us assign complex **7** as a new $Mn^{II}Mn^{III}$ species. A postulated pathway for the formation of the new species **7** was given below. We proposed that upon addition of a strong acid to **5**, the peroxo O-O bond cleaved to form H_2O_2 and another $Mn^{II}Mn^{III}$ adduct (**7**, Scheme 4.1).

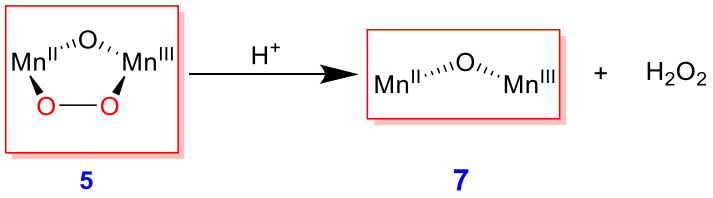

Scheme 4.1. Addition of a strong acid (H^+ = $HClO_4$, HBF_4) to **5** forming a new $Mn^{II}Mn^{III}$ species (**7**) and H_2O_2.

4.3.1.1 Characterisation of complex 7

Direct cold injection mass spectrometry experiments on complex **7** were performed. However, even though the characteristic isotopic pattern of chlorine was present in the mass spectrometry data, we were unable to assign any of the peaks.

The putative $Mn^{II}Mn^{III}$ species (**7**) was also characterised by EPR spectroscopy. EPR analysis of **7**, at 77 K exhibited a 6 multiline signal centred at $g \sim 2$ (Figure 4.3). This signal was characteristic of free Mn^{II}.[41-44] The EPR spectrum of **7** was also measured at 30 and 2 K and the same 6 multiline signal was observed. Saturation of the EPR spectrum of **7** by the presence of the Mn^{II} entity was observed at all temperatures used, 77, 30 and 2 K. Different attenuations at all three temperatures were used to avoid the saturation of the EPR spectrum by the Mn^{II} signal but it was unsuccessful. Even by changing the temperature and the attenuation of the EPR spectrum of species **7**, the saturation of the EPR spectrum by the Mn^{II} signal was still observed. Thus, the formation of free Mn^{II} ions (6 multiline EPR signal), upon addition of a

strong acid to **5**, could be ascribed to de-metalation, however the mechanism of this reaction is unclear.

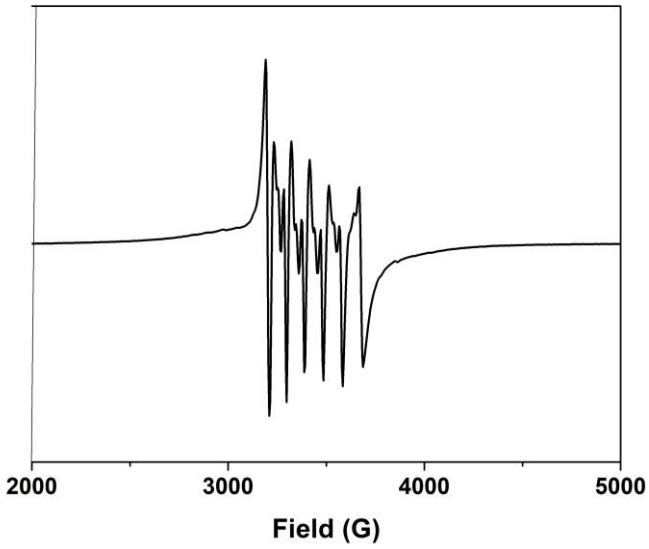

Figure 4.3. Perpendicular mode EPR spectrum of **7** at 2 K (black trace, obtained from the reaction of **5** and 8 equivalents $HClO_4$ in 1:9 CH_3CN/THF) (9.64 GHz, 0.2 mW microwave power).

The 2 K EPR spectrum of $Mn(ClO_4)_2.6H_2O$ was also measured under exactly the same conditions as that of species **7** at 2 K. The two spectra were overlaid, and they matched perfectly (Figure A.37). Since a known concentration of the Mn salt was used (2.25 mM) for measuring the EPR spectrum, we wanted to use it to get a yield of the Mn^{II} ions formed. However, this was not possible because of saturation of the EPR spectrum by the Mn^{II} signal. Thus, the yield of Mn^{II} present in species **7** could not be obtained at either 2 or 30 K. Furthermore, an EPR spectrum of a Cu salt ($Cu(NO_3)_2.3H_2O$) was measured under the same conditions as those of **7** (Figure A.38). The higher temperature (30 K) was used for the quantification to avoid saturating the Cu standard. Even using the Cu as a standard, a yield of the Mn^{II} signal could not be measured. Since the EPR spectrum of species **7** was saturated by the Mn^{II} signal, a yield for the formation of free Mn^{II} was not obtained.

Therefore, the addition of a strong acid ($HClO_4$/HBF_4) to **5** resulted in the formation of a new species **7**. Adduct **7** exhibited electronic absorption features comparable to previously reported $Mn^{II}Mn^{III}$ complexes supported by polydentate ligands.[37, 40] The EPR spectrum of **7** was saturated by a 6 multiline signal characteristic of a Mn^{II} entity, and we were unable to determine the presence of a $Mn^{II}Mn^{III}$ species. However it is important to notice that the electronic absorption spectrum of **7** (Figure 4.2, black and red trace) was different to the one observed for a Mn^{II} complex ($Mn(ClO_4)_2.6H_2O$, Figure 4.2, blue trace). Thus, the Mn^{II} signal could be

attributed to a de-complexation, although further studies must be done to determine the reaction mechanism.

4.3.2 HCl addition to 5

Another strong acid that **5** was reacted with, was hydrochloric acid (HCl, 8 equivalents, 0.25 M) in 1:9 CH_3CN/THF at -90 °C. The formation of a new species was observed by electronic absorption spectroscopy with λ_{max} = 446, 555 and 720 nm (Figure 4.4), which had electronic absorbance features slightly different to **7** (**5** + HCl, λ_{max} = 400, 510, 745 nm) (Figure 4.5). We postulated that Cl^- coordinated to one of the Mn centres and that caused the shift in the absorbance energies when compared to **7** (Figure 4.5). Moreover, these features were also in the range for a mixed valent $Mn^{II}Mn^{III}$ species with absorbance bands between 580-630 nm (555 nm) attributed to *d-d* transitions of the Mn^{III} ion.[37, 40] Furthermore, the absorbance bands obtained upon addition of HCl to **5** were also similar, but not identical to those obtained for the mixed valent $[Mn^{II}Mn^{III}(O_2CCH_3)_2(BPMP)](ClO_4)_2$ complex (λ_{max} = 427, 478 and 620 nm).[40] Thus, treatment of **5** with HCl resulted in the formation of a new adduct, that displayed features typical of a mixed valent $Mn^{II}Mn^{III}$ species.

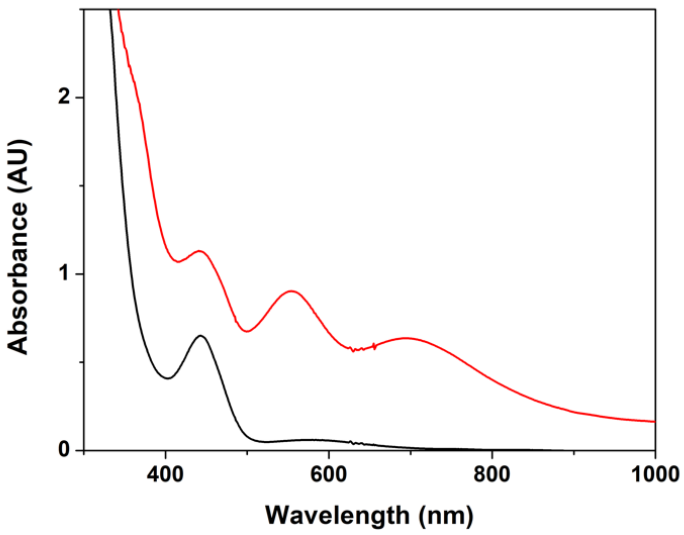

Figure 4.4. Electronic absorption spectra upon addition of HCl (8 equivalents, 0.25 M, red trace) to **5** (black trace) in 1:9 CH_3CN/THF at -90 °C (path length = 1 cm).

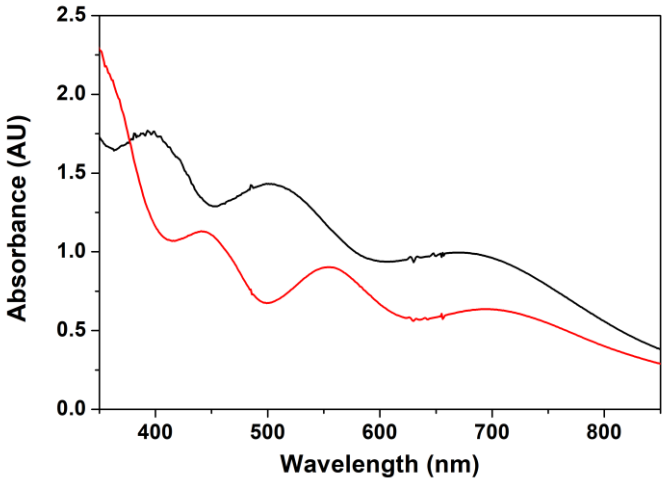

Figure 4.5. Comparison of electronic absorption spectra obtained upon reaction of **5** with $HClO_4$ (forming **7**, 8 equivalents, 0.25 M, black trace) and HCl (8 equivalents, 0.25 M, red trace) in 1:9 CH_3CN/THF at -90 °C (path length = 1 cm).

EPR characterisation of the species obtained upon HCl addition to **5** exhibited a 6-multiline signal centred at g ~ 2 (Figure 4.6), the same EPR signal observed for **7** (reaction of adduct **5** with 8 equivalents $HClO_4$/HBF_4). As mentioned above, the EPR signal was saturated by the presence of a Mn^{II} species,[41-44] thus we could not asses the yield of Mn^{II} or the presence of the $Mn^{II}Mn^{III}$ species.

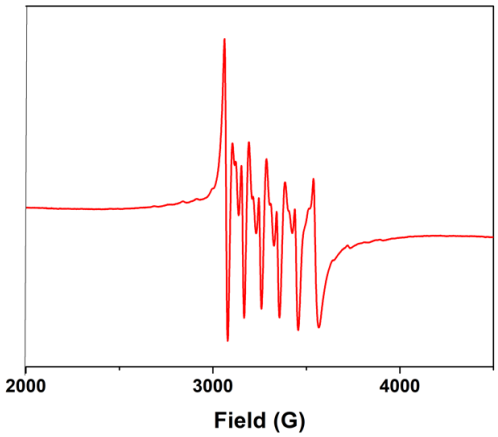

Figure 4.6. EPR spectrum after addition of HCl (8 equivalents, 0.25 M) to **5** measured at 77 K (9.21 GHz, 2 mW microwave power).

The post reaction mixture upon HCl addition to **5** was also characterised by mass spectrometry. The data obtained showed characteristic isotopic patterns of chlorine but unfortunately, we were unable to assign the peaks.

4.3.3 Cl^- addition to 7

Since a large excess (8 equivalents) of HCl was added to **5**, and Cl^- is a good ligand we were interested to see whether the Cl^- anion could influence the reaction between **5** and acids. Thus, HCl was added (8 equivalents, 0.2 M) to **7** (**5** + $HClO_4$) and a shift in the electronic absorption features corresponding to **7** (λ_{max} = 400, 510, 745 nm) to those corresponding to species formed upon addition of HCl to **5** (λ_{max} = 446, 555 and 720 nm) (Figure 4.7, left) was observed. If instead of HCl, tetrabutylammonium chloride (TBACl, 6 equivalents, 0.12 M) was used as a Cl^- source and added to **7**, the same changes in the electronic absorption spectra were observed, leading to the formation of **5** + HCl (Figure 4.7, right). Thus, the Cl^- anion was likely bound to one of the Mn centres when it was found in a large excess in the reaction mixture. Moreover, the addition of different Cl^- sources to **7** (**5** + $HClO_4$) resulted in the formation of the same species formed upon addition of HCl to **5**. This added further evidence that the Cl^- anion was coordinated to one of the Mn centres.

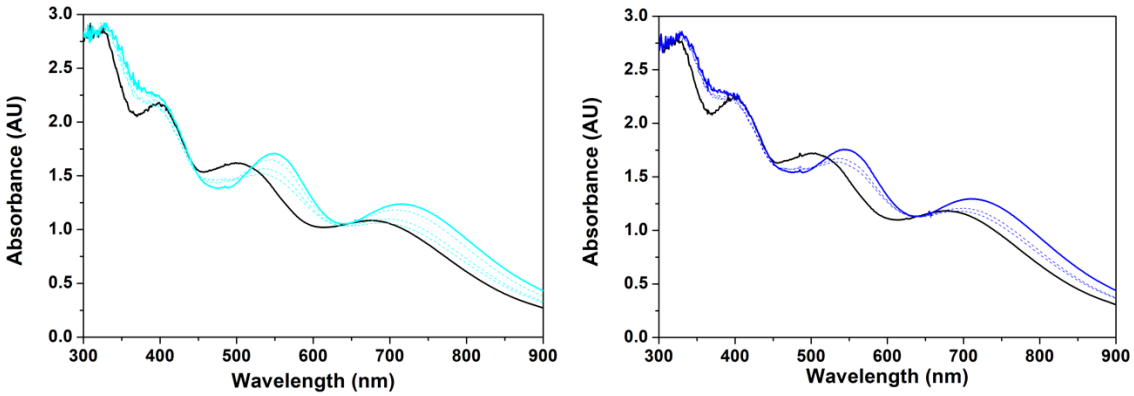

Figure 4.7. Electronic absorption spectra after addition of HCl (8 equivalents, 0.25 M, green trace, left figure) and TBACl (6 equivalents, 0.12 M, blue trace, right figure) to **7** (**5** + $HClO_4$, solid black trace) in 1:9 CH_3CN/THF at -90 °C (path length = 1 cm).

In conclusion, addition of strong acids ($HClO_4$/HBF_4) to **5** resulted in the formation of adduct **7**. Complex **7** was postulated as a $Mn^{II}Mn^{III}$ species based on electronic absorption features comparable to other mixed valent $Mn^{II}Mn^{III}$ complexes.[37, 40] The EPR spectrum of **7** was saturated by a Mn^{II} signal, no yield of the Mn^{II} species was obtained and the presence of a $Mn^{II}Mn^{III}$ species by EPR was not determined. Moreover, the addition of Cl^- sources to **7** (**5** + $HClO_4$) resulted in the formation of the species formed upon addition of HCl to **5**. Possibly the Cl^- anion coordinated to one of the Mn centres, causing slight changes in the electronic absorption spectra of species **7** and the addition of HCl to **5**. Furthermore, the reactivity of the putative $Mn^{II}Mn^{III}$ species (**7**) was probed, as described below.

4.4 Reactivity studies of 7 (5 + $HClO_4$)

Complex **7** was postulated as a new $Mn^{II}Mn^{III}$ species based on the electronic absorption maxima observed in the absorbance bands when compared to the mixed valent $[Mn^{II}Mn^{III}(O_2CCH_3)_2(BPMP)](ClO_4)_2$ complex reported by Hendrickson and co-workers[40] and other $Mn^{II}Mn^{III}$ complexes supported by polydentate ligands.[37, 40] We wanted to investigate its reactivity with substrates to see whether **7** was an electrophilic or nucleophilic oxidant.

The electronic absorption spectrum of adduct **7** (at -90 °C in 1:9 CH_3CN/THF) was unaffected by the addition of triphenylphosphine (PPh_3) or cyclohexene, suggesting that **7** was not capable of oxidising these substrates and thus incapable of OAT reactions. Furthermore, **7** was exposed to substrates containing weak C–H bonds (including 1-methyl-1,4-cyclohexadiene (C–H bond dissociation energy (= BDE) = 77 kcal/mol),[45] dihydroanthracene ($BDE_{C\text{-}H}$ = 78 kcal/mol),[46] and 2,4-di-*tert*-butylphenol ($BDE_{C–H}$ = 82 kcal/mol))[47, 48] but did not react. This demonstrated that **7** was not a capable HAA reagent. Thus, at -90 °C, **7** was not an electrophilic oxidant, being incapable of either OAT or HAA. Furthermore, **7** showed no reaction with aldehydes, indicating it was also a poor nucleophilic oxidant.

To gain further insight into the nature of species **7** and its reactivity, bases (triethylamine (= Et_3N), 2,6-lutidine, and tetrabutylammonium hydroxide (= TBAOH)) were added to **7** in 1:9 CH_3CN/THF at -90 °C. Et_3N was used as a base, but it could also act as a weak reducing agent. Addition of Et_3N (60 equivalents, 1 M) to a solution of **7** resulted in the disappearance of the electronic absorbance features associated with **7**, with the formation of a new species with a broad absorption in the visible region (Figure 4.8). Even if more equivalents of Et_3N were added, the same changes in the electronic absorption spectrum of **7** were observed. Further characterisation of the product obtained upon treatment of **7** with Et_3N must be done.

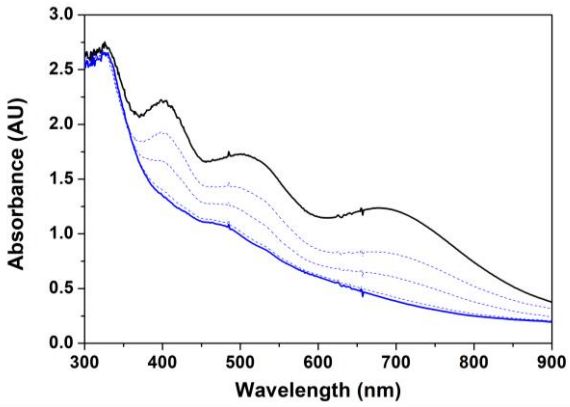

Figure 4.8. Electronic absorption spectra showing changes after addition of Et_3N (60 equivalents, 1 M, blue trace) to **7** (black trace) in 1:9 CH_3CN/THF at -90 °C (path length = 1 cm).

The addition of 2,6-lutidine (100 equivalents, 1 M, Figure 4.9, left) and TBAOH (100 equivalents, 1 M, Figure 4.9, right) to **7** resulted in the decay of the electronic absorbance features associated with **7** and the formation of new electronic absorption features (red traces, Figure 4.9). Thus, base addition to **7** formed new species by electronic absorption spectroscopy, that must be further characterised by EPR and mass spectrometry.

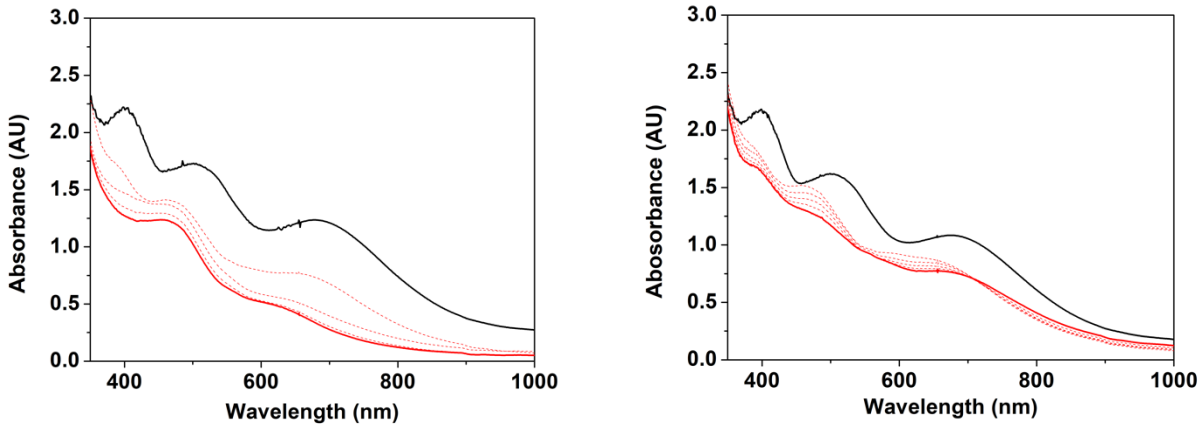

Figure 4.9. Electronic absorption spectra showing changes after addition of 2,6-lutidine (100 equivalents, 1 M, solid red trace, left) and TBAOH (100 equivalents, 1 M, solid red trace, right) to **7** (black trace) in 1:9 CH_3CN/THF at -90 °C (path length = 1 cm).

Ferrocene as a reducing agent was added to **7**. Indeed, complex **7** reacted with ferrocene (1 equivalent, 0.25 M), simultaneously with the oxidation of ferrocene to ferrocenium as observed by electronic absorption spectroscopy (Fc^+ = 620 nm, Figure 4.10). The yield of ferrocenium formed by electronic absorption spectroscopy was calculated to be ~50% with respect to the initial concentration of the precursor Mn^{II}_2 complex (**4**). This yield was comparable to the yield

of adduct **5**, also calculated to be ~50% by EPR (chapter 3, Figure A.9). Thus, all adduct **7** was reduced by ferrocene, resulting in ferrocenium formation (50% yield by electronic absorption spectroscopy).

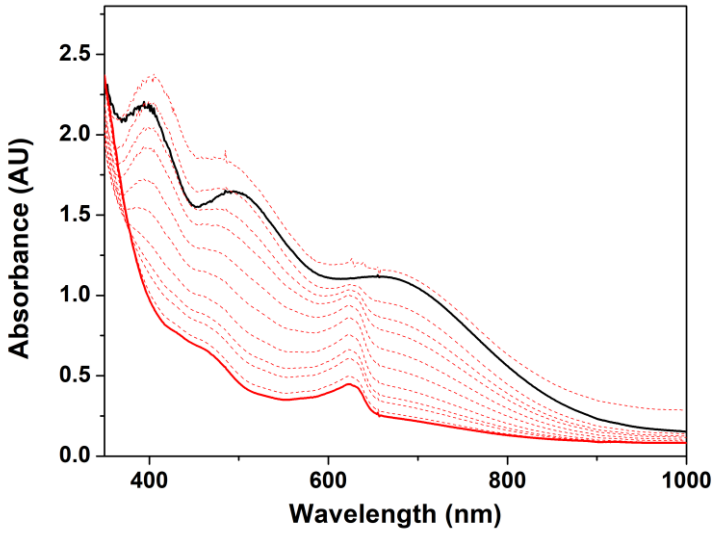

Figure 4.10. Electronic absorption spectra showing changes after addition of ferrocene (1 equivalent, 0.25 M) to **7** (black trace) and formation of ferrocenium (red trace, λ_{max} = 620 nm, path length = 1 cm).

In summary, the putative $Mn^{II}Mn^{III}$ species **7** reacted with base (Et_3N, 2,6-lutidine and TBAOH) to generate new species, whose structures are unknown. Further characterisations must be done to determine the products obtained upon base addition to **7**. Additionally, adduct **7** was reduced by ferrocene, with the formation of ferrocenium by electronic absorption spectroscopy. Furthermore, we decided to investigate the reactivity of **5** towards weaker acids as described below, to explore whether strong and weak acids played the same role in the reactivity of peroxo-$Mn^{II}Mn^{III}$ adduct (**5**).

4.5 Reactivity studies of 5 with weak acids

4.5.1 *p*TsOH addition to 5

Treatment of **5** with an excess of *para*-toluene sulfonic acid (*p*TsOH > 4 equivalents) in 1:9 CH_3CN/THF at -90 °C resulted in formation of a species (compound **8**) with weak absorbance bands at λ_{max} = 400, 510, 760 nm (Figure 4.11). These electronic absorbance features have previously been observed in $Mn^{II}Mn^{III}$ complexes (chapter 1, section 1.5.3). Additionally, the absorbance bands of **8** were comparable to the ones observed for compound **7** (**5** + $HClO_4$,

Figure 4.12). Also, as observed for complex **7**, complex **8** (Figure 4.12) displayed different electronic absorbance features to $Mn^{II}(ClO_4)_2.6H_2O$ (Figure 4.2, blue trace). The formation of a $Mn^{II}Mn^{III}$ species was proposed upon addition of an excess of *p*TsOH (> 4 equivalents) to complex **5**.

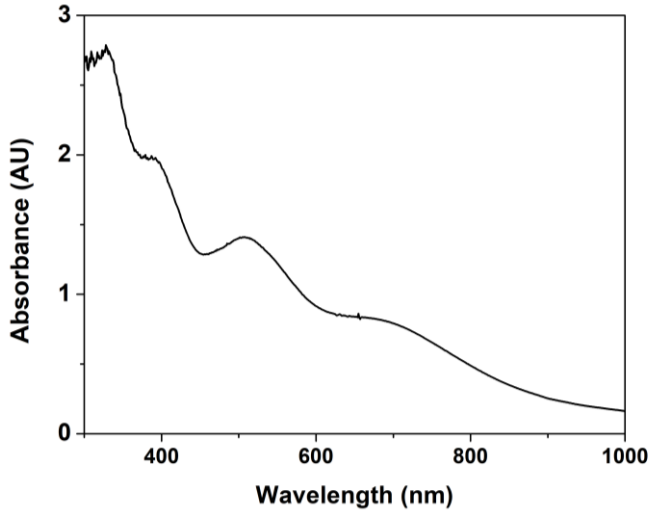

Figure 4.11. Electronic absorption spectra of **8** (**5** + 4 equivalents of *p*TsOH, black trace) in 1:9 CH_3CN/THF at -90 °C (path length = 1 cm).

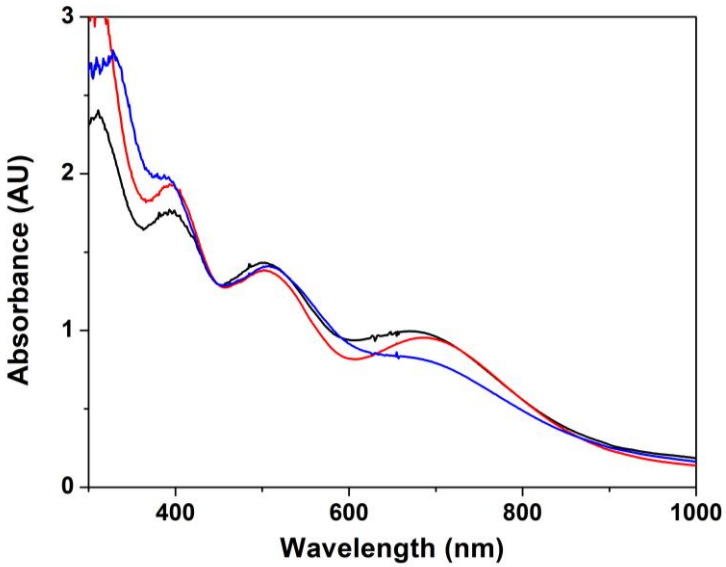

Figure 4.12. Comparison of electronic absorption spectra of **7** (**5** + $HClO_4$ (8 equivalents, 0.25 M, black trace) or **5** + HBF_4 (8 equivalents, 0.25 M, red trace)) and **8** (**5** + *p*TsOH (4 equivalents, 0.5 M, blue trace)) at -90 °C in 1:9 CH_3CN/THF (path length = 1 cm).

Compound **8** was also examined by EPR spectroscopy. The perpendicular mode EPR spectrum of **8** (**5** + 4 equivalents *p*TsOH, Figure A.39) at 77 K displayed a 6 multiline signal, characteristic of a Mn^{II} entity. Additionally, as seen above, the Mn^{II} signal saturated the EPR spectrum and an EPR signal for a $Mn^{II}Mn^{III}$ species was not acquired. Moreover, the presence

of the Mn^{II} signals in the EPR spectrum of **8** could be ascribed to a de-metalation reaction, as postulated for compound **7**.

The addition of 1 or 2 equivalents of *p*TsOH to **5** was also monitored by electronic absorption spectroscopy. The addition of 1 and 2 equivalents of *p*TsOH to **5** resulted in the formation of a new species (**9**, Figure 4.13) with a broad absorbance band at ~540 nm.

As described in the introduction (section 1.5.2), previously reported bis(μ-oxo)$Mn^{III}Mn^{IV}$ complexes in the literature, exhibited slight differences in the electronic absorption spectra, having a characteristic absorption band between 520-570 nm attributed to a *d-d* transition band and bands between 590-700 nm assigned to O to Mn charge transfer band.[17, 18, 20, 22, 34, 39, 49, 50]

Since compound **9** displayed an absorbance band at ~ 540 nm, attributed to a *d-d* transition, we postulated that upon addition of 1 or 2 equivalents of *p*TsOH to **5**, a high valent $Mn^{III}Mn^{IV}$ complex formed. Additionally, different electronic absorbance features were observed for compound **9** (Figure 4.14) when compared to complexes **7** and **8** (Figure 4.14). Thus complex **9** was postulated as a mixed valent $Mn^{III}Mn^{IV}$ complex.

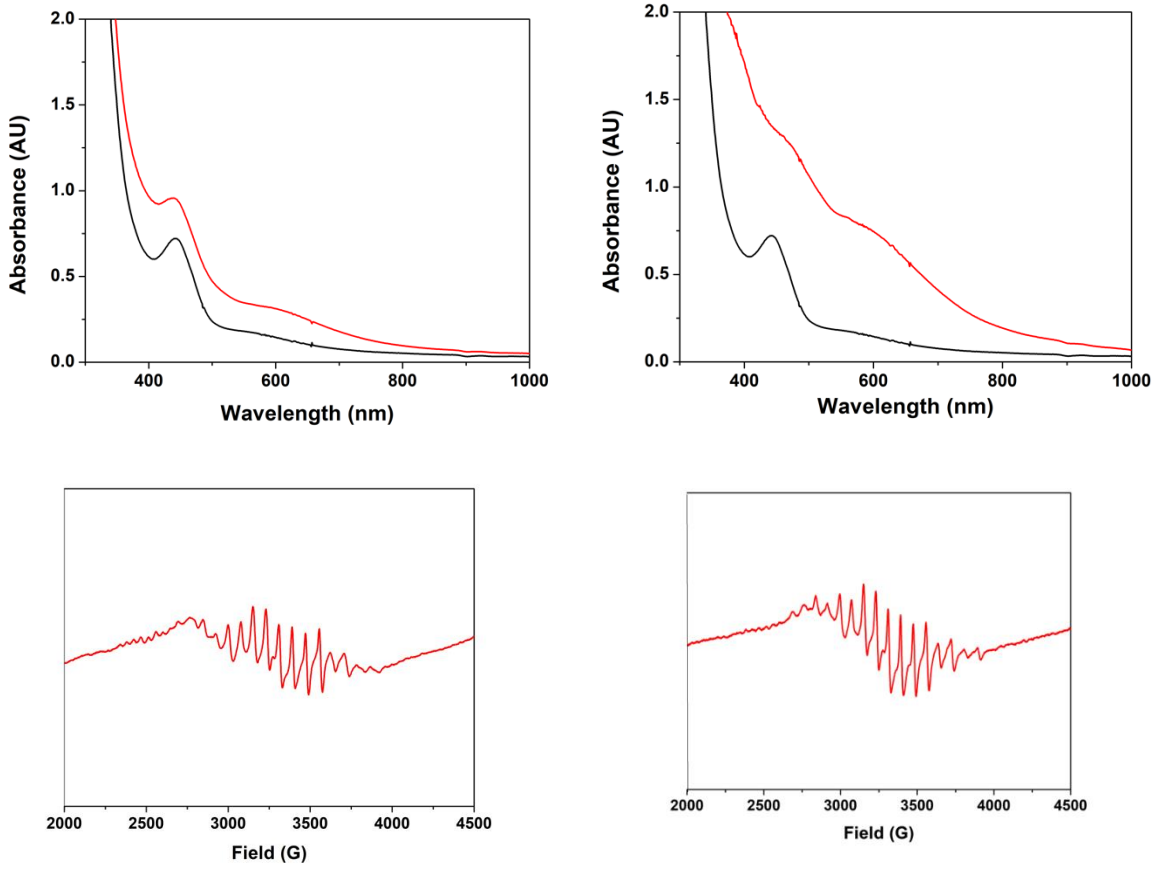

Figure 4.13. Top: Electronic absorption spectra upon addition of 1 equivalent *p*TsOH (left figure, red trace) to **5** (black trace) and 2 equivalents of *p*TsOH (right figure, red trace) to **5** (black trace) in 1:9 CH_3CN/THF at -90 °C (path length = 1 cm). Bottom: EPR spectra of the same reactions measured at 77 K (9.21 GHz, 2 mW microwave power).

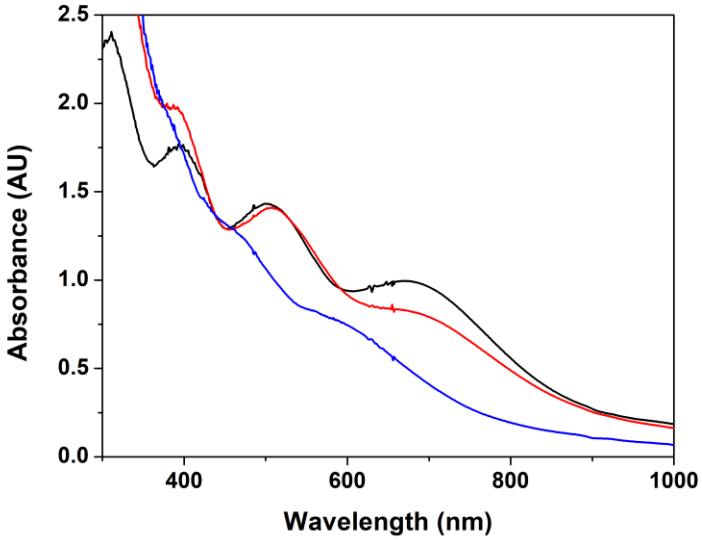

Figure 4.14. Comparison of electronic absorption spectra of compound **7** (**5** + $HClO_4$, black trace), **8** (**5** + 4 equivalents *p*TsOH, red trace) and **9** (**5** + 2 equivalents *p*TsOH, blue trace) in 1:9 CH_3CN/THF at -90 °C (path length = 1 cm).

The effect of adding less equivalents (1 or 2) of *p*TsOH to complex **5** (forming **9**), was also monitored by EPR spectroscopy (Figures 4.13 and A.40). At 77 K, compound **9** exhibited a 16-line EPR signal centred at g ~ 2.05 (Figure 4.13, bottom). The signal displayed a narrow spectral width and was observed at 77 K. Such signals have previously been observed in $Mn^{III}Mn^{IV}$ complexes, where the 16-line signals have been ascribed to the high valent $Mn^{III}Mn^{IV}$ oxidation state.[30, 31, 34-37] The 16 multiline EPR spectrum of **9** was comparable to those observed for mixed valent $Mn^{III}Mn^{IV}$ complexes, and thus compound **9** was postulated as a high valent $Mn^{III}Mn^{IV}$ entity.

In contrast to complex **9**, the EPR spectrum of adduct **5** (peroxo-$Mn^{II}Mn^{III}$) displayed a 22-line EPR signal (chapter 3, Figure 3.3) centred at g ~ 1.96. While the EPR signal of complex **9** had a narrow spectral width, compound **5** displayed a wide spectral width. Another difference was the temperature the EPR spectra of complexes **9** and **5** were measured at. While the 16-line EPR spectrum of complex **9** ($Mn^{III}Mn^{IV}$) was measured at 77 K, the EPR spectrum of compound **5** (peroxo-$Mn^{II}Mn^{III}$) was only observed below 10 K. Therefore, mixed valent $Mn^{II}Mn^{III}$ and $Mn^{III}Mn^{IV}$ exhibited different EPR signals.

In summary, adduct **7** was prepared upon addition of a strong acid ($HClO_4$/HBF_4) to **5**, compound **8** was prepared upon treatment of **5** with *p*TsOH (4 equivalents), while the addition of less equivalents of a weak acid (1 or 2 equivalents of *p*TsOH) to **5** resulted in the formation of complex **9**. All species were characterised by electronic absorption and EPR spectroscopies. Based on the electronic absorption, complexes **7** and **8** were assigned as mixed valent $Mn^{II}Mn^{III}$

species while species **9** was postulated as a high valent $Mn^{II}Mn^{IV}$ species. By EPR spectroscopy, the addition of strong acids ($HClO_4$ and HBF_4 – 8 equivalents, forming complex **7**) and *p*TsOH (> 4 equivalents, forming complex **8**) to complex **5** resulted in the formation of free Mn^{II} ions by EPR, attributed to a de-complexation reaction although the reaction mechanism is ambiguous. Importantly, the EPR spectrum of complex **9** exhibited EPR features characteristic of high valent $Mn^{III}Mn^{IV}$ species.

4.5.2 Comparison of complexes 6 and 9

The thermal decay of complex **5** formed a new species, complex **6** (section 4.2). Upon characterisation complex **6** was proposed to be a $Mn^{III}Mn^{IV}$ entity. Furthermore, the addition of *p*TsOH (1 or 2 equivalents) to **5** resulted in the formation of complex **9**, that also exhibited features of a $Mn^{III}Mn^{IV}$ species. A comparison of complexes **6** and **9** will be given below.

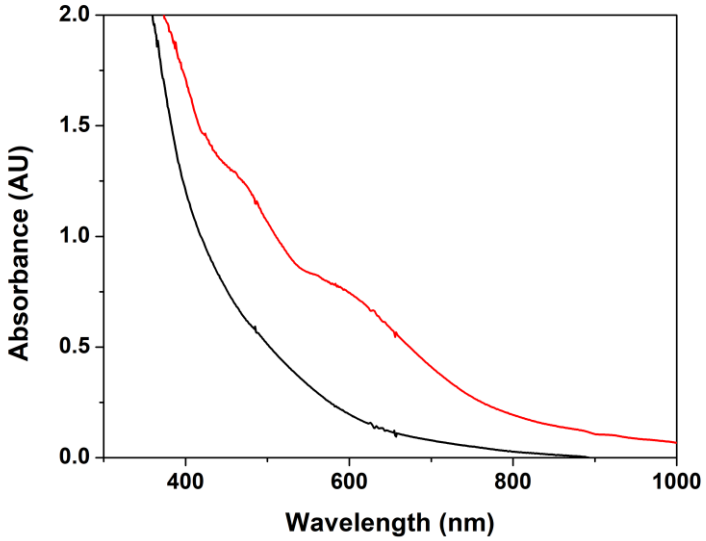

Figure 4.15. Comparison of electronic absorption spectra of complexes **6** (thermal decay of **5**) and **9** (**5** + 2 equivalents *p*TsOH) at -90 °C in 1:9 CH_3CN/THF (path length = 1 cm).

Complexes **6** and **9** displayed slight differences in their electronic absorption spectra (Figure 4.15). While a broad absorption band was observed for adduct **6**, complex **9** had a weak shoulder at ~ 540 nm. Both electronic absorption spectra were measured at -90 °C and exhibited features of high valent $Mn^{III}Mn^{IV}$ complexes. Furthermore, the EPR spectra of complexes **6** and **9** were recorded. A 16-line EPR signal was observed for both complexes (Figure A.41), the signal was centred at g ~ 2.02 for complex **6** and at g ~ 2.05 for complex **9**. The EPR spectra of complexes **6** and **9** were recorded at 77 K and exhibited slightly different EPR signals (Figure A.41). More

importantly, regardless of the EPR temperature the EPR spectra of the complexes was measured at, either 2 or 77 K, they both displayed a narrow spectral width (Figure A.41). $Mn^{III}Mn^{IV}$ complexes previously reported in the literature displayed these EPR features, a 16-line signal with a narrow spectral width. Therefore, complexes **6** and **9** had similar electronic absorbance features and EPR signals and have been postulated as high valent $Mn^{III}Mn^{IV}$ entities.

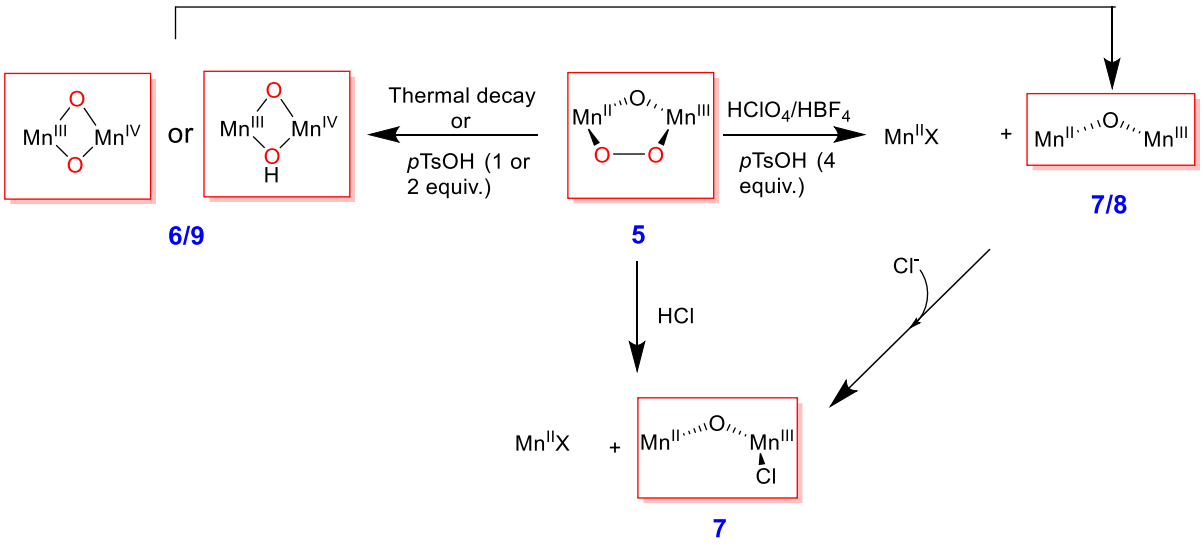

Scheme 4.2. Postulated adducts formed upon reaction of the peroxo-$Mn^{II}Mn^{III}$ complex (**5**) with $HClO_4/HBF_4$ (forming **7**), *p*TsOH (> 4 equivalents, forming **8**), and *p*TsOH (1 or 2 equivalents, forming **9**).

In conclusion, the addition of strong acids ($HClO_4$ and HBF_4 - 8 equivalents) and *p*TsOH (> 4 equivalents) to the peroxo-$Mn^{II}Mn^{III}$ complex **5** resulted in the formation of $Mn^{II}Mn^{III}$ species (**7** and **8**). The generation of complexes **7** and **8** might also occur with the formation of high valent $Mn^{III}Mn^{IV}$ intermediates first (Scheme 4.2). Furthermore, the thermal decay of compound **5** or treatment of **5** with *p*TsOH (1 or 2 equivalents) formed a high valent $Mn^{III}Mn^{IV}$ species (**6**/**9**) (Scheme 4.2). The formation of the mixed valent $Mn^{II}Mn^{III}$ species (**7** and **8**) and the high valent $Mn^{III}Mn^{IV}$ complexes (**6** and **9**) was monitored by electronic absorption and EPR spectroscopies. Moreover, the generation of mixed valent $Mn^{II}Mn^{III}$ and $Mn^{III}Mn^{IV}$ species was an interesting result as both species were postulated intermediates in the catalytic cycle of class Ib Mn_2 RNRs.

4.6 Conclusions

To conclude, the thermal decay of peroxo-$Mn^{II}Mn^{III}$ complex (**5**) was complex **6**, that upon characterisation might be high valent $Mn^{III}Mn^{IV}$ species. Furthermore, complex **5** reacted with strong acids ($HClO_4$, HBF_4 and HCl) to form adduct **7**, whose electronic absorption spectrum

exhibited features characteristic of a mixed valent $Mn^{II}Mn^{III}$ complex. The EPR spectrum of **7** was saturated by a Mn^{II} signal and the presence of a $Mn^{II}Mn^{III}$ species was not observed.

The postulated $Mn^{II}Mn^{III}$ complex **7** proved to be a poor electrophilic oxidant, not being involved in OAT or HAA reactions. Furthermore, adduct **7** reacted with different bases (Et_3N, 2,6-lutidine, TBAOH) to form new species. Additional experiments must be performed to determine the structure of the new species formed upon treatment of adduct **7** with bases.

The reactivity of the peroxo-$Mn^{II}Mn^{III}$ species **5** was also probed using *p*TsOH. The addition of *p*TsOH (> 4 equivalents) to **5** resulted in the formation of a new species **8**, that was proposed to be a mixed valent $Mn^{II}Mn^{III}$ entity, upon UV-Vis characterisation. Interestingly, the addition of less equivalents of *p*TsOH (1 or 2) to compound **5** formed a putative high valent $Mn^{III}Mn^{IV}$ species (compound **9**).

Therefore, the peroxo-$Mn^{II}Mn^{III}$ complex (**5**) was susceptible to acids, providing spectroscopic evidence for formation of $Mn^{II}Mn^{III}$ species by using strong acids ($HClO_4$, HBF_4 and HCl) and formation of a high valent $Mn^{III}Mn^{IV}$ adducts with the use of weak acids (1 or 2 equivalents of *p*TsOH). The formation of $Mn^{II}Mn^{III}$ and $Mn^{III}Mn^{IV}$ adducts was exciting as such species have been postulated as intermediates in the catalytic cycle of class Ib Mn_2 RNRs. Further characterisation by mass spectrometry and XAS could provide more insight into the structure of these species (**7**, **8** and **9**).

4.7 Experimental section

Materials

All reactions with air sensitive materials were conducted in a glove box under an N_2 atmosphere or under an inert atmosphere using standard Schlenk techniques. All reagents and solvents were purchased from commercial sources. Anhydrous N,N-dimethylformamide (DMF) was purchased and used without further purification. Anhydrous tetrahydrofuran (THF), acetonitrile (CH_3CN), and diethyl ether (Et_2O) were dispensed through an Innovative Technology PureSolvEN solvent purification system and deoxygenated by purging with Ar.

The ligand HBPMP (2,6-bis[(bis(2-pyridylmethyl)amino)methyl]-4-methylphenol) was synthesised as previously reported.[51] Synthesis of complex **4** ($[Mn_2(O_2CCH_3)_2(BPMP)](ClO_4)$) was carried out as previously reported.[52]

Caution: KO_2 and perchlorate salts of metal complexes are potentially explosive and must be handled with care and in small quantities. No problems were encountered during the synthesis of the above Mn_2 complexes.

Physical Methods

Electronic absorption spectra were recorded in quartz cuvettes on a Hewlett Packard (Agilent) 8453 diode array spectrophotometer (190-1100 nm range) coupled to a liquid nitrogen cooled cryostat from Unisoku Scientific Instruments (Osaka, Japan). X-ray crystallography was performed on a Bruker APEX Kappa Duo system at 100 K using an Oxford Cobra cryosystem. EPR (Electron Paramagnetic Resonance) spectra were measured on a Bruker EMX spectrometer equipped with an Oxford Instruments CE 5396, ESR9 continuous flow cryostat and an Oxford Instruments CE 5396 Precision temperature controller for the 77 K measurements. At 2 K, the measurements were conducted on a Bruker EPP 300 spectrometer equipped with an Oxford ESR 910 liquid helium cryostat and an Oxford temperature controller.

General procedure for the reaction of 4 with KO_2

A 1:9 CH_3CN/THF solution (1.5 mM) of complex **4** was prepared. In a quartz cuvette 2 mL of a 1.5 mM solution of complex **4** was cooled to -90 °C. KO_2 (15 mM) and 18-crown-6 (40 mM) were dissolved in DMF. 250 μL of this solution was added to the solution containing the Mn_2 complex. The reaction progress was monitored using electronic absorption spectroscopy.

EPR sample preparation

Samples for EPR analysis were prepared by transferring ~1 mL of the desired solution from the quartz cuvette at -90 °C, via a pre-cooled pipette into a pre-cooled EPR tube and immediately freezing it in liquid nitrogen. All EPR spectra were recorded at either 77 K (9.21 GHz, 2 mW microwave power and a 0.5 mT field modulation amplitude) or 2 K (9.64 GHz, 0.2 mW microwave power and a 1 mT field modulation amplitude).

Reactivity studies

A solution of **5** in 1:9 CH_3CN/THF at -90 °C was prepared using the above procedure. Substrates were added as concentrated CH_3CN/THF solutions to solutions of **5** at -90 °C. The reactions were monitored using electronic absorption spectroscopy. To a solution of **5** (1.5 mM, 2 mL, 1:9 CH_3CN/THF) at -90 °C was added the appropriate substrate. For the acid reactivity studies of adduct **5**, the substrate was added as a concentrated CH_3CN/THF solution of perchloric acid (= $HClO_4$), tetrafluoroboric acid (= HBF_4), and *para*-toluenesulfonic acid (= *p*TsOH). Likewise, for reactivity studies of **7**, the substrate was added as a 1 M concentrated CH_3CN/THF solution of triethylamine (= Et_3N), 2,6-lutidine and tetrabutylammonium hydroxide (= TBAOH). Ferrocene (0.25 M, 1 equivalent) as a reducing agent was added to **7** and ferrocenium was observed by electronic absoprtion spectroscopy (Fc^+, λ_{max} = 620 nm). All reactions were monitored using UV-Vis spectroscopy.

References

[1] A. M. Magherusan, A. Zhou, E. R. Farquhar, M. Garcia-Melchor, B. Twamley, L. Que, Jr., A. R. McDonald, *Angew. Chem. Int. Ed. Engl.* **2018**, *57*, 918-922.

[2] J. A. Cotruvo, Jr., T. A. Stich, R. D. Britt, J. Stubbe, *J. Am. Chem. Soc.* **2013**, *135*, 4027-4039.

[3] N. Kitajima, H. Komatsuzaki, S. Hikichi, M. Osawa, Y. Moro-oka, *J. Am. Chem. Soc.* **1994**, *116*, 11596.

[4] U. P. Singh, A. K. Sharma, S. Hikichi, H. Komatsuzaki, Y. Moro-oka, M. Akita, *Inorg. Chim. Acta* **2006**, *359*, 4407-4411.

[5] M. S. Seo, J. Y. Kim, J. Annaraj, Y. Kim, Y. M. Lee, S. J. Kim, J. Kim, W. Nam, *Angew. Chem. Int. Ed.* **2007**, *46*, 377-380.

[6] J. Annaraj, J. Cho, Y. M. Lee, S. Y. Kim, R. Latifi, S. P. de Visser, W. Nam, *Angew. Chem. Int. Ed.* **2009**, *48*, 4150-4153.

[7] J. Cho, R. Sarangi, W. Nam, *Acc. Chem. Res.* **2012**, *45*, 1321-1330.

[8] H. Kang, J. Cho, K. B. Cho, T. Nomura, T. Ogura, W. Nam, *Chem. Eur. J.* **2013**, *19*, 14119-14125.

[9] H. E. Colmer, R. A. Geiger, D. F. Leto, G. B. Wijeratne, V. W. Day, T. A. Jackson, *Dalton Trans.* **2014**, *43*, 17949-17963.

[10] R. A. Geiger, G. B. Wijeratne, V. W. Day, T. A. Jackson, *Eur. J. Inorg. Chem.* **2012**, *2012*, 1598-1608.

[11] R. A. Geiger, D. F. Leto, S. Chattopadhyay, P. Dorlet, E. Anxolabehere-Mallart, T. A. Jackson, *Inorg. Chem.* **2011**, *50*, 10190-10203.

[12] R. A. Geiger, S. Chattopadhyay, V. W. Day, T. A. Jackson, *J. Am. Chem. Soc.* **2010**, *132*, 2821-2831.

[13] R. A. Geiger, S. Chattopadhyay, V. W. Day, T. A. Jackson, *Dalton Trans.* **2011**, *40*, 1707-1715.

[14] N. Saravanan, M. Sankaralingam, M. Palaniandavar, *RSC Advances* **2014**, *4*, 12000.

[15] H. So, Y. J. Park, K. B. Cho, Y. M. Lee, M. S. Seo, J. Cho, R. Sarangi, W. Nam, *J. Am. Chem. Soc.* **2014**, *136*, 12229-12232.

[16] M. Sankaralingam, Y. M. Lee, S. H. Jeon, M. S. Seo, K. B. Cho, W. Nam, *Chem. Commun.* **2018**, *54*, 1209-1212.

[17] O. Horner, M.-F. Charlot, A. Boussac, E. Anxolabéhère-Mallart, L. Tchertanov, J. Guilhem, J.-J. Girerd, *Eur. J. Inorg. Chem.* **1998**, *1998*, 721-727.

[18] H. Yamazaki, T. Ueno, K. Aiso, M. Hirahara, T. Aoki, T. Nagata, S. Igarashi, M. Yagi, *Polyhedron* **2013**, *52*, 455-460.

[19] D. F. Leto, S. Chattopadhyay, V. W. Day, T. A. Jackson, *Dalton Trans.* **2013**, *42*, 13014-13025.

[20] L. Dubois, J. Pecaut, M. F. Charlot, C. Baffert, M. N. Collomb, A. Deronzier, J. M. Latour, *Chemistry* **2008**, *14*, 3013-3025.

[21] D. Huang, W. Wang, X. Zhang, C. Chen, F. Chen, Q. Liu, D. Liao, L. Li, L. Sun, *Eur. J. Inorg. Chem.* **2004**, *2004*, 1454-1464.

[22] J. Glerup, P. A. Goodson, A. Hazell, R. Hazell, D. J. Hodgson, C. J. McKenzie, K. Michelsen, U. Rychlewska, H. Toftlund, *Inorg. Chem.* **1994**, *33*, 4105-4111.

[23] Y. Gultneh, T. B. Yisgedu, Y. T. Tesema, R. J. Butcher, *Inorg. Chem.* **2003**, *42*, 1857-1867.

[24] C. Hureau, G. Blondin, M. F. Charlot, C. Philouze, M. Nierlich, M. Cesario, E. Anxolabehere-Mallart, *Inorg. Chem.* **2005**, *44*, 3669-3683.

[25] C. Baffert, M.-N. Collomb, A. Deronzier, J. Pécaut, J. Limburg, R. H. Crabtree, G. W. Brudvig, *Inorg. Chem.* **2002**, *41*, 1404-1411.

[26] H. Yamazaki, S. Igarashi, T. Nagata, M. Yagi, *Inorg. Chem.* **2012**, *51*, 1530-1539.

[27] H. Chen, R. Tagore, S. Das, C. Incarvito, J. W. Faller, R. H. Crabtree, G. W. Brudvig, *Inorg. Chem.* **2005**, *44*, 7661-7670.

[28] J. Limburg, J. S. Vrettos, H. Chen, J. C. de Paula, R. H. Crabtree, G. W. Brudvig, *J. Am. Chem. Soc.* **2001**, *123*, 423-430.

[29] C. Hureau, G. Blondin, M. Cesario, S. Un, *J. Am. Chem. Soc.* **2003**, *125*, 11637-11645.

[30] S. Mukhopadhyay, W. H. Armstrong, *J. Am. Chem. Soc.* **2003**, *125*, 13010-13011.

[31] J. A. Lessa, A. Horn, Jr., E. S. Bull, M. R. Rocha, M. Benassi, R. R. Catharino, M. N. Eberlin, A. Casellato, C. J. Noble, G. R. Hanson, G. Schenk, G. C. Silva, O. A. Antunes, C. Fernandes, *Inorg. Chem.* **2009**, *48*, 4569-4579.
[32] J. Glerup, P. A. Goodson, A. Hazell, R. Hazell, D. J. Hodgson, C. J. McKenzie, K. Michelsen, U. Rychlewska, H. Toftlund, *Inorg. Chem.* **2002**, *33*, 4105.
[33] S. Groni, P. Dorlet, G. Blain, S. Bourcier, R. Guillot, E. Anxolabehere-Mallart, *Inorg. Chem.* **2008**, *47*, 3166-3172.
[34] S. Schindler, O. Walter, J. Z. Pedersen, H. Toftlund, *Inorg. Chim. Acta* **2000**, *303*, 215-219.
[35] H. M. Berends, A. M. Manke, C. Nather, F. Tuczek, P. Kurz, *Dalton. Trans.* **2012**, *41*, 6215-6224.
[36] R. Chatterjee, S. Milikisiyants, K. V. Lakshmi, *Phys. Chem. Chem. Phys.* **2012**, *14*, 7090-7097.
[37] L. Dubois, D. F. Xiang, X. S. Tan, J. Pecaut, P. Jones, S. Baudron, L. Le Pape, J. M. Latour, C. Baffert, S. Chardon-Noblat, M. N. Collomb, A. Deronzier, *Inorg. Chem.* **2003**, *42*, 750-760.
[38] S. R. Cooper, M. Calvin, *J. Am. Chem. Soc.* **1977**, *99*, 6623-6630.
[39] M. Suzuki, S. Tokura, M. Suhara, A. Uehara, *Chem. Lett.* **1988**, *17*, 477-480.
[40] H. Diril, H. R. Chang, M. J. Nilges, X. Zhang, J. A. Potenza, H. J. Schugar, S. S. Isied, D. N. Hendrickson, *J. Am. Chem. Soc.* **1989**, *111*, 5102-5114.
[41] J. Chaignon, S. E. Stiriba, F. Lloret, C. Yuste, G. Pilet, L. Bonneviot, B. Albela, I. Castro, *Dalton Trans.* **2014**, *43*, 9704-9713.
[42] A. E. M. Boelrijk, S. V. Khangulov, G. C. Dismukes, *Inorg. Chem.* **2000**, *39*, 3009-3019.
[43] K. S. Banu, T. Chattopadhyay, A. Banerjee, M. Mukherjee, S. Bhattacharya, G. K. Patra, E. Zangrando, D. Das, *Dalton Trans.* **2009**, *40*, 8755-8764.
[44] M. Retegan, M. N. Collomb, F. Neese, C. Duboc, *Phys. Chem. Chem. Phys.* **2013**, *15*, 223-234.
[45] T. Matsumoto, K. Ohkubo, K. Honda, A. Yazawa, H. Furutachi, S. Fujinami, S. Fukuzumi, M. Suzuki, *J. Am. Chem. Soc.* **2009**, *131*, 9258-9267.
[46] C. Arunkumar, Y. M. Lee, J. Y. Lee, S. Fukuzumi, W. Nam, *Chem. Eur. J.* **2009**, *15*, 11482-11489.
[47] J. S. Wright, E. R. Johnson, G. A. DiLabio, *J. Am. Chem. Soc.* **2001**, *123*, 1173-1183.
[48] T. Osako, K. Ohkubo, M. Taki, Y. Tachi, S. Fukuzumi, S. Itoh, *J. Am. Chem. Soc.* **2003**, *125*, 11027-11033.
[49] M.-N. Collomb, A. Deronzier, A. l. Richardot, J. Pe´caut, *New J. Chem.* **1999**, *23*, 351-354.
[50] L. J. R.Y. Wei, Z. F. Xing, Z. J. Hua, G. Hui, *Chin. J. Chem.* **2005**, *23*, 418-420.
[51] S. Torelli, C. Belle, I. Gautier-Luneau, J. L. Pierre, E. Saint-Aman, J. M. Latour, L. Le Pape, D. Luneau, *Inorg. Chem.* **2000**, *39*, 3526-3536.
[52] M. Suzuki, M. Mikuriya, S. Murata, A. Uehara, H. Oshio, S. Kida, K. Saito, *Bull. Chem. Soc. Jpn.* **1987**, *60*, 4305-4312.

Chapter 5

Synthesis of a Mn^{II}_2 and a $Mn^{III}_2Mn^{II}_4$ complex

XRD data collection and structure solutions and refinements were done by Dr Brendan Twamley (Trinity College Dublin).

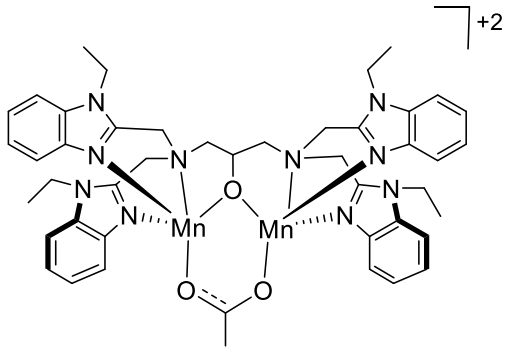

$[Mn^{II}Mn^{II}(O_2CCH_3)((N\text{-}Et\text{-}HPTB)]^{2+}$

1

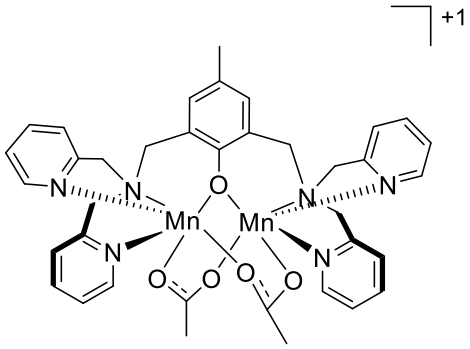

$[Mn^{II}Mn^{II}(O_2CCH_3)_2(BPMP)]^{1+}$

4

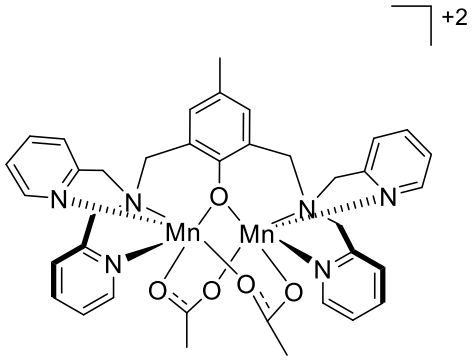

$[Mn^{II}Mn^{III}(O_2CCH_3)_2(BPMP)]^{2+}$

10

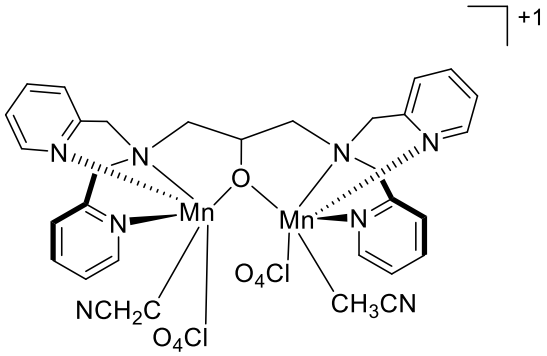

$[Mn^{II}Mn^{II}(ClO_4^-)_2(CH_3CN)_2(HPTP)]^{1+}$

11

5.1 Introduction

The work described in chapters 2-4 demonstrated that Mn^{II}_2 complexes supported by poly-benzimidazole ((N,N,N',N'-tetrakis(2-(1-ethylbenzimidazolyl))-2-hydroxy-1,3-diaminopropane (= N-Et-HPTB)) and polypyridine ligands ((2,6-bis[(bis(2-pyridylmethyl)amino)methyl]-4-methylphenol (= HBPMP)) can react with $O_2^{\bullet-}$, forming a peroxo-$Mn^{II}Mn^{III}$ species (adducts **2** and **5**, chapters 2 and 3 respectively), mimicking one of the intermediates in class Ib Mn_2 RNRs.[1] A description of the X-ray crystal structure of complex **4** ($[Mn^{II}_2(O_2CCH_3)_2(BPMP)](ClO_4)$), the precursor of adduct **5** will be given below. While the peroxo-$Mn^{II}Mn^{III}$ unit in **2** was unreactive at -40 °C, the $Mn^{II}Mn^{III}$-peroxide complex **5** proved to be a good nucleophilic oxidant, in aldehyde deformylation (chapter 4). Furthermore, the majority of mononuclear peroxo-Mn^{III} complexes previously reported exhibited nucleophilic character.[2-13] We set out to synthesise another Mn^{II}_2 complex supported by a polypyridine ligand (N,N,N'N'-tetrakis(2-pyridylmethyl)1,3-diamino-2-hydroxypropane (= HPTP), Figure 5.1),[14] similar to the ligand system (HBPMP) used in chapter 3. We wanted to prepare another $Mn^{II}Mn^{III}$-peroxide complex (using the HPTP ligand) and investigate its reactivity. The Mn_2-peroxide complexes described in chapters 2 and 3, were unable to form a Mn_2-hydroperoxide species upon their reaction with acids. The preparation of a synthetic Mn_2-hydroperoxide species was important as a Mn-hydroperoxide was one of the postulated intermediates in class Ib Mn_2 RNRs,[15] the class of metalloenzymes we are trying to mimic. Furthermore, we wanted to better understand the reactivity (electrophilic/nucleophilic character) of the metastable adducts formed in the reaction of the Mn_2-HPTP complex (**11**) with $O_2^{\bullet-}$. Before the synthesis of complex **11**, a brief description of the X-ray crystal structures of complexes **4** ($[Mn^{II}_2(O_2CCH_3)_2(BPMP)](ClO_4)$) and **10** ($[Mn^{II}Mn^{III}(O_2CCH_3)_2(BPMP)](ClO_4)_2$) will be given below.

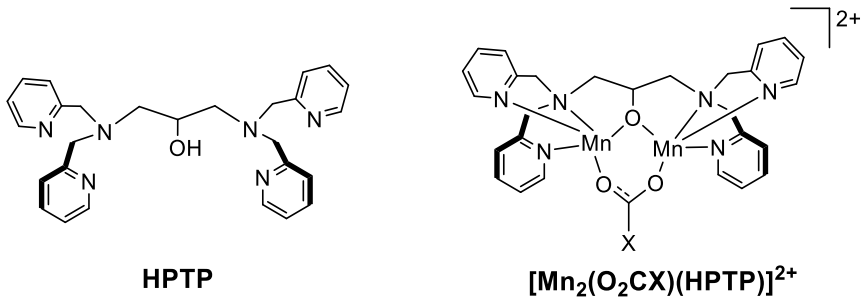

HPTP **$[Mn_2(O_2CX)(HPTP)]^{2+}$**

Figure 5.1. Structure of the HPTP ligand and postulated structure of the $[Mn_2(X)(HPTP)]^{2+}$ (X = part of carboxylate bridge) complex.

5.2 Crystal structure of a $Mn^{II}Mn^{II}$ (4) and a $Mn^{II}Mn^{III}$ complex (10)

The crystal structure of the precursor Mn^{II}_2 complex (**4**, $[Mn^{II}_2(O_2CCH_3)_2(BPMP)](ClO_4)$) was recrystallised from CH_3CN/Et_2O and it was reported in the experimental section, appendix (Table 5.2, Figure A.42). The crystal structure of **4** was previously reported in the literature.[16] Moreover, the mixed valent form of **4**, the $Mn^{II}Mn^{III}$ complex supported by the HBPMP ligand ($[Mn^{II}Mn^{III}(O_2CCH_3)_2(BPMP)](ClO_4)_2$, **10**) was synthesised using a previously reported procedure.[17] Recrystallisation of complex **10** from CH_3CN/Et_2O gave crystals suitable for X-ray diffraction measurements. The crystal structure of **10** (Table 5.3, Figure A.43) was similar to the one previously reported by Hendrickson and co-workers.[17] The only difference between the two crystal structures consisted in a H_2O molecules, that was not present in the crystal lattice of **10**.

Comparison of the crystal structures of complexes **4** and **10**, where **4** was represented by $[Mn^{II}_2(O_2CCH_3)_2(BPMP)](ClO_4)$ and complex **10** was the mixed valent form of complex **4** ($[Mn^{II}Mn^{III}(O_2CCH_3)_2(BPMP)](ClO_4)_2$) resulted in very small differences in the bond lengths (Table 5.6). The Mn-$O_{alkoxide}$ and Mn-$O_{carboxylate}$ bonds had almost the same length in complexes **4** and **10**. The main difference observed in complexes **4** and **10** was a slightly larger Mn-Mn distance in complex **10**, ~0.5 Å when compared to **4**. This was not unexpected as the same trend was previously observed for Mn_2 complexes supported by the HBPMP ligand.[16-18] Therefore, since only one of the Mn^{II} centres in **4** was oxidised to Mn^{III}, no major bond length differences between complexes **4** and **10** were found.

5.3 Attempted synthesis of a Mn^{II}_2 complex: formation of a Mn_6 complex

Firstly, the synthesis of the Mn^{II}_2 complex using the HPTP ligand was carried out in air, at room temperature, just as the syntheses of complexes **1** and **4** (chapters 2 and 3). The synthesis of the Mn^{II}_2 complex supported by the HPTP ligand was first performed in methanol, similar to the synthesis of a Cu_2 complex supported by the HPTP ligand.[19, 20] The $[Cu_2(O_2CCH_3)(BPMP)](ClO_4)_2$ was prepared using the ligand HPTP, $Cu(ClO_4)_2.6H_2O$, acetic acid and triethylamine (Et_3N) in methanol.[19] No reaction was observed when the ligand HPTP was reacted with $Mn(ClO_4)_2.6H_2O$, benzoic acid and Et_3N in methanol. A Mn^{II}_2 complex

bridged by the HPTP ligand and a benzoate carboxylate bridge was expected ($[Mn_2(O_2CC_6H_5)(HPTP)](ClO_4)_2$, Figure 5.2).

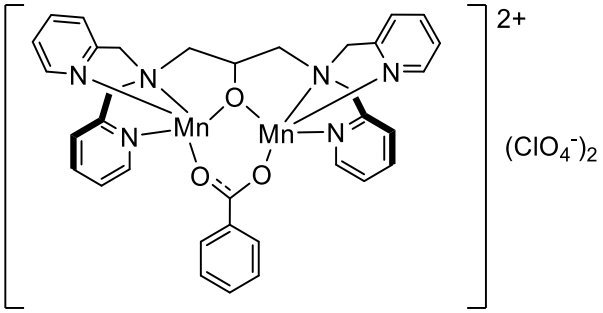

Figure 5.2. Expected structure of the $[Mn_2(O_2CC_6H_5)(HPTP)](ClO_4)_2$ complex.

The reaction was then carried out in dichloromethane (DCM) using the ligand HPTP, $Mn(ClO_4)_2.6H_2O$ as the metal source, and benzoic acid. The reaction was carried out in an air atmosphere and a pink powder was obtained (see experimental section 5.6). The pink powder was recrystallised from CH_3CN/Et_2O. Crystals suitable for X-ray diffraction measurements were obtained. Unfortunately, the crystal structure obtained was not of a Mn_2 complex as expected. Instead, the crystal structure of a Mn-hexamer (Mn_6) complex supported by ten benzoate carboxylate bridges, four acetonitrile solvent molecules and two oxygen atoms ($[Mn^{III}_2Mn^{II}_4(O)_2(CH_3CN)_4(O_2CC_6H_5)_{10}]$, Figure 5.3) was obtained. The oxygen atoms were positioned in the middle of the Mn_6, one of them bridging three Mn atoms and the another one bridging four Mn atoms (Figure 5.4, Figure A.44). The HPTP ligand was not part of the crystal structure of the Mn_6 complex. Thus, as this was not the expected Mn^{II}_2 complex, we believed the formation of the Mn_6 cluster was due to the synthesis being performed in the presence of oxygen.

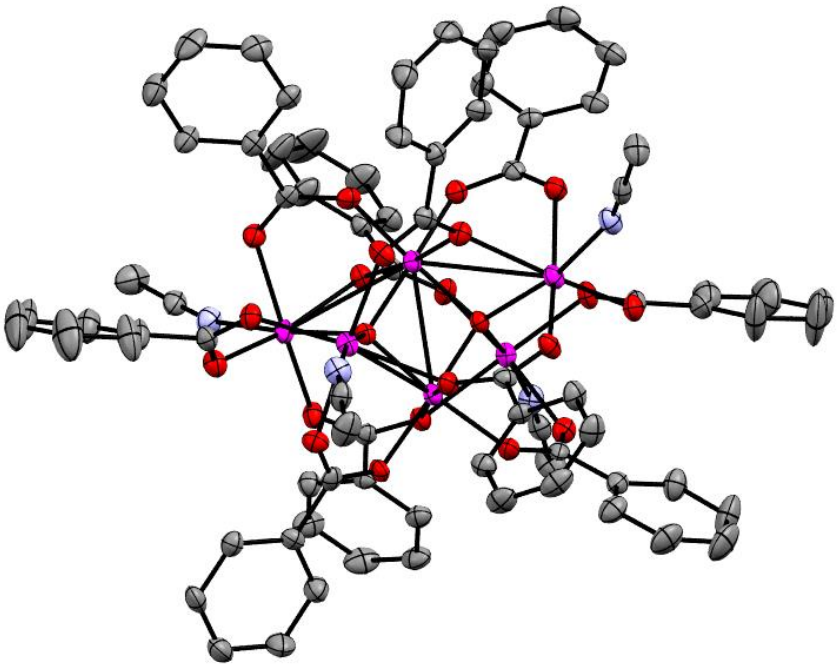

Figure 5.3. ORTEP plot of a mixed-valent Mn_6 ($[Mn^{III}_2Mn^{II}_4(O)_2(CH_3CN)_4(O_2CC_6H_5)_{10}]$) complex. Hydrogen atoms have been omitted for clarity (purple = Mn, grey = C, blue = N, red = O). Ellipsoids are shown at 50% probability.

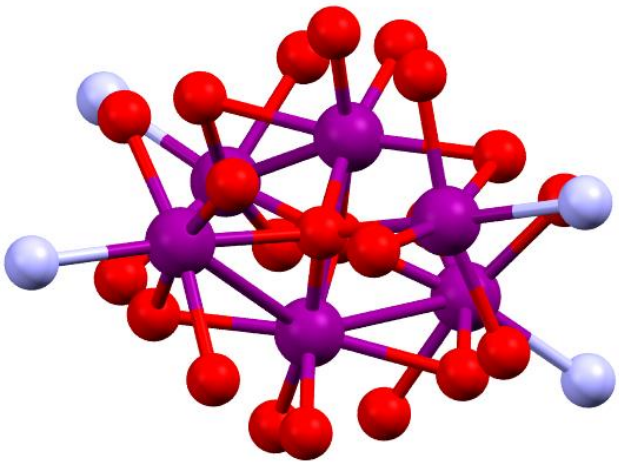

Figure 5.4. ORTEP plot of the Mn_6 core. Carboxylate groups, hydrogen atoms and acetonitrile molecules have been omitted for clarity (purple = Mn, red = O, blue = N). Ellipsoids are shown at 50% probability.

Moreover, a few mixed-valent Mn_6 clusters have previously been reported in the literature.[21-26] The hexanuclear clusters had either a Mn^{III}_6,[26] a $Mn^{III}_2Mn^{II}_4$[21, 22, 25, 27] or a $Mn^{II}Mn^{III}_5$ core.[26] The most common motif found in these Mn_6 clusters was the $Mn^{III}_2Mn^{II}_4$ core. The

syntheses of these Mn_6 clusters were carried out in air, using a Mn metal salt ($Mn(ClO_4)_2.6H_2O$, $Mn_2(O_2CPh)_2.4H_2O$), a source of a carboxylate bridge and a base. Most of these synthetic procedures were carried out in methanol or acetonitrile solution. These syntheses were comparable to the preparation of the Mn_6 complex described here, which was prepared using $Mn(ClO_4)_2.6H_2O$ and benzoic acid. While the previously reported Mn_6 complexes were prepared in methanol or acetonitrile, the solvent used for the Mn_6 complex (Figure 5.3) was DCM.

More importantly, two Mn_6 cluster's crystal structures previously reported were very similar to the Mn_6 complex described here. The first one is a Mn_6 cluster ($[Mn^{III}_2Mn^{II}_4(O)_2(O_2CC_6H_5)_{10}(DMF)_4]$) published by Pavlishchuk and co-workers.[22] The coordination sphere of each metal was completed by ten bridging benzoates and four DMF molecules. This complex was synthesised in a one-pot reaction by redox generation of benzoate ligands from benzaldehyde.[22] The only difference between this Mn_6 cluster and the Mn_6 complex described here consisted of the terminal ligands, DMF versus acetonitrile. Another very similar structure to the Mn_6 described here, was a mixed-valent Mn_6 complex ($[Mn^{III}_2Mn^{II}_4(O)_2(O_2CC_6H_5)_{10}(hmt)_4]$) where hmt = hexamethylenetetramine) reported by Ghosh and co-workers.[21] The X-ray crystal structure of this complex consisted of a $[Mn^{III}_2Mn^{II}_4O_2]$ core, coordinated by ten bridging benzoates and four terminal hmt groups. This complex was involved in catecholase activity with 3,5-di-*tert*-butylcatechol (3,5-DTBC) as a substrate.[21] Catechol oxidase is a type-3 copper protein, that utilises a process known as catecholase activity to catalyse the oxidation of *o*-diphenols (catechols) to the corresponding quinones.[28] Thus, the $[Mn^{III}_2Mn^{II}_4(O)_2(O_2CC_6H_5)_{10}(hmt)_4]$ complex was an efficient catechol oxidase mimic. Furthermore, as above, the only difference between the Mn_6 crystal structure reported by Ghosh and co-workers and that of the Mn_6 cluster described here, was the presence of different terminal ligands, hmt versus acetonitrile.

In summary, the synthesis of a new mixed-valent Mn_6 cluster was reported. A crystal structure of the Mn_6 complex was also obtained. Moreover, two Mn_6 clusters have previously been reported in the literature,[21, 22] having a very similar structure to the mixed-valent Mn_6 complex reported here. While the $[Mn^{III}_2Mn^{II}_4(O)_2]$ core reported here had CH_3CN as terminal ligands, the previously reported Mn_6 clusters were supported by either hmt or DMF as terminal ligands.[21, 22] The $[Mn^{III}_2Mn^{II}_4(O_2)(O_2CC_6H_5)_{10}(hmt)_4]$ complex proved to be an efficient catechol oxidase mimic. The catecholase reactivity of the mixed valent Mn_6 complex described here could also be investigated, to study whether different terminal ligands influence complex reactivity. Besides the RNRs (chapters 1-4), we were also interested in catechol oxidase

enzymes (chapter 6). Probing the catecholase reactivity of the Mn_6 cluster would be interesting, as Mn^{II}_2 and Cu^{II}_2 complexes proved to be efficient catechol oxidase mimics (chapter 6).

5.4 Synthesis and characterisation of a new Mn^{II}_2 complex (complex 11)

The attempted syntheses of the Mn^{II}_2 complex supported by the HPTP ligand described below were performed in a glove box, under an inert atmosphere. The synthesis of the Mn^{II}_2 complex using the HPTP ligand was carried out in either DCM or CH_3CN, using $MnCl_2$ as the metal salt, Et_3N as a base, and a series of acids, 2,6-dimethylbenzoic acid, *ortho*-toluic acid, 2-nitrobenzoic acid and benzoic acid as the source of the carboxylate bridge. Furthermore, sodium acetate and tetrabutylammonium acetate were also used as a source for the carboxylate bridge instead of the acids. Unfortunately, we were unable to obtain any powder/solid under these reaction conditions. Thus, all the above syntheses were repeated using tetrahydrofuran (THF) as a solvent instead of DCM or CH_3CN. A Mn^{II}_2 complex supported by the HPTP ligand and a carboxylate bridge was not obtained under these conditions.

An alternative procedure, the synthesis of the Mn^{II}_2 complex using the HPTP ligand without a carboxylate bridge, provided better results. As above, Et_3N was used to deprotonate the HPTP ligand in THF, after which $Mn(ClO_4)_2.6H_2O$ was added. A colour change upon addition of the metal salt was observed. After the reaction mixture was stirred for 0.5 h, a white powder precipitated out of solution (see experimental section, section 5.6). The white powder was filtered and upon recrystallisation from CH_3CN/Et_2O, crystals suitable for X-ray diffraction measurements were obtained.

A crystal structure of a Mn^{II}_2 complex supported by the HPTP ligand was obtained (**11**, $[Mn_2(ClO_4^-)_2(CH_3CN)_2(HPTP)](ClO_4^-)$, Figure 5.5). Additionally, one CH_3CN and one ClO_4^- ion were coordinated to each of the Mn centres. The coordination of the ClO_4^- ions to the Mn atoms was unexpected as perchlorate ions are weak ligands, they are usually found as counterions in metal complexes not bound to the metal centre. Also, without the perchlorate ions and the acetonitrile solvent molecules bound to the Mn centres, the Mn ions would have been in a tetrahedral environment. Both Mn atoms in complex **11** displayed an octahedral coordination geometry. The X-ray crystal structure of complex **11** exhibited a Mn1···Mn2 distance of 3.84 Å (Figure 5.5). Also the Mn1-$O_{alkoxide}$ and Mn2-$O_{alkoxide}$ bonds had very similar lengths, 2.08 and 2.1 Å respectively. Additionally, the Mn1-N35 (CH_3CN) and Mn2-N38

(CH_3CN) distances were very close in values, 2.23 and 2.19 Å. A slight difference in bond lengths was observed for Mn1-O1 (ClO_4^-) and Mn2-O5 (ClO_4^-), with values of 2.29 and 2.39 Å respectively. The Mn1-N_{amine} and Mn2-N_{amine} bond lengths of complex **11** also had comparable values of 2.31 and 2.29 Å respectively. Finally, the average Mn1-N_{benz} and Mn2-N_{benz} bond lengths displayed values of 2.29 and 2.23 Å respectively. Therefore bond lengths measurement of the two Mn centers as seen above, showed that compound **11** was a relatively symmetric complex.

Complex **11** was extremely oxygen and water sensitive. As mentioned above, the synthesis of complex **11** was carried out in a glove box, under an inert atmosphere. It was noticed that if the synthesis of complex **11** was not performed under a completely inert atmosphere, the white powder obtained after the synthesis changed colour to a brown powder within seconds. When a clear CH_3CN solution of **11** was exposed to oxygen and water, an immediate colour change to yellow was observed.

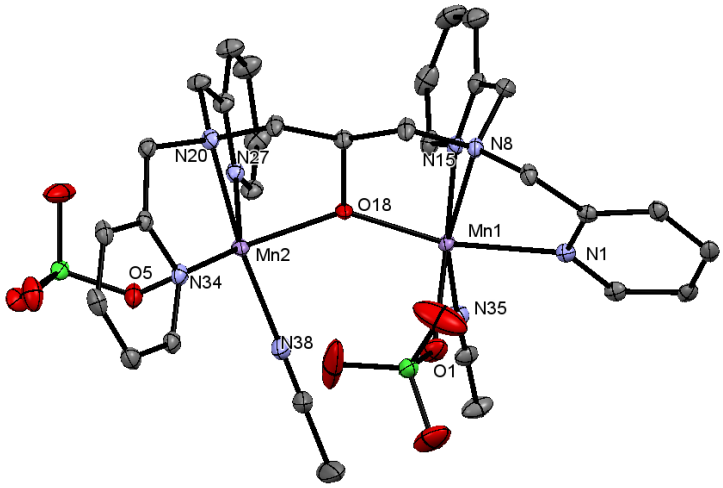

Figure 5.5. ORTEP plot of complex **11**. Hydrogen atoms and one perchlorate anion have been omitted for clarity. Ellipsoids are shown at 50% probability. Selected bond distances (Å): Mn1-Mn2: 3.84, Mn1-N1: 2.29, Mn1-N15: 2.29, Mn1-N8: 2.31, Mn1-N35: 2.23, Mn1-O1: 2.29, Mn1-O18: 2.08, Mn2-N27: 2.22, Mn2-N20: 2.29, Mn2-N34: 2.24, Mn2-N38: 2.19, Mn2-O5: 2.39, Mn2-O18: 2.1.

A comparison of selected bond lengths found in complex **11** to the other two Mn^{II}_2 complexes **1** (chapter 2) and **4** (chapter 4) is shown in Table 5.1. A significant difference was observed in the Mn1···Mn2 bond lengths of complex **11** (3.84 Å) when compared to the Mn1···Mn2 distance in Mn^{II}_2 complexes **1** and **4**, 3.6 and 3.41 Å respectively. This difference was not unexpected as **1** and **4** were bridged by acetate carboxylate bridges while complex **11** did not have a carboxylate bridge. Complex **11** had perchlorate and CH_3CN molecules instead of the acetate

carboxylate bridge. Thus, the longer Mn···Mn distance observed in complex **11** was probably due to the absence of the carboxylate bridge; the two Mn centres were not pulled together by its bridging coordination mode. Furthermore, the Mn1-$O_{alkoxide}$, Mn2-$O_{alkoxide}$ and the average Mn-N_{amine} and Mn-N_{benz} bond lengths obtained for **11** had very similar values to the bond lengths observed in complexes **1** and **4** (Table 5.1). Moreover, while complex **1** had a trigonal bypiramidal geometry, the Mn centers in complexes **4** and **11** were in an octahedral environment. Thus in complexes **4** and **11**, one of the ligands had to dissociate from the Mn centres, upon reaction of these complexes with the oxidant ($O_2^{\bullet-}$). To conclude, the X-ray crystal structures for complexes **1**, **4** and **11** showed that these complexes exhibited similar bond length values. One of the main differences observed in complex **11** was a longer Mn1···Mn2 bond distance when compared to compounds **1** and **4**. Furthermore, the Mn centres in these complexes were either in a trigonal bypiramidal (complex **1**) or an octahedral (complexes **4** and **11**) environment.

Table 5.1. Comparison of selected bond lengths of Mn^{II}_2 complexes **1**, **4** and **11**.

Selected Bond Lengths (Å)		**Complexes**		
		1[1]	**4**	**11**
Mn1···Mn2		3.6	3.41	3.84
Mn1-$O_{alkoxide}$		2.05	2.11	2.08
Mn2-$O_{alkoxide}$		2.04	2.1	2.1
Average Bond Lengths	Mn-N_{amine}	2.42	2.32	2.3
	Mn-N_{benz}	2.13	2.29	2.23

Similar to complexes **1** and **4** (chapters 2 and 4), complex **11** was prepared as a synthetic model of class Ib Mn_2 RNRs. The X-ray crystal structures of class Ib Mn_2 RNRs from *E. coli*, *B. subtilis* and *C. ammoniagenes* were previously reported (see introduction, section 1.4). The Mn···Mn bond distance from *E. coli* was 3.7 Å,[29] from *B. subtilis* was 3.9 Å,[30] while in *C. ammoniagenes* a 3.3 Å bond length[31] was established. The Mn ions in *E. coli* and *B. subtilis* were determined to be in a +2 oxidation state,[29, 30] while for *C. ammoniagenes* a +3 oxidation state for both Mn ions was established.[31] The Mn···Mn separation for complex **11** (3.84 Å) was very similar to the Mn^{II}_2 active sites of *E. coli* (3.7 Å) and *B. subtilis* (3.9 Å). Furthermore, the Mn centres of the enzymes of class Ib Mn_2 RNRs were either in a 5- or 6-coordination environment. Complex **11** also had both Mn centres in an octahedral geometry. Therefore, complex **11** was a better structural mimic of class Ib Mn_2 RNRs than complexes **1** and **4**,

because it had the same coordination environment and similar Mn···Mn bond lengths to class Ib Mn_2 RNRs.

5.5 Conclusions

In conclusion, while trying to synthesise a Mn^{II}_2 complex supported by the HPTP ligand, the formation of a Mn_6 complex was observed when the reaction was performed in air. Moreover, the ligand HPTP was not part of the crystal structure of the Mn_6 ($[Mn^{III}_2Mn^{II}_4(O_2)(CH_3CN)_4(O_2CC_6H_5)_{10}]$) complex. The mixed-valent Mn_6 was bridged by ten benzoate carboxylate bridges, two oxygen atoms and four CH_3CN molecules. After the X-ray crystal structure of the Mn_6 complex was obtained, the rest of the syntheses were carried out under an inert atmosphere, in a glove box. Many attempts were made in the synthesis of a Mn^{II}_2 complex bearing the HPTP ligand and a carboxylate bridge, but they were unsuccessful.

Nevertheless we managed to synthesise a Mn^{II}_2 complex supported by HPTP, without a carboxylate bridge (**11**, $[Mn_2(ClO_4^-)_2(CH_3CN)_2(HPTP)](ClO_4^-)$), when the reaction was performed under an inert atmosphere. The crystal structure revealed that each Mn atom was in an octahedral geometry, being coordinated by the ligand HPTP, one perchlorate and one CH_3CN molecule. Moreover, the X-ray crystal structure of complex **11** was very similar to that of complexes **1** and **4**, with small differences. While both Mn centres in complexes **1** and **4** were supported by acetate carboxylate bridges, complex **11** did not have a carboxylate bridge in its structure. Furthermore, complexes **1** and **4** were not susceptible to O_2, only towards $O_2^{\bullet-}$, while complex **11** was extremely oxygen and water sensitive. This was an important result as the absence of a carboxylate bridge in **11** increased its oxidative reactivity.

Finally, complex **11** exhibited a similar Mn···Mn separation and the same coordination geometry as *E. coli* and *B. subtilis* of class Ib Mn_2 RNRs. Complex **11** was another structural mimic of this class of enzymes, besides complexes **1** and **4**. Next, the reaction of **11** towards $O_2/O_2^{\bullet-}$ will be explored to gain a better understanding of the reactivity of this complex.

5.6 Experimental section

Materials

All reactions with air sensitive materials were conducted in a glove box under an N_2 atmosphere or under an inert atmosphere using standard Schlenk techniques. All reagents and solvents were purchased from commercial sources. Anhydrous N,N-dimethylformamide (DMF) was purchased and used without further purification. Anhydrous tetrahydrofuran, acetonitrile (CH_3CN), and diethyl ether (Et_2O) were dispensed through an Innovative Technology PureSolvEN solvent purification system and deoxygenated by purging with Ar.

The ligand HBPMP (2,6-bis[(bis(2-pyridylmethyl)amino)methyl]-4-methylphenol) was synthesised as previously reported.[32] Synthesis of complex **4** ($[Mn_2(O_2CCH_3)_2(BPMP)](ClO_4)$) was carried out as previously reported.[18] The product was recrystallised from CH_3CN/Et_2O to give crystals suitable for X-ray diffraction. A unit cell check confirmed the crystal structure already published. The crystal structure of **4** reported here was similar to the one previously published.[16]

The mixed valent $Mn^{II}Mn^{III}$ complex ($[Mn_2(O_2CCH_3)_2(BPMP)](ClO_4)_2$, **10**) was synthesised as previously reported and a crystal structure was obtained,[17] similar to the one published, except complex **10** does not have a H_2O molecule in the crystal lattice. A comparison of the bond lengths of the crystal structures reported here to those previosuly published was given in Table 5.6.

N,N-bis(2-picolyl)amine was synthesised according to a previously reported procedure.[33] The ligand HPTP was synthesised as previously described[34] by the reaction of epichlorohydrin with N,N-bis(2-picolyl)amine.[34]

Caution: Perchlorate salts of metal complexes are potentially explosive and must be handled with care and in small quantities. No problems were encountered during the synthesis of the above Mn_2 complexes.

Synthesis of Mn_6: $[Mn^{II}_4Mn^{III}_2(O_2)(CH_3CN)_4(O_2CC_6H_5)_{10}]$

The synthesis of the Mn_6 was carried out in air. HPTP (0.09 g, 0.11 mmol) and Et_3N (0.1 mL, 0.073 g, 0.72 mmol) were stirred in dichloromethane (5 mL) for 2 h at room temperature. After 2 h, benzoic acid (0.01 g, 0.082 mmol) dissolved in 2 mL of DCM was added and the reaction mixture was left to stir for half an hour. Following that, $Mn(ClO_4)_2.6H_2O$ (0.142 g, 0.39 mmol) was added and left stirring for another hour. A pink powder was obtained (0.06 g, 67 %). The

pink powder was recrystallised from CH_3CN/Et_2O to give crystals suitable for X-ray diffraction measurements.

Synthesis of complex 11 ($[Mn_2(ClO_4^-)_2(CH_3CN)_2(HPTP)](ClO_4^-)$)

The synthesis of $[Mn_2(ClO_4^-)_2(CH_3CN)_2(HPTP)](ClO_4^-)$ was carried out in a nitrogen filled glove box as the synthesised complex was extremely oxygen sensitive. Dry solvents were used in the synthesis. HPTP (0.09 g, 0.11 mmol) and Et_3N (0.1 mL, 0.073 g, 0.72 mmol) were left stirring in 7 mL of THF for 20 mins. Then $Mn(ClO_4)_2.6H_2O$ (0.096 g, 0.27 mmol) dissolved in 3 mL of THF was added to the reaction mixture. A colour change from yellow to white was observed after addition of the metal salt. A white powder was obtained (0.07 g, 70%), which was recrystallised from CH_3CN/Et_2O. White crystals were obtained suitable for X-ray diffraction measurements.

X-Ray Diffraction Methods and Structure Refinements

Single crystal X-ray data were collected at 100(2) K on a Bruker Apex II CCD diffractometer using graphite-monochromated Mo-Kα radiation (λ = 0.71073 Å), an Oxford Cryosystems Cobra low temperature device and a MiTeGen micromount. Bruker APEX47 software was used to correct for Lorentz and polarization effects. The structures were solved and refined using the Bruker SHELXTL Software Package.

Complex 4. A specimen of $C_{41}H_{49}ClMn_2N_6O_{10}$, approximate dimensions 0.050 mm x 0.080 mm x 0.480 mm, was used for the X-ray crystallographic analysis. Bruker APEX software was used to collect, correct for Lorentz and polarization effects, and reduce the data.[35] The structure was solved with the XT[36] structure solution program using Intrinsic Phasing and refined with the XL[37] refinement package using Least Squares minimisation with Olex2, using the space group $P\bar{1}$, with Z = 2 for the formula unit, $C_{41}H_{49}ClMn_2N_6O_{10}$.

Refinement Note: Diethyl ether solvent disordered over two positions and refined with restraints (SIMU, SADI) with 85:15% occupancy.

Complex 10. A specimen of $C_{37}H_{39}Cl_2Mn_2N_6O_{13}$, approximate dimensions 0.040 mm x 0.070 mm x 0.190 mm, was used for the X-ray crystallographic analysis. Bruker APEX software was used to collect, correct for Lorentz and polarization effects, and reduce the data.[35] The structure was solved and refined using the Bruker SHELXTL Software Package,[35] using the space group $P2_1/c$, with Z = 4 for the formula unit, $C_{37}H_{39}Cl_2Mn_2N_6O_{13}$

Mn6: ($[Mn^{II}_4Mn^{III}_2(O_2)(CNCH_3)_4(O_2CC_6H_5)_{10}]$): Refined as an inversion twin.

Complex 11. A specimen of $C_{31}H_{35}Cl_3Mn_2N_8O_{13}$, approximate dimensions 0.060 mm x 0.100 mm x 0.170 mm, was used for the X-ray crystallographic analysis. Bruker APEX software was used to correct for Lorentz and polarization effects.

Table 5.2. Crystal data and structure refinement for $[Mn_2(O_2CCH_3)_2(BPMP)](ClO_4)$ (**4**).

Empirical formula	$C_{41}H_{49}ClMn_2N_6O_{10}$	
Formula weight	931.19	
Temperature	100(2) K	
Wavelength	0.71073 Å	
Crystal system	Triclinic	
Space group	$P\bar{1}$	
Unit cell dimensions	a = 10.1121(5) Å	α = 102.7359(18)°.
	b = 12.2093(6) Å	β = 93.6573(17)°.
	c = 17.7134(9) Å	γ = 94.8898(18)°.
Volume	2117.67(18) $Å^3$	
Z	2	
Density (calculated)	1.460 Mg/m^3	
Absorption coefficient	0.724 mm^{-1}	
F(000)	968	
Crystal size	0.48 x 0.08 x 0.05 mm^3	
Theta range for data collection	2.434 to 26.489°.	
Index ranges	$-12\leq h\leq 12$, $-15\leq k\leq 15$, $-22\leq l\leq 22$	
Reflections collected	27769	
Independent reflections	8739 [R(int) = 0.0662]	
Completeness to theta = 25.242°	99.8 %	
Absorption correction	Semi-empirical from equivalents	
Max. and min. transmission	0.7454 and 0.6238	
Refinement method	Full-matrix least-squares on F^2	
Data / restraints / parameters	8739 / 55 / 592	
Goodness-of-fit on F^2	1.029	
Final R indices [$I>2\sigma(I)$]	R1 = 0.0601, wR2 = 0.1372	
R indices (all data)	R1 = 0.1037, wR2 = 0.1593	
Largest diff. peak and hole	0.726 and -0.663 $e.Å^{-3}$	

Table 5.3. Crystal data and structure refinement for mixed valent [$Mn^{II}Mn^{III}(O_2CCH_3)_2(BPMP)](ClO_4)_2$ (**10**).

Empirical formula	$C_{37}H_{39}Cl_2Mn_2N_6O_{13}$	
Formula weight	956.52	
Temperature	100(2) K	
Wavelength	0.71073 Å	
Crystal system	Monoclinic	
Space group	$P2_1/c$	
Unit cell dimensions	a = 9.9694(5) Å	α = 90°.
	b = 36.1013(16) Å	β = 104.1260(18)°.
	c = 11.4752(5) Å	γ = 90°.
Volume	4005.1(3) $Å^3$	
Z	4	
Density (calculated)	1.586 Mg/m^3	
Absorption coefficient	0.838 mm^{-1}	
F(000)	1964	
Crystal size	0.19 x 0.07 x 0.04 mm^3	
Theta range for data collection	2.680 to 25.400°.	
Index ranges	$-11\leq h\leq 12$, $-43\leq k\leq 43$, $-13\leq l\leq 13$	
Reflections collected	37317	
Independent reflections	7331 [R(int) = 0.1867]	
Completeness to theta = 25.242°	99.8 %	
Absorption correction	Semi-empirical from equivalents	
Max. and min. transmission	0.7452 and 0.6391	
Refinement method	Full-matrix least-squares on F^2	
Data / restraints / parameters	7331 / 0 / 544	
Goodness-of-fit on F^2	1.021	
Final R indices [I>2σ(I)]	R1 = 0.0659, wR2 = 0.1463	
R indices (all data)	R1 = 0.1519, wR2 = 0.1891	
Largest diff. peak and hole	0.929 and -0.560 $e.Å^{-3}$	

Table 5.4. Crystal data and structure refinement for $[Mn^{II}_4Mn^{III}_2(O)_2(CNCH_3)_4(O_2CC_6H_5)_{10}]$.

Empirical formula	$C_{78}H_{62}Mn_6N_4O_{22}$	
Formula weight	1736.95	
Temperature	100(2) K	
Wavelength	0.71073 Å	
Crystal system	Orthorhombic	
Space group	$P2_12_12_1$	
Unit cell dimensions	a = 17.1478(6) Å	α = 90°.
	b = 24.1221(8) Å	β = 90°.
	c = 37.6032(13) Å	γ = 90°.
Volume	15554.2(9) $Å^3$	
Z	8	
Density (calculated)	1.483 Mg/m^3	
Absorption coefficient	1.021 mm^{-1}	
F(000)	7072	
Crystal size	0.260 x 0.075 x 0.060 mm^3	
Theta range for data collection	1.373 to 27.506°.	
Index ranges	$-21\leq h\leq 21$, $-30\leq k\leq 31$, $-48\leq l\leq 48$	
Reflections collected	322299	
Independent reflections	34641 [R(int) = 0.1022]	
Completeness to theta = 25.242°	100.0 %	
Absorption correction	Semi-empirical from equivalents	
Max. and min. transmission	0.7456 and 0.6143	
Refinement method	Full-matrix least-squares on F^2	
Data / restraints / parameters	34641 / 12 / 1990	
Goodness-of-fit on F^2	1.054	
Final R indices [$I>2\sigma(I)$]	R1 = 0.0469, wR2 = 0.0732	
R indices (all data)	R1 = 0.0964, wR2 = 0.0859	
Absolute structure parameter	0.492(13)	
Largest diff. peak and hole	0.460 and -0.473 $e.Å^{-3}$	

Table 5.5. Crystal data and structure refinement for $[Mn_2(ClO_4^-)_2(CH_3CN)_2(HPTP)](ClO_4^-)$ (**11**).

Empirical formula	$C_{31}H_{35}Cl_3Mn_2N_8O_{13}$	
Formula weight	943.90	
Temperature	100(2) K	
Wavelength	0.71073 Å	
Crystal system	Monoclinic	
Space group	$P2_1/n$	
Unit cell dimensions	a = 12.9129(6) Å	α = 90°.
	b = 14.8713(7) Å	β = 96.0556(11)°.
	c = 19.7026(9) Å	γ = 90°.
Volume	3762.4(3) $Å^3$	
Z	4	
Density (calculated)	1.666 Mg/m^3	
Absorption coefficient	0.960 mm^{-1}	
F(000)	1928	
Crystal size	0.170 x 0.100 x 0.060 mm^3	
Theta range for data collection	2.079 to 29.263°.	
Index ranges	$-17\leq h\leq 17$, $-20\leq k\leq 20$, $-27\leq l\leq 27$	
Reflections collected	72108	
Independent reflections	10219 [R(int) = 0.0643]	
Completeness to theta = 25.242°	99.9 %	
Absorption correction	Semi-empirical from equivalents	
Max. and min. transmission	0.7458 and 0.6290	
Refinement method	Full-matrix least-squares on F^2	
Data / restraints / parameters	10219 / 0 / 516	
Goodness-of-fit on F^2	1.022	
Final R indices [I>2σ(I)]	R1 = 0.0365, wR2 = 0.0920	
R indices (all data)	R1 = 0.0582, wR2 = 0.1020	
Largest diff. peak and hole	0.522 and -0.507 $e.Å^{-3}$	

Table 5.6. Comparison of selected bond lengths of the complexes **4** and **10** synthesised by us to those previously reported.

Selected Bond Lengths (Å)	**Complex**			
	4[this work]	$[Mn^{II,II}_2(O_2CCH_3)_2(BPMP)](ClO_4)$ [16]	**10**[this work]	$[Mn^{II,III}_2(O_2CCH_3)_2(BPMP)](ClO_4)_2$ [17]
Mn1-Mn2	3.41	3.41	3.45	3.45
Mn1-$O_{alkoxide}$	2.11	2.12	1.90	1.90 (O5)
Mn2-$O_{alkoxide}$	2.1	2.10	2.18	2.19 (O5)
Mn1-O_{carb48}	2.11	2.1 (O4)	2.12	2.17 (O2)
Mn1-O_{carb44}	2.15	2.16 (O2)	1.91	2.07 (O4)
Mn2-O_{carb45}	2.15	2.15 (O5)	2.09	1.93 (O1)
Mn2-O_{carb41}	2.09	2.11 (O3)	2.14	2.09 (O3)

References

[1] A. M. Magherusan, A. Zhou, E. R. Farquhar, M. Garcia-Melchor, B. Twamley, L. Que, Jr., A. R. McDonald, *Angew. Chem. Int. Ed. Engl.* **2018**, *57*, 918-922.

[2] N. Kitajima, H. Komatsuzaki, S. Hikichi, M. Osawa, Y. Moro-oka, *J. Am. Chem. Soc.* **1994**, *116*, 11596.

[3] U. P. Singh, A. K. Sharma, S. Hikichi, H. Komatsuzaki, Y. Moro-oka, M. Akita, *Inorg. Chim. Acta* **2006**, *359*, 4407-4411.

[4] M. S. Seo, J. Y. Kim, J. Annaraj, Y. Kim, Y. M. Lee, S. J. Kim, J. Kim, W. Nam, *Angew. Chem. Int. Ed.* **2007**, *46*, 377-380.

[5] J. Annaraj, J. Cho, Y. M. Lee, S. Y. Kim, R. Latifi, S. P. de Visser, W. Nam, *Angew. Chem. Int. Ed.* **2009**, *48*, 4150-4153.

[6] J. Cho, R. Sarangi, W. Nam, *Acc. Chem. Res.* **2012**, *45*, 1321-1330.

[7] H. Kang, J. Cho, K. B. Cho, T. Nomura, T. Ogura, W. Nam, *Chem. Eur. J.* **2013**, *19*, 14119-14125.

[8] H. E. Colmer, R. A. Geiger, D. F. Leto, G. B. Wijeratne, V. W. Day, T. A. Jackson, *Dalton Trans.* **2014**, *43*, 17949-17963.

[9] R. A. Geiger, G. B. Wijeratne, V. W. Day, T. A. Jackson, *Eur. J. Inorg. Chem.* **2012**, *2012*, 1598-1608.

[10] R. A. Geiger, D. F. Leto, S. Chattopadhyay, P. Dorlet, E. Anxolabehere-Mallart, T. A. Jackson, *Inorg. Chem.* **2011**, *50*, 10190-10203.

[11] R. A. Geiger, S. Chattopadhyay, V. W. Day, T. A. Jackson, *J. Am. Chem. Soc.* **2010**, *132*, 2821-2831.

[12] R. A. Geiger, S. Chattopadhyay, V. W. Day, T. A. Jackson, *Dalton Trans.* **2011**, *40*, 1707-1715.

[13] N. Saravanan, M. Sankaralingam, M. Palaniandavar, *RSC Advances* **2014**, *4*, 12000.

[14] S. Y. Dong, Menage, B. A. Brennan, T. E. Elgren, H. G. Jang, L. L. Pearce, L. Que, *J. Am. Chem. Soc.* **1993**, *115*, 1851-1859.

[15] J. A. Cotruvo, Jr., T. A. Stich, R. D. Britt, J. Stubbe, *J. Am. Chem. Soc.* **2013**, *135*, 4027-4039.

[16] S. Blanchard, G. Blondin, E. Riviere, M. Nierlich, J. J. Girerd, *Inorg. Chem.* **2003**, *42*, 4568-4578.

[17] H. Diril, H. R. Chang, M. J. Nilges, X. Zhang, J. A. Potenza, H. J. Schugar, S. S. Isied, D. N. Hendrickson, *J. Am. Chem. Soc.* **1989**, *111*, 5102-5114.

[18] M. Suzuki, M. Mikuriya, S. Murata, A. Uehara, H. Oshio, S. Kida, K. Saito, *Bull. Chem. Soc. Jpn.* **1987**, *60*, 4305-4312.

[19] G. S. Siluvai, N. N. Murthy, *Polyhedron* **2009**, *28*, 2149-2156.

[20] S. T. Frey, N. N. Murthy, S. T. Weintraub, L. K. Thompson, K. D. Karlin, *Inorg. Chem.* **1997**, *36*, 956-957.

[21] P. Seth, A. Ghosh, *RSC Advances* **2013**, *3*, 3717.

[22] K. S. Gavrilenko, S. V. Punin, O. Cador, S. Golhen, L. Ouahab, V. V. Pavlishchuk, *Inorg. Chem.* **2005**, *44*, 5903-5910.

[23] C.-I. Yang, K.-H. Cheng, M. Nakano, G.-H. Lee, H.-L. Tsai, *Polyhedron* **2009**, *28*, 1842-1851.

[24] P. Kar, Y. Ida, T. Kanetomo, M. G. Drew, T. Ishida, A. Ghosh, *Dalton Trans.* **2015**, *44*, 9795-9804.

[25] A. D. Fedorenko, L. N. Mazalov, E. Y. Fursova, V. I. Ovcharenko, A. V. Kalinkin, S. A. Lavrukhina, *J. Struct. Chem.* **2017**, *58*, 1166-1172.

[26] C. C. Stoumpos, R. Inglis, O. Roubeau, H. Sartzi, A. A. Kitos, C. J. Milios, G. Aromi, A. J. Tasiopoulos, V. Nastopoulos, E. K. Brechin, S. P. Perlepes, *Inorg. Chem.* **2010**, *49*, 4388-4390.

[27] J. Adhikary, P. Chakraborty, S. Das, T. Chattopadhyay, A. Bauza, S. K. Chattopadhyay, B. Ghosh, F. A. Mautner, A. Frontera, D. Das, *Inorg. Chem.* **2013**, *52*, 13442-13452.

[28] A. L. Hughes, *Immunogenetics* **1999**, *49*, 106-114.

[29] A. K. Boal, J. A. Cotruvo, Jr., J. Stubbe, A. C. Rosenzweig, *Science* **2010**, *329*, 1526-1530.

[30] A. K. Boal, J. A. Cotruvo, Jr., J. Stubbe, A. C. Rosenzweig, *Biochemistry* **2012**, *51*, 3861-3871.

[31] N. Cox, H. Ogata, P. Stolle, E. Reijerse, G. Auling, W. Lubitz, *J. Am. Chem. Soc.* **2010**, *132*, 11197-11213.
[32] S. Torelli, C. Belle, I. Gautier-Luneau, J. L. Pierre, E. Saint-Aman, J. M. Latour, L. Le Pape, D. Luneau, *Inorg. Chem.* **2000**, *39*, 3526-3536.
[33] M. A. Raycroft, C. I. Maxwell, R. A. Oldham, A. S. Andrea, A. A. Neverov, R. S. Brown, *Inorg. Chem.* **2012**, *51*, 10325-10333.
[34] Y. Dong, S. Menage, B. A. Brennan, T. E. Elgren, H. G. Jang, L. L. Pearce, L. Que, *J. Am. Chem. Soc.* **1993**, *115*, 1851-1859.
[35] Bruker, *APEX2 Ver. 2014.11-0, Bruker AXS Inc., Madison, WI, USA.*, 1-142.
[36] G. M. Sheldrick, *Acta Crystallogr. C Struct. Chem.* **2015**, *71*, 3-8.
[37] G. M. Sheldrick, *Acta Crystallogr. A* **2008**, *64*, 112-122.

Chapter 6

Catechol oxidase activity of comparable dimanganese and dicopper complexes

A manuscript detailing the work described in this chapter has been submitted for publication. Daniel Nelis (Trinity College Dublin) carried out the copper complexes syntheses; XRD data collection and structure solutions and refinements were done by Dr Brendan Twamley (Trinity College Dublin).

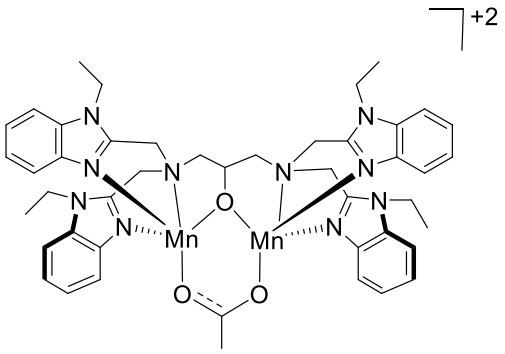
+2
N
Mn
O

1

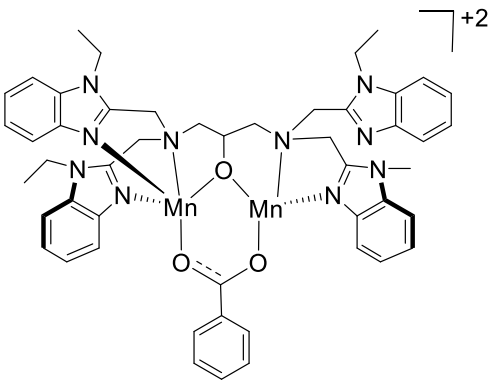
+2
N
Mn
O

12

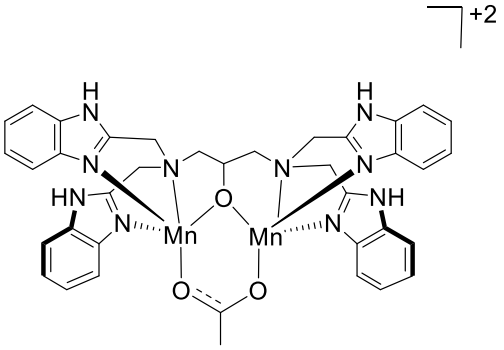
+2
H
N
HN
NH
Mn
O

3

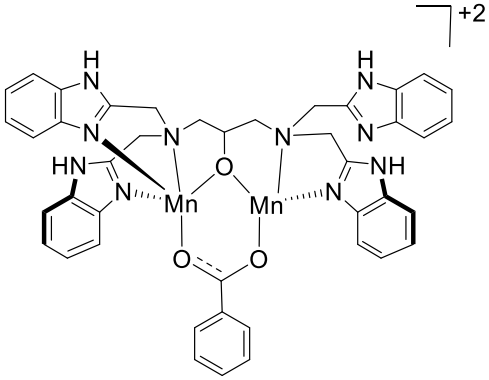
+2
H
N
HN
NH
Mn
O

13

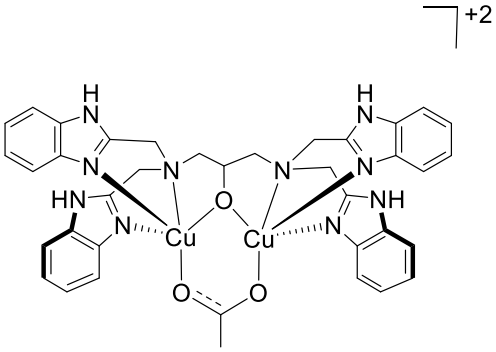
+2
H
N
HN
NH
Cu
O

14

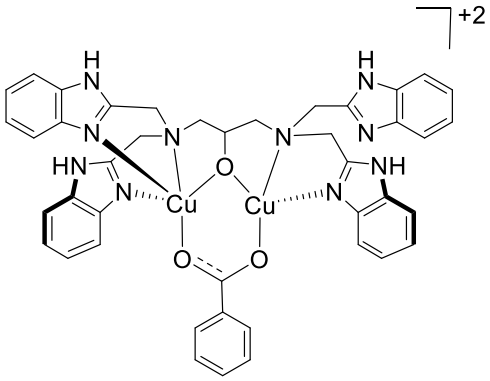
+2
H
N
HN
NH
Cu
O

15

6.1 Introduction

Metalloproteins containing copper (Cu) atoms in their active site are involved as catalysts in a variety of biological processes such as the oxidation of organic substrates or electron transfer. Three different Cu proteins have been reported: type-1, type-2 and type-3 based on their different spectroscopic features.[1, 2]

Type-1 Cu proteins exhibit an intense blue colour in the oxidised state and thus they were known as "blue copper proteins". The type-1 active site is found in Cu proteins such as ascorbate oxidase and nitrite reductase.[1, 3] Type-2 Cu proteins have a light blue colour in the oxidised state arising from *d-d* transitions of the Cu(II) ions. In the case of type-1 Cu proteins the blue colour originated from a sulfur to Cu^{II} charge transfer. The type-2 Cu proteins are known as "normal" Cu proteins. Examples of this class included: copper-zinc superoxide dismutase, dopamine-β-hydroxylase, galactose oxidase.[4] The active site of type-3 Cu proteins consist of a Cu_2 core, in which the two Cu ions are surrounded by three nitrogen donor atoms from histidine residues.[5] The proteins that belong to this class are the tyrosinases, catechol oxidases and the hemocyanins.[6, 7] All of these three proteins are able to reversibly bind dioxygen at ambient conditions.

We are mainly interested in catechol oxidase, a type-3 Cu protein, that uses a process known as catecholase activity to catalyse the oxidation of *o*-diphenols (catechols) to the corresponding quinones. Catechol oxidases are found in plant tissues, some insects and crustaceans.[8] One of the key roles of catechol oxidases is to maintain disease resistance in plants, to protect damaged tissues against pathogens and insects.[7] Moreover the conversion of the catechol to the quinone is very important in medical diagnosis for the determination of the hormonal catecholamines adrenaline, noradrenaline, and dopa.[9, 10]

The oxidation of catechol to the corresponding quinones occurs through a 4-electron reduction of dioxygen to water.[1] A mechanism for the catalytic process was proposed by Krebs and co-workers, based on biochemical, spectroscopic[5, 11, 12] and structural data (Scheme 6.1).[13] The catalytic cycle started with the *met* (resting form of the enzyme) form of catechol oxidase. The Cu^{II}_2 centre of the *met* form reacted with one equivalent of catechol.[1] This resulted in the formation of the quinone and the reduced *deoxy* Cu^{I}_2 state of the catechol oxidase. Subsequently, the Cu^{I}_2 active site reacted with O_2 replacing the solvent molecule (H_2O) bonded to CuA site in the reduced enzyme form. Dioxygen was proposed to be bound in a bridging side-on μ-η^2:η^2 binding mode based on UV-Vis spectroscopy and Raman data.[11] A Cu···Cu separation of 3.8 Å was determined by extended X-ray absorption fine structure (EXAFS)

spectroscopy for the *oxy* state.[11] In this model (Scheme 6.1), the CuB site was six-coordinated, in a tetragonal planar geometry and the CuA site was in a tetragonal pyramidal geometry, having a vacant sixth coordination site. In this proposed catechol structure, two electrons were transferred from the substrate to the peroxide, the O-O bond was cleaved, water was lost and the quinone product formed. Thus, the catalytic cycle was complete with the restoration of the *met* state of the catechol enzyme.

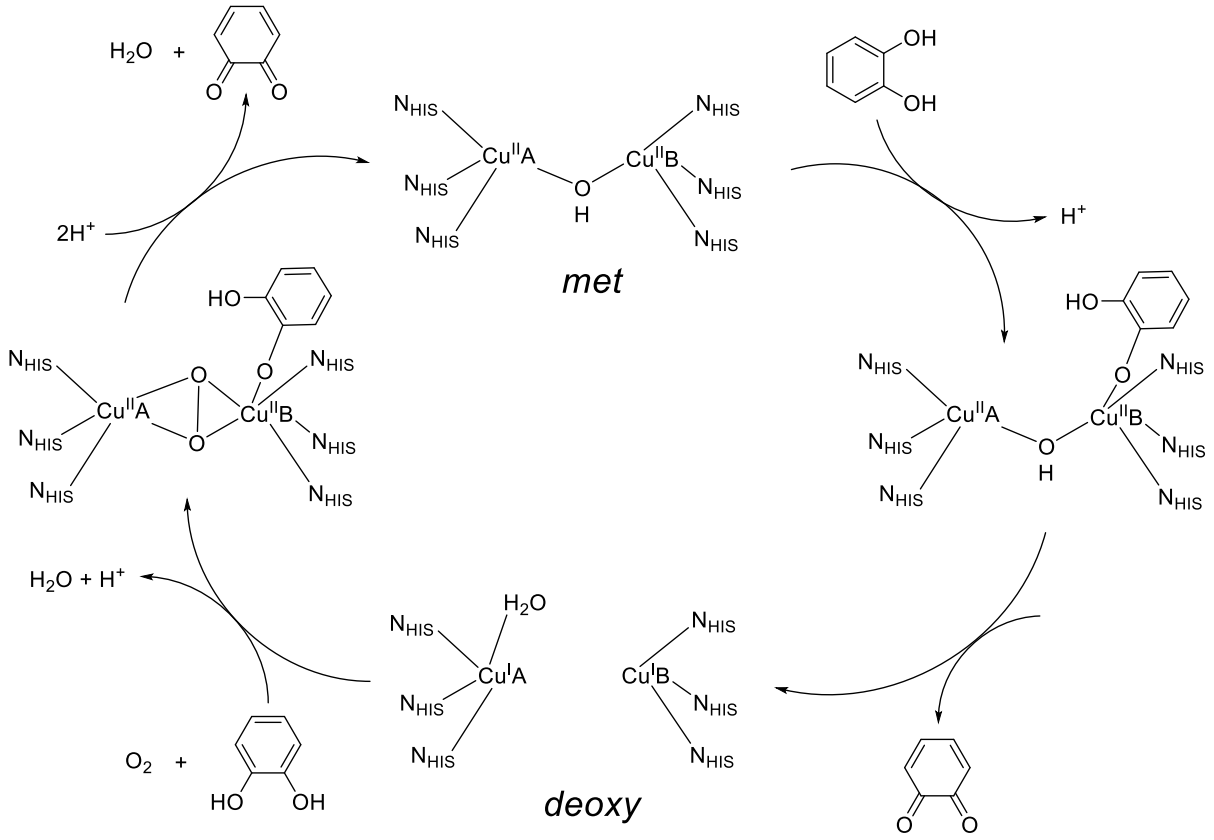

Scheme 6.1. Catalytic cycle of catechol oxidase from sweet potatoes (*Ipomoea batatas*). Two molecules of catechol are oxidised, coupled with the reduction of molecular oxygen to water.[5]

A variety of biomimetic catalysts that mimic the catechol oxidase activity have been reported to get a better understanding of the active site and mechanism of reaction of these Cu proteins.[14-20] Recently Mn complexes have emerged for studying the catecholase activity even though no Mn containing catechol oxidase enzyme has been discovered to date.[21-24] The postulated mechanism of catechol oxidase and Cu synthetic models action is the reduction of Cu^{II} to Cu^{I} by the catechol, inducing oxidation to the quinone product.[14, 16-19] For Mn, Ni, and Zn mimics, electron paramagnetic resonance (EPR) experiments show the generation of radicals when complexes were reacted with the catechol. Thus a mechanism, involving a radical pathway has been proposed for these systems.[25-27] Das and co-workers proposed a reaction mechanism for a series of mononuclear Mn^{III} complexes involving the reduction of the Mn^{III}

centre to Mn^{II} with the concomitant oxidation of the catechol substrate.[28] We were interested in exploring further the role of the metal ion in catechol oxidase reactivity. Specifically, we wanted to explore the relative effects of exchanging Mn for Cu in the same ligand environment and the effect of employing an early transition metal (Mn) versus a late transition metal (Cu) in catechol oxidation.

Besides the catechol oxidases, we maintain a keen interest in the analogous Mn_2 ribonucleotide reductases (RNRs). The active site of this enzyme contains a Mn_2 core. RNRs are involved in DNA biosynthesis (chapters 1-3). Class Ib RNRs can use either a Mn^{II}_2 or a Fe^{II}_2 metallocofactor for catalytic activity. We have previously investigated one of the Mn^{II}_2 complexes described below as class Ib RNR models. The Mn^{II}_2 complex **1** proved to be an excellent RNR model (chapter 2).[29] One of the goals of this research was to synthesise further synthetic mimics of the class Ib Mn^{II}_2 RNRs active site.

To the best of our knowledge Mn_2 and Cu_2 complexes supported by the same ligand framework have not been investigated for comparison of their catecholase activity. We wanted to investigate their catecholase activity under nearly identical experimental conditions to compare their catalytic efficiency and to understand the role of the central metal ion. We herein report the synthesis of six dinuclear complexes (Figure 6.1), their full characterisation, and their aerobic catecholase reactivity (Scheme 6.2).

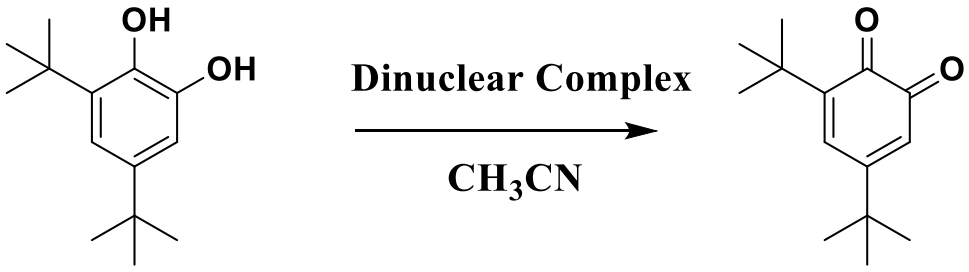

Scheme 6.2. Oxidation of 3,5-di-*tert*-butylcatechol (3,5-DTBC) by Mn^{II}_2 and Cu^{II}_2 complexes.

6.2 Synthesis and characterisation of Mn^{II}_2 and Cu^{II}_2 complexes

The di-nucleating ligands N,N,N',N'-tetrakis(2-benzimidazolylmethyl)-2-hydroxo-1,3-diaminopropane (HPTB) and N,N,N',N'-tetrakis(2-(1-ethylbenzimidazolyl))-2-hydroxy-1,3-diaminopropane (N-Et-HPTB) were synthesised as previously described (see experimental section and appendix for details).[30] $[Mn_2(O_2CR)(X\text{-}HPTB)](ClO_4)_2$ (where X = C_2H_5: R =

CH_3 (**1**), C_6H_5 (**12**); and X = H: R = CH_3 (**3**), R = C_6H_5 (**13**)) (Figure 6.1) were synthesised using slight modifications of the procedure reported for the preparation of $[Mn_2(O_2CCH_3)(HPTB)](ClO_4)_2$ (**3**).[31] $[Cu_2(O_2CR)(HPTB)](ClO_4)_2$ (where R = CH_3 (**14**), C_6H_5 (**15**)) were synthesised using a procedure reported by Reed and co-workers for the preparation of $[Cu_2(O_2CCH_3)(N\text{-Et-HPTB})](ClO_4)_2$.[30, 32] All complexes were obtained in reasonably good yields (**1**, 87%; **12**, 86%; **3**, 57%; **13**, 56%; **14**, 43%; **15**, 45%).

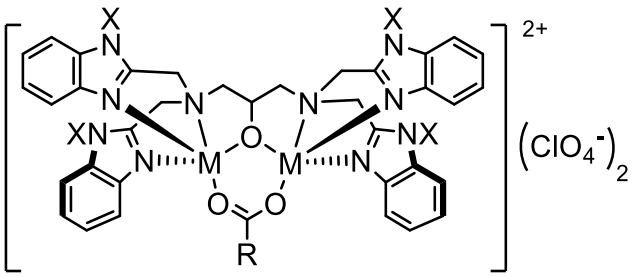

M = Mn; X = C_2H_5; R = CH_3 (**1**), C_6H_5 (**12**)
M = Mn; X = H; R = CH_3 (**3**), C_6H_5 (**13**)
M = Cu; X = H; R = CH_3 (**14**), C_6H_5 (**15**)

Figure 6.1. Structure of Mn^{II}_2 and Cu^{II}_2 complexes **1**, **3**, **12**-**15**.

6.2.1 Mass Spectrometry

Matrix assisted laser desorption/ionisation time of flight (MALDI-ToF) mass spectrometry analysis of complexes **1** and **2** showed prominent mass peaks attributable to the mono-cations $\{[Mn_2(O_2CR)(N\text{-Et-HPTB})](ClO_4)\}^+$ (where R = CH_3 (**1**), C_6H_5 (**12**), Figures A.45-A.46).[29] Electrospray ionisation mass spectrometry (ESI-MS) analysis of complexes **3** and **13** displayed mass peaks that correlate with the di-cations $[Mn_2(O_2CR)(HPTB)]^{2+}$ (R = CH_3 (**3**), R = C_6H_5 (**13**), Figures A.47-A.48). ESI-MS analysis of **14** and **15** also exhibited mass peaks corresponding to the monocations $\{[Cu_2(O_2CR)(HPTB)](ClO_4)\}^+$ (R = CH_3 (**14**), C_6H_5 (**15**), Figures A.49-A.50). ^{1}H nuclear magnetic resonance (NMR) analysis of complexes **1**, **3** and **12**-**13** yielded featureless spectra, presumably due to the broadening effect caused by the paramagnetic Mn^{II} ions. ^{1}H NMR analysis for complexes **14** and **15** matched those previously reported (Figures A.51-A.52).[32] Finally, elemental combustion analysis confirmed the elemental composition for complexes **1**, **3** and **12**-**15** (see experimental section).

6.2.2 ATR-FTIR

A comparison of the attenuated total reflectance Fourier transform infrared (ATR-FTIR) spectra of complexes **1**, **3** and **12-15** (Figures A.53-A.55, Table 6.1) showed that they all displayed very similar vibrational properties. The $\nu_{C=O}$ values obtained for the asymmetric (1540-1560 cm^{-1}) and symmetric (1410-1450 cm^{-1}) stretches in complexes **1**, **3** and **12-15** agree well with those previously reported for complex **3** as well as other Cu^{II}_2 complexes bearing carboxylate bridges.[31, 33] Furthermore, the difference between the asymmetric and symmetric stretches (Δ, Table 6.1) for each complex was in the range expected for a bridging bidentate carboxylate ligand.[34, 35] Previously reported carboxylate-bridged Mn^{II}_2 complexes $[Mn_2(O_2CPh)_2(BPMP)](ClO_4)$ (HBPMP = 2,6-bis[bis(2-pyridylmethyl)aminomethyl]-4-methylphenol) displayed features at $\nu_{C=O}$ = 1570 cm^{-1} and 1400 cm^{-1},[36] while analogous Cu^{II}_2 complexes $[Cu_2(OAc)(P2\text{-}O)](ClO_4)_2$ and $[Cu_2(P2'\text{-}O)(OAc)(H_2O)](ClO_4)_2$, (P2-OH = N,N',N'',N'''-tetrakis(2-pyridylethyl)-1,3-diamino-2-propanol, OAc = O_2CCH_3), exhibited $\nu_{C=O}$ = 1560 and 1460 cm^{-1}.[33] All six complexes displayed a strong stretch at ν = 1080 cm^{-1} corresponding to free ClO_4^- anion (Figures A.53-A.55). Unfortunately, the ν_{asym}(Mn–O–Mn) stretch, expected around 720-750 cm^{-1},[37] could not be assigned in complexes **1**, **3** and **12-13** due to a strong ligand-based feature that was present (730-760 cm^{-1}, Figures A.56-A.57 for ligand spectra). Overall, the vibrational properties of complexes **1**, **3** and **12-15** compared well to analogous complexes previously reported in the literature and indicated that an anionic carboxylate ligand bridged the metal centres.

Table 6.1. Comparison of carboxylate ν_{asym} and ν_{sym} in dinuclear complexes **1**, **3** and **12-15** (all values in cm^{-1}).

	1[29]	**12**	**3**this work	**3**[31]	**13**	**14**	**15**
ν_{asym}C=O	1560	1547	1540	1564	1549	1560	1541
ν_{sym}C=O	1447	1450	1412	1428	1450	1451	1448
Δ	113	97	128	136	99	109	93

6.2.3 X-ray crystallography

Complexes **12**, **13**, **14**, and **15** were recrystallized from acetonitrile by diethylether (Et_2O) vapour diffusion to yield crystals suitable for X-ray diffraction measurements (Tables 6.7-6.8). We previously reported the structure of **1**,[29] while the structure of **3** has been described elsewhere.[31] Each complex was found to consist of two five-coordinate metal atoms in either a square pyramidal or a distorted trigonal-bipyramidal geometry (Figure 6.2). The geometry at each metal centre was determined by the calculation of the corresponding τ_5 value.[38] This allowed us to determine if the metal site had more trigonal bipyramidal or square pyramidal character.

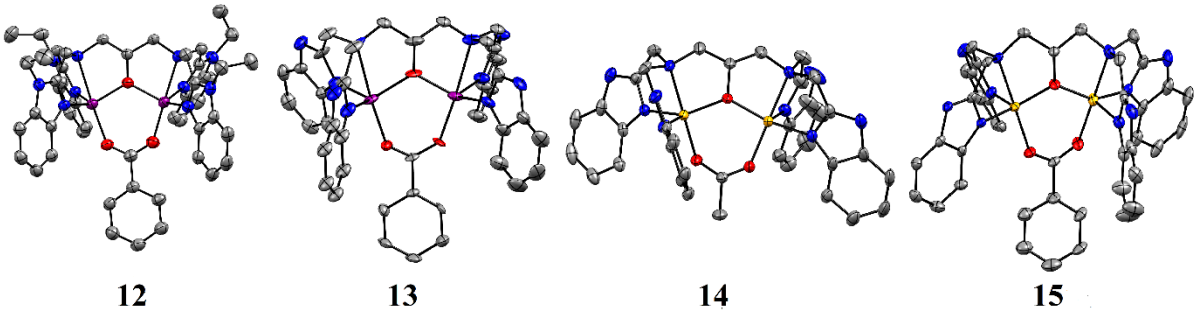

Figure 6.2. ORTEP plots of complexes **12-15** (from left to right). Hydrogen atoms and counter anions have been removed for clarity (purple = Mn, yellow = Cu, grey = C, blue = N, red = O). Ellipsoids are shown at 50% probability level.

A τ_5 value of 0 corresponds to a perfect square pyramidal geometry, while a τ_5 value of 1 indicates a perfect trigonal bipyramidal geometry.[38] Intermediary values indicated that the metal centre had a distorted structure, in between the two extremes. The Mn centres in complexes **1**, **12** and **13** were in an almost perfect trigonal bipyramidal geometry (Table 6.2), while for complex **14**, one of the Cu centres was best described as distorted square pyramidal. The axial position of this square pyramid was capped by a long Cu-N_{benz} bond. This increased bond length was likely due to Jahn-Teller distortion of the square pyramid. For the other Cu centre in **14** and one of the Cu centres of complex **6**, the τ_5 value was ~0.5, while the second Cu centre in complex **15** had a τ_5 value of 0.7, a distorted trigonal bipyramidal structure. In summary, the Mn ions in complexes **1**, **3**, **12-13** displayed trigonal bipyramidal geometry in all complexes, and the Cu ions in **14** and **15** tended to display more distorted structures (Figure 6.2, Table 6.2).

Table 6.2. τ_5 values of dinuclear complexes **1**, **12-15** (M = Mn or Cu).

τ_5	**1**[29]	**12**	**13**	**14**	**15**
M(1)-left	0.81	1.03	0.96	0.34	0.51
M(2)-right	0.98	1.05	0.96	0.55	0.7

In the X-ray crystallography determined structures of **12-15**, the O-atoms of the carboxylate ligand (acetate or benzoate) bridged the two metal atoms in an axial position, corroborating our ATR-IR results that indicated a bridging carboxylate was present. The alkoxide O-atom of the heptadentate (N-Et-)HPTB ligand coordinated to the two metal atoms in equatorial sites, while the remaining N-atoms of the HPTB ligand occupied equatorial (benzimidazole N) and axial (amine N) sites. These observations were consistent with the structures reported for **1**[29] and **3**[31] and other complexes supported by the HPTB family of ligands.[32, 39-42] However, in the previously described structure of **3**, a butanol ligand was bound to one of the Mn^{II} ions, making it hexacoordinate, while the second Mn ion was pentacoordinate. In contrast, in **1**, **12** and **13-15** all metal ions displayed coordination numbers of five, with no solvent bound.

We originally prepared Mn_2 complexes **1**, **3**, **12-13** as mimics of the active site of the class Ib Mn_2 Ribonucleotide Reductases (RNRs). The Mn···Mn distance in the X-ray crystal structure reported for class Ib Mn_2 RNR from *E. coli* was 3.7 Å,[43] from *B. subtilis* was 3.9 Å,[44] while from *C. ammoniagenes* a 3.3 Å metal-metal distance[45] was determined. In both *E. coli* and *B. subtilis*, the Mn ions were determined to be in the +2-oxidation state, but in *C. ammoniagenes* in the +3-oxidation state. The metal-metal separation for all four Mn_2 complexes **1**, **3**, **12-13** were very similar to each other (Table 6.3: 3.6, 3.5, 3.54, 3.55 Å, respectively). The Mn···Mn distances were slightly larger in the Mn^{II}_2 enzymatic active sites than in complexes **1**, **3**, **12-13**. The coordination number in the class Ib Mn_2 RNR active sites were either 5- or 6-coordinate, with a vacant site often postulated as the site of O_2-activation. The coordination numbers in **1**, **3**, **12-13** were five. Overall complexes **1**, **3**, **12-13** are thus reasonably reliable structural mimics for class Ib Mn_2 RNRs (Table 6.3).

Table 6.3. Comparison of structural properties of complexes **1**, **3**, **12-13** and class Ib Mn_2 RNR active sites.

	Model Complex								Class Ib Mn_2-RNRs					
	1[29]		**12**		**3**[31]		**13**		*E. coli* (Mn^{II}_2)[43]		*B. subtilis* (Mn^{II}_2)[44]		*C. ammoniagenes* (Mn^{III}_2)[45]	
	Mn1	Mn2	Mn1	Mn2	Mn1	Mn2	Mn1	Mn2	Mn1	Mn2	Mn1	Mn2	Mn1	Mn2
Coordination Number	5	5	5	5	5	6	5	5	6	6	6	5	6	5
Mn···Mn (Å)	3.6		3.5		3.54		3.55		3.7		3.9		3.3	

The average Mn-N_{amine} and Mn-N_{benz} bond lengths of complex **12** were very close in values when compared to that of previously reported complex **1**.[29] Likewise, the average Mn-N_{amine} and Mn-N_{benz} bond lengths of complex **13** were very close in values when compared to that of previously reported complex **3** (Table 6.7). This was expected as complexes **1** and **12** were supported by the same ligand (N-Et-HPTB) while complexes **3**[31] and **13** were supported by the HPTB ligand. Comparison of the average Mn-N_{amine} and Mn-N_{benz} bond lengths of the Mn complexes **1**/**12** to that of **3**/**13**, showed those of complexes **1**/**12** to be shorter (Table 6.7). This was most likely due to the higher basicity of the alkylated ligand (N-Et-HPTB) versus the unalkylated HPTB ligand. Finally, a comparison of average metal-N_{amine} and metal-N_{benz} bond lengths of Cu complexes **14**/**15** to that of Mn complexes **1**, **3**, **12-13** showed those of complexes **14**/**15** to be shorter (Table 6.7). This can be attributed to a slightly larger atomic radius of the Mn atoms in **1**, **3**, **12-13** compared to the Cu atoms in **14** and **15**.

Apart from differences in Mn–N/O bond lengths in complexes **1**, **3**, **12-15** we also noticed some structural differences between the acetate (**1**) and benzoate (**12**) bridged complexes. By overlaying the crystal structures of complexes **1** with **12**, a noticeable difference in the positioning of the benzimidazole groups was observed depending on whether an acetate or benzoate bridge was present (Figure 6.3). This was evident as an apparent closing of the benzimidazole 'wings' in the acetate bridged complex **1** and an opening of the benzimidazole 'wings' in the benzoate bridged complex **12**. The closing of the benzimidazole 'wings' resulted in a slightly longer Mn···Mn distance in complex **1** (3.6 Å) while the opening of the 'wings' resulted in shorter distances in **12** (3.5 Å). However, no such difference was observed in the other complexes **3**, **13-15** (Figure A.58). We believe the opening of the wings can be attributed to the benzoate bridge causing steric repulsion with the benzimidazole 'wings', forcing the benzimidazoles to rotate slightly when benzoate was present.

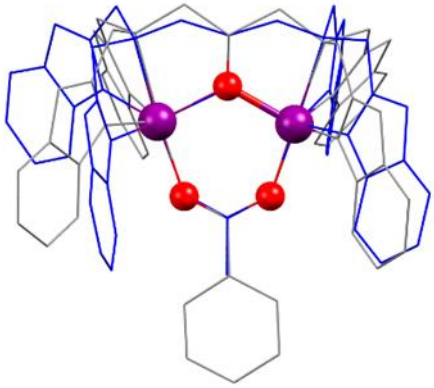

Figure 6.3. Overlapping structure of Mn^{II}_2 complexes **1** (blue wireframe) and **12** (grey wireframe) (ethyl groups have been removed for clarity).

6.2.4 Electrochemical properties

The electrochemistry of complexes **1**, **3**, **12-15** was studied by cyclic voltammetry (CV) to preliminary characterise the electrochemical properties of these compounds. The cyclic voltammograms of Mn_2 complexes **1**, **3**, **12-13** showed oxidation peaks while those of the Cu^{II}_2 complexes **14-15** exhibited reduction peaks (Figures A.59-A.64). The electrochemical data are summarised in Table 6.4.

Table 6.4. Electrochemical data for dinuclear complexes **1**, **3**, **12-15** (a- Mn^{II}_2/Mn^{III}_2 redox couple, b-$Cu^{II}_2/Cu^{II}Cu^{I}$ and $Cu^{II}Cu^{I}/Cu^{I}_2$ redox couple).

Complex	E_{pa} (V vs SCE)	E_{pc} (V vs SCE)[14]
1	0.70[a]	-
12	0.78[a]	-
3	-	-
13	0.77[a]	-
14	-	0.41/-0.47[b]
15	-	0.42/-0.41[b]

The initial oxidation of Mn_2 complexes **1** at 0.7 V vs SCE, **12** at 0.78 V, and **13** at 0.77 V vs SCE was assigned to a two-electron process which was irreversible. This was supported by the in-equivalence of the relative peak currents $I_{ox}/I_{red} \neq 1$ (1.46 for complex **1**, 1.8 for complex **12** and 1.7 for complex **13**) as well as a doubling of the peak potential difference with the scan rate between 50 and 100 mV/s.[46] Such two electron oxidation was previously observed for other Mn^{II}_2 complexes $[Mn_2(tmpdtne)Cl_2](ClO_4)_2.2DMF$ and $[Mn_2(tmpdtnb)Cl_2](ClO_4)_2.DMF.2H_2O$ (where tmpdtne = 1,2-bis[4,7-bis(2-pyridylmethyl)-1,4,7-triazacyclonon-1-yl]-ethane and

tmpdtnb = 1,4-bis[4,7-bis(2-pyridylmethyl)-1,4,7-triazacyclonon-1-yl]-butane.[47] Pessiki and co-workers first reported the electrochemical data for complex **3** in 1994, where they found an initial two electron oxidation process (0.86 V) followed by a second oxidation (1.3 V) which was irreversible.[31] We did not observe the first oxidation of **3** using our instrumental set-up. We did observe one irreversible oxidation process of **3** at 1.38 V vs SCE. The slight differences between the peak potential values reported by Pessiki and measurement problems we had could be due to the different working electrodes used: platinum versus glassy carbon.

For complexes **14** and **15**, an initial reduction peak 0.41 V and 0.42 V vs SCE respectively was measured. Similarly, Cu^{II}_2 systems such as $[Cu_2(H_3bbppnol)(\mu\text{-}OAc)(H_2O)_2]Cl_2.2H_2O$ ($H_3bbppnol$ = N,N`-bis(2-hydroxybenzyl)-N,N`-bis-(pyridylmethyl)]-2-hydroxy-1,3-propanediamine), $[Cu_2(H_2btppnol)(\mu\text{-}OAc)](ClO_4)_2$ ($H_2btppnol$ = N-(2-hydroxybenzyl)-N,N`,N`-tris(2-pyridylmethyl)]-1,3-diaminopropan-2-ol) and $[Cu_2(P1\text{-}O)(OAc)](ClO_4)_2$ (P1-O = 1,3-bis[(2-pyridylmethyl)amino]-propanolate) showed irreversible cathodic reduction peaks.[14] Furthermore Cu^{II}_2 complexes supported by Schiff-base ligands ($[Cu_2(H_2L2^2)(OH)(H_2O)(NO_3)](NO_3)_3.2H_2O$ ($L2^2$ = 2,6-bis(N-ethylpiperazine-iminomethyl)-4methyl-phenolato) and $[Cu_2(L2^3)(OH)(H_2O)_2](NO_3)_2$ ($L2^3$ = 2,6-bis(N-ethylpyrrolidine-iminomethyl)-4methyl-phenolato)) also exhibited an irreversible redox couple.[15] Thus, the electrochemical behaviour of the biomimetic complexes could provide further insight into the catecholase reaction mechanism.

6.3 Catechol oxidase reactivity

The catalytic oxidation of catechol by complexes **1**, **3**, **12-15** was examined in acetonitrile solutions, under aerobic conditions using 3,5-di-*tert*-butylcatechol (3,5-DTBC) as a biomimetic catechol substrate. 3,5-DTBC was used as a substrate as it had a low redox potential and its oxidised quinone form, 3,5-di-*tert*-butylquinone (3,5-DTBQ), was easily identified using electronic absorption spectroscopy.[15, 28] Moreover 3,5-DTBC has bulky substituents that prevented other side-reactions such as oxidative ring opening. The oxidation product 3,5-DTBQ exhibited an absorption band at λ_{max} = 400 nm (ε = 1900 $M^{-1}cm^{-1}$, Figure 4).[48] For complexes **1**, **3**, **12-15** we observed the catalytic formation of 3,5-DTBQ from 3,5-DTBC (Figures 6.4 and A.65-A.69).

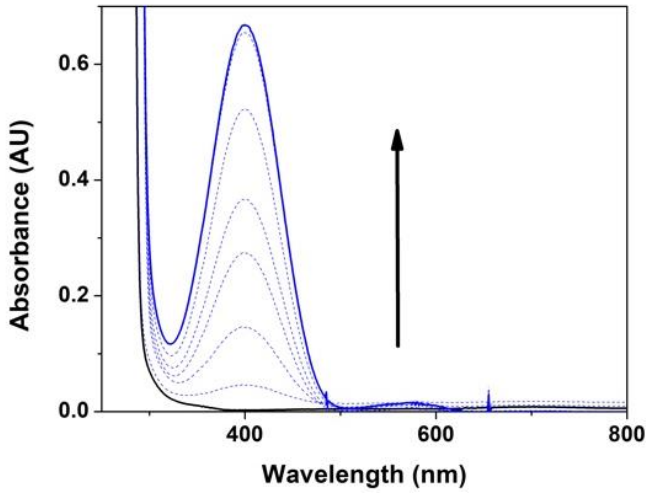

Figure 6.4. Electronic absorption spectral changes showing formation of 3,5-DTBQ (solid blue trace) after addition of 3,5-DTBC (25 equivalents, 50 µl) to complex **12** (0.1 mM, black trace) in acetonitrile at 25 °C (path length = 1 cm).

6.3.1 Catechol oxidase reactivity of complexes 14-15

Cu^{II}_2 complexes have previously been demonstrated to be excellent catechol oxidase mimics, we therefore explored the reactivity of **14** and **15** first.[14-20] A plot of quinone produced (λ_{max} = 400 nm) versus time displayed a biphasic kinetic behaviour (Figure 6.5) for both complexes. Such biphasic kinetic behaviour has been previously observed by Monzani *et al*.[16, 17] for Cu^{II}_2-mediated catechol oxidation where three Cu^{II}_2 complexes supported by *m*-xylyl tetrabenzimidazole showed a fast initial phase followed by a slower phase of the reaction.[16, 17] Other Cu^{II} systems investigated in catecholase activity showed no biphasic behaviour.[1] For Cu^{II}_2 complexes **14** and **15** the biphasic behaviour was typified by an initial fast phase and a slower second reaction phase. The initial phase was about 10-fold faster than the second phase for both complexes (Figure A.70). Additionally, we observed that the rate of the first phase was dependent on the concentration of 3,5-DTBC while the second phase rate was independent of the substrate concentration (Figure A.70).

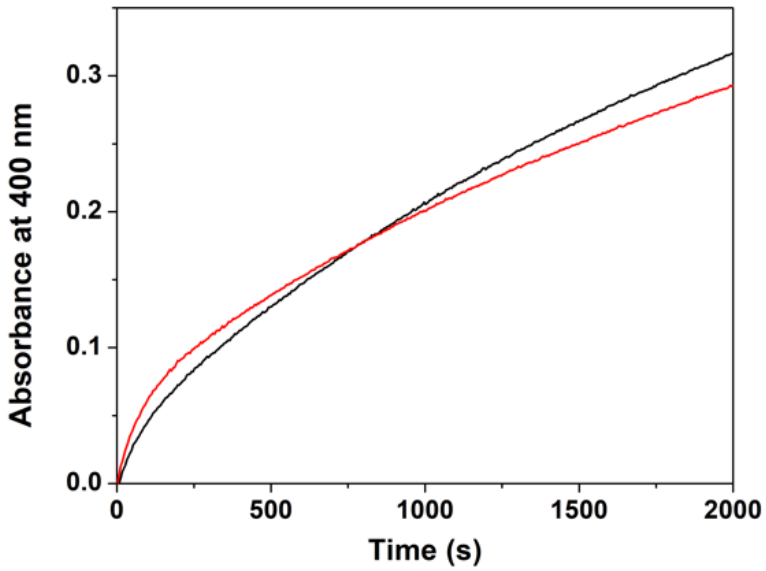

Figure 6.5. Plot of absorbance at λ_{max} = 400 nm versus time for the reaction of complexes **14** (black trace) and **15** (red trace) with 50 equivalents 3,5-DTBC in acetonitrile.

The measured kinetic results for the first phase of the reaction were consistent with Michaelis-Menten behaviour, and correlated well with previous observations.[1, 14, 15, 18] A Michaelis-Menten treatment was performed and Lineweaver-Burk analyses were used to determine the binding constant (K_M), maximum velocity (V_{max}), and the k_{cat} (Figure 6.6, Table 6.5).[19, 28] The V_{max} values for **14** and **15** were almost the same. However, the K_M parameter, which reflects the substrate's dissociation constant, was four times higher for complex **14** than complex **15**. This implied a relatively weak binding of the catechol (3,5-DTBC), meaning the catechol could more easily dissociate from the Cu^{II}_2 core in **14**. The slightly lower V_{max} of **15** could be attributed to the increased steric bulk of the benzoate carboxylate bridge in complex **15** (0.020 Ms^{-1}) when compared to the acetate bridge in complex **14** (0.024 Ms^{-1}). This also resulted in a slightly lower k_{cat} value for complex **15** (44 h^{-1}) when compared to complex **14** (48 h^{-1}). Therefore, based on the kinetic parameters, the Cu^{II}_2 complex **15** proved to have a slighter higher catalytic efficiency than the Cu^{II}_2 complex **14**.

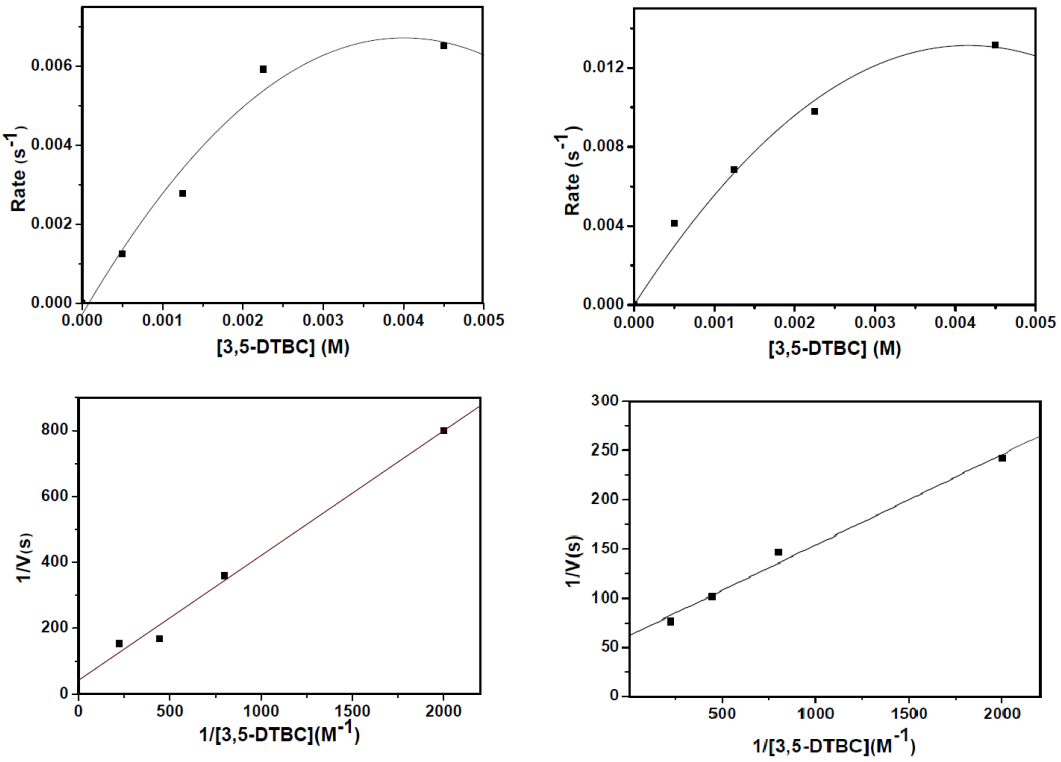

Figure 6.6. **Top**: Plots of first order reaction rate of the first phase of the reactions of **14** (top) and **15** (bottom) against 3,5-DTBC concentrations; **Bottom**: Lineweaver-Burk plots for the same reactions.

6.3.2 Catechol oxidase reactivity of complexes 1, 3 and 12-13

We were interested in comparing the catecholase reactivity of Cu^{II}_2 complexes **14-15** to that of Mn^{II}_2 complexes **1**, **3**, **12-13** supported by the same ligands. We explored the catecholase reactivity of **1**, **3**, **12-13** using 3,5-DTBC as a substrate under the same conditions outlined for **14** and **15** above. In contrast to complexes **14** and **16**, complexes **1**, **12**, and **13** displayed a kinetic trace that appeared to display non-linear multi-phasic behaviour (Figures 6.7, A.71-A.75). The kinetic trace was made up of a slow initiation phase, followed by a faster hyperbolic phase and a subsequent slower phase again. In contrast, the oxidation of 3,5-DTBC by **3** exhibited an almost linear behaviour (Figure A.73). For **1**, **12**, and **13**, we surmise that the initial reaction phase was possibly attributed to the oxidation of the Mn^{II}_2 complexes to a higher oxidation state by atmospheric O_2. The subsequent reaction phases are presumably analogous to the biphasic reactivity observed for **14** and **15**. The (estimated) rate constants estimated for the first and third phase of the reaction were independent of substrate concentration (Table 6.9). The rate of the second phase of the reaction was substrate concentration dependent. However,

at higher substrate concentrations, the rate of the second phase of the reaction reached a saturation point (Figure A.76).

Unfortunately, it was not possible to accurately ascertain when one phase finished, and the next phase started. Therefore, the accuracy of any kinetic measurement would be very low, and it is not possible to garner kinetic insight into these reactions. We were able to determine the k_{cat} values for the reaction of complexes **1**, **3**, **12**-**13** with 3,5-DTBC (Table 6.5). Complex **1** had a higher k_{cat} value (44 h^{-1}) than complex **12** (24 h^{-1}), both being supported by the alkylated HPTB ligand, and the change in rate seemingly caused by the change from acetate (**1**) to benzoate (**12**) bridging ligand. Complexes **3** and **13** supported by the non-alkylated HPTB ligand resulted in the same k_{cat} value (8 h^{-1}). The dramatic drop-off in k_{cat} for the complexes supported by the unalkylated HPTB ligand (8 h^{-1} versus 44 h^{-1}) suggests that the Mn^{II}_2 core prefers to be electron-rich for efficient catecholase reactivity. Thus, based only on the k_{cat} values, the Mn^{II}_2 complex **1** supported by the more electron rich N-Et-HPTB and smaller bridging acetate ligands proved to display the highest overall reaction rate in the series of Mn^{II}_2 complexes **1**, **3**, **12**-**13**.

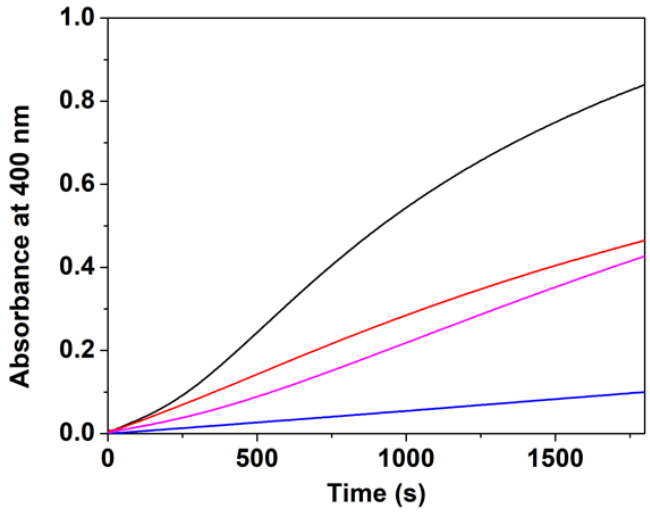

Figure 6.7. Plot of absorbance at λ_{max} = 400 nm versus time for the reaction between Mn^{II}_2 complexes **1** (black trace), **12** (red trace), **3** (blue trace), and **13** (pink trace), and 25 equivalents 3,5-DTBC in acetonitrile at 25 °C.

While the catechol oxidase reactivity of a series of mononuclear Mn^{III} complexes has been widely investigated,[21, 23, 28] Mn^{II}_2 complexes have been less explored in catecholase oxidase reactivity.[49] Mn^{III} complexes showed a high catalytic efficiency with k_{cat} = 270-336 h^{-1}.[21, 50] For a Mn^{II}_2 complex supported by a binucleating ligand (1,4-di(2'-pyridyl)aminophthalazine) a k_{cat} of 167 h^{-1} was obtained.[49] This value was comparable to the values reported for

mononuclear Mn^{III} complexes[23, 50] but higher than the k_{cat} obtained for Mn^{II}_2 complexes **1**, **3**, **12-13** (Table 6.5). Furthermore, Ray and co-workers probed the catecholase activity of a mixed valent $Mn^{III}_2Mn^{II}$ complex in the catalytic oxidation of 3,5-DTBC which showed a k_{cat} = 644 h^{-1}.[27] Thus, the Mn^{II}_2 complexes **1**, **3**, **12-13** exhibited moderate catecholase activity when compared to previously reported complexes, indicating that catalysts in the higher Mn^{III} oxidation state are likely to be more reactive.

We were unable to find a correlation between the catalytic rate constants and the individual redox potentials or $(\Delta E)_{1,2}$ of Mn^{II}_2 complexes **1**, **3**, **12-13** or of Cu^{II}_2 complexes **14** and **15**. Similarly, Krebs *et al.* failed to establish any relationship between the electrochemical properties of their Cu^{II}_2 complexes and the oxidation potential of 3,5-di-*tert*-butylcatechol (3,5-DTBC), the substrate used.[2, 11, 48, 51] The same observation was reported by Das and co-workers in 2014.[19] In contrast, Neves *et. al* found a good correlation between the kinetic parameter k_2 (= k_{cat}/K_M) and $(\Delta E)_{1,2}$ (= $E(red)_1$-$E(red)_2$) in their Cu^{II}_2 complexes.[14] However they could not establish any correlation between k_{cat}/K_M and the individual redox potentials of the complexes ($E(red)_1$ and $E(red)_2$).

Table 6.5. Kinetic parameters for the oxidation of 3,5-DTBC by complexes **1**, **3**, **12-15**.

Complex	k_{cat} (h^{-1})	V_{max} (Ms^{-1})	K_M	k_{cat}/K_M ($M^{-1}h^{-1}$)
1	44	-	-	-
12	24	-	-	-
3	8	-	-	-
13	8	-	-	-
14	48	0.024	8.98 $x10^{-3}$	5345
15	44	0.02	1.8 x 10^{-3}	24444

In the series **1**, **3**, **12-15** (Table 6.5), we noticed that Cu^{II}_2 complexes **14** and **15** had the highest k_{cat} values, whereas Mn^{II}_2 complex **1**, **3**, **12-13** displayed lower k_{cat} values. We surmise the lower activity of the Mn^{II}_2 complexes can be attributed to the initiation phase in their reaction with 3,5-DTBC. This initiation phase is presumably the oxidation of the Mn^{II}_2 precursor to a higher oxidation state to facilitate catechol oxidation through electron transfer. This postulate is supported by observations previously made on Mn^{III} and Mn^{II} catechol oxidants, where the Mn^{III} catalysts generally displayed higher reaction rates. A trend could be observed where the acetate bridged carboxylate complexes (**1** and **14**) had higher k_{cat} values than the corresponding benzoate bridged complexes (**12** and **15**). Also, complexes supported by the un-alkylated ligand (complexes **3** and **13**) had a lower turnover number when compared to complexes supported by the alkylated ligand (complexes **1** and **12**). Overall, in this series of dinuclear complexes the

Cu^{II}_2 complexes **14** and **15** proved to be somewhat more reactive catalysts for the catechol oxidase reaction of 3,5-DTBC when compared to the Mn^{II}_2 complexes **1**, **3**, **12-13**.

Table 6.6. Comparison of kinetic parameters (k_{cat} and k_{cat}/K_M) of complexes **1**, **3**, **12-15** to previously reported Mn and Cu complexes.

Complex	k_{cat} (s^{-1})	k_{cat}/K_M ($M^{-1}s^{-1}$)	Ref
1	0.012	-	this work
12	0.007	-	this work
3	0.002	-	this work
13	0.002	-	this work
$[Mn(bpia)(OAc)(OCH_3)](PF_6)$	0.024	16	[23]
$[Mn(bipa)(OAc)(OCH_3)](PF_6)$	0.028	23	[23]
$[MnL^1Cl].2H_2O$	0.5	710	[28]
$[MnL^4Cl].4H_2O$	5	602	[28]
14	0.013	1.45	this work
15	0.012	6.7	this work
$[Cu_2(H_2bbppnol)(\mu\text{-}OAc)(H_2O)_2]Cl_2.2H_2O$	0.0079	10	[14]
$[Cu_2(Hbtppnol)(\mu\text{-}OAc)](ClO_4)_2$	0.0078	8.1	[14]
$[Cu_2(LB5)](ClO_4)_4$	0.31	590	[16]
$[Cu_2(L\text{-}55)](ClO_4)_4$	1.40	900	[16]
$[Cu_2(EBA)](PF_6)_4$	0.7	60	[17]
$[Cu_2(L_2^3)(OH)(H_2O)](NO_3)_2$	4	526	[15]

(Bpia = bis-(picolyl)(N-methylimidazole-2-yl)amine; Bipa = bis(N-methylimidazole-2-yl)(picolyl)amine; L^1 = N, N'-ethylenebis(3-formyl-5-methyl-salicylaldimine); L^4 = N, N'-cyclohexenebis(3-formyl-5-methylsalicylaldimine); H_2bbppnol = N, N'-bis(2-hydroxybenzyl)-N,N'-bis-(pyridylmethyl)-2-hydroxy-1,3-propanediamine; Hbtppnol = N-(2-hydroxybenzyl)-N,N',N''-tris(2-pyrisylmethyl)-1,3-diaminopropan-2-ol; LB5 = N,N,N',N',N''-pentakis[(1-methyl-2-benzimidazolyl)methyl]dipropylenetriamine; L-55 = α,α'-bis{bis[(1-methyl-2-bezimidazolyl)methyl]amino}-*m*-xylene; EBA = 1,6-bis[[bis(1-methyl-2-benzimidazolyl)methyl]amino]-*n*-hexane; L_2^3 = 2,6-bis(N-ethylpyrrolidine-iminomethyl)-4-methyl-phenolato).

A comparison of kinetic parameters (k_{cat}, k_{cat}/K_M) of complexes **1**, **3**, **12-15** to those previously reported for Mn and Cu complexes is given in Table 6.6. The turnover numbers of Mn^{II}_2 complexes **1**, **3**, **12-13** are slightly lower than those obtained for mononuclear Mn^{III} complexes supported by tetradentate tripodal ligands (bpia and bipa) (Table 6.6). Likewise, mononuclear

Mn^{III} complexes supported by the L^1 (= N, N'-ethylenebis(3-formyl-5-methyl-salicylaldimine) and L4 (= N, N'-cyclohexenebis(3-formyl-5-methylsalicylaldimine) ligands exhibited higher turnover numbers than the Mn^{II}_2 complexes reported here (Table 6.6). Furthermore, the Cu^{II}_2 complexes **14** and **15** exhibited comparable turnover numbers to the Cu^{II}_2 complexes supported by the H_2bbppnol and Hbtppnol but a lower k_{cat}/K_M value than these complexes. Moreover, the Cu^{II}_2 complexes bearing the LB5, L-55, EBA and $L_2{}^3$ ligands displayed higher turnover numbers and a better catalytic efficiency that the Cu^{II}_2 complexes described here.

6.4 Conclusions

We have reported the synthesis and characterisation of a family of Mn^{II}_2 and Cu^{II}_2 complexes supported by the same dinucleating ligands. These complexes were structurally characterised using X-ray crystallography, demonstrating the Mn^{II}_2 complexes to be reliable mimics of the active site of class Ib Mn_2 RNRs. Four Mn^{II}_2 (**1**, **3**, **12-13**) and two Cu^{II}_2 (**14-15**) complexes were investigated as catechol oxidase mimics. All six dinuclear complexes were found to be effective catalysts for aerobic catechol oxidation. The k_{cat} values for all six complexes were calculated and our analysis revealed that Cu^{II}_2 complexes **14** and **15** were slightly more efficient catalysts when compared to Mn^{II}_2 complexes **1**, **3**, **12-13** supported by the same ligand framework. Furthermore, complexes support by the more electron-rich N-Et-HPTB ligand displayed higher activity. These results suggest that for more efficient catecholase activity, relatively electron rich late transition metals (Cu) and good donor ligands are ideal.

6.5 Experimental

Materials

All reactions with air sensitive materials were conducted in a glove box under an N_2 atmosphere. All reagents and solvents were purchased from commercial sources. Anhydrous N,N-dimethylformamide was purchased and used without further purification. Anhydrous tetrahydrofuran, acetonitrile, and diethyl ether were dispensed through an Innovative Technology PureSolvEN solvent purification system and de-oxygenated by purging with Ar. N,N,N',N'-tetrakis(2-benzimidazolylmethyl)-2-hydroxo-1,3-diaminopropane (HPTB) and N,N,N',N'-tetrakis(2-(1-ethylbenzimidazolyl))-2-hydroxy-1,3-diaminopropane (N-Et-HPTB) were synthesised as previously described.[52] Complex **1** was synthesised as previously described.[29] Complex **3** ($[Mn_2(O_2CCH_3)(HPTB)](ClO_4)_2$) was synthesised using a modification of a procedure reported by Dismukes and co-workers,[31] (here complex **3** was recrystallized from acetonitrile/diethyl ether).

Instrumentation

^{1}H NMR analysis was performed on a Bruker Avance III 400 MHz instrument. Electrospray ionisation (ESI) mass spectra were obtained using a Micromass time of flight spectrometer. Matrix assisted laser desorption ionisation (MALDI) mass spectra were acquired using a Maldi QTOF Premier MS System. Infra-red spectra were recorded using a Perkin-Elmer Spectrum FT-IR spectrometer. Electronic absorption spectra were recorded in quartz cuvettes on a Hewlett Packard (Agilent) 8453 diode array spectrophotometer (190-1100 nm range) coupled to a liquid nitrogen cooled cryostat from Unisoku Scientific Instruments (Osaka, Japan). X-ray crystallography was performed on a Bruker APEX Kappa Duo system at 100 K using an Oxford Cobra cryosystem. Cyclic voltammetry (CV) experiments were conducted with a CH Instruments 600E electrochemical analyser, using a glassy carbon working electrode, a platinum wire counter electrode and an $AgNO_3$ reference electrode.

Synthesis

Synthesis of $[Mn_2(O_2CPh)(N\text{-}Et\text{-}HPTB)](ClO_4)_2$ (12)

N-Et-HPTB (0.18 g, 0.25 mmol), benzoic acid (1.11 mmol), and sodium benzoate (0.12 g, 0.81 mmol) were combined in a premixed 3:1 ethanol-water solution (70 mL). After stirring for 15 min, $Mn^{II}(OAc)_2.4H_2O$ (0.11 g, 0.45 mmol) dissolved in ethanol (10 mL) was added. The mixture was allowed to stir for 30 min, after which time $NaClO_4$ (0.39 g, 3.19 mmol) was added as an ethanol/water solution (10 mL). The reaction mixture was allowed to stir for 2 h and then

it was allowed to stand at 0 °C overnight. A pink/white crystalline precipitate formed that was collected by filtration. Re-crystallisation from CH_3CN/Et_2O yielded crystals suitable for X-ray diffraction analysis.

Yield: 0.25 g, 86%. Anal. Calcd (found) for $C_{50}H_{54}Cl_2Mn_2N_{10}O_{11}.H_2O$: C, 51.34 (51.23); H, 4.83 (4.44); N, 11.97 (11.83). ν_{max} (ATR-FTIR)/cm^{-1}: μ_2-carboxylate 1596 (asymmetric) and 1493 (symmetric). Maldi-Tof MS (*m/z*): Found 1051.2595 ($[M\text{-}ClO_4^-]^+$. $C_{50}H_{54}ClMn_2N_{10}O_7^+$ Requires 1051.2632).

$[Mn_2(O_2CCH_3)(HPTB)](ClO_4)_2$ (3)

Complex **3** was synthesised according to a previously reported procedure on half the scale.[31] While the previously reported complex **3** was recrystallized from dichloromethane/chloroform/butanol,[31] we recrystallized complex **3** from acetonitrile/diethyl ether. The ligand HPTB (0.12 g, 0.2 mmol), acetic acid (0.02 g, 0.33 mmol), and sodium acetate (0.09 g, 0.66 mmol) were combined in 34 mL of a premixed 3:1 ethanol/water solution. After stirring for 15 mins, $Mn^{II}(OAc)_2.4H_2O$ (0.08 g, 0.33 mmol) dissolved in 5 mL of ethanol was added. The mixture was allowed to stir for 30 mins at room temperature after which time $NaClO_4$ (0.4 g, 2.7 mmol) was added as a 1:1 ethanol/water solution. The reaction mixture was allowed to stir for 1 h after which the volume was reduced under vacuum and placed in a fridge overnight. A white powder was obtained that was filtered.

Yield: 0.1 g, 57%. ν_{max} (ATR-FTIR)/cm^{-1}: μ_2-carboxylate 1540 (asymmetric) and 1412 (symmetric). Maldi-Tof MS (*m/z*): Found 389.0936 ($[M\text{-}(ClO_4^-)_2]^{2+}$. $C_{42}H_{38}Mn_2N_{10}O_3^{2+}$ Requires 389.0866).

$[Mn_2(O_2CPh)(HPTB)](ClO_4)_2$ (13)

The ligand HPTB (0.25 g, 0.41 mmol), benzoic acid (0.2 g, 1.65 mmol), and sodium benzoate (0.19 g, 1.3 mmol) were combined in 70 mL of a premixed 3:1 ethanol/water solution. After stirring for 15 mins, $Mn^{II}(OAc)_2.4H_2O$ (0.18 g, 0.73 mmol) dissolved in 10 mL of ethanol was added. The mixture was allowed to stir for 30 mins at room temperature after which time $NaClO_4$ (0.6 g, 4.95 mmol) was added as a 1:1 ethanol/water solution (10 mL). The reaction mixture was allowed to stir for 1 h after which the volume was reduced under vacuum and put in the fridge for 2 days. A white powder was obtained that was collected by filtration.

Yield: 0.16 g, 56%. Anal. Calcd (found) for $C_{42}H_{38}Cl_2Mn_2N_{10}O_{11}$: C, 48.52 (48.13); H, 3.68 (3.7); N, 13.47 (13.07). ν_{max} (ATR-FTIR)/cm^{-1}: μ_2-carboxylate 1549 (asymmetric) and 1450

(symmetric). Maldi-Tof MS (*m/z*): Found 420.1008 ($[M-(ClO_4^-)_2]^{2+}$. $C_{42}H_{38}Mn_2N_{10}O_3^{2+}$ Requires 420.0945).

General procedure for synthesis of complexes 14-15

HPTB (0.3 g, 0.49 mmol) and $Cu(ClO_4)_2.6H_2O$ (0.37 g, 0.98 mmol) were dissolved separately in ethanol (5 mL each). The two solutions were mixed and stirred together for 2 hours at room temperature. To the resulting blue solution NaO_2CX (X = CH_3, C_6H_5) (0.49 mmol) was added and the reaction was stirred overnight. A blue green precipitate formed that was collected by filtration. Recrystallisation from CH_3CN/Et_2O yielded crystals suitable for x-ray diffraction structural analysis of complexes **14** and **15**.

$[Cu_2(O_2CCH_3)(HPTB)](ClO_4)_2$ (14)

Yield: 0.22 g, 43%. Anal. Calcd (found) for $C_{37}H_{36}Cl_2Cu_2N_{10}O_{11}.H_2O$: C, 43.88 (43.53); H, 3.41 (3.41); N, 13.83 (13.42). ν_{max} (ATR-FTIR)/cm^{-1}: μ_2-carboxylate 1560 (asymmetric) and 1451 (symmetric). ESI-MS (*m/z*): Found 893.1071 ($[M-(ClO_4)]^{1+}$. $C_{37}H_{36}ClCu_2N_{10}O_7^+$ requires 893.1064).

$[Cu_2(O_2CPh)(HPTB)](ClO_4)_2$ (15)

Yield: 0.23 g, 45%. Anal. Calcd (found) for $C_{42}H_{38}Cl_2Cu_2N_{10}O_{11}.H_2O$: C, 46.93 (46.51); H, 3.75 (3.42); N, 13.03 (12.58). ν_{max} (ATR-FTIR)/cm^{-1}: μ_2-carboxylate 1541 (asymmetric) and 1448 (symmetric). ESI-MS (*m/z*): Found 955.1213 ($[M-(ClO_4)]^{1+}$. $C_{42}H_{38}ClCu_2N_{10}O_7^+$ Requires 955.1211).

Reactivity Studies

In quartz cuvettes, stirring solutions of complexes **1**, **3**, **12-15** (0.1 mM, 2 mL) in acetonitrile (CH_3CN) were treated with different concentrations (5 x 10^{-4}, 12.5 x 10^{-3}, 2.25 x 10^{-3} or 4.5 x 10^{-3} M) of 3,5-di-*tert*-butylcatechol (3,5-DTBC) in CH_3CN, under aerobic conditions at 25 °C. The reaction was monitored by electronic absorption spectroscopy by following the formation of the oxidised product 3,5-di-*tert*-butylquinone (3,5-DTBQ) which exhibited an absorption band at λ_{max} = 400 nm (ε = 1900 $M^{-1}cm^{-1}$ in acetonitrile).[48]

Cyclic Voltammograms of Complexes 1, 3, 12-15

The oxidation potentials for complexes **1**, **3**, **12-13** and reduction potentials for complexes **14-15** were measured by CV using a glassy carbon working electrode in acetonitrile solution

containing 0.1 M NBu_4PF_6 as the supporting electrolyte. The counter electrode used was platinum while the reference electrode was $AgNO_3$.

X-Ray Diffraction Methods and Structure Refinements

Complex 12. A specimen of $C_{56}H_{63}Cl_2Mn_2N_{13}O_{11}$, approximate dimensions 0.050 mm x 0.075 mm x 0.080 mm, was used for the X-ray crystallographic analysis using a MiTeGen micromount. Bruker APEX software was used to collect, correct for Lorentz and polarization effects and reduce the data.[53] One perchlorate molecule was disordered. This disorder was modelled with constraints and restraints (DFIX, EADP) yielding a three-positional model with occupancies of 0.38217, 0.39796 and 0.21986.

Complex 13. A specimen of $C_{46}H_{43}Cl_2Mn_2N_{12}O_{11}$, approximate dimensions 0.090 mm x 0.110 mm x 0.180 mm, was used for the X-ray crystallographic analysis using a MiTeGen micromount. Bruker APEX software was used to correct for Lorentz and polarization effects. [53] Three benzimidazoles modelled as disordered as well as two linking carbons C20, C36 and the bridge carbons C22 and C25. These were modelled with 80:20% occupancy with restraints (DFIX, SADI, FLAT) and constraints (EADP, AFIX 66). Both perchlorates were also modelled in two positions with 58% and 67% major occupancy. Constraints (EADP, rigid model) used. The molecule was refined as a racemic twin with a refined twin ratio of 0.49(5).

Complex 14. A specimen of $C_{42}H_{41.50}Cl_2Cu_2N_{11.50}O_{11.50}$, approximate dimensions 0.070 mm x 0.110 mm x 0.340 mm, was used for the X-ray crystallographic analysis using a MiTeGen micromount. Bruker APEX software was used to correct for Lorentz and polarization effects. [53] There were 4 partially occupied MeCN molecules in asymmetric unit. N51, 43; N54, 62; N59, 31; N62, 14% occupied. Total = 1.5 MeCN per asymmetric unit. One perchlorate Cl1/Cl3 is disordered over two positions with occupancies of 54:46%. Cl3 perchlorate shares space with a half-occupied diethyl ether molecule. Restraints (DFIX, SADI, ISOR, SUMP for MeCN occupancy) and constraints (EADP) were used in the model.

Complex 15. A specimen of $C_{45}H_{42.50}Cl_2Cu_2N_{11.50}O_{11}$, approximate dimensions 0.140 mm x 0.190 mm x 0.370 mm, was used for the X-ray crystallographic analysis using a MiTeGen micromount. Bruker APEX software was used to collect, correct for Lorentz and polarization effects and reduce the data.[53] One perchlorate was modelled in two positions with a refined occupancy of 54:46% with one shared oxygen atom O68. Constraints were used to model this

disorder (EADP). Restraints were used in the model of the free solvent MeCN groups (SADI, ISOR) one of which is only half occupied.

Table 6.7. Comparison of average bond lengths in complexes **1**, **3**, **12-15**.

Complexes		**1**[1]	**12**	**3**[2]	**13**	**14**	**15**
Average Bond Lengths (M = metal)	M-N_{amine} (Å)	2.42	2.39	2.45	2.43	2.13	2.12
	M-N_{benz} (Å)	2.13	2.13	2.18	2.13	2.08	2.08

	(**12**)	(**13**)	(**14**)	(**15**)
Name:	$[Mn_2(O_2CPh)(N\text{-}Et\text{-}HPTB)](ClO_4)_2$	$[Mn_2(O_2CPh)(HPTB)](ClO_4)_2$	$[Cu_2(O_2CCH_3)(HPTB)](ClO_4)_2$	$[Cu_2(O_2CPh)(HPTB)](ClO_4)_2$
Empirical formula	$C_{56}H_{63}Cl_2Mn_2N_{13}O_{11}$	$C_{46}H_{43}Cl_2Mn_2N_{12}O_{11}$	$C_{42}H_{45.50}Cl_2Cu_2N_{11.50}O_{11.50}$	$C_{45}H_{42.50}Cl_2Cu_2N_{11.50}O_{11}$
Formula weight	1274.97	1120.70	1093.38	1118.38
Temperature (K)	100(2)	100(2)	100(2)	100(2)
Wavelength (Å)	1.54178	0.71073	0.71073	0.71073
Crystal system	Triclinic	Monoclinic	Triclinic	Monoclinic
Space group	$P\bar{1}$	Cc	$P\bar{1}$	Cc
a (Å)	13.0800(4)	21.3934(11)	12.8864(8)	20.4647(8)
b (Å)	14.4180(5)	21.7926(11)	13.1530(8)	21.8424(8)
c (Å)	17.9989(5)	11.6260(6)	16.6060(11)	11.5893(4)
α (°)	73.3874(19)	90	80.111(2)	90
β (°)	78.3545(18)	115.314(3)	71.250(2)	111.2580(10)
γ (°)	66.9439(18)	90	61.8690(10)	90
Volume ($Å^3$)	2977.27(17)	4899.8(4)	2349.7(3)	4827.9(3)
Z	2	4	2	4
Density (calc, Mg/m^3)	1.422	1.519	1.545	1.539
ρ (mm^{-1})	4.860	0.698	1.092	1.064
F(000)	1324	2300	1124	2292
Crystal size (mm^3)	0.080 x 0.075 x 0.050	0.18 x 0.11 x 0.09	0.34 x 0.11 x 0.07	0.37 x 0.19 x 0.14
Index ranges	-15≤h≤15, -17≤k≤17, -21≤l≤21	-26≤h≤26, -26≤k≤26, -14≤l≤14	-16≤h≤16, -16≤k≤16, -20≤l≤20	-25≤h≤25, -27≤k≤27, -14≤l≤14
Reflections collected	56368	68365	55045	41111
Independent reflections	10484 [R(int) = 0.0970]	9586 [R(int) = 0.0788]	9654 [R(int) = 0.0227]	10007 [R(int) = 0.0394]
Absorption correction	Numerical	Semi-empirical from equivalents	Semi-empirical from equivalents	Semi-empirical from equivalents
Max. and min. transmission	0.9694 and 0.7652	0.7455 and 0.6867	0.7454 and 0.6674	0.7454 and 0.7002
Data / restraints / parameters	10484 / 31 / 787	9586 / 27 / 544	9654 / 35 / 690	10007 / 34 / 656
Goodness-of-fit on F^2	1.038	1.120	1.042	1.059
R indices [I>2σ(I)]	R1 = 0.0593, wR2 = 0.1470	R1 = 0.0766, wR2 = 0.1598	R1 = 0.0658, wR2 = 0.1727	R1 = 0.0427, wR2 = 0.1082
R indices (all data)	R1 = 0.0876, wR2 = 0.1665	R1 = 0.0977, wR2 = 0.1703	R1 = 0.0713, wR2 = 0.1770	R1 = 0.0487, wR2 = 0.1123
Flack Parameter	-	0.49(5)	-	0.276(15)
Largest diff. peak and hole ($e.Å^{-3}$)	0.531 and -0.702	0.722 and -0.642	2.020 and -2.020	0.866 and -0.724

Table 6.8. Crystal data and structure refinement for complexes **12-15**.

Table 6.9. Approximate (estimated) rate constant values of the three phases of reaction for Mn^{II}_2 complexes **1**, **12** and **13**.

Complex 1		**Complex 12**		**Complex 13**	
[3,5-DTBC] (M)	**Rate constant (s^{-1})**	**[3,5-DTBC] (M)**	**Rate constant (s^{-1})**	**[3,5-DTBC] (M)**	**Rate constant (s^{-1})**
2.5×10^{-4}		5×10^{-4}		5×10^{-4}	
1st phase	1.9×10^{-3}	First phase	2.65×10^{-3}	First phase	6.13×10^{-3}
Second phase	4×10^{-4}	Second phase	1.33×10^{-4}	Second phase	2.4×10^{-4}
Third phase	3.5×10^{-4}	Third phase	5.4×10^{-4}	Third phase	4.6×10^{-4}
5×10^{-4}		8×10^{-4}		8×10^{-4}	
First phase	2.05×10^{-3}	First phase	2.1×10^{-3}	First phase	6.27×10^{-3}
Second phase	6.2×10^{-4}	Second phase	2.25×10^{-4}	Second phase	2.8×10^{-4}
Third phase	3.6×10^{-4}	Third phase	5.1×10^{-4}	Third phase	4.8×10^{-4}
8×10^{-4}		1.25×10^{-3}		1.25×10^{-3}	
First phase	2.5×10^{-3}	First phase	2.2×10^{-4}	First phase	5.9×10^{-3}
Second phase	7.4×10^{-4}	Second phase	2.8×10^{-4}	Second phase	3.6×10^{-4}
Third phase	3.9×10^{-4}	Third phase	4.8×10^{-4}	Third phase	3.11×10^{-4}
		2.25×10^{-3}		2.25×10^{-3}	
		First phase	2.6×10^{-3}	First phase	5.8×10^{-3}
		Second phase	3.35×10^{-4}	Second phase	4.1×10^{-4}
		Third phase	3.6×10^{-4}	Third phase	2.8×10^{-4}

References

[1] I. A. Koval, P. Gamez, C. Belle, K. Selmeczi, J. Reedijk, *Chem. Soc. Rev.* **2006**, *35*, 814-840.
[2] R. Than, A. A. Feldmann, B. Krebs, *Coord. Chem. Rev.* **1999**, *182*, 211-241.
[3] S. Dong, J. A. Ybe, M. H. Hecht, T. G. Spiro, *Biochemistry* **1999**, *38*, 3379-3385.
[4] J.-L. Pierre, *Chem. Soc. Rev.* **2000**, *29*, 251-257.
[5] E. I. Solomon, U. M. Sundaram, T. E. Machonkin, *Chem. Rev.* **1996**, *96*, 2563-2606.
[6] S. Itoh, S. Fukuzumi, *Acc. Chem. Res.* **2007**, *40*, 592-600.
[7] C. Gerdemann, C. Eicken, B. Krebs, *Acc. Chem. Res.* **2002**, *35*, 183-191.
[8] A. L. Hughes, *Immunogenetics* **1999**, *49*, 106-114.
[9] S. Torelli, C. Belle, I. Gautier-Luneau, J. L. Pierre, E. Saint-Aman, J. M. Latour, L. Le Pape, D. Luneau, *Inorg. Chem.* **2000**, *39*, 3526-3536.
[10] C. Belle, K. Selmeczi, S. Torelli, J.-L. Pierre, *C. R. Chim.* **2007**, *10*, 271-283.
[11] C. Eicken, F. Zippel, K. Büldt-Karentzopoulos, B. Krebs, *FEBS Lett.* **1998**, *436*, 293-299.
[12] D. E. Wilcox, A. G. Porras, Y. T. Hwang, K. Lerch, M. E. Winkler, E. I. Solomon, *J. Am. Chem. Soc.* **1985**, *107*, 4015-4027.
[13] T. Klabunde, C. Eicken, J. C. Sacchettini, B. Krebs, *Nat. Struct. Biol.* **1998**, *5*, 1084-1090.
[14] A. Neves, L. M. Rossi, A. J. Bortoluzzi, B. Szpoganicz, C. Wiezbicki, E. Schwingel, W. Haase, S. Ostrovsky, *Inorg. Chem.* **2002**, *41*, 1788-1794.
[15] K. S. Banu, T. Chattopadhyay, A. Banerjee, S. Bhattacharya, E. Suresh, M. Nethaji, E. Zangrando, D. Das, *Inorg. Chem.* **2008**, *47*, 7083-7093.
[16] E. Monzani, L. Quinti, A. Perotti, L. Casella, M. Gullotti, L. Randaccio, S. Geremia, G. Nardin, P. Faleschini, G. Tabbì, *Inorg. Chem.* **1998**, *37*, 553-562.
[17] E. Monzani, G. Battaini, A. Perotti, L. Casella, M. Gullotti, L. Santagostini, G. Nardin, L. Randaccio, S. Geremia, P. Zanello, G. Opromolla, *Inorg. Chem.* **1999**, *38*, 5359-5369.
[18] S. Mandal, J. Mukherjee, F. Lloret, R. Mukherjee, *Inorg. Chem.* **2012**, *51*, 13148-13161.
[19] P. Chakraborty, J. Adhikary, B. Ghosh, R. Sanyal, S. K. Chattopadhyay, A. Bauza, A. Frontera, E. Zangrando, D. Das, *Inorg. Chem.* **2014**, *53*, 8257-8269.
[20] J. Reim, B. Krebs, *J. Chem. Soc., Dalton. Trans.* **1997**, 3793-3804.
[21] A. Majumder, S. Goswami, S. R. Batten, M. Salah El Fallah, J. Ribas, S. Mitra, *Inorg. Chim. Acta.* **2006**, *359*, 2375-2382.
[22] P. Kar, Y. Ida, T. Kanetomo, M. G. Drew, T. Ishida, A. Ghosh, *Dalton Trans.* **2015**, *44*, 9795-9804.
[23] M. U. Triller, D. Pursche, W. Y. Hsieh, V. L. Pecoraro, A. Rompel, B. Krebs, *Inorg. Chem.* **2003**, *42*, 6274-6283.
[24] A. Jana, N. Aliaga-Alcalde, E. Ruiz, S. Mohanta, *Inorg. Chem.* **2013**, *52*, 7732-7746.
[25] A. Guha, T. Chattopadhyay, N. D. Paul, M. Mukherjee, S. Goswami, T. K. Mondal, E. Zangrando, D. Das, *Inorg. Chem.* **2012**, *51*, 8750-8759.
[26] J. Adhikary, P. Chakraborty, S. Das, T. Chattopadhyay, A. Bauza, S. K. Chattopadhyay, B. Ghosh, F. A. Mautner, A. Frontera, D. Das, *Inorg. Chem.* **2013**, *52*, 13442-13452.
[27] K. Chattopadhyay, G. A. Craig, M. J. Heras Ojea, M. Pait, A. Kundu, J. Lee, M. Murrie, A. Frontera, D. Ray, *Inorg. Chem.* **2017**, *56*, 2639-2652.
[28] K. S. Banu, T. Chattopadhyay, A. Banerjee, M. Mukherjee, S. Bhattacharya, G. K. Patra, E. Zangrando, D. Das, *Dalton Trans.* **2009**, *40*, 8755-8764.
[29] A. M. Magherusan, A. Zhou, E. R. Farquhar, M. Garcia-Melchor, B. Twamley, L. Que, Jr., A. R. McDonald, *Angew. Chem. Int. Ed. Engl.* **2018**, *57*, 918-922.
[30] V. McKee, M. Zvagulis, J. V. Dagdigian, M. G. Patch, C. A. Reed, *J. Am. Chem. Soc.* **1984**, *106*, 4765-4772.
[31] P. J. Pessiki, S. V. Khangulov, D. M. Ho, G. C. Dismukes, *J. Am. Chem. Soc.* **1994**, *116*, 891-897.
[32] J. M. Brink, R. A. Rose, R. C. Holz, *Inorg. Chem.* **1996**, *35*, 2878-2885.
[33] G. S. Siluvai, N. N. Murthy, *Polyhedron* **2009**, *28*, 2149-2156.
[34] W. B. T. R. R. Lynn, S. J. Lippard, *New. J. Chem.* **1991**, *15*, 417-430.

[35] G. Deacon, *Coord. Chem. Rev.* **1980**, *33*, 227-250.
[36] M. Suzuki, M. Mikuriya, S. Murata, A. Uehara, H. Oshio, S. Kida, K. Saito, *Bull. Chem. Soc. Jpn.* **1987**, *60*, 4305-4312.
[37] R. Hage, B. Krijnen, J. B. Warnaar, F. Hartl, D. J. Stufkens, T. L. Snoeck, *Inorg. Chem.* **1995**, *34*, 4973-4978.
[38] A. W. Addison, T. N. Rao, J. Reedijk, J. van Rijn, G. C. Verschoor, *J. Chem. Soc., Dalton Trans.* **1984**, 1349-1356.
[39] J. R. Frisch, V. V. Vu, M. Martinho, E. Munck, L. Que, Jr., *Inorg. Chem.* **2009**, *48*, 8325-8336.
[40] A. L. Feig, M. T. Bautista, S. J. Lippard, *Inorg. Chem.* **1996**, *35*, 6892-6898.
[41] S. Y. Dong, Menage, B. A. Brennan, T. E. Elgren, H. G. Jang, L. L. Pearce, L. Que, *J. Am. Chem. Soc.* **1993**, *115*, 1851-1859.
[42] W. F. Zeng, C. P. Cheng, S. M. Wang, M.-C. Cheng, G.-H. Lee, Y. Wang, *Inorg. Chem.* **1995**, *34*, 728-736.
[43] A. K. Boal, J. A. Cotruvo, Jr., J. Stubbe, A. C. Rosenzweig, *Science* **2010**, *329*, 1526-1530.
[44] A. K. Boal, J. A. Cotruvo, Jr., J. Stubbe, A. C. Rosenzweig, *Biochemistry* **2012**, *51*, 3861-3871.
[45] N. Cox, H. Ogata, P. Stolle, E. Reijerse, G. Auling, W. Lubitz, *J. Am. Chem. Soc.* **2010**, *132*, 11197-11213.
[46] P. J. Pessiki, S. V. Khangulov, D. M. Ho, G. C. Dismukes, *J. Am. Chem. Soc* **1994**, *116*, 891-897.
[47] S. J. Brudenell, L. Spiccia, A. M. Bond, G. D. Fallon, D. C. R. Hockless, G. Lazarev, P. J. Mahon, E. R. T. Tiekink, *Inorg. Chem.* **2000**, *39*, 881-892.
[48] P. Gentschev, N. Moller, B. Krebs, *Inorg. Chim. Acta* **2000**, *300-302*, 442-452.
[49] J. Kaizer, R. Csonka, G. Baráth, G. Speier, *Transit. Metal Chem.* **2007**, *32*, 1047-1050.
[50] Y. Hitomi, A. Ando, H. Matsui, T. Ito, T. Tanaka, S. Ogo, T. Funabiki, *Inorg. Chem.* **2005**, *44*, 3473-3478.
[51] M. Merkel, N. Moller, M. Piacenza, S. Grimme, A. Rompel, B. Krebs, *Chemistry* **2005**, *11*, 1201-1209.
[52] V. McKee, M. Zvagulis, J. V. Dagdigian, M. G. Patch, C. A. Reed, *J. Am. Chem. Soc.* **1984**, *106*, 4765-4772.
[53] Bruker, *APEX2 Ver. 2014.11-0, Bruker AXS Inc., Madison, WI, USA.*, 1-142.

Chapter 7

Conclusions and Future Work

7.1 Summary and conclusions

The focus of this thesis was to explore the postulated mechanism of class Ib Mn_2 ribonucleotide reductases (RNRs). Thus, Mn^{II}_2 complexes as models of class Ib Mn_2 RNRs were prepared and characterised, and their reactivity with $O_2^{\bullet-}$ was explored. We initially investigated the reactivity of Mn^{II}_2 complex **1** with $O_2^{\bullet-}$, resulting in the formation of a metastable $Mn^{II}Mn^{III}$-peroxide species (adduct **2**, chapter 2). **2** was prepared at a low temperature (≤-40 °C) and characterised by electronic absorption and EPR spectroscopy, XANES and ESI-MS, confirming its identity as a $Mn^{II}Mn^{III}$-peroxide species (**2**, Scheme 7.1). Adduct **2** represented the first synthetic model of a peroxide-intermediate postulated in the catalytic cycle of class Ib Mn_2 RNRs. The $Mn^{II}Mn^{III}$-peroxide unit in **2** proved to be totally unreactive as either an electrophilic or nucleophilic oxidant. Furthermore, it was only capable of oxidising ferrocene and weak O-H bonds (TEMPO-H (= 2,2,6,6-tetramethyl-piperidine-1-ol)) upon activation with strong acids. The findings described in this chapter provided support for the postulated mechanism of $O_2^{\bullet-}$ activation at class Ib Mn_2 RNRs.

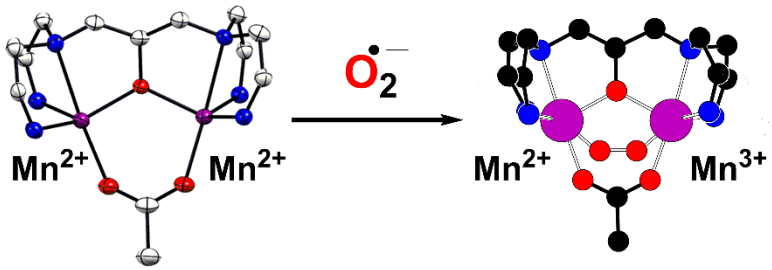

Scheme 7.1. Reaction of complex **1** with $O_2^{\bullet-}$ yielding a $Mn^{II}Mn^{III}$-peroxide species (**2**).

In subsequent work, we demonstrated that Mn^{II}_2 complex **4** (chapter 3) reacted with $O_2^{\bullet-}$ to form a $Mn^{II}Mn^{III}$-peroxide adduct (**5**), like adduct **2** prepared in chapter 2. Likewise, adduct **5** was prepared at low temperature (≤-80 °C) and characterised by electronic absorption and EPR spectroscopies, ESI-MS, XANES, endorsing its identity as a $Mn^{II}Mn^{III}$-peroxide species. Different ligands, poly-benzimidazole (N-Et-HPTB, chapter 2) versus polypyridine (HBPMP, chapter 3) were used for preparation of Mn-peroxide species **2** and **5**. Importantly, while the $Mn^{II}Mn^{III}$-peroxide moiety in **2** was unreactive at -40 °C, the $Mn^{II}Mn^{III}$-peroxide **5** proved to be a nucleophilic oxidant at -90 °C, being involved in aldehyde deformylation (Scheme 7.2). A Hammett plot gave a positive ρ value of 0.64, consistent with a nucleophilic character of the peroxo-unit in **5** in the oxidation of *para*-substituted benzaldehydes. Furthermore, adduct **5** exhibited comparable aldehyde deformylation reaction rates to previously reported mononuclear Mn-peroxide complexes. Whereas adduct **2** (chapter 2) was able to perform

oxidation reactions only upon activation with proton donors, the metastable adduct **5** prepared in chapter 3 proved to be a better oxidant, demonstrating a nucleophilic character in the reaction with aldehydes.

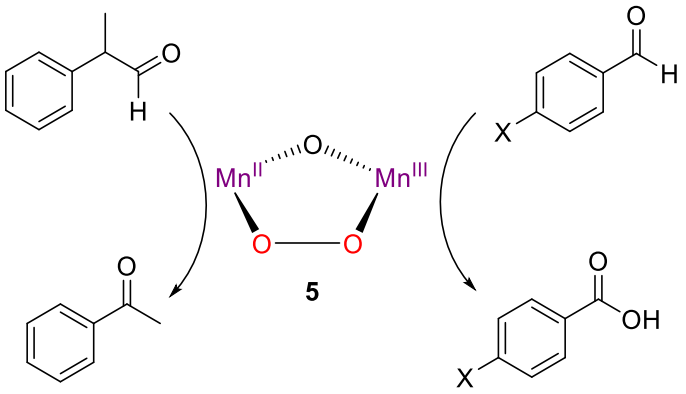

Scheme 7.2. Reaction of **5** with 2-phenylpropionaldehyde (PPA, left) and *para*-substituted benzaldehydes (right, X = H, Cl, CF_3, CN, NO_2) forming acetophenone and benzoate products respectively.

The thermal decay of **5** resulted in the formation of a new species (**6**), postulated as a high valent $Mn^{III}Mn^{IV}$ adduct. This was an important result as a mixed valent $Mn^{III}Mn^{IV}$ intermediate was responsible for tyrosine oxidation in class Ib Mn_2 RNRs.

Since the $Mn^{II}Mn^{III}$-peroxide complex **2** was activated with proton donors, we proposed that the nucleophilic oxidant **5** could also react with acids. Indeed, adduct **5** reacted with strong acids to form **7**, whose electronic absorption features were characteristic of a mixed valent $Mn^{II}Mn^{III}$ species. Unfortunately, characterisation of **7** by EPR, showed only a signal typical of a Mn^{II} species and the presence of the $Mn^{II}Mn^{III}$ adduct was not observed. **7** was postulated as a mixed valent $Mn^{II}Mn^{III}$. Nevertheless, when **5** was reacted with a weaker acid (1 or 2 equivalents of *p*TsOH), a 16-line EPR signal was observed by EPR spectroscopy. These signals were characteristic of high valent $Mn^{III}Mn^{IV}$ complexes. Additionally, the electronic absorption spectrum obtained upon addition of *p*TsOH (2 equivalents) to **5** was characteristic of a $Mn^{III}Mn^{IV}$ species. In summary, upon addition of strong acids to **5** the formation of a $Mn^{II}Mn^{III}$ species was proposed, while upon activation of adduct **5** with weaker acids a mixed valent $Mn^{III}Mn^{IV}$ species was postulated. Besides a $Mn^{II}Mn^{III}$ intermediate postulated in class Ib Mn_2 RNRs, the presence of a mixed valent $Mn^{III}Mn^{IV}$ species was also found by EPR spectroscopy. Therefore, investigation of reactivity of adduct **5** with acids provided further evidence into the mechanism of $O_2^{\bullet-}$ activation at class Ib Mn_2 RNRs.

Owing to the fact that the $Mn^{II}Mn^{III}$-peroxide species **2** did not react with proton donors to form a hydroperoxo-Mn_2 complex (postulated intermediate in class Ib RNRs), we decided to synthesise a new Mn^{II}_2 complex supported by the HPTP ligand (complex **11**). We wanted to investigate the reactivity of **11** towards $O_2^{\bullet-}$ and subsequently proton donors. Unfortunately, the synthesis of complex **11** bearing the HPTP proved to be challenging. Nevertheless, after many attempts, complex **11** was synthesised under anaerobic conditions. The crystal structure of **11** (see chapter 5) displayed two Mn atoms bonded by the HPTP ligand and one CH_3CN and one ClO_4^- anion bound to each of the Mn centres (Figure 7.1). No carboxylate bridge was present in the crystal structure of **11**, when compared to the Mn^{II}_2 complexes **1** and **4** (chapters 2 and 3 respectively). Since finding the right procedure for the preparation of complex **11** took longer than expected, we could not investigate its reactivity with $O_2^{\bullet-}$ or O_2 until now.

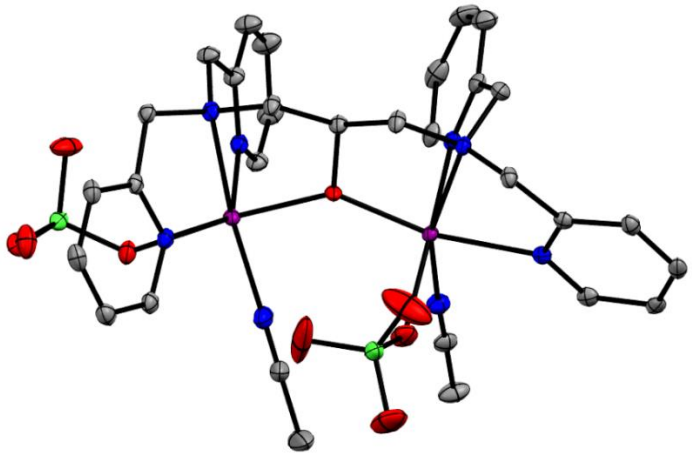

Figure 7.1. Crystal structure of complex **11**. Hydrogen atoms and one perchlorate anion have been omitted for clarity.

In the last chapter of the thesis (chapter 6) we explored and compared the reactivity of synthetic Cu^{II}_2 and Mn^{II}_2 complexes as catechol oxidase mimics. Cu^{II}_2 complexes have been widely investigated as model systems for catechol oxidase enzyme but the catechol oxidase reactivity of Mn^{II}_2 complexes has been less explored. A series of Mn^{II}_2 complexes (**1**, **3**, **12-13**) and Cu^{II}_2 complexes (**14-15**) supported by the same ligand framework (HPTB) have been synthesised. The catecholase activity of complexes **1**, **3**, **12-15** in CH_3CN medium using 3,5-DTBC as a substrate was explored. The Cu^{II}_2 complexes (**14** and **15**) proved to be better catechol oxidase mimics (Scheme 7.3) with moderate k_{cat} values (~45 h^{-1}) when compared to Mn^{II}_2 complexes, that exhibited lower k_{cat} values (~8-40 h^{-1}). Unfortunately, our study showed no relationship between the electrochemical properties of complexes and their catalytic efficiency. Our

findings demonstrate that later transition metals supported by relatively rich ligands yield the highest k_{cat} values for catechol oxidation.

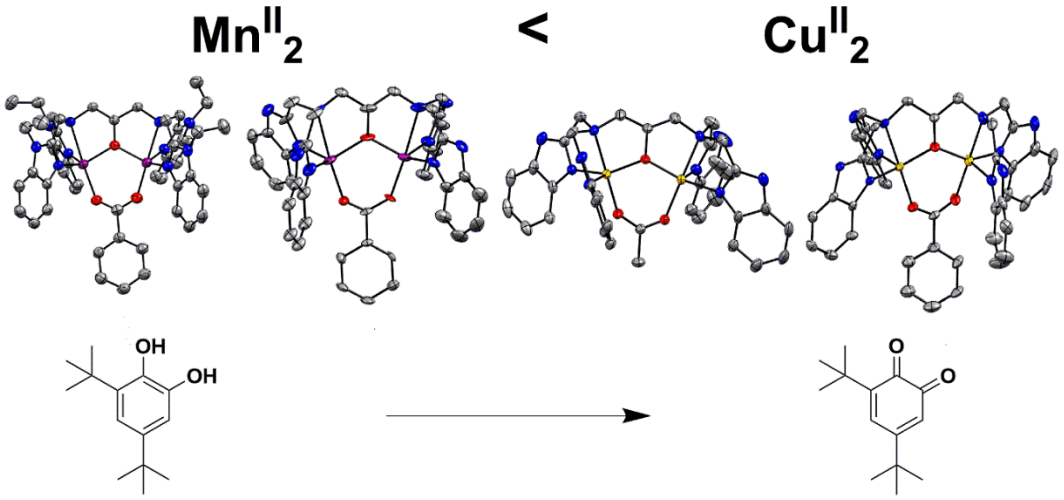

Scheme 7.3. Comparison of catechol oxidase reactivity of Cu^{II}_2 and Mn^{II}_2 complexes supported by the same ligand framework.

In conclusion, Stubbe and co-workers have shown that the Mn^{II}_2 cofactor of class Ib RNRs reacted with $O_2^{\bullet-}$ in the presence of a proton source, to form $Mn^{II}Mn^{III}$-hydroperoxide, $Mn^{III}Mn^{IV}$ and $Mn^{III}Mn^{III}$ intermediates. One of the intermediates, a high valent $Mn^{III}Mn^{IV}$ was capable to oxidise tyrosine, which has a weak O-H bond to tyrosyl radical. This radical was then involved in the conversion of ribonucleotides to deoxyribonucleotides. Here we provided experimental support for this biological mechanism. A synthetic Mn^{II}_2 model complex of RNRs was prepared and reacted with $O_2^{\bullet-}$ at low temperature to form a $Mn^{II}Mn^{III}$-peroxide (**2**) adduct (chapter 2). Complex **2** was shown to be activated by a proton donor in the presence of TEMPO-H, which has a weak O-H bond to form TEMPO$^{\bullet}$. Thus, experimentally by using TEMPO-H as a substrate we mimicked the tyrosine/tyrosyl reactivity performed by RNRs.

Furthermore, a second peroxo-$Mn^{II}Mn^{III}$ complex (**5**) was prepared and it proved to be a nucleophilic oxidant capable of aldehyde deformylation (chapter 3). Through kinetic analysis, it was determined that the rate-limiting step in this oxidation was nucleophilic attack of the peroxide core on the aldehyde substrate. Additionally, the thermal decay of the peroxo-$Mn^{II}Mn^{III}$ (**5**) complex was postulated to be a high valent $Mn^{III}Mn^{IV}$ species, upon UV-Vis and EPR characterisation (chapter 4). Moreover, upon activation of **5** with weak acids, the formation of a high valent $Mn^{III}Mn^{IV}$ species was also proposed. A mixed valent $Mn^{III}Mn^{IV}$ intermediate was also present in the catalytic cycle of class Ib Mn_2 RNRs. Our studies provided insight into

the mechanism of O_2-activation in class Ib Mn_2 RNRs, and the highly reactive intermediates in their catalytic cycle.

7.2 Future work

The results discussed in this thesis leave several routes to be investigated, to further understand class Ib Mn_2 RNRs.

1) We have prepared a $Mn^{II}Mn^{III}$-peroxide species (**2**) in chapter 1, by reaction of a Mn^{II}_2 complex (**1**) with $O_2^{\bullet-}$. **2** was fully characterised by electronic absorption and EPR spectroscopies, XAS and ESI-MS. Since until now resonance Raman spectroscopy studies on **2** failed to provide any insight, perhaps a more detailed analysis of species **2** using different laser wavelengths would provide ν_{O-O} and ν_{Mn-O} stretches of the Mn-peroxide species (**2**). Obtaining resonance Raman data on **2** would provide insight into the structure of **2** and allow comparison of ν_{O-O} and ν_{Mn-O} parameters to those previously reported. An important theoretical tool will be DFT calculations on the reaction of complex **1** with $O_2^{\bullet-}$, resulting in the formation of adduct **2**. DFT analysis will be fundamental to provide insight into the reaction mechanism. Adduct **2** was not involved in OAT or HAT reactions and could only be activated by acids. One interesting question is whether the preparation of the Mn^{II}_2 complex **1** without the carboxylate bridge and investigation of its reactivity with $O_2^{\bullet-}$ can still result in the formation of a $Mn^{II}Mn^{III}$-peroxide complex. Furthermore, the OAT and HAT reactivity of this species could be investigated. Perhaps the absence of carboxylate bridge in the Mn^{II}_2 complex **1** can lead to the formation of a more reactive adduct, upon reaction of the Mn^{II}_2 complex with $O_2^{\bullet-}$.
2) Furthermore, the central motivation behind our research was the preparation of model compounds of intermediates postulated in class Ib Mn_2 RNRs. In chapter 2 and 3, two $Mn^{II}Mn^{III}$-peroxide species (**2** and **5**) were prepared and fully characterised. Another postulated intermediate in the catalytic cycle of class Ib Mn_2 RNRs was a bis(μ-oxo)$Mn^{III}Mn^{IV}$ species. Interestingly, the thermal decay of **5** and the reaction of **5** with weak acids resulted in the formation of species that exhibited electronic absorption features typical of $Mn^{III}Mn^{IV}$ complexes (chapter 4). Furthermore, EPR signals characteristic of mixed valent $Mn^{III}Mn^{IV}$ entities (16-line EPR signal) were observed for these adducts. Moreover, a yield of the mixed valent $Mn^{III}Mn^{IV}$ species could be obtained by EPR spectroscopy with the help of an EPR standard. XAS analysis of this species would provide

further insight into the structure and oxidation state. Furthermore, DFT calculations will be essential for a full grasp of reaction mechanism of **5** and acids.

3) Finally, the central inspiration behind our research was preparation of model complexes that mimic the postulated intermediates in the catalytic cycle of class Ib Mn_2 RNRs. In this view, it will be highly interesting to investigate the reactivity of complex **11**, not bridged by a carboxylate (in comparison to complexes **1** and **4**) with $O_2^{\bullet-}$. We plan next to fully characterise the adduct obtained in the reaction of complex **11** with O_2 and $O_2^{\bullet-}$ by electronic absorption, EPR, XAS and mass spectrometry. Moreover, the nucleophilic and electrophilic character of the adducts formed will be explored. A synthetic $Mn^{II}Mn^{III}$-hydroperoxide species has not been previously reported in the literature. Ideally, we would be able to isolate a Mn_2-hydroperoxide species, upon reaction of **11** with $O_2^{\bullet-}$ and a proton source. One of the postulated intermediates in class Ib Mn_2 RNRs was a Mn_2-hydroperoxide adduct. Once such a species will be prepared, its reactivity in OAT and HAT reactions will be probed. A compelling study will be the determination of Mn-decay products obtained from the oxidation reactions. This will be achieved by EPR, mass spectrometry and XAS studies. Moreover, theoretical tools (i.e DFT calculations) will be essential for an understanding of the reaction mechanism of complex **11** with $O_2^{\bullet-}$ and proton sources. An interesting result will be to compare the oxidative reactivity of adducts formed in the reaction of carboxylate bridged Mn_2 complexes with $O_2^{\bullet-}$ and non-carboxylate Mn_2 complexes with $O_2^{\bullet-}$.

   We also explored the catechol oxidase reactivity of a series of Mn^{II}_2 and Cu^{II}_2 complexes. Cu^{II}_2 complexes proved to be better catechol oxidase mimics than the Mn^{II}_2 complexes. Further DFT calculations will be performed to compare the energy parameters of all the complexes. Therefore, a better knowledge of the reaction mechanism of Mn^{II}_2- and Cu^{II}_2-catecholate adducts will be acquired.

4) Therefore, $Mn^{II}Mn^{III}$-peroxide and high valent $Mn^{III}Mn^{IV}$ adducts were prepared as model complexes for the postulated intermediates in class Ib Mn_2 RNRs. One of the peroxo-$Mn^{II}Mn^{III}$ compounds (**5**) proved to have a nucleophilic character while the reactivity of the postulated $Mn^{III}Mn^{IV}$ species will have to be explored. By changing the ligand system of the Mn^{II}_2 complexes might improve their reactivity with $O_2^{\bullet-}$. As seen above, while the peroxo-$Mn^{II}Mn^{III}$ complex **2** (supported by the N-Et-HPTB ligand) proved to be a poor nucleophilic/electrophilic oxidant at low temperatures, the peroxo adduct **5** (supported by the HBPMP ligand) had a nucleophilic character. Furthermore, the Mn^{II}_2 complex supported by the HPTP ligand was susceptible to O_2, while complexes **1** and **4** were not. Therefore,

changing the ligand system of the Mn^{II}_2 complexes plays an important role in the reactivity of the complexes towards different oxidants (O_2, $O_2^{\bullet-}$).

While until now, synthetic mononuclear Mn^{III}-peroxide complexes proved to have a nucleophilic character, their electrophilic reactivity is scarce. Possibly the preparation of a $Mn^{II}Mn^{III}$-hydroperoxide species using a different ligand system to N-Et-HPTB and HBPMP, might provide access to a more powerful electrophilic oxidant. Additionally, the generation of a powerful $Mn^{III}Mn^{IV}$ oxidant is important as a high valent $Mn^{III}Mn^{IV}$ intermediate was responsible for tyrosine oxidation. Besides, investigation of the synthetic $Mn^{III}Mn^{IV}$ complex with substrates in hydrogen atom abstraction (HAA) might form $Mn^{III}Mn^{III}$ as a product, another postulated intermediate in class Ib Mn_2 RNRs. The synthesis of model complexes for the intermediates postulated in class Ib Mn^{II}_2 RNRs will provide further support for the postulated mechanism of $O_2^{\bullet-}$ activation at class Ib Mn_2 RNRs. Understanding the catalytic cycle of RNR enzymes is essential as they are involved in DNA synthesis and repair and thus an important target for anticancer and antiviral agents.

Appendix A

A.1 Chapter 2

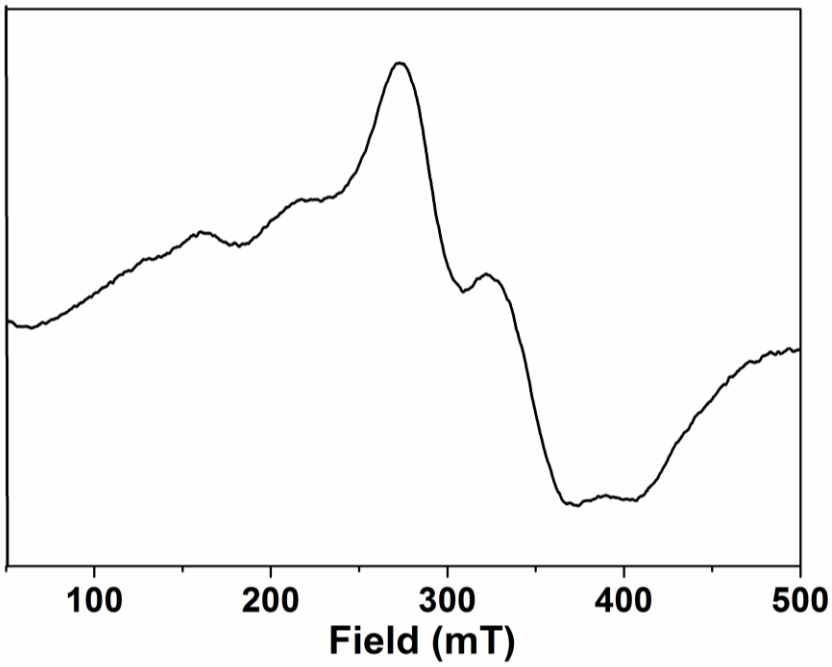

Figure A.1. X-Band EPR spectrum of complex **1** in CH_3CN at 77 K (9.21 GHz, 2 mW microwave power).

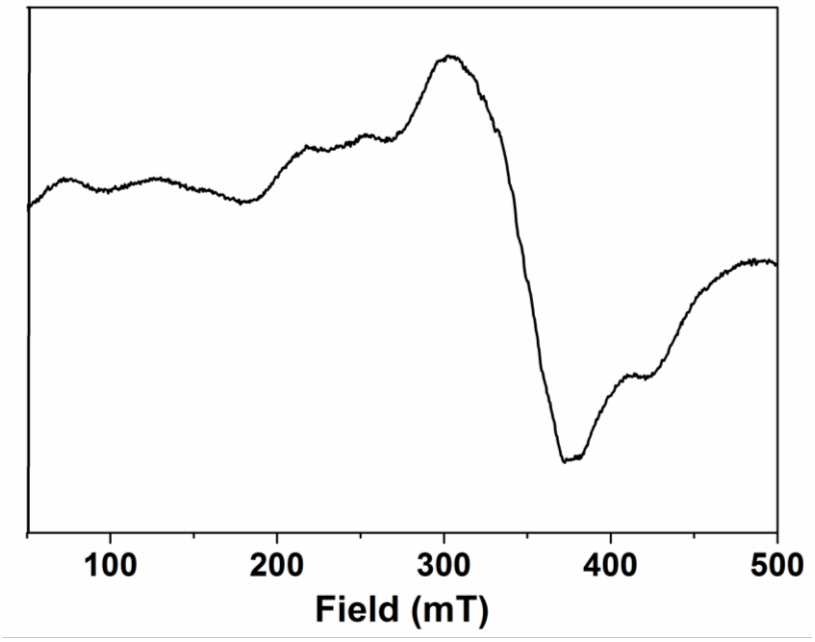

Figure A.2. X-Band EPR spectrum of complex **1** in CH_3CN at 2 K (9.64 GHz, 0.2 mW microwave power).

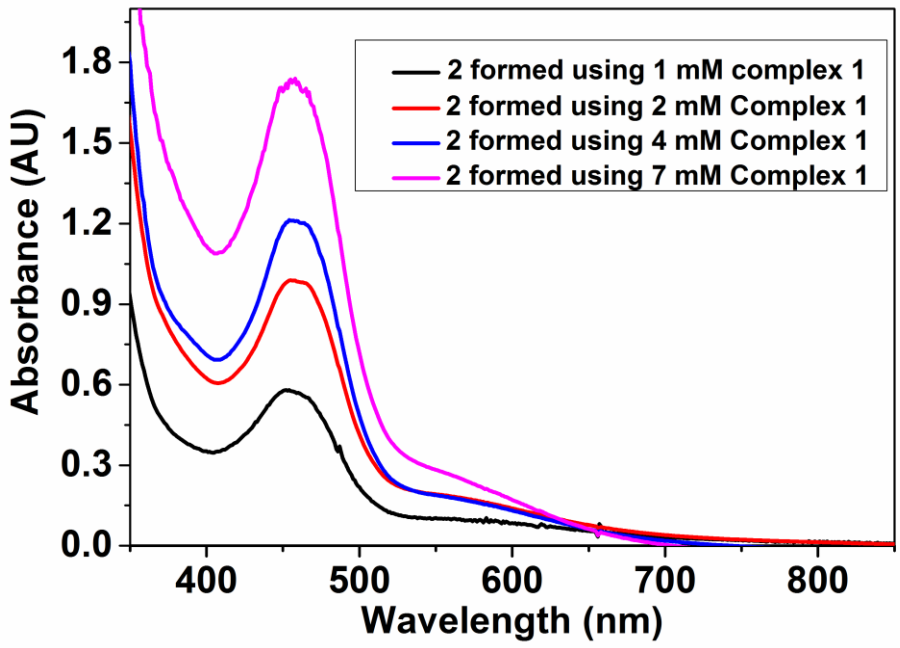

Figure A.3. Electronic absorption spectra of **2** at -40 °C in CH_3CN formed from the reaction of **1** with 3 equivalents of KO_2 and 1.5 equivalents of 18-crown-6 in DMF. Initial concentration of **1**: 1 mM (black band), 2 mM (red band), 4 mM (blue band) and 7 mM (pink band) (path length = 1 cm).

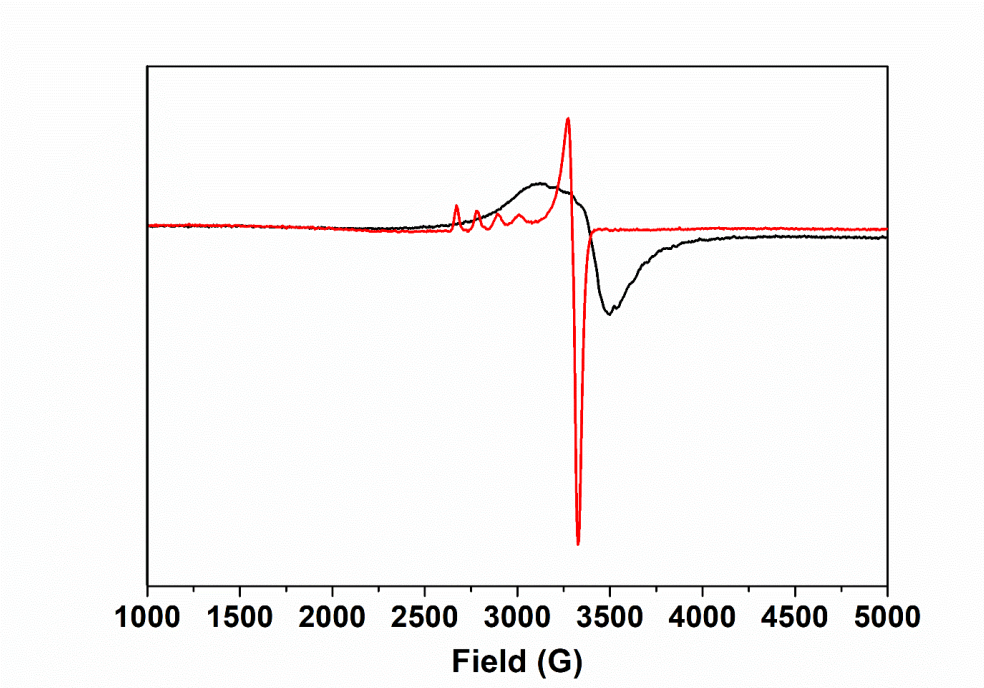

Figure A.4. Perpendicular mode EPR spectra of **2** in CH_3CN (obtained from the reaction of 1 mM **1** with KO_2 in CH_3CN-black line) and $Cu(NO_3)_2$ standard (0.25 mM) in CH_3OH (red line) (15 K, 9.64 GHz, 0.2 mW microwave power).

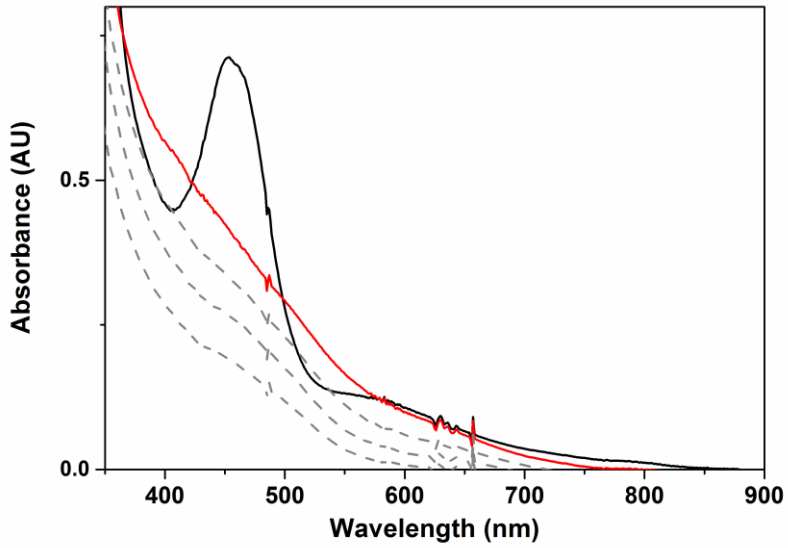

Figure A.5. UV-Vis spectral changes observed in the reaction between **2** (solid black trace), TEMPO-H (40 mM, 75 µl, 1.5 equivalents in acetonitrile), and HBF_4 (60 mM, 50 µl, 1.5 equivalents) in CH_3CN at -40 °C (path length = 1 cm).

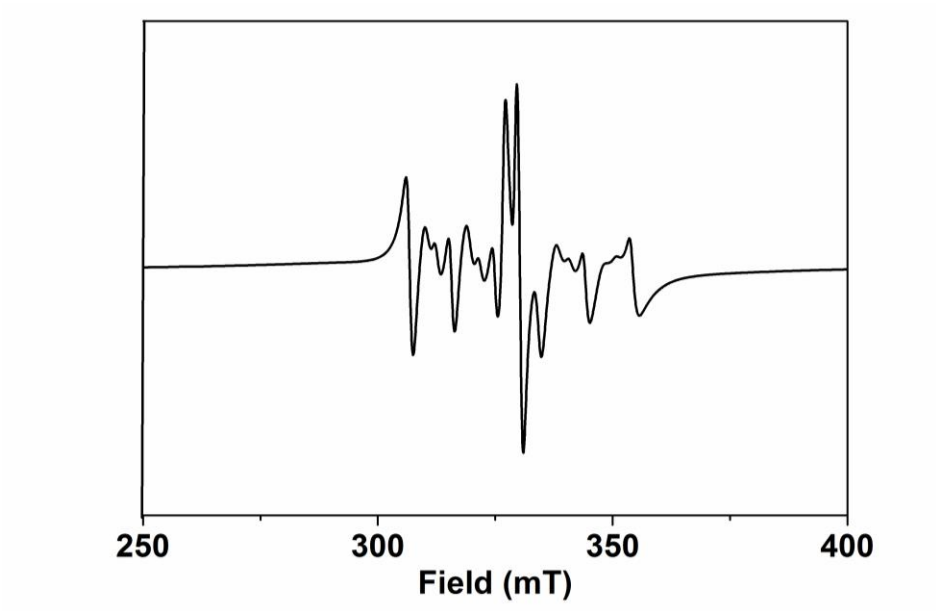

Figure A.6. X-Band EPR spectrum of the reaction between **2**, TEMPO-H (40 mM, 75 µl, 1.5 equivalents in acetonitrile), and HBF_4 (60 mM, 50 µl, 1.5 equivalents) at 77 K (9.21 GHz, 2 mW microwave power) in CH_3CN.

A.2 Chapter 3

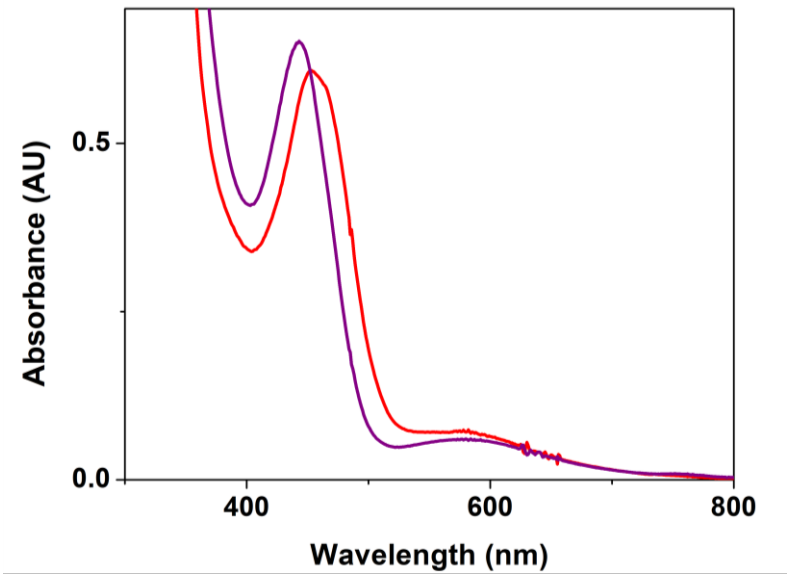

Figure A.7. Comparison of electronic absorption spectra of **5** (purple trace) at -90 °C in 1:9 CH_3CN/THF and that of the $Mn^{II}Mn^{III}$-peroxide supported by N-Et-HPTB ligand (**2**, red trace) at -40 °C in CH_3CN (path length = 1 cm).

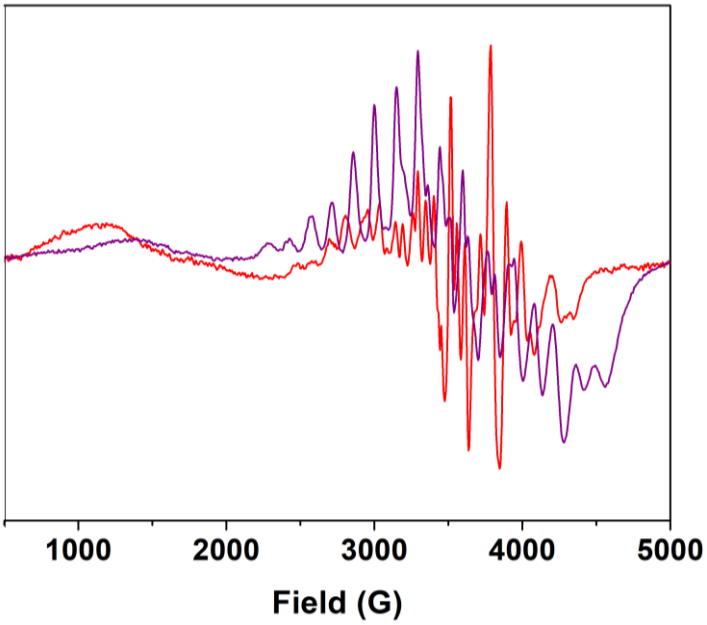

Figure A.8. Comparison of perpendicular mode EPR spectra of **5** at 2 K (purple trace, obtained from the reaction of 1.5 mM **1** and KO_2 in 1:9 CH_3CN/THF) (9.64 GHz, 0.2 mW microwave power, 1.5 mM of **1**) and that of $Mn^{II}Mn^{III}$-peroxide supported by N-Et-HPTB ligand at 2 K (**2**, red trace, 9.64 GHz, 0.2 mW microwave power).

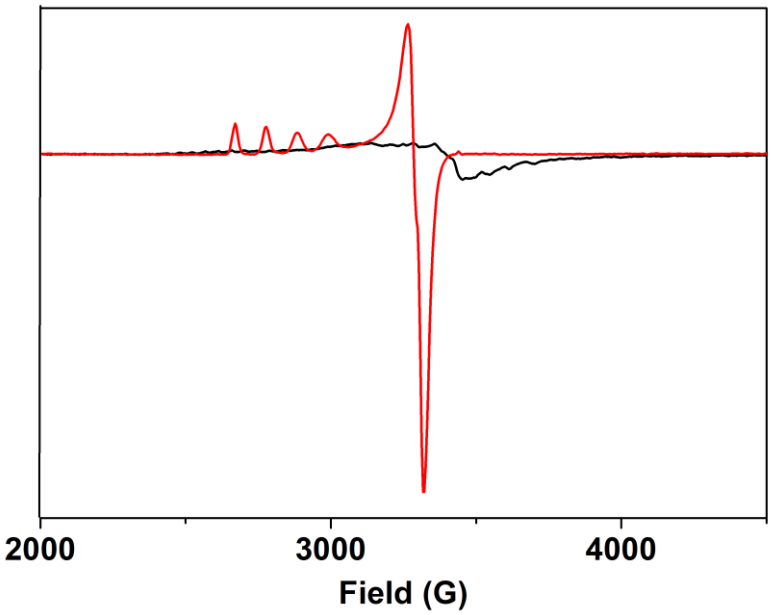

Figure A.9. Perpendicular mode EPR spectra of **5** in 1:9 CH_3CN/THF (obtained from the reaction of 1.5 mM **4** with KO_2 in 1:9 CH_3CN/THF-black line) and $Cu(NO_3)_2$ standard (0.25 mM) in CH_3OH (red line) (30 K, 9.64 GHz, 0.2 mW microwave power).

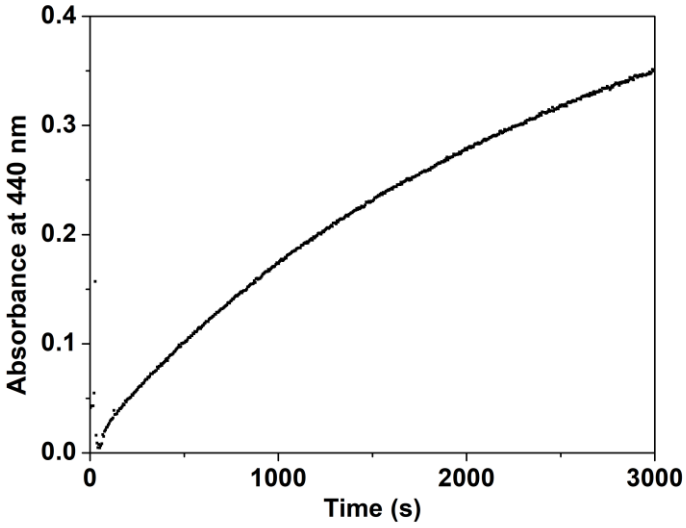

Figure A.10. Plot of absorptivity change at 440 nm versus time during the reaction between **5** and PPA.

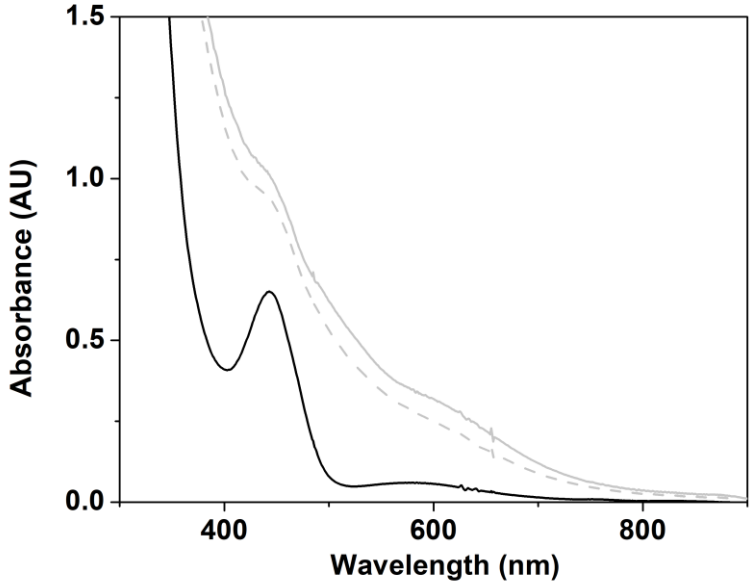

Figure A.11. UV-Vis spectral changes observed in the reaction between **5** (solid black trace) and PPA (4 M, 500 equivalents, solid grey trace) at -90 °C in 1:9 CH_3CN/THF (path length = 1 cm).

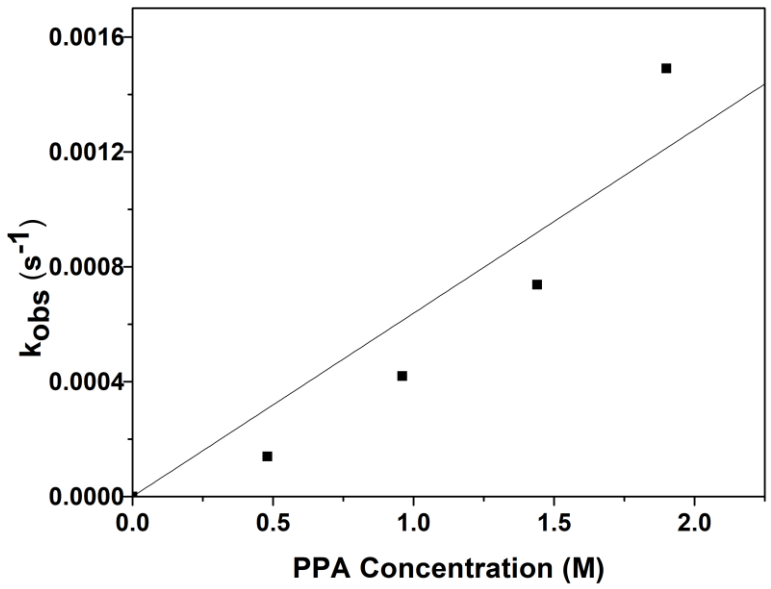

Figure A.12. Plot of k_{obs} versus PPA concentration determined for the reaction between **5** and PPA. $k_2 = 6.38 \times 10^{-4}$ $M^{-1}s^{-1}$

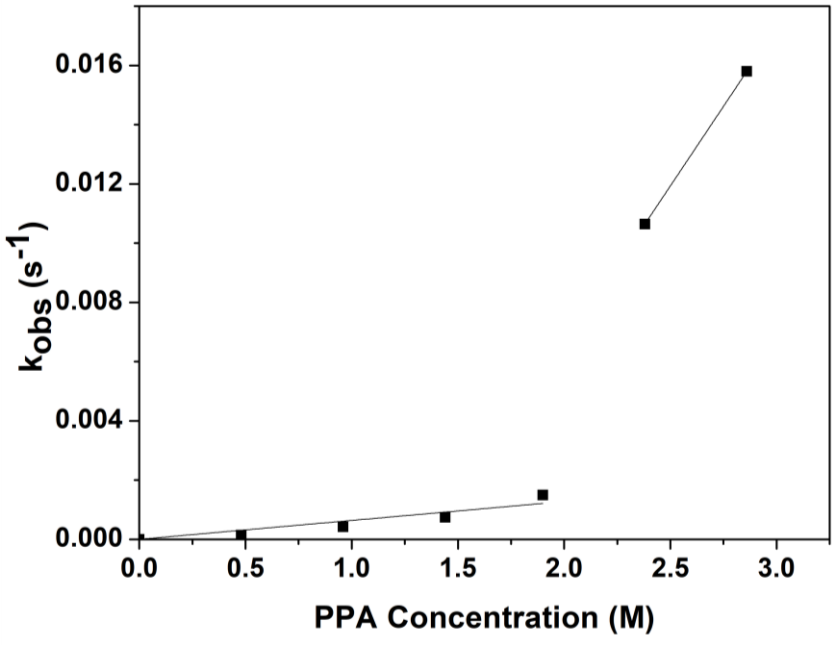

Figure A.13. Plot of k_{obs} versus PPA concentration determined for the reaction between **5** and PPA. $k_2 = 6.38 \times 10^{-4}$ $M^{-1}s^{-1}$; 0.011 $M^{-1}s^{-1}$.

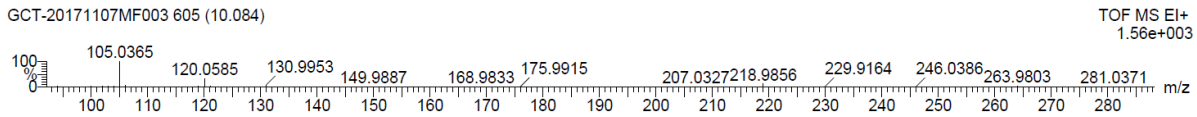

Minimum:				-1.5		
Maximum:		5.0	50.0	50.0		
Mass	Calc. Mass	mDa	PPM	DBE	i-FIT	Formula
120.0585	120.0575	1.0	8.3	5.0	1.0	C8 H8 O

Figure A.14. Mass spectrometry showing acetophenone formation from the post reaction mixture of **5** and PPA.

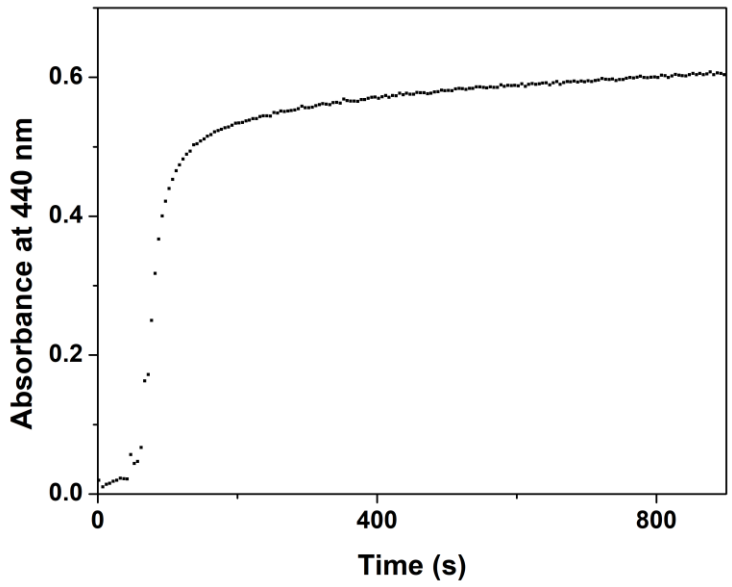

Figure A.15. Plot of absorptivity change at 440 nm versus time during the reaction between **5** and CCA.

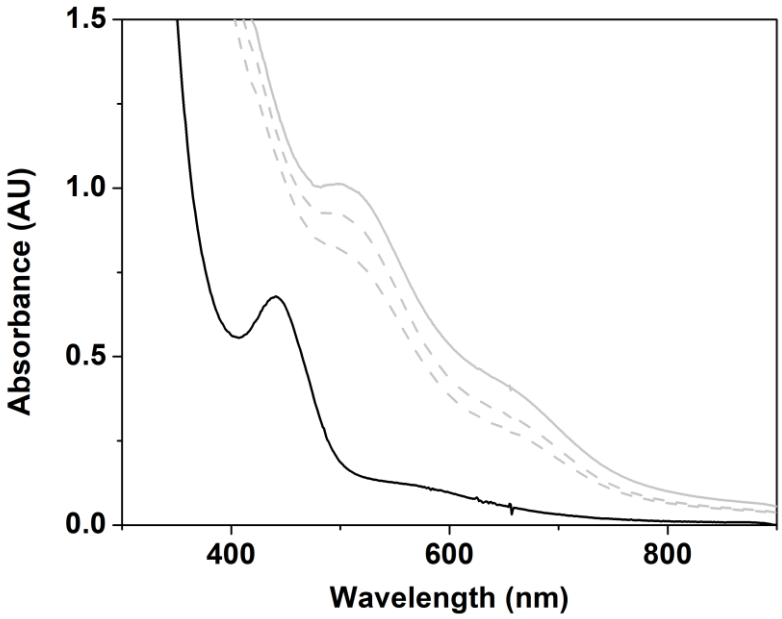

Figure A.16. UV-Vis spectral changes observed in the reaction between **5** (solid black trace) and CCA (4 M, 500 equivalents, solid grey trace) at -90 °C in 1:9 CH_3CN/THF (path length = 1 cm).

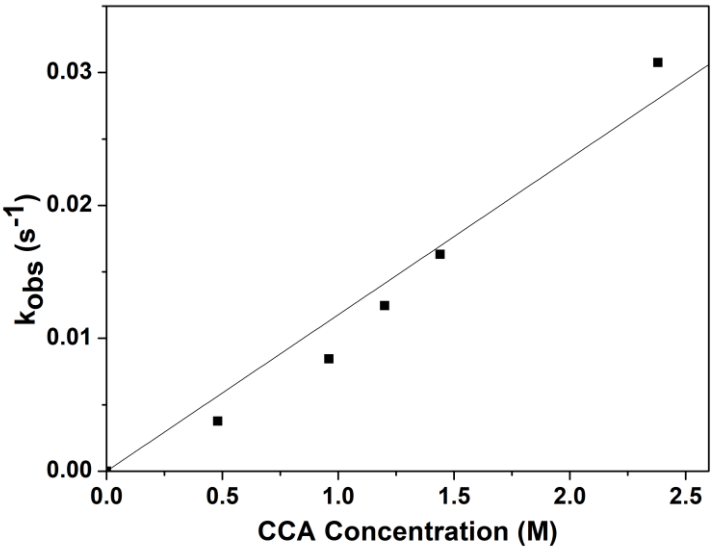

Figure A.17. Plot of k_{obs} versus CCA concentration determined for the reaction between **5** and CCA. k_2 = 0.012 $M^{-1}s^{-1}$.

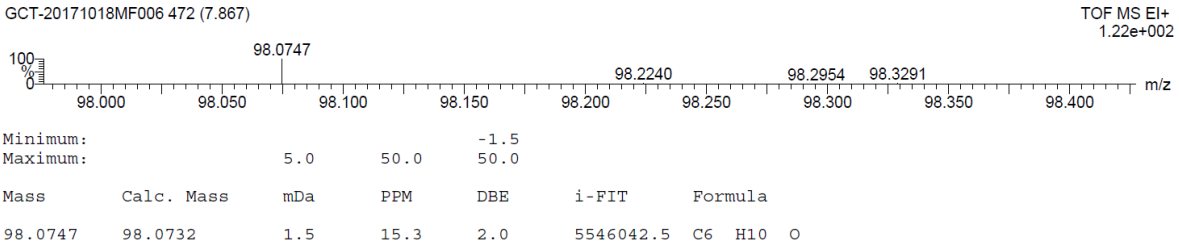

Minimum:				-1.5		
Maximum:		5.0	50.0	50.0		
Mass	Calc. Mass	mDa	PPM	DBE	i-FIT	Formula
98.0747	98.0732	1.5	15.3	2.0	5546042.5	C6 H10 O

Figure A.18. Mass spectrometry showing cyclohexanone formation from the post reaction mixture of **5** and CCA.

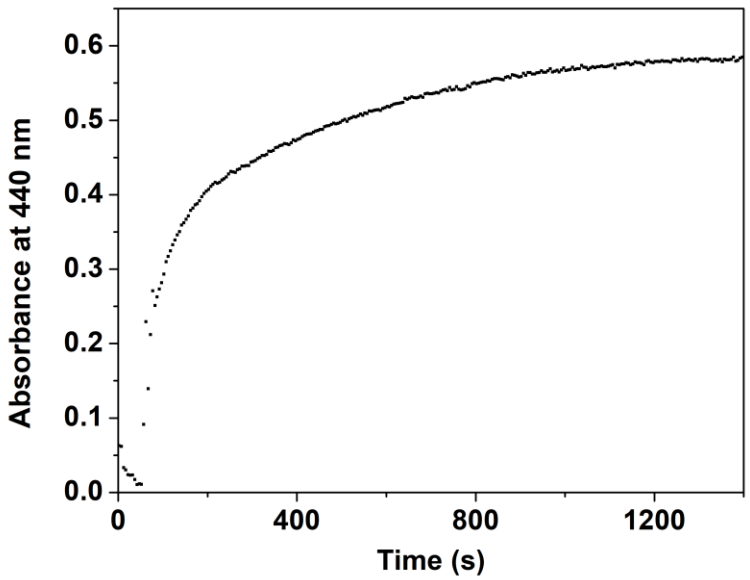

Figure A.19. Plot of absorptivity change at 440 nm versus time during the reaction between **5** and *p*-H-PhC(O)H.

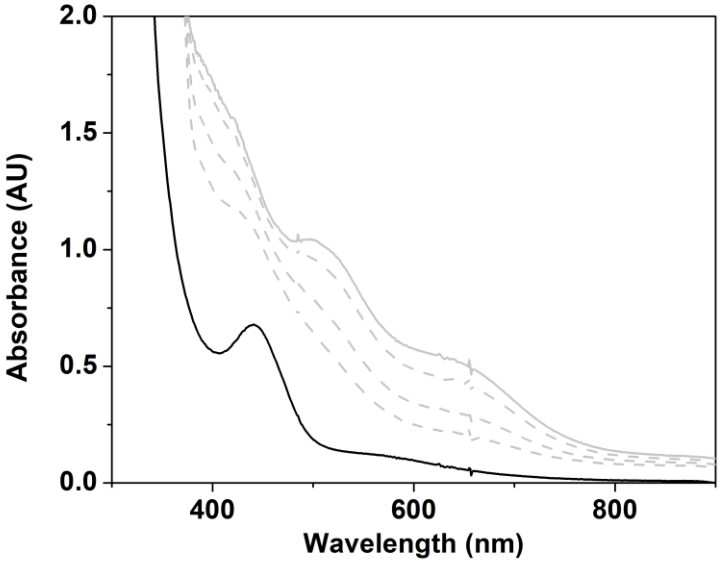

Figure A.20. UV-Vis spectral changes observed in the reaction between **5** (solid black trace) and *p*-H-PhC(O)H (4 M, 500 equivalents, solid grey trace) at -90 °C in 1:9 CH_3CN/THF (path length = 1 cm).

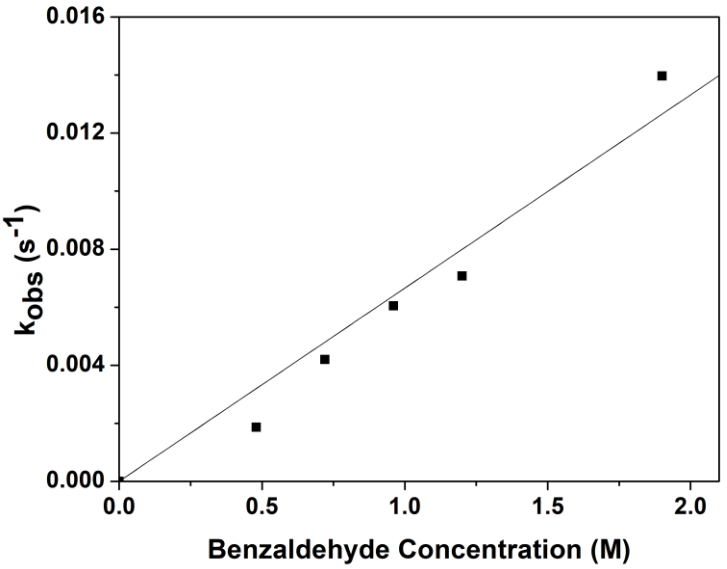

Figure A.21. Plot of k_{obs} versus *p*-H-PhC(O)H concentration determined for the reaction between **5** and *p*-H-PhC(O)H. k_2 = 0.0067 $M^{-1}s^{-1}$.

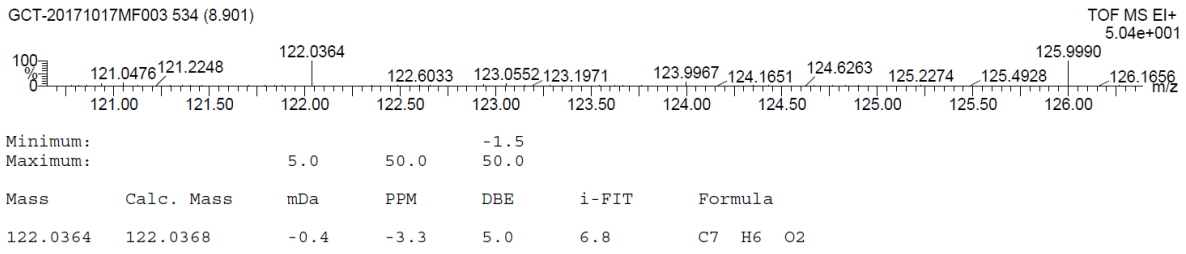

Minimum:				-1.5		
Maximum:		5.0	50.0	50.0		
Mass	Calc. Mass	mDa	PPM	DBE	i-FIT	Formula
122.0364	122.0368	-0.4	-3.3	5.0	6.8	C7 H6 O2

Figure A.22. Mass spectrometry showing benzoic acid formation from the post reaction mixture of **5** and *p*-H-PhC(O)H.

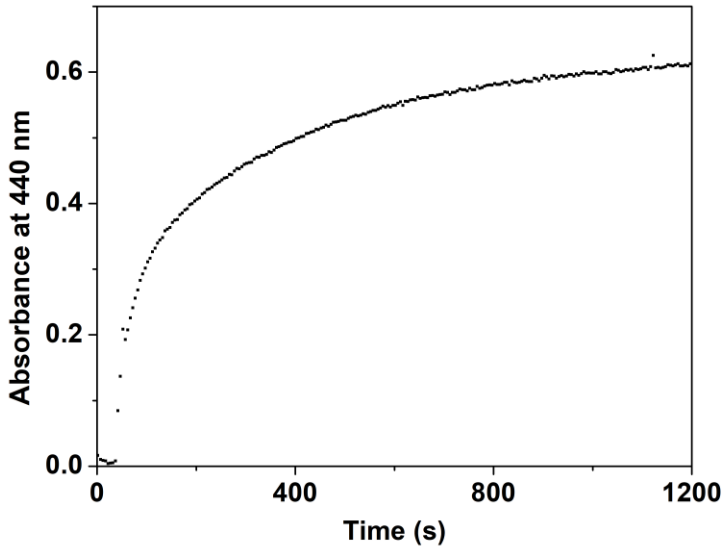

Figure A.23. Plot of absorptivity change at 440 nm versus time during the reaction between **5** and *p*-Cl-PhC(O)H.

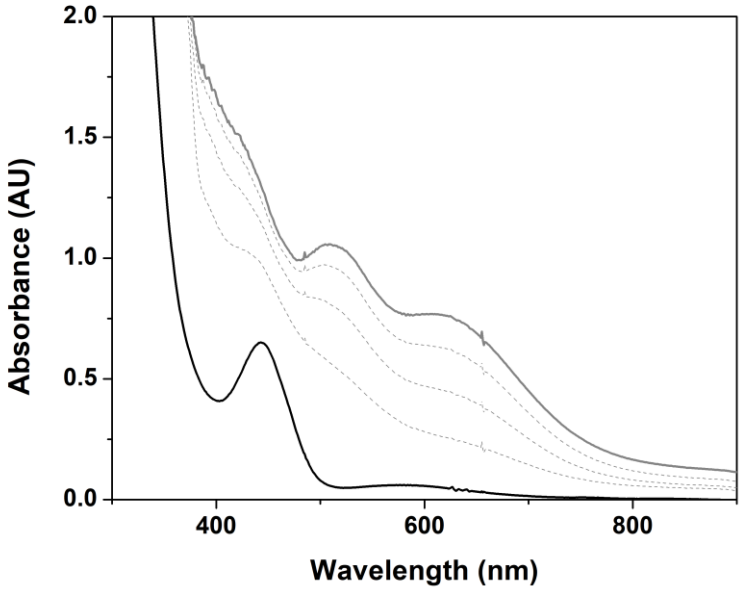

Figure A.24. UV-Vis spectral changes observed in the reaction between **5** (solid black trace) and *p*-Cl-PhC(O)H (4 M, 400 equivalents, solid grey trace) at -90 °C in 1:9 CH_3CN/THF (path length = 1 cm).

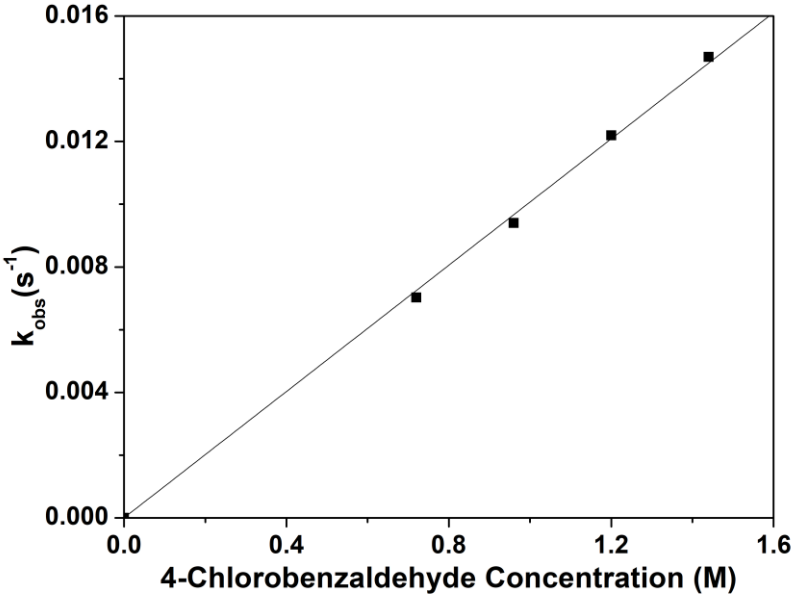

Figure A.25. Plot of k_{obs} versus *p*-Cl-PhC(O)H concentration determined for the reaction between **5** and *p*-Cl-PhC(O)H. k_2 = 0.01 $M^{-1}s^{-1}$.

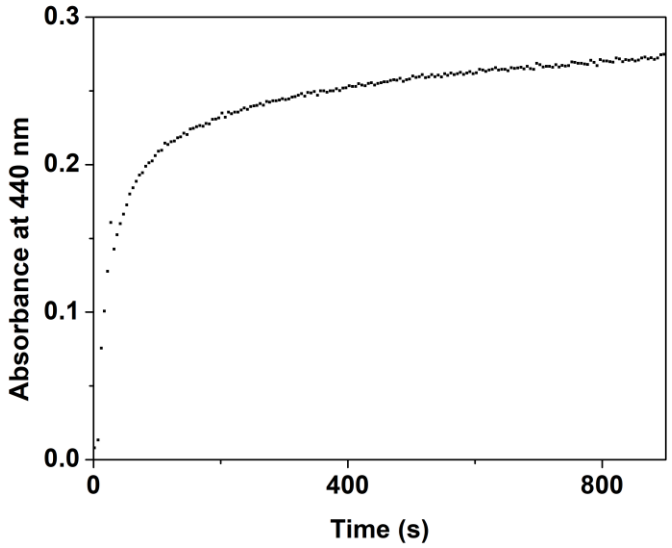

Figure A.26. Plot of absorptivity change at 440 nm versus time during the reaction between **5** and *p*-CF_3-PhC(O)H.

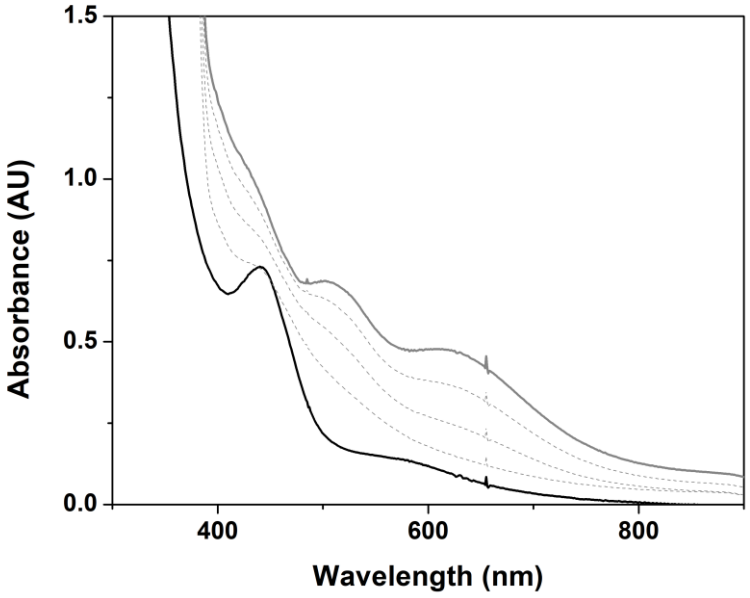

Figure A.27. UV-Vis spectral changes observed in the reaction between **5** (solid black trace) and *p*-CF_3-PhC(O)H (4 M, 400 equivalents, solid grey trace) at -90 °C in 1:9 CH_3CN/THF (path length = 1 cm).

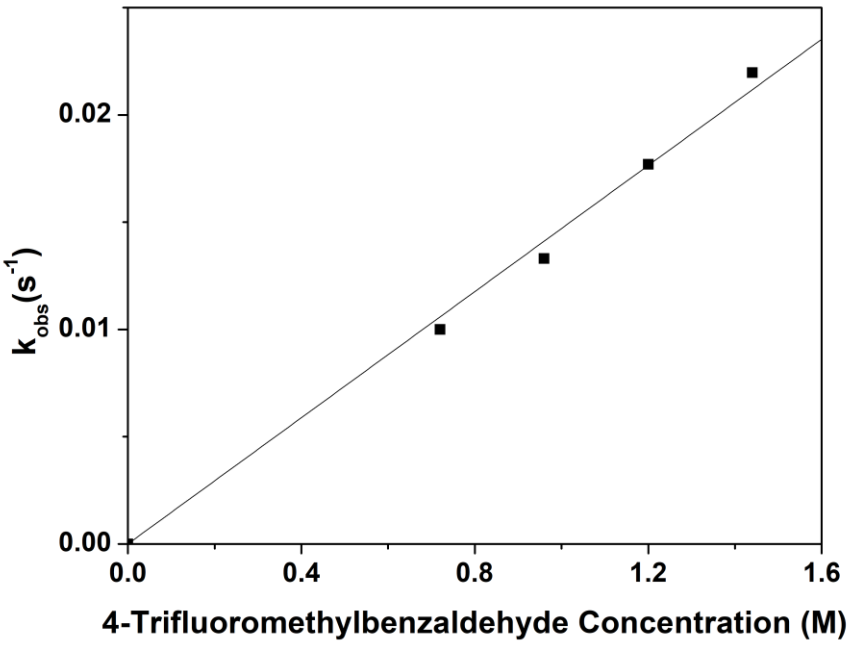

Figure A.28. Plot of k_{obs} versus *p*-CF_3-PhC(O)H concentration determined for the reaction between **5** and *p*-CF_3-PhC(O)H. k_2 = 0.015 $M^{-1}s^{-1}$.

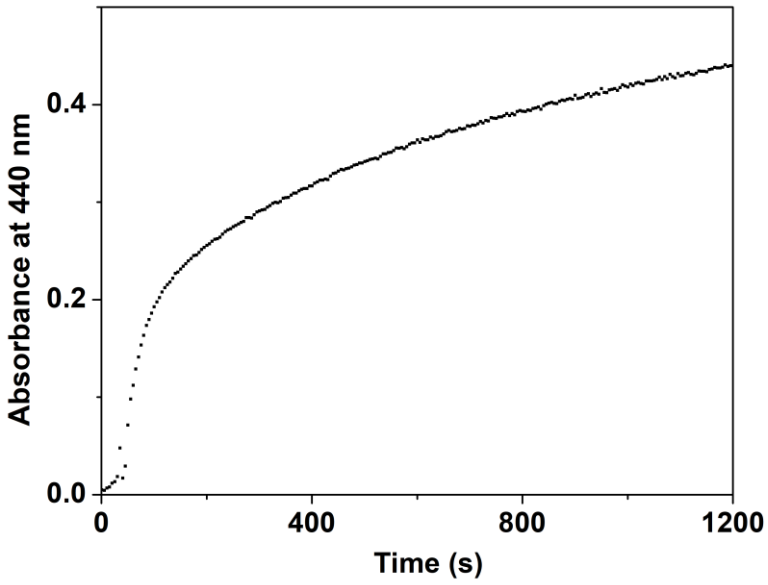

Figure A.29. Plot of absorptivity change at 440 nm versus time during the reaction between **5** and *p*-CN-PhC(O)H.

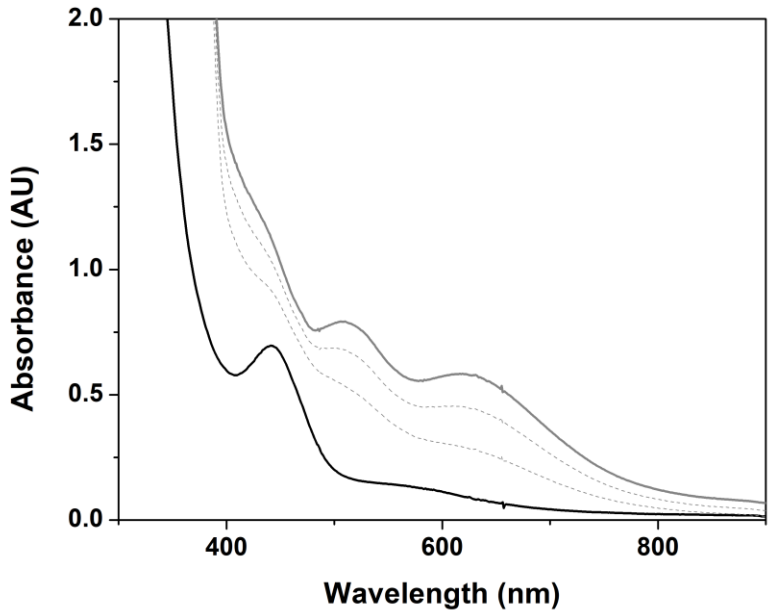

Figure A.30. UV-Vis spectral changes observed in the reaction between **5** (solid black trace) and *p*-CN-PhC(O)H (4 M, 300 equivalents, solid grey trace) at -90 °C in 1:9 CH_3CN/THF (path length = 1 cm).

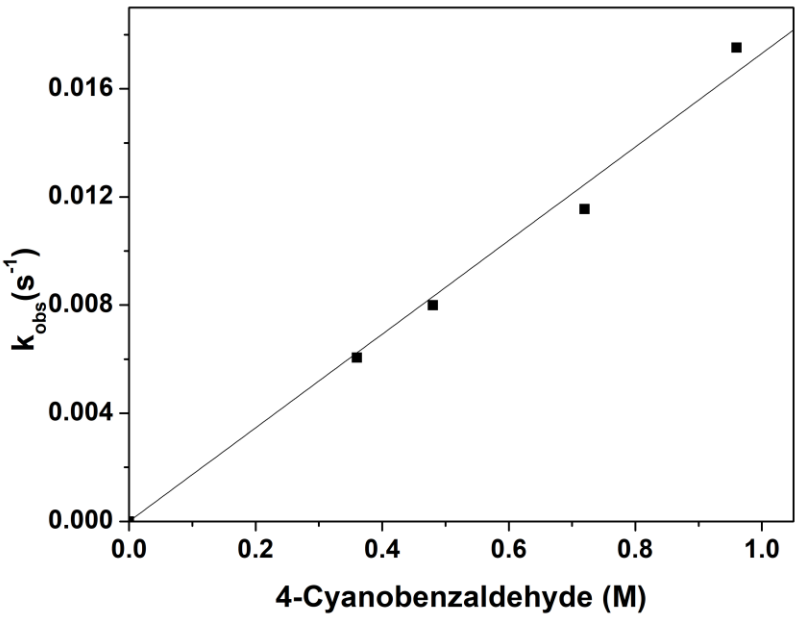

Figure A.31. Plot of k_{obs} versus *p*-CN-PhC(O)H concentration determined for the reaction between **5** and *p*-CN-PhC(O)H. $k_2 = 0.017\ M^{-1}s^{-1}$.

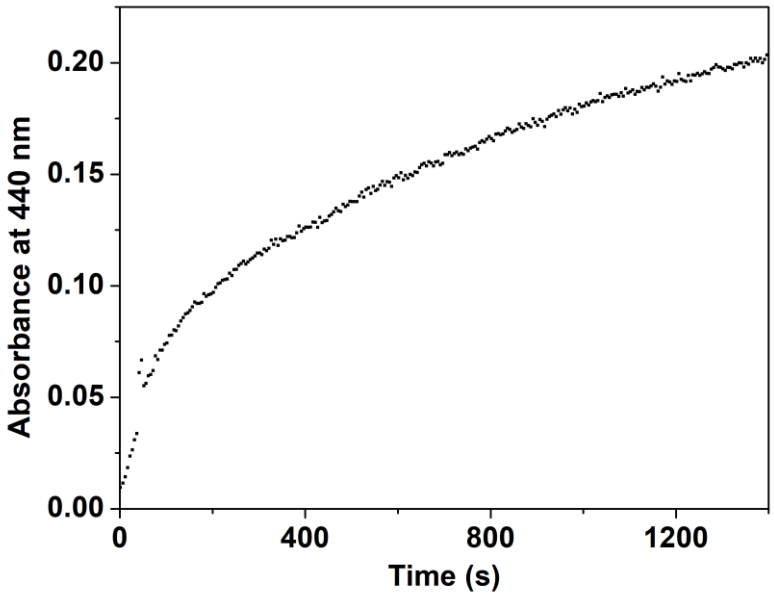

Figure A.32. Plot of absorptivity change at 440 nm versus time during the reaction between **5** and *p*-NO_2-PhC(O)H.

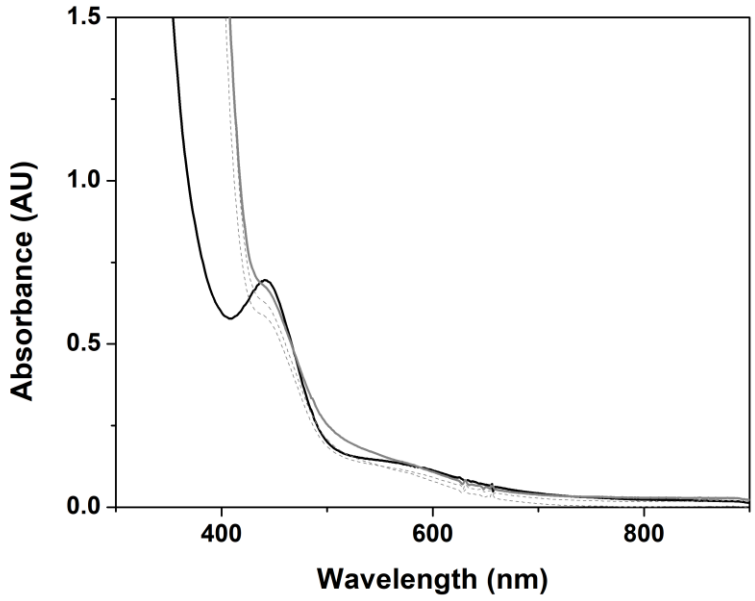

Figure A.33. UV-Vis spectral changes observed in the reaction between **5** (solid black trace) and *p*-NO_2-PhC(O)H (4 M, 100 equivalents, solid grey trace) at -90 °C in 1:9 CH_3CN/THF (path length = 1 cm).

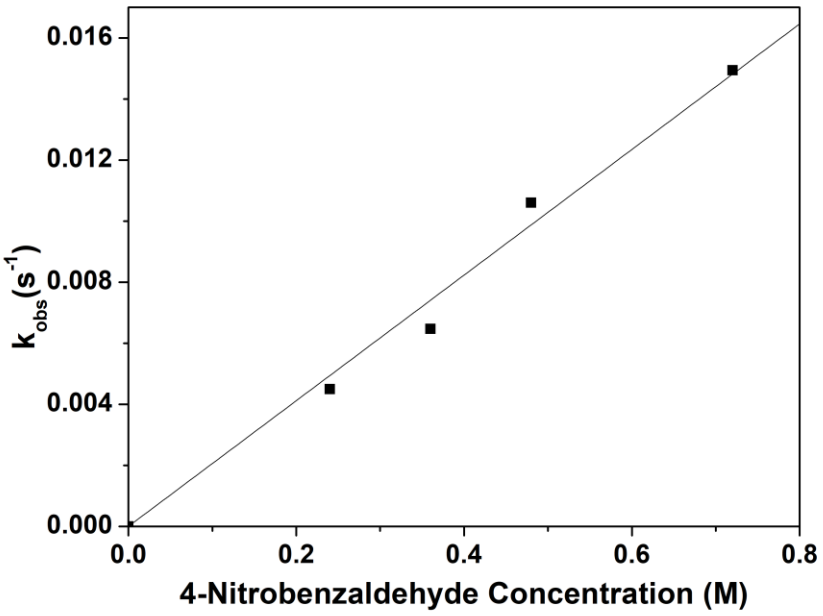

Figure A.34. Plot of k_{obs} versus *p*-NO_2-PhC(O)H concentration determined for the reaction between **5** and *p*-NO_2-PhC(O)H. k_2 = 0.021 $M^{-1}s^{-1}$.

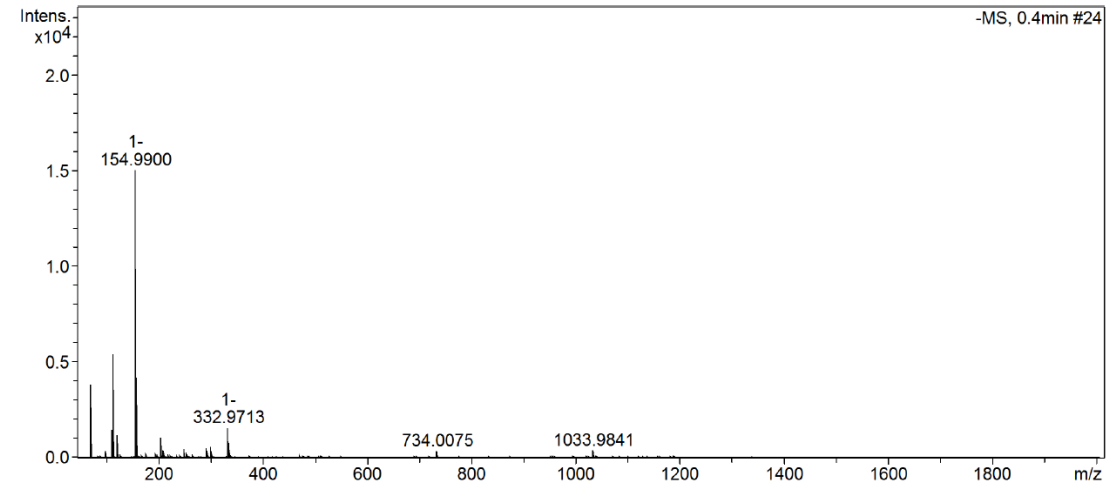

Meas. m/z	#	Ion Formula	m/z	err [mDa]	err [ppm]	rdb	N-Rule	e⁻ Conf	mSigma
154.990012	1	C7H4ClO2	154.990531	-0.5	-3.3	5.5	ok	even	26.4

Figure A.35. Mass spectrometry showing Cl-PhC(OO)$^-$ formation from the post reaction mixture of **5** and *p*-Cl-PhC(O)H.

A.3 Chapter 4

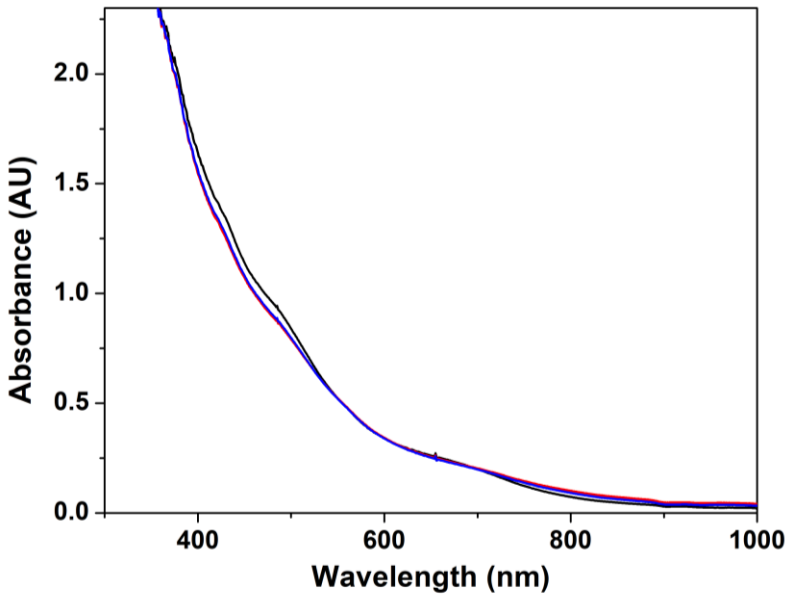

Figure A.36. Electronic absorption spectrum after species **5** was warmed up from -90 °C, to -50 °C (black trace), to -20 °C and to 0 °C in 1:9 CH_3CN/THF (path length = 1 cm).

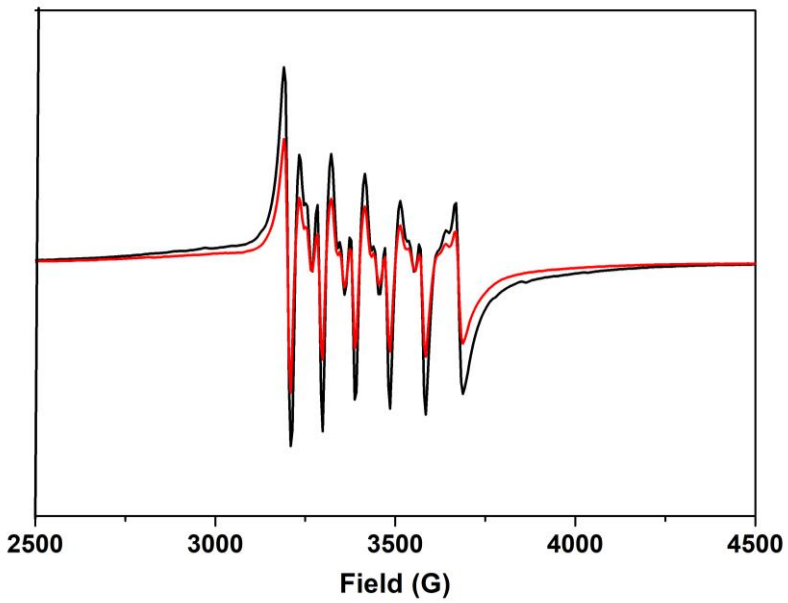

Figure A.37. Perpendicular mode EPR spectra of **7** at 2 K (black trace, obtained from the reaction of **5** and $HClO_4$ in 1:9 CH_3CN/THF) (9.64 GHz, 0.2 mW microwave power, 1.5 mM of **4**) and $Mn(ClO_4)_2.6H_2O$ standard (2.25 mM) at 2 K (red trace, 9.64 GHz, 0.2 mW microwave power).

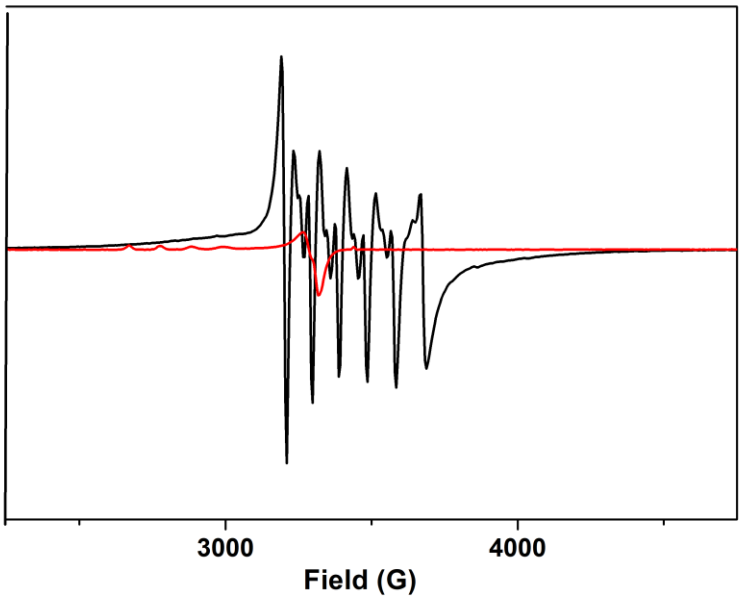

Figure A.38. Perpendicular mode EPR spectra of **7** in 1:9 CH_3CN/THF (obtained from the reaction of **5** with $HClO_4$ in 1:9 CH_3CN/THF-black line) and $Cu(NO_3)_2.3H_2O$ standard (0.25 mM) in CH_3OH (red line) (30 K, 9.64 GHz, 0.2 mW microwave power).

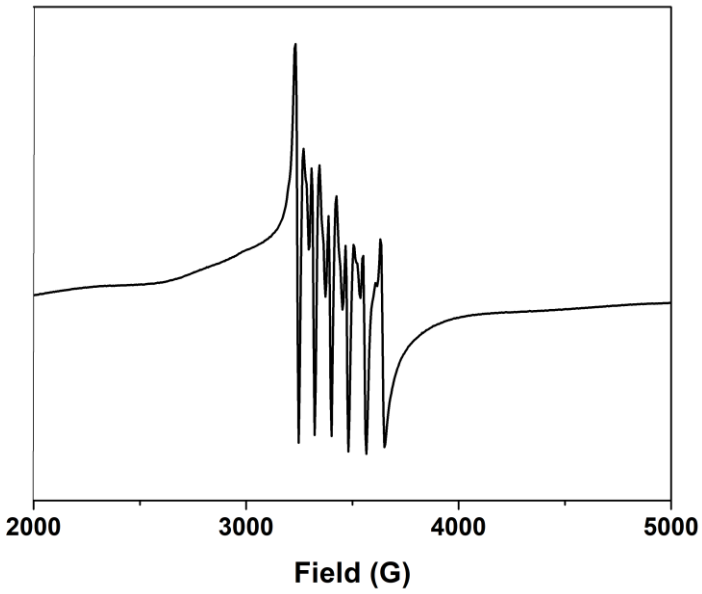

Figure A.39. Perpendicular mode EPR spectra of **8** (obtained from the reaction of **5** with 4 equivalents *p*TsOH in 1:9 CH_3CN/THF, black line) at 77 K in 1:9 CH_3CN/THF.

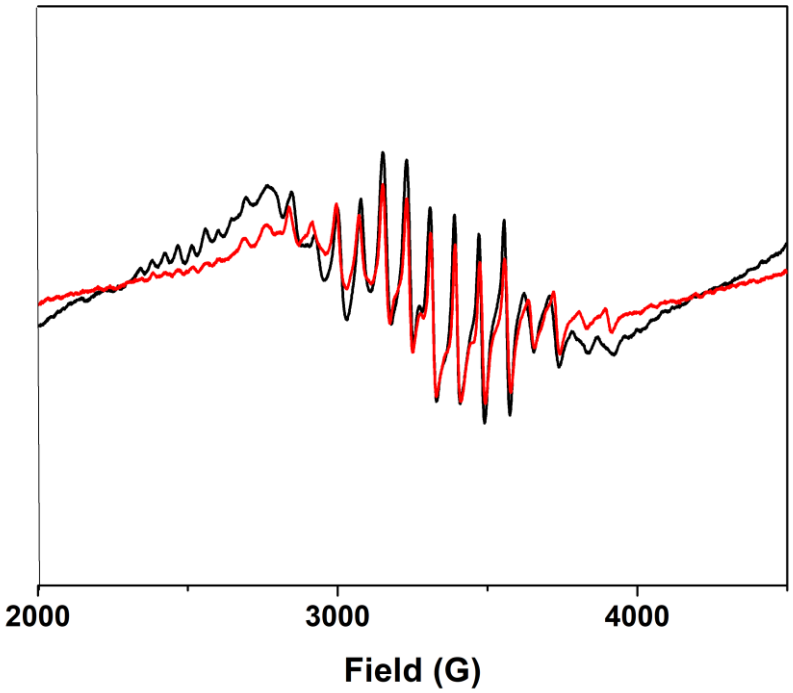

Figure A.40. Comparison of EPR spectra after addition of 1 (black trace) and 2 (red trace) equivalents of *p*TsOH to **5** at 77 K (9.21 GHz, 2 mW microwave power).

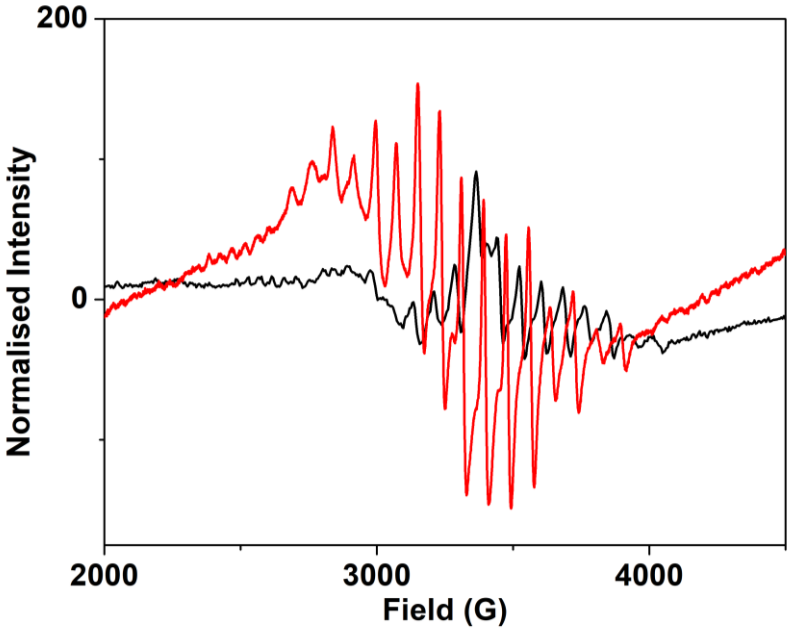

Figure A.41. Comparison of normalised EPR spectra of complex **6** (thermal decay of **5**) with that of complex **9** (**5** + 2 equivalents of *p*TsOH) at 77 K.

A.4 Chapter 5

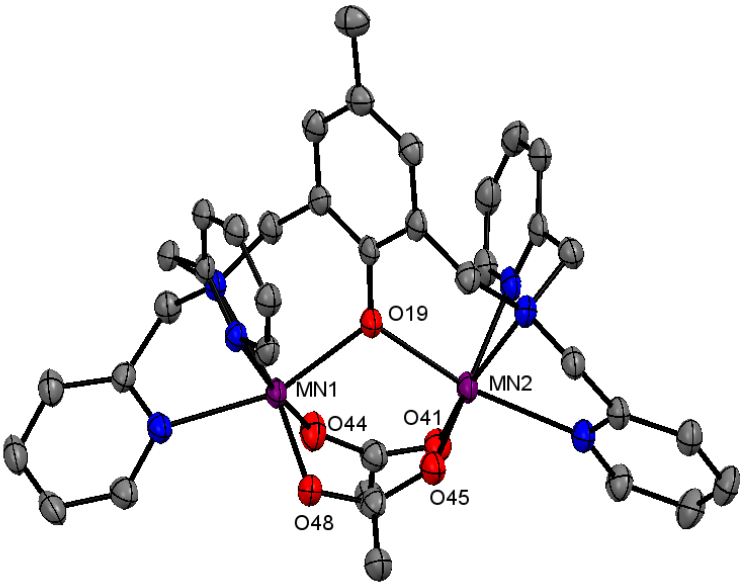

Figure A.42. ORTEP plot of complex **4**. Hydrogen atoms, a perchlorate anion and an ether molecule have been removed for clarity (purple = Mn, grey = C, blue = N, red = O). Ellipsoids are shown at 50% probability. Selected bond distances (Å): Mn1-Mn2: 3.41, Mn1-O19: 2.11, Mn1-O44: 2.15, Mn1-O48: 2.11, Mn2-O19: 2.1, Mn2-O41: 2.09, Mn2-O45: 2.15.

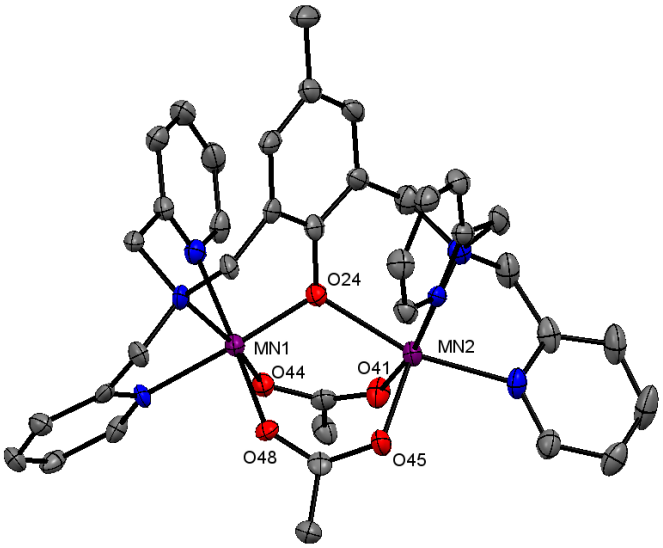

Figure A.43. ORTEP plot of **10**. Hydrogen atoms and perchlorate anions have been removed for clarity (purple = Mn, grey = C, blue = N, red = O). Ellipsoids are shown at 50% probability. Selected bond distances (Å): Mn1-Mn2: 3.45, Mn1-O24: 1.9, Mn1-O44: 1.9, Mn1-O48: 2.12, Mn2-O24: 2.18, Mn2-O41: 2.14, Mn2-O45: 2.09.

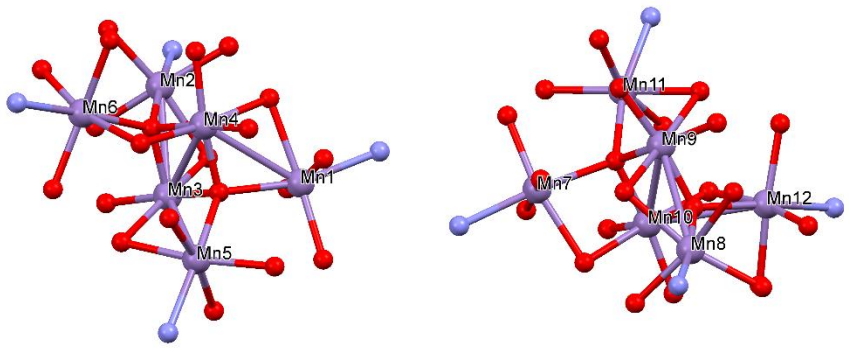

Figure A.44. ORTEP plot of the Mn_6 core. Hydrogen atoms, acetonitrile molecules and carboxylate groups have been omitted for clarity. Ellipsoids are shown at 50% probability.

A.5 Chapter 6

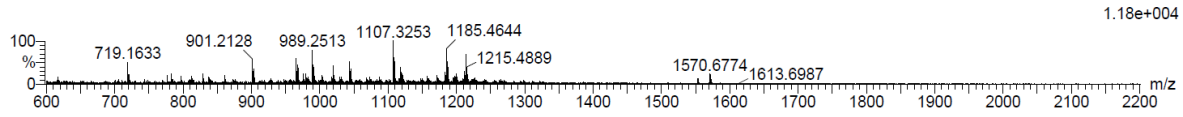

Minimum:				-1.5			
Maximum:		5.0	10.0	200.0			
Mass	Calc. Mass	mDa	PPM	DBE	i-FIT	i-FIT (Norm)	Formula
989.2513	989.2470	4.3	4.3	24.5	55.4	0.0	C45 H52 N10 O7 Cl Mn2

Figure A.45. Maldi-ToF mass spectrometry showing formation of complex **1**.

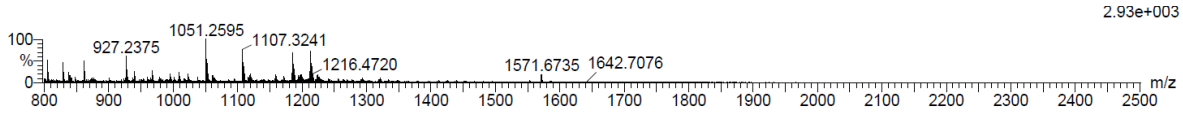

Minimum:				-1.5			
Maximum:		5.0	5.0	500.0			
Mass	Calc. Mass	mDa	PPM	DBE	i-FIT	i-FIT (Norm)	Formula
1051.2595	1051.2626	-3.1	-2.9	28.5	50.3	0.0	C50 H54 N10 O7 Cl Mn2

Figure A.46. Maldi-ToF mass spectrometry showing formation of complex **12**.

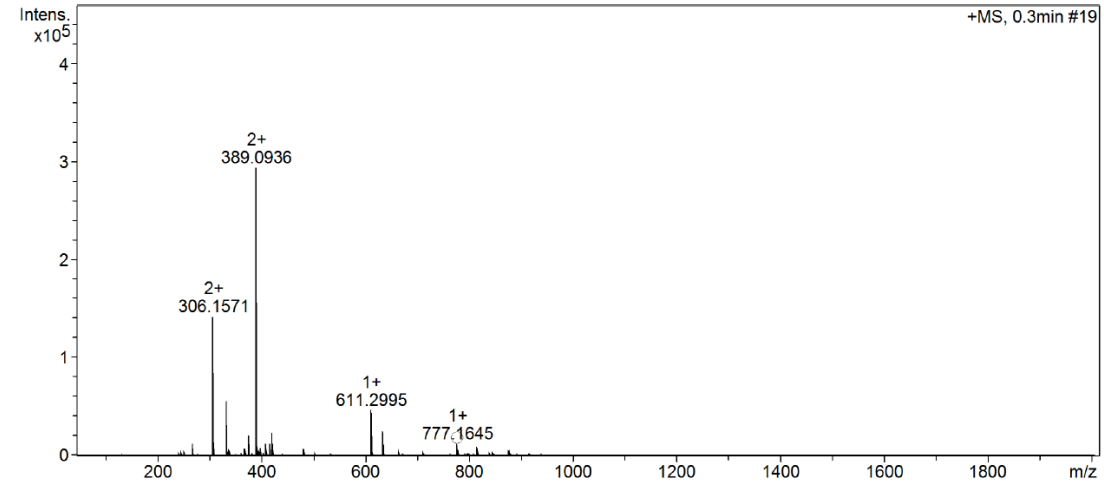

Meas. m/z	#	Ion Formula	m/z	err [mDa]	err [ppm]	rdb	N-Rule	e⁻ Conf	mSigma
777.164474	1	C37H35Mn2N10O3	777.164902	-0.4	-0.5	25.5	ok	even	44.1

Figure A.47. ESI-MS showing formation of complex **3**.

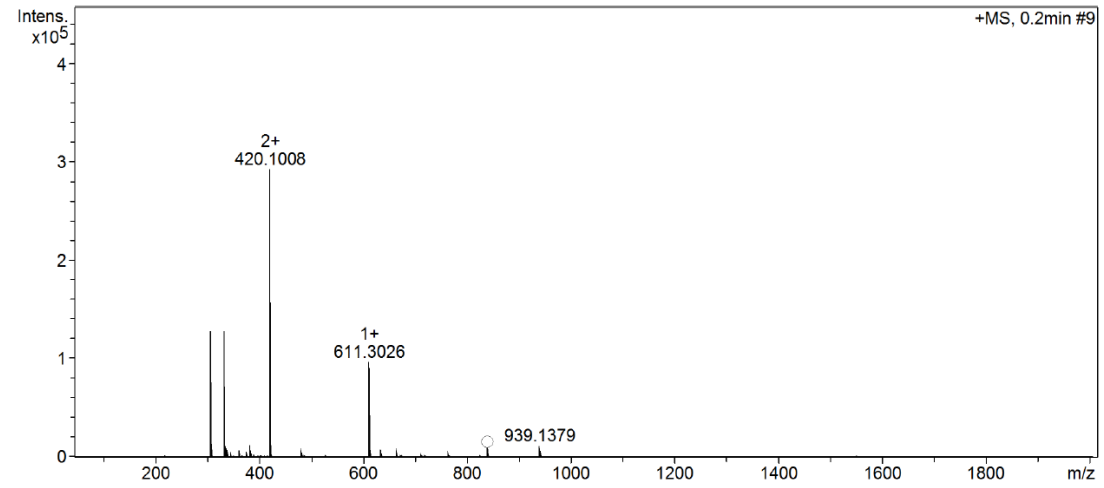

Meas. m/z	#	Ion Formula	m/z	err [mDa]	err [ppm]	rdb	N-Rule	e⁻ Conf	mSigma
839.179958	1	C42H37Mn2N10O3	839.180552	-0.6	-0.7	29.5	ok	even	13.5

Figure A.48. ESI-MS showing formation of complex **13**.

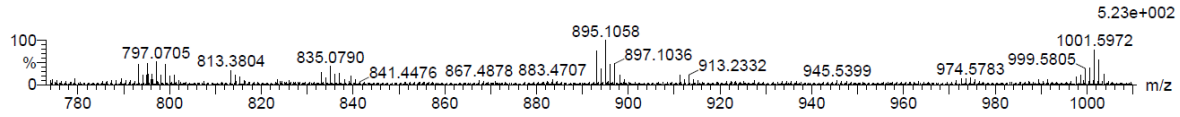

Minimum:				-1.5			
Maximum:		5.0	20.0	500.0			
Mass	Calc. Mass	mDa	PPM	DBE	i-FIT	i-FIT (Norm)	Formula
893.1071	893.1049	2.2	2.5	24.5	73.1	0.0	C37 H36 N10 O7 Cl Cu2

Figure A.49. ESI-MS showing formation of complex **14**.

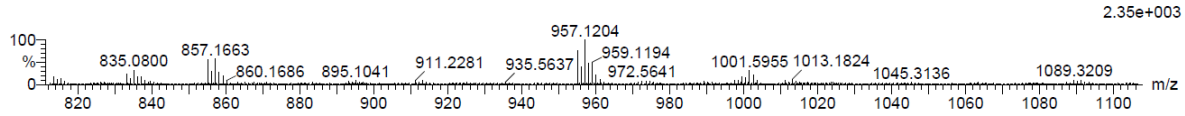

Minimum:				-1.5								
Maximum:		5.0	20.0	500.0								
Mass	Calc. Mass	mDa	PPM	DBE	i-FIT	i-FIT (Norm)	Formula					
955.1213	955.1205	0.8	0.8	28.5	79.5	0.0	C42	H38	N10	O7	Cl	Cu2

Figure A.50. ESI-MS showing formation of complex **15**.

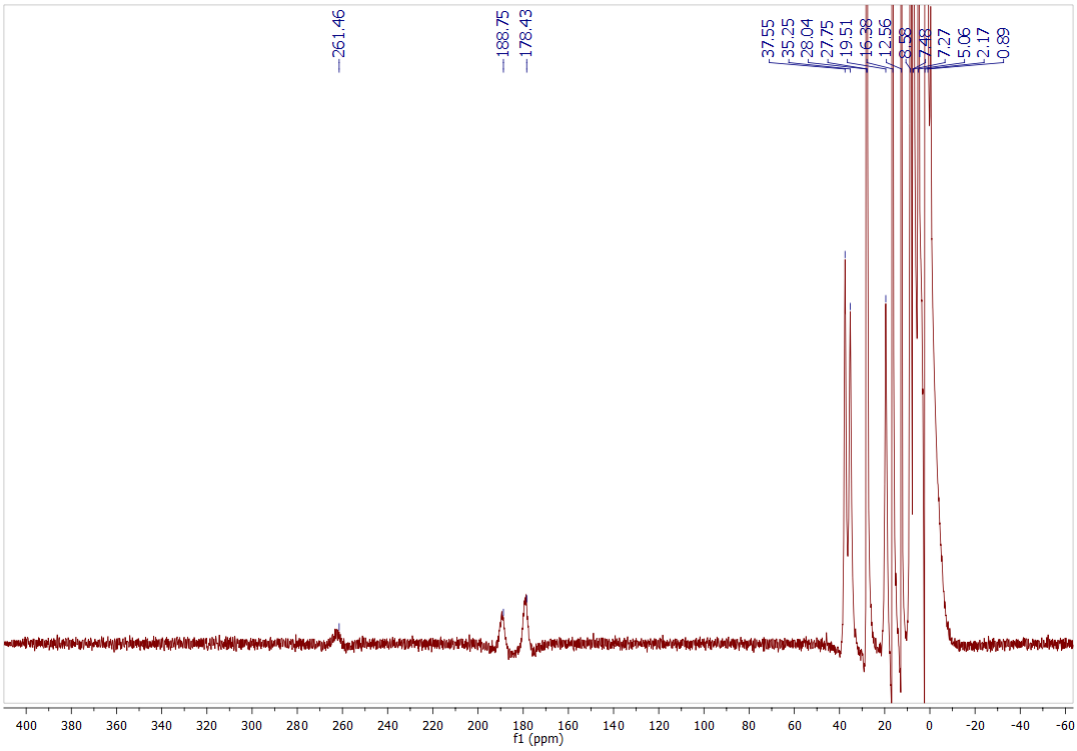

Figure A.51. ^{1}H NMR of complex **14** in CD_3CN.

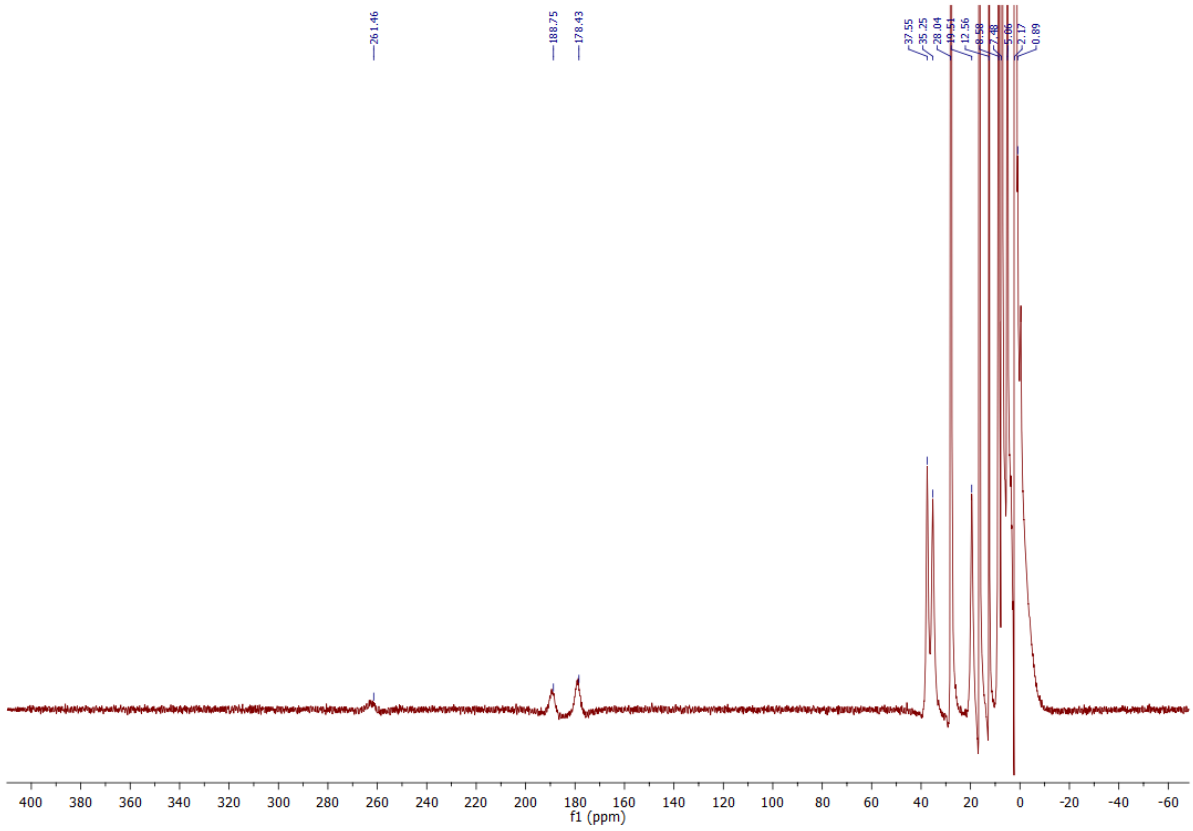

Figure A.52. ^{1}H NMR of complex **15** in CD_3CN.

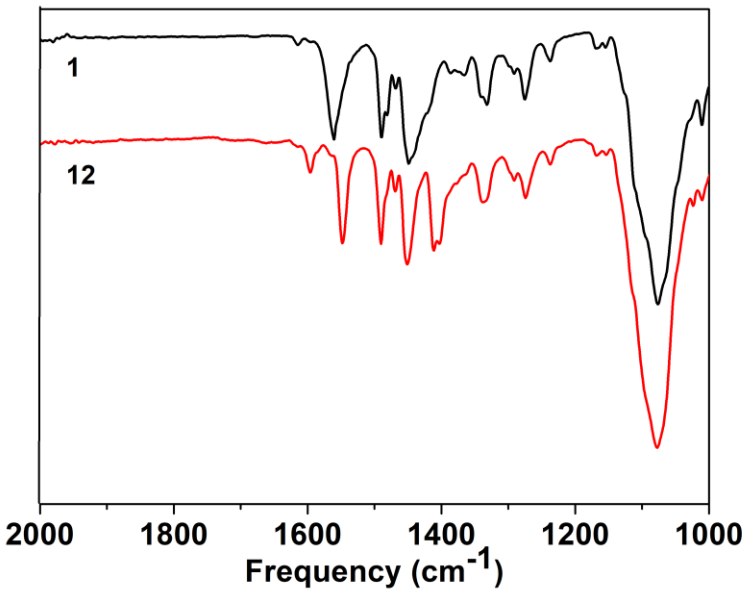

Figure A.53. ATR-FTIR spectra of manganese complexes **1-12**. Black = **1**, red = **12**.

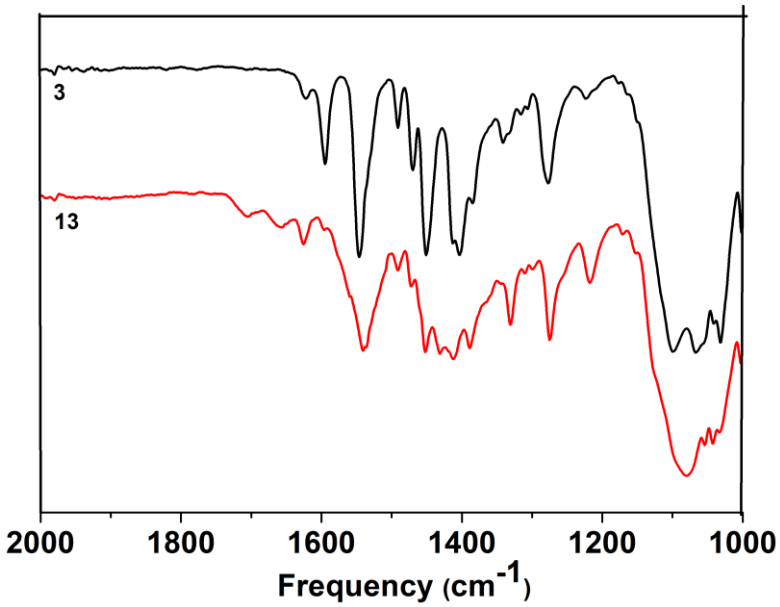

Figure A.54. ATR-FTIR spectra of manganese complexes **3-13**. Black = **3**, red = **13**.

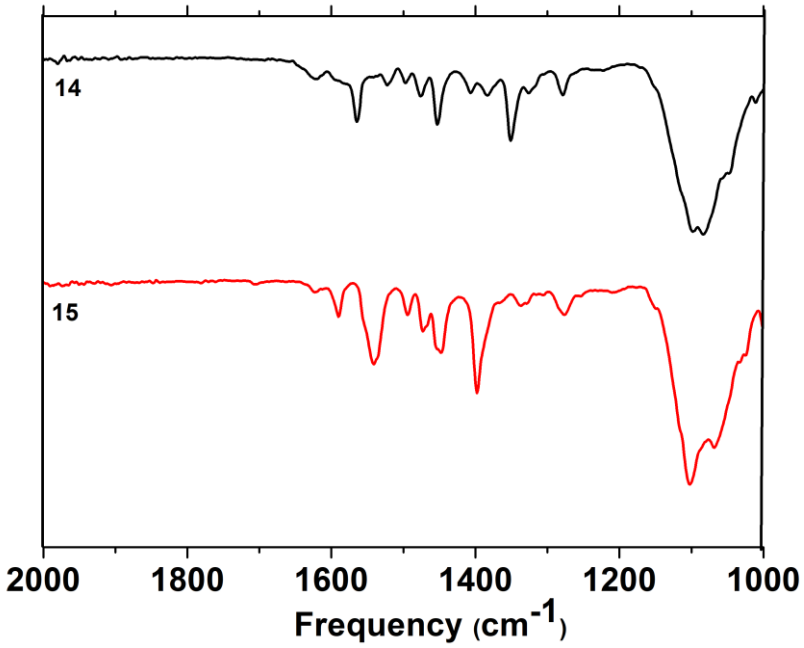

Figure A.55. ATR-FTIR spectra of copper complexes **14-15**. Black = **14**, red = **15**.

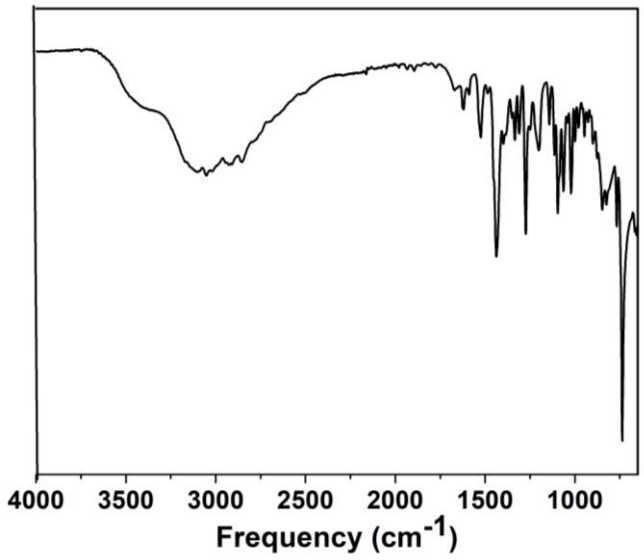

Figure A.56. ATR-FTIR spectrum of ligand HPTB.

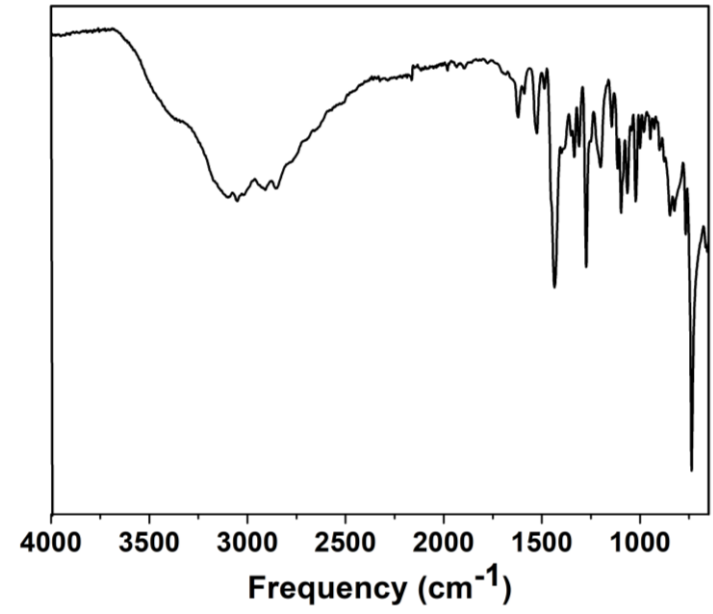

Figure A.57. ATR-FTIR of ligand N-Et-HPTB.

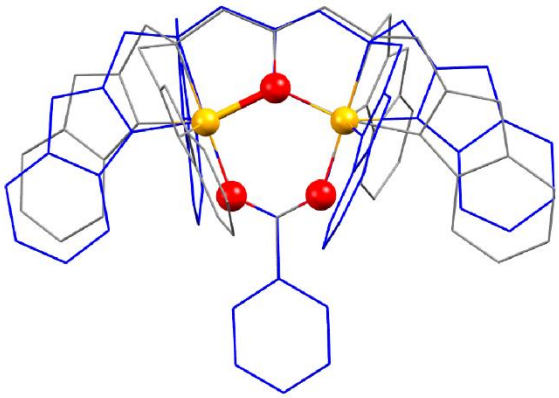

Figure A.58. Overlapping structure of Cu^{II}_2 complexes **14** (grey wireframe) and **15** (blue wireframe)**.**

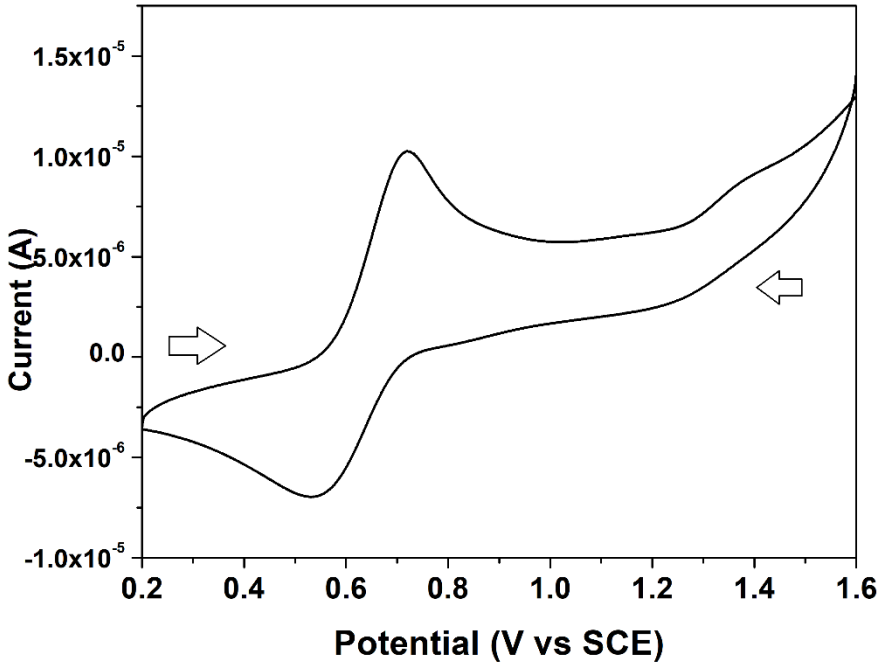

Figure A.59. Cyclic voltammogram of complex **1** (1 mM) in acetonitrile containing NBu_4PF_6 (0.1 M) as supporting electrolyte at 100 mV/s. The initial scan voltammogram of the first cycle was done from left to right (initial potential 0.2 V vs SCE).

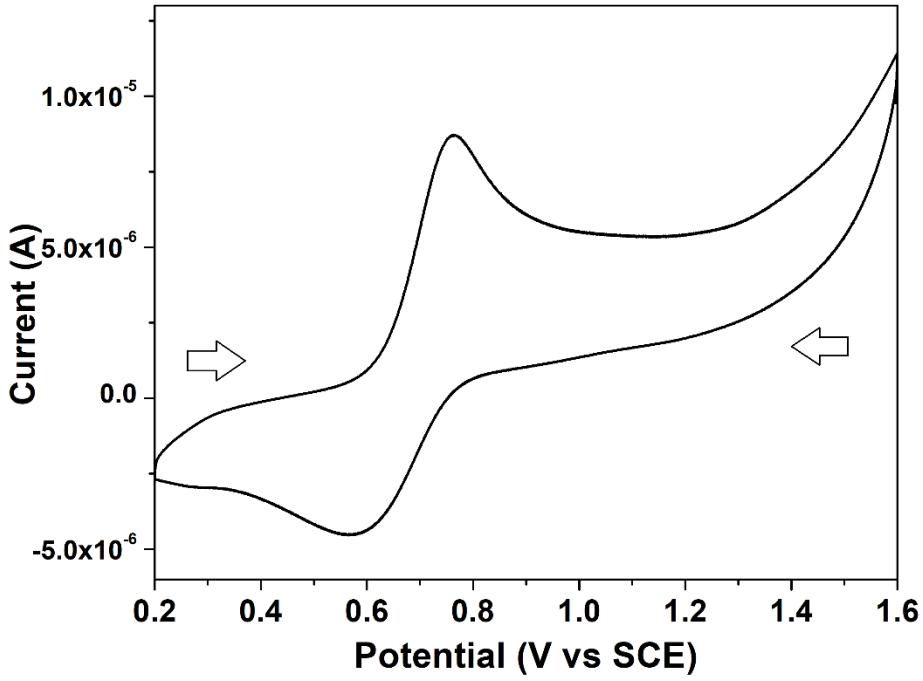

Figure A.60. Cyclic voltammogram of complex **12** (1 mM) in acetonitrile containing NBu_4PF_6 (0.1 M) as supporting electrolyte at 100 mV/s. The initial scan voltammogram of the first cycle was measured from left to right (initial potential 0.2 V vs SCE).

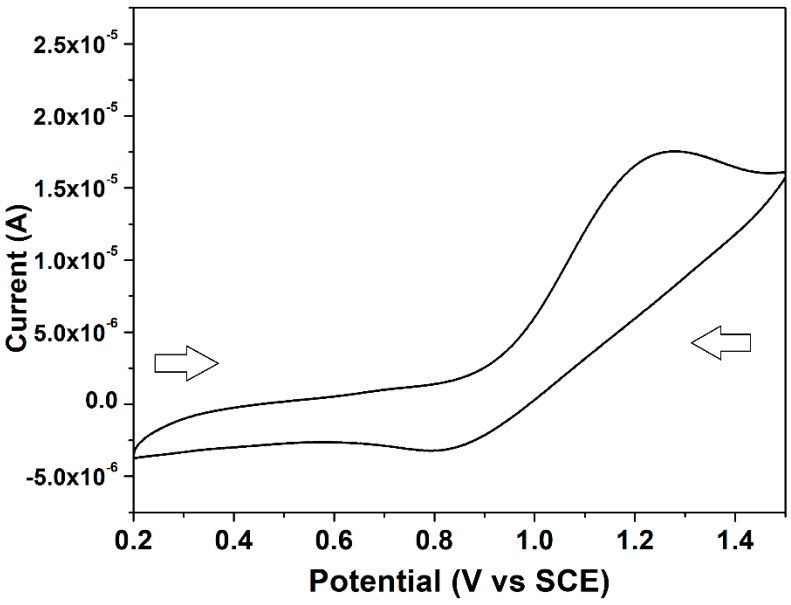

Figure A.61. Cyclic voltammogram of complex **3** (1 mM) in acetonitrile containing NBu_4PF_6 (0.1 M) as supporting electrolyte at 100 mV/s. The initial scan voltammogram of the first cycle was measured from left to right (initial potential 0.2 V vs SCE).

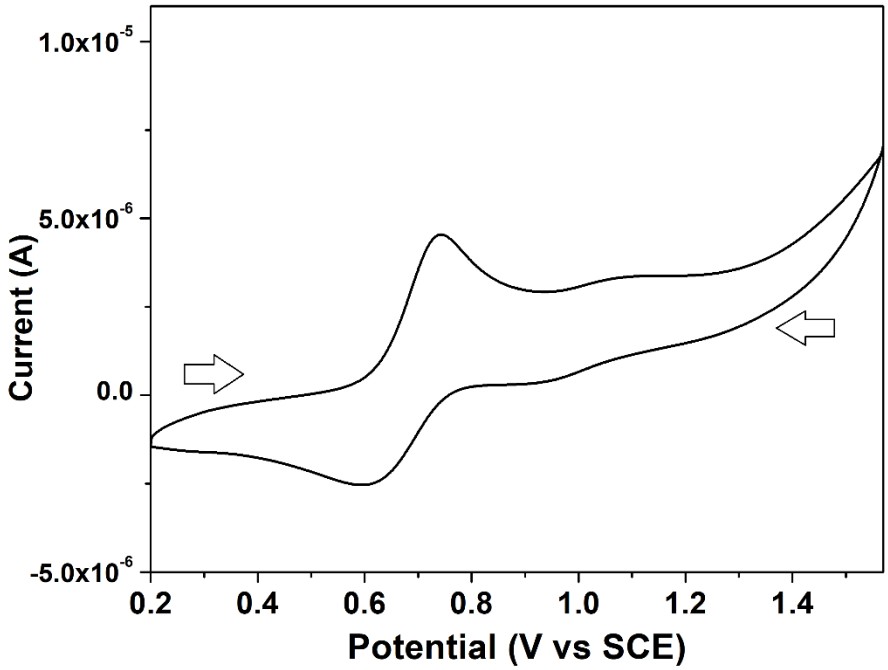

Figure A.62. Cyclic voltammogram of complex **13** (1 mM) in acetonitrile containing NBu_4PF_6 (0.1 M) as supporting electrolyte at 50 mV/s. The initial scan voltammogram of the first cycle was measured from left to right (initial potential 0.2 V vs SCE).

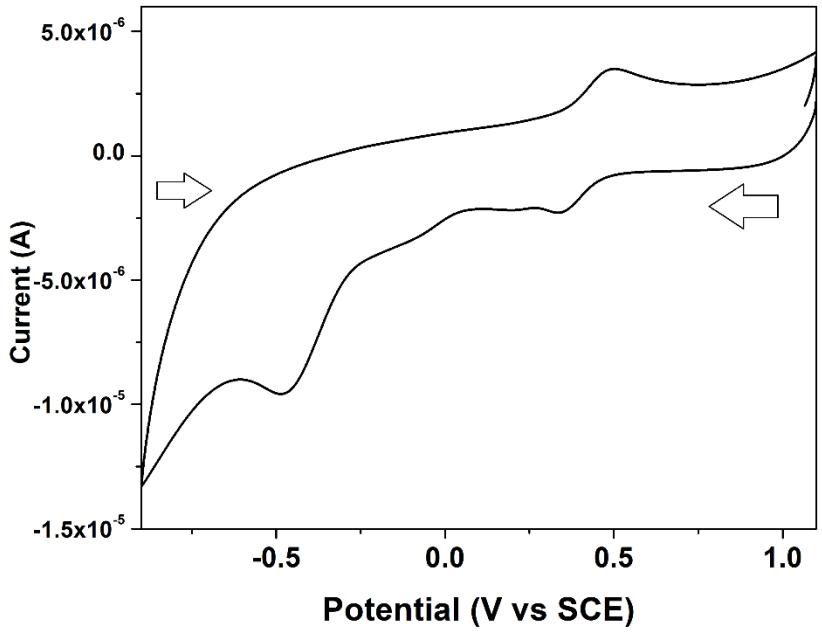

Figure A.63. Cyclic voltammogram of complex **14** (1 mM) in acetonitrile containing NBu_4PF_6 (0.1 M) as supporting electrolyte at 50 mV/s. The initial scan voltammogram of the first cycle was measured from right to left (initial potential 1.1 V vs SCE).

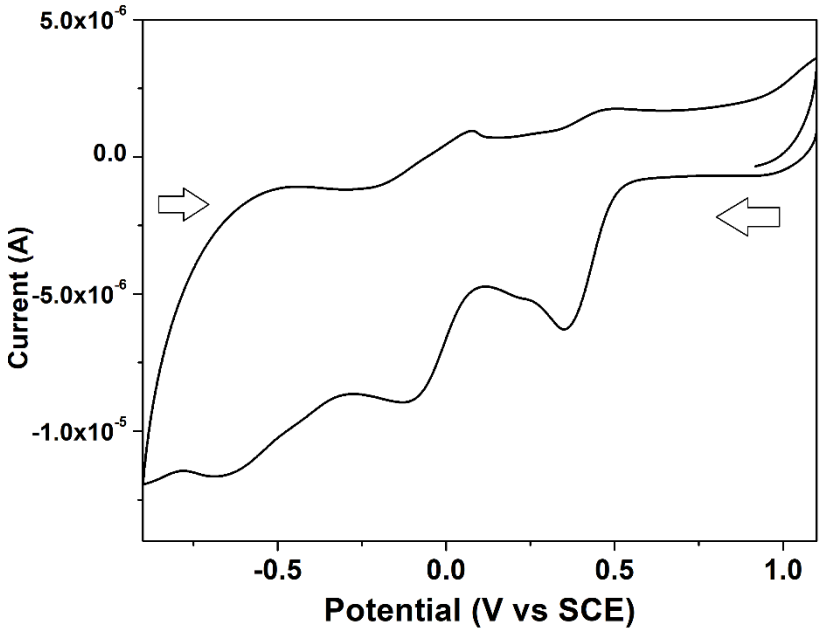

Figure A.64. Cyclic voltammogram of complex **15** (1 mM) in acetonitrile containing NBu_4PF_6 (0.1 M) as supporting electrolyte at 50 mV/s. The initial scan voltammogram of the first cycle was measured from right to left (initial potential 1.1V vs SCE).

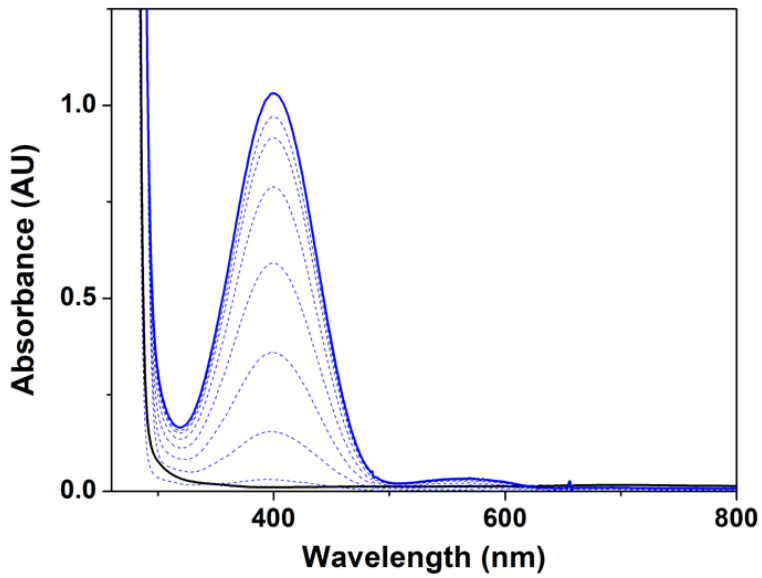

Figure A.65. Electronic absorption spectral changes showing formation of 3,5-DTBQ (blue trace) after addition of 3,5-DTBC (25 equivalents, 50 µl) to complex **1** (0.1 mM, black trace) in acetonitrile at 25 °C (path length = 1 cm).

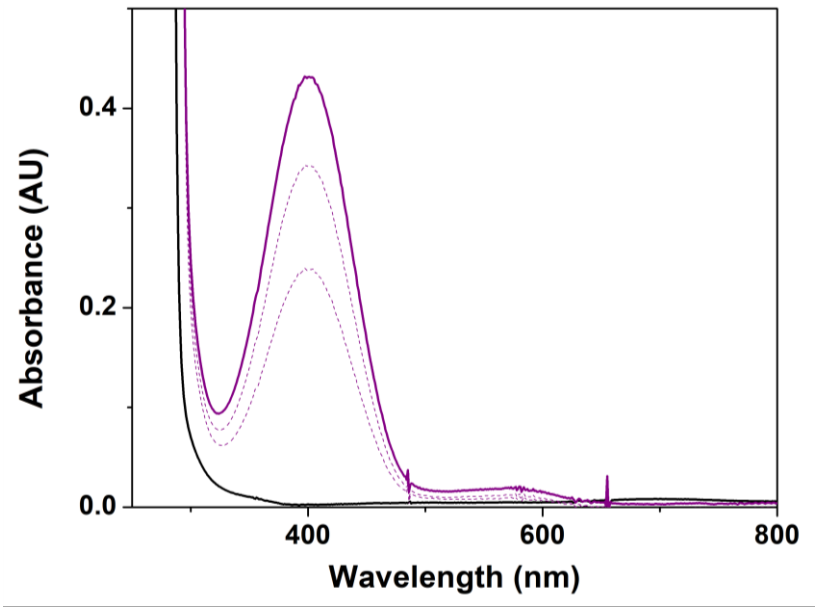

Figure A.66. Electronic absorption spectral changes showing formation of 3,5-DTBQ (purple trace) after addition of 3,5-DTBC (25 equivalents, 50 µl) to complex **3** (0.1 mM, black trace) in acetonitrile at 25 °C (path length = 1 cm).

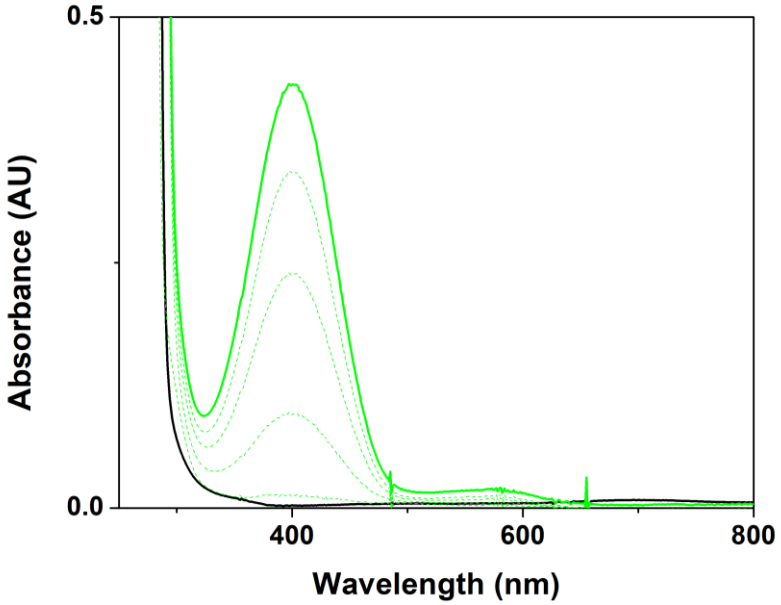

Figure A.67. Electronic absorption spectral changes showing formation of 3,5-DTBQ (green trace) after addition of 3,5-DTBC (25 equivalents, 50 µl) to complex **13** (0.1 mM, black trace) in acetonitrile at 25 °C (path length = 1 cm).

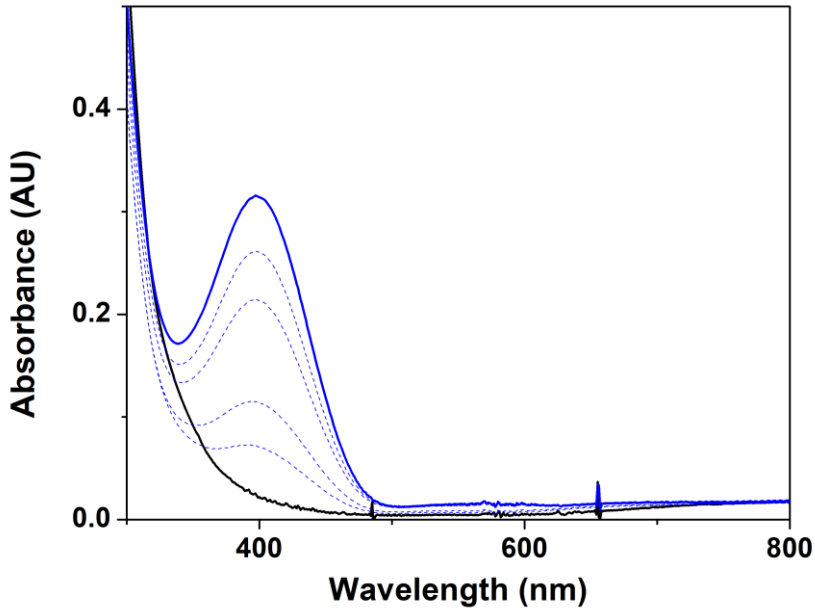

Figure A.68. Electronic absorption spectral changes showing formation of 3,5-DTBQ (blue trace) after addition of 3,5-DTBC (25 equivalents, 50 µl) to complex **14** (0.1 mM, black trace) in acetonitrile at 25 °C (path length = 1 cm).

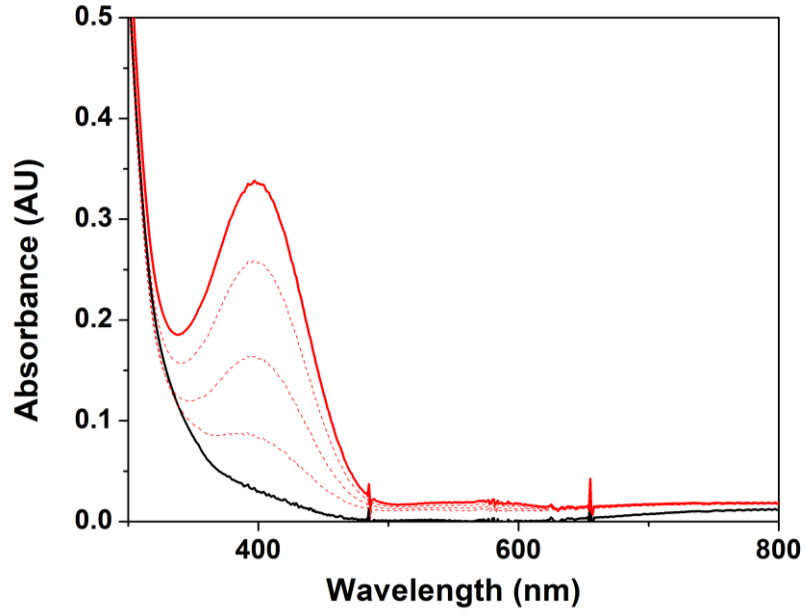

Figure A.69. Electronic absorption spectral changes showing formation of 3,5-DTBQ (red trace) after addition of 3,5-DTBC (25 equivalents, 50 µl) to complex **15** (0.1 mM, black trace) in acetonitrile at 25 °C (path length = 1 cm).

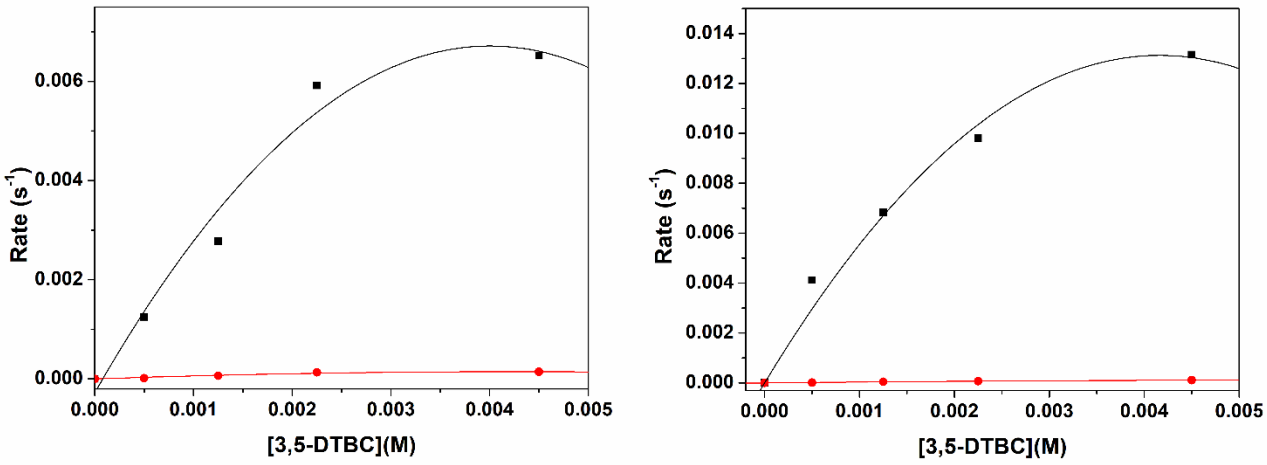

Figure A.70. Dependence of the first order reaction rate of the first (black trace) and second phases (red trace) on 3,5-DTBC concentrations for complexes **14** (left) and **15** (right).

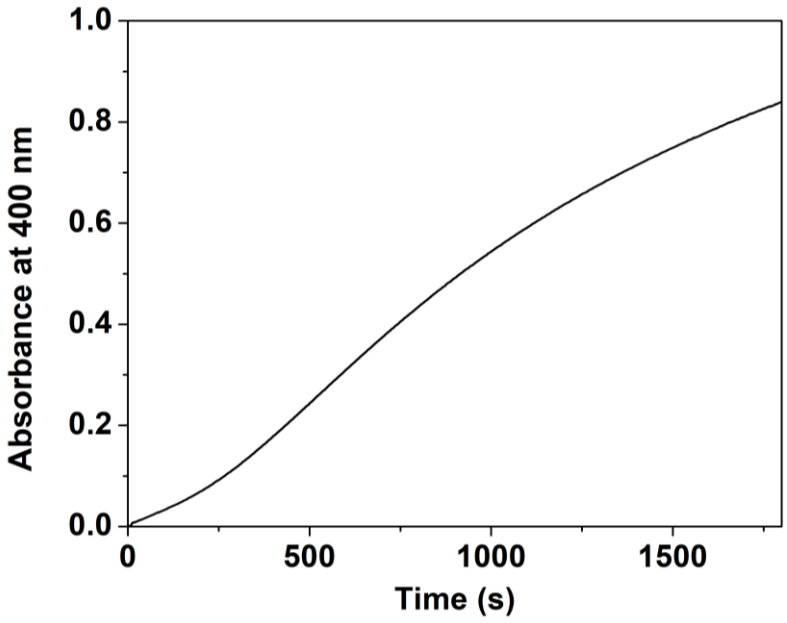

Figure A.71. Plot of absorbance at 400 nm versus time for Mn^{II}_2 complex **1**.

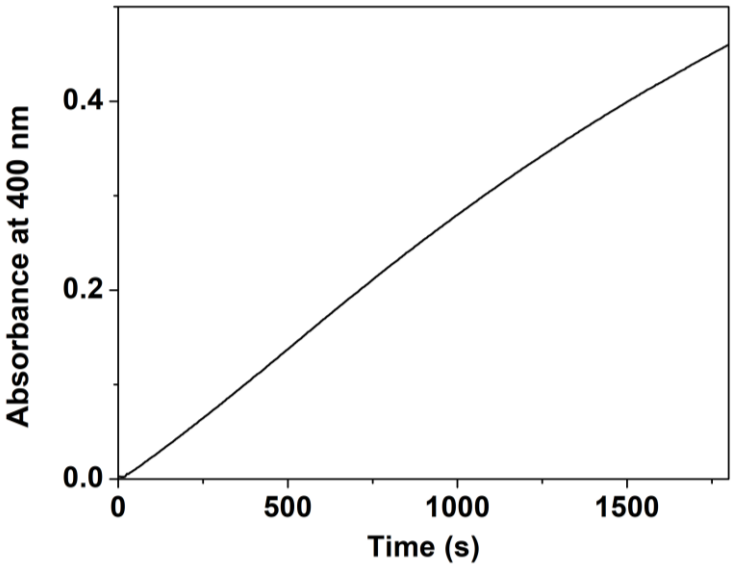

Figure A.72. Plot of absorbance at 400 nm versus time for Mn^{II}_2 complex **12**.

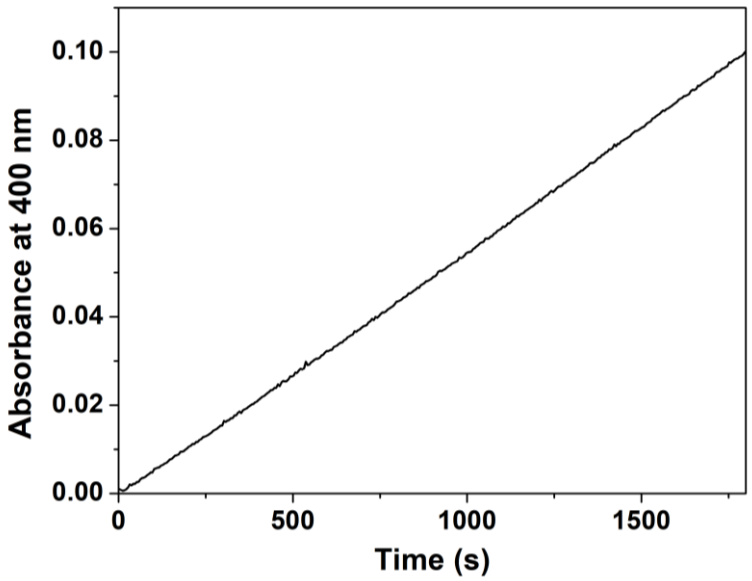

Figure A.73. Plot of absorbance at 400 nm versus time for Mn^{II}_2 complex **3**.

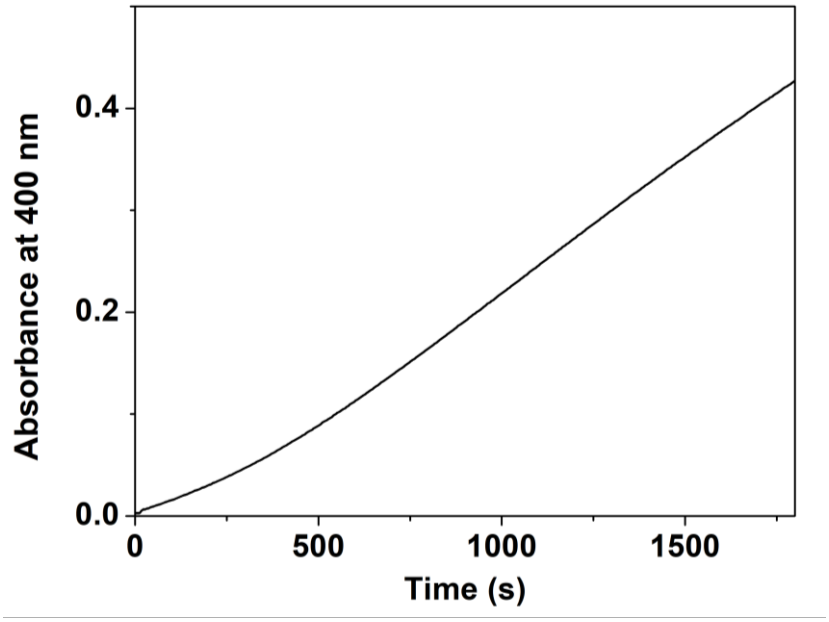

Figure A.74. Plot of absorbance at 400 nm versus time for Mn^{II}_2 complex **13**.

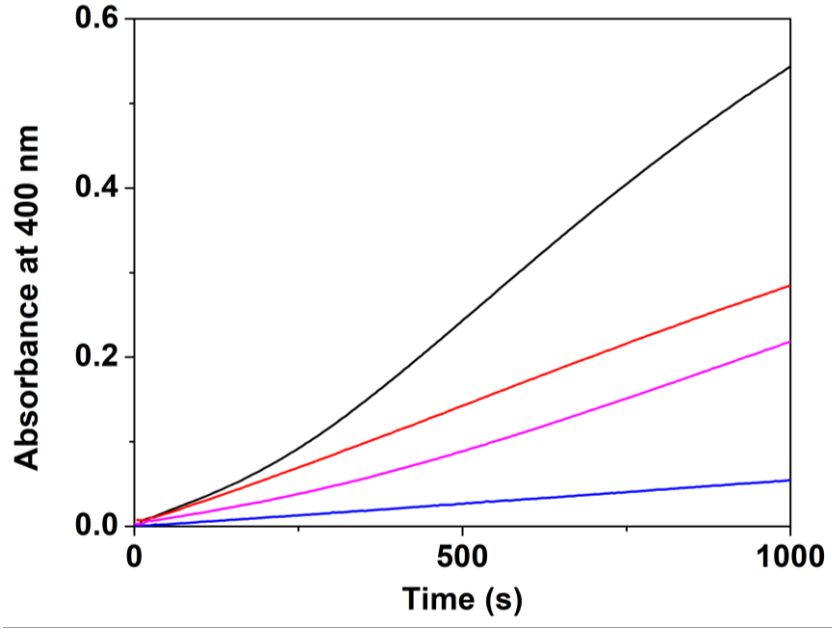

Figure A.75. Expansion of Figure 6.7, plot of absorbance at λ_{max} = 400 nm versus time for the reaction between Mn^{II}_2 complexes **1** (black trace), **12** (red trace), **3** (blue trace), and **13** (pink trace) and 25 equivalents 3,5-DTBC in acetonitrile.

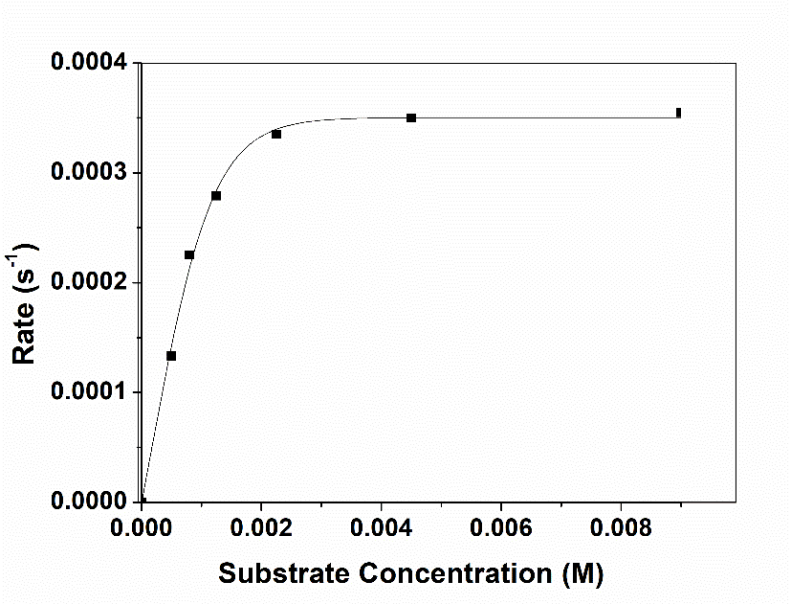

Figure A.76. Plot of first order approximate reaction rates of the second phase of the reaction of complex **12** against 3,5-DTBC concentrations.